

See discussions, stats, and author profiles for this publication at: <https://www.researchgate.net/publication/24316528>

An Experimental Investigation of Turbulent Boundary Layers Along Curved Surfaces--NASA CR-1940

Technical Report · April 1972

Source: NTRS

CITATIONS
58

READS
239

2 authors, including:



R.M.C. So

The Hong Kong Polytechnic University

419 PUBLICATIONS 6,300 CITATIONS

[SEE PROFILE](#)

Some of the authors of this publication are also working on these related projects:



Project

Laser interferometry [View project](#)



Project

Lattice Boltzmann Method [View project](#)

N72-22339

ASA CONTRACTOR
REPORT



NASA CR-1940

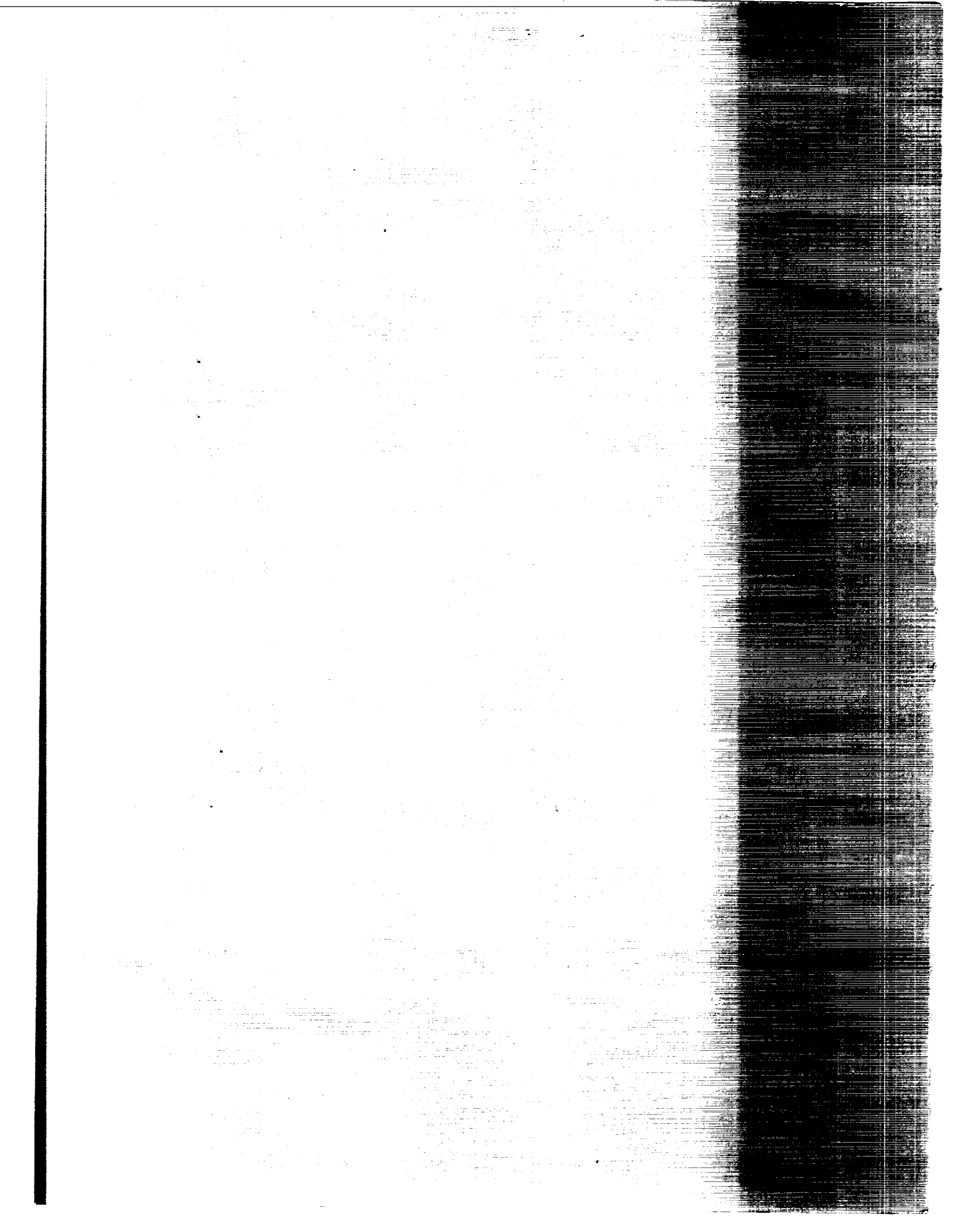
CAUTION
FILE COPY

AN EXPERIMENTAL INVESTIGATION
OF TURBULENT BOUNDARY LAYERS
ALONG CURVED SURFACES

by Ronald M. C. So and George L. Mellor

Prepared by
PRINCETON UNIVERSITY
Princeton, N.J.
for Lewis Research Center

NATIONAL AERONAUTICS AND SPACE ADMINISTRATION • WASHINGTON, D. C. • APRIL 1972



1. Report No. CR-1940	2. Government Accession No.	3. Recipient's Catalog No.	
4. Title and Subtitle AN EXPERIMENTAL INVESTIGATION OF TURBULENT BOUNDARY LAYERS ALONG CURVED SURFACES		5. Report Date April 1972	
		6. Performing Organization Code	
7. Author(s) Ronald M. C. So and George L. Mellor		8. Performing Organization Report No. ASM 979	
		10. Work Unit No.	
9. Performing Organization Name and Address Princeton University Princeton, New Jersey		11. Contract or Grant No. NGR 31-001-074	
		13. Type of Report and Period Covered Contractor Report	
12. Sponsoring Agency Name and Address National Aeronautics and Space Administration Washington, D.C. 20546		14. Sponsoring Agency Code	
15. Supplementary Notes Project Managers, S. Lieblein and A. V. Saule, V/STOL and Noise Division, NASA Lewis Research Center, Cleveland, Ohio			
16. Abstract <p>A curved wall tunnel was designed, and an equilibrium turbulent boundary layer was set up on the straight section preceding the curved test section. Turbulent boundary layer flows with uniform and adverse pressure distributions along convex and concave walls were investigated. Hot-wire measurements along the convex surface indicated that turbulent mixing between fluid layers was very much reduced. However, the law of the wall held and the skin friction, thus determined, correlated well with other measurements. Hot-wire measurements along the concave test wall revealed a system of longitudinal vortices inside the boundary layer and confirmed that concave curvature enhances mixing. A self-consistent set of turbulent boundary layer equations for flows along curved surfaces was derived together with a modified eddy viscosity. Solution of these equations together with the modified eddy viscosity gave results that correlated well with the present data on flows along the convex surface with arbitrary pressure distribution. However, it could only be used to predict the mean characteristics of the flow along concave walls because of the existence of the system of longitudinal vortices inside the boundary layer.</p>			
17. Key Words (Suggested by Author(s)) Turbulent boundary layers Curved surfaces Experimental investigation		18. Distribution Statement Unclassified - unlimited	
19. Security Classif. (of this report) Unclassified	20. Security Classif. (of this page) Unclassified	21. No. of Pages 269	22. Price* \$3.00

* For sale by the National Technical Information Service, Springfield, Virginia 22151

TABLE OF CONTENTS

	<u>Page</u>
CHAPTER I General Consideration	1
1.1 Introduction	1
1.2 A Brief Discussion of Previous Work	3
1.2.1 Fully Developed Curved Turbulent Flows	3
1.2.2 Turbulent Boundary Layers Along Curved Surfaces	5
1.3 Present Objectives	7
CHAPTER II Experimental Program	10
2.1 Curved Wall Tunnel	10
2.1.1 Description of Tunnel	10
2.1.2 Geometry of Curved Test Walls	11
2.2 Measurement Techniques and Instrumentations	12
2.2.1 Wall Static Pressure	12
2.2.2 Yaw Measurements	13
2.2.3 Velocity Profiles	15
2.2.4 Hot-Wire Equipment and Calibration	19
2.2.5 Hot-Wire Technique	21
2.2.6 Mapping of the Longitudinal Vortex System	24
2.3 Qualification of Curved Wall Tunnel	26
2.3.1 Two-Dimensional Equilibrium Turbulent Flow in Straight Section	26
2.3.2 Pressure Distribution on Curved Test Walls	29
2.3.3 Secondary Flow in Curved Test Sections	32
2.4 Data Reduction	35
2.4.1 Calculation of Velocity Profiles	35
2.4.2 Skin Friction Deduction	36
2.4.3 Calculation of Reynolds Stresses	37
CHAPTER III Results and Discussion	41
3.1 Constant Pressure Flow Along Convex Wall	41

TABLE OF CONTENTS
(con.)

	<u>Page</u>	
3.2 Separating Flow Along Convex Wall	50	
3.3 Constant Pressure Flow Along Concave Wall	55	
CHAPTER IV	Theoretical Predictions of Curved Turbulent Boundary Layers	64
4.1 Introduction		64
4.2 Boundary Layer Equations for Curved Flow and the Momentum Integral		67
4.3 The Eddy Viscosity Hypothesis		74
4.4 Determination of ℓ_1/Λ		77
4.5 Reduction of the Set of Boundary Layer Equations to an Ordinary Differential Equation		81
4.6 Comparison with Present Data		85
4.6.1 Turbulent Boundary Layers along Convex Surfaces		86
4.6.2 Turbulent Boundary Layers along Concave Surfaces		89
CHAPTER V	Concluding Remarks	93
5.1 Conclusions		93
5.1.1 Turbulent Boundary Layers along Convex Surfaces		93
5.1.2 Turbulent Boundary Layers along Concave Surfaces		95
5.1.3 Theoretical Predictions		96
5.2 Recommendations for Future Work		97
APPENDICES	A Construction Details of Curved Wall Tunnel	98
	B Positioning and Accuracy of the Various Probes	102
	C Fully Developed Turbulent Pipe Flow Experiment	108
	D Curved Boundary Layer Equations Through Method of Matched Asymptotic Expansion	110
	E Derivation of the Turbulence Energy Equations for Curved Boundary Layers	119
REFERENCES		124
FIGURES		128

TABLE OF CONTENTS
(con.)

	<u>Page</u>	
TABLES OF RESULTS		
Tables 1-12	Constant Pressure Flow Along Convex Wall	226
Tables 13-25	Separating Flow Along Convex Wall	238
Tables 26-35	Constant Pressure Flow Along Concave Wall	251

NOTATION

English Letters

A	constant as defined in equations (2.2.4-1) or (3.1-3) or (4.4-1)
$a = \frac{\delta}{R}$ or $\frac{\delta^*}{R}$	curvature parameter
B	constant as defined in equations (2.2.4-1) or (3.1-2) or (4.4-2)
$b_1 \dots b_5$	functions as defined in equation (4.5-10)
$c_1 \dots c_b$	functions as defined in equation (4.5-8)
$c_f = \frac{\tau_w}{1/2 U_{pw}^2}$	skin friction at the wall
\bar{e}	mean value of hot-wire signal
$\overline{e'}^2$	mean square value of hot-wire signal
e_o	zero flow voltage of hot-wire signal
$f'(x, \eta) = \frac{U_p - U}{U_p}$	non-dimensional velocity defect
$H = \frac{\delta^*}{\theta}$	shape factor
h	linearizer calibration constant
K	non-dimensional curvature of surface
$k = \frac{1}{R}$	curvature of surface
ℓ	Prandtl's mixing length or characteristic length
ℓ_1	length scale as defined by Mellor and Herring (1970) and in equation (E-7)

English Letters

m	constant as defined in equation (2.2.4-1) or an integer in equation (4.4-2)
n	an integer in equation (4.4-1)
P	mean pressure
p	fluctuating pressure
Q	magnitude of mean flow velocity
\bar{q}	velocity vector
$q^2 (\bar{u}^2 + \bar{v}^2 + \bar{w}^2)$	turbulence energy
R_e	Reynolds number
$R(x)$	radius of curvature of surface
R_o	radius of curvature of surface at entrance to curved section
r	radius of curvature
s	arc length
T_{ij}	viscous stress tensor
U	mean flow velocity in x-direction
U_p	potential velocity
U_{pw}	potential velocity at the wall
u	fluctuating velocity in x-direction
u_t	characteristic velocity inside boundary layer
$u^2 = \frac{\tau_w}{\rho}$	friction velocity
u'	root mean square of u
v	mean flow velocity in y-direction

English Letters

v	fluctuating velocity in y-direction
v'	root mean square of v
w	fluctuating elocity in z-direction
w'	root mean square of w
X	non-dimensional x-coordinate
x	x-coordinate
Y	non-dimensional y-coordinate in Outer or Inviscid Region
y	y-coordinate or non-dimensional y-coordinate in Middle or Defect Region
\hat{y}	non-dimensional y-coordinate in Inner or Viscous Region
z	z-coordinate

Greek Letters

β	angle between mean flow velocity and x-coordinate as defined in Figure 18
γ	angle of inclination of slanted hot-wire; 45°
$\Delta = \int_0^\infty \frac{U_p - U}{U_\tau} dy$	characteristic boundary layer length scale
Δ_t	length scale in Middle or Defect Region
δ	boundary layer thickness or angle of rotation as defined in Figure 18
$\delta^* = \int_0^\infty (1 - \frac{U}{U_p}) dy$	displacement thickness
$\epsilon = \frac{u_t}{U_0}$	small parameter as defined by Mellor (1970)
$\hat{\epsilon} = \frac{1}{2} \frac{v}{U_0 \ell}$	small parameter as defined by Mellor (1970)

Greek Letters

ζ	vorticity in z-direction
$\eta = \frac{y}{\delta^*}$	non-dimensional y-coordinate
$\theta = \int_0^\infty \frac{U}{U_p} (1 - \frac{U}{U_p}) dy$	momentum thickness
θ	angle of inclination of slanted probe; 46°
κ	von Karman constant
Λ	length scale as defined by Mellor and Herring (1970) and in equation (E-6)
ν	molecular viscosity
ν_e	eddy viscosity
ν_{e_F}	corresponding flat plate eddy viscosity
ρ	density
τ	shear stress
τ_{ij}	fluctuating viscous stress tensor
ϕ	angle between normal to sensor and direction of mean flow
$\phi = \frac{\nu_e}{U_{pw} \delta^*}$	eddy viscosity function
$\phi_{\ell_1}(x) = \frac{\ell_1 q}{\nu}$	
$\phi_{\Lambda}(x) = \frac{\Lambda q}{\nu}$	wall function as defined by Mellor and Herring (1970)
$x = \frac{yq}{\nu}$	

Subscripts

1	free stream condition
---	-----------------------

Subscripts

F	corresponding flat plate quantities
i	inner wall or indicated value
L	linearizer output
o	outer wall
p	potential quantities
pw	potential quantities at the wall
r	reference state
s	static quantities
sw	static quantities at the wall
t	total quantities
w	wall quantities

Chapter I
GENERAL CONSIDERATIONS

1.1 Introduction

In both external and internal aerodynamics, most of the problems involve boundary layer flows over curved surfaces. Some of these flows are fully developed, while others are not. In the past, investigators have been content to treat these boundary layer flows by assuming that the curvature of the mean flow streamlines in planes normal to the surface, and the associated static pressure variation across the boundary layers do not influence the flow significantly, if the radius of curvature of the surface is much larger than the boundary layer thickness. With such simplification, the many problems in viscous aerodynamics can be solved by making use of the vast amount of data collected in the study of fully developed pipe/channel flows and two-dimensional boundary layers. This assumption is known to be correct approximately in laminar flow, since the effects of the additional curvature of the mean flow streamlines are known to be of second order smallness (see van Dyke 1962). These small effects arise from the kinematics of curved flow, and the curvature of mean flow streamlines has little influence on the magnitude and distribution of the viscous stresses.

On the other hand, turbulent flows are very sensitive to the curvature of the mean flow streamlines. The additional curvature influences the flow in a manner which is not known at present, but is believed to be significant enough to change the detail flow mechanism completely. This is evident from an examination in some detail of the observed phenomena in a turbulent boundary layer on a flat surface.

Very close to the wall, there appears to be a region where the fluid motion is still predominantly viscous, and the velocity rises steeply. Further away, the flow becomes unstable, and finally, a

region is reached where the entire flow is involved in turbulent motion. Recent detailed experimental studies by Schraub and Kline (1965) have revealed that the viscous region is not truly undisturbed. Rather, relatively large elements of low velocity fluids adjacent to the surface of the viscous sublayer periodically lift off the surface and move towards the fully turbulent region. There they join a pattern of decaying turbulence. The mechanism responsible for this phenomenon is not fully understood. However, it can be attributed to the instability of the flow near the outer edge of the viscous sublayer, and also due to the action of the outer flow which operates mainly by pressure fluctuations transmitted to the sublayer. Since continuity dictates that fluid must replace the elements which lift off the surface, elements of highly energetic fluid will have to move in from further out. In turn, these highly energetic fluid may supply the energy to eject the elements from the surface. At any rate, turbulence in the fully turbulent region is generated and maintained by the elements originating at the surface.

With this picture in mind, one can see why turbulent flows are very sensitive to curvature of the mean flow streamlines. For flows over convex surfaces, the centrifugal force on a fluid particle must be balanced by an inward pressure gradient. If a particle is moving too slowly, its centrifugal force is too small, and it moves inwards. As a result, the fluid elements, which lift off from the surface carrying with them the velocities at the points where they come from, will have a smaller centrifugal force at their new locations. Therefore, they will be pushed inwards by the pressure gradient and the interchange of momentum and energy between the faster and the more slowly moving fluids are hindered. As a result, the boundary layer is thinner at the wall. Observations of flows between rotating cylinders by Taylor (1936) confirmed this and showed a very large reduction in turbulent shear stress. In contrast with this, the destabilizing effect of

centrifugal forces on concave walls leads to the formation of Taylor-Gortler type vortices which promote transition to turbulence. Therefore, it is quite possible that turbulent boundary layers on curved surfaces may differ appreciably from that on a flat plate with the same distribution of external pressure.

Before proceeding any further, it is felt that a discussion of previous work is most essential in that it not only points the way for further work in curved turbulent flows, but that it also indicates the logical line of attack for the present investigation. For purpose of clarity, the discussion is divided into two sections. The first section deals mainly with fully developed flows, while the second touches on turbulent boundary layers along curved surfaces. In anticipation of the fact that the flow phenomenon in turbulent boundary layers along concave surfaces are different from that along convex surfaces, distinction will be made between these two types of flow in the discussion below.

1.2 A Brief Discussion of Previous Work

1.2.1 Fully Developed Curved Turbulent Flows

Since the flow near a surface is determined to a large extent by local conditions and to a lesser extent by the action of the outer flow which operates mainly through pressure fluctuation transmitted to the region near the surface, one can expect the flow in the vicinity of the wall to be the same, be it a boundary layer flow or a fully developed flow. This is true for straight flows and data obtained from pipe flow measurements lead to the establishment of the Law of the Wall. With only the additional effects of the curvature of the mean flow streamlines which are known to be of second order smallness only if the flow is viscosity dominant, one would expect the curvature to have very little effect on the flow close to the wall*. As a result, one can expect

*This fact is at least partially supported by the vast amount of flat plate pressure gradient data in which the mean flow streamlines are also curved due to rapid boundary layer growth.

the Law of the Wall to hold also in a curved flow. However, the measurements of Wattendorf (1935) in two curved channels of constant curvature and a ratio α of half channel width to mean radius of curvature of 1/19 and 1/9 do not lend evidence to such an argument. Rather, Wattendorf found that the deviation from the Law of the Wall was in opposite directions for opposite signs of curvature, and that the deviation increased with curvature.

Eskinazi and Yeh (1956) did similar measurements in a curved channel of constant curvature and with $\alpha = 1/19$. They found that the deviation from the Law of the Wall does not start until about $y_{\tau}/v \sim 200$. Indeed, the deviation was in opposite directions for opposite signs of curvature. This did seem to indicate the existence of the Law of the Wall region. From their data, Eskinazi and Yeh concluded that U/u_{τ} is not only a function of y_{τ}/v , but also of y/r or some combination of the two.

For fully developed turbulent flow in a curved channel of constant curvature, the turbulent shearing stress would, in the momentum transfer theory, be given by

$$- \overline{uv} = \nu_e \left\{ \frac{1}{r} \frac{\partial}{\partial r} (ur) \right\}$$

where ν_e is the eddy viscosity. This requires the shearing stress to vanish at $\frac{\partial}{\partial r}(ur) = 0$. However, both Wattendorf and Eskinazi and Yeh found that the point of zero \overline{uv} did not coincide with the point of zero $\frac{\partial}{\partial r}(ur)$. Hence, Eskinazi and Yeh concluded that there was a region between these two points in which the product $\overline{uv} \frac{\partial}{\partial r}(ur)$ was positive. This meant that in this region, the turbulent energy in $\overline{u^2}$ was being suppressed by Reynolds stress working on the mean momentum gradient.

Besides mean flow measurements Eskinazi and Yeh also made detailed turbulence measurements and found that the turbulence intensities were

greater on the outer (concave) wall and smaller on the inner (convex) wall compared to corresponding points in a straight channel. In an inviscid, irrotational curved flow, the radial equilibrium of a fluid element is stable if the radial gradient of angular momentum is negative. Eskinazi and Yeh were the first to show that these considerations also apply to curved turbulent flows.

1.2.2 Turbulent Boundary Layers on Curved Surfaces

The effect of curvature on turbulent boundary layer was first investigated by Wilcken (1930) on both the convex and concave surfaces. It was then followed by Schmidbauer (1936) who studied the flow over convex surfaces only. In both these experiments, δ/R was at most .025 . From his measurements, Wilcken concluded that the eddy viscosity was much greater for the flow near the outer (concave) wall than that near the inner (convex) wall, and that the mixing length at the outer wall was found to be considerably larger than for a flat surface. Although no turbulence measurements were made, these results seem to lend evidence to the fact that with concave surface, the turbulence is strongly increased while with convex walls, it is reduced. Wilcken explained this by arguing that the centrifugal forces at the outer wall promote, while it diminishes near the inner wall, the turbulent exchange between adjacent fluid layers. Hence, the rapid thickening of the boundary layer on the outer wall is due also to the increased turbulence activity. The opposite is true on the convex wall. In connection with this, Schmidbauer's data also showed a decrease in the boundary layer thickness. However, Wilcken's results were somewhat obscured by disturbing side influences, which were mainly caused by pressure conditions at the beginning and end of the channel. In addition, the disturbing effect of the secondary flow may also have influenced the boundary layer development on both the inner and outer walls of the channel.

The work of Schneider and Wade (1967) did nothing to eliminate the

secondary flow influences. In fact, it is quite a bit more pronounced because the aspect ratio of the test section varies from 1 at the entrance to 2 at the exit. Also, the flow in the test section was one of constant acceleration. As a result, it was little wonder why their data do not correlate well with the Law of the Wall.

Through detailed measurements in a 180° bend, Patel (1968b) demonstrated that the boundary layer on the convex wall was relatively two-dimensional near the center line for the first 80° of the bend. Thus, he managed to establish that the boundary layer development on the convex wall near the center line of an 80° curved duct was relatively free from the influence of secondary flow. In contrast to previous work, the boundary layer investigated by Patel (1968a) has a maximum value of $\delta/R \sim 0.1$. However, Patel did nothing to change the pressure distribution on the convex wall of the curved duct, and in the opinion of the present author, his data is subjected to the same shortcomings as that of Wilcken in that it is hard to separate the curvature effects from the pressure gradient effects.

The flow between two concentric cylinders with the inner one in motion while the outer one remains at rest affords a good example of the unstable stratification causes by the additional centrifugal forces acting on the fluid particles. Since the velocity is higher near the inner cylinder, the fluid particles experience a higher centrifugal force, and as a result, the fluid particles will have a tendency to move outward. Taylor (1938) was the first to observe that when a certain Reynolds number is exceeded, longitudinal vortices with axes located along the circumference begins to appear. A similar vortex system was being observed by Gortler (1940) for flows along concave walls. The analogy can also be drawn between the flow along a concavely curved surface and that along a heated horizontal plate. Gortler (1959) showed that the buoyant force in the thermally stratified layer also gives rise to a system of longitudinal vortices. Noting that the

mechanism responsible for the existence of the longitudinal vortex system is the same for these three different flows, one will naturally ask whether such a system would also exist in a fully turbulent flow along a concave surface, and if so, would the system of vortex be stationary. In addition, one would like to find out the effect of such a vortex system on the development of the boundary layer along the concavely curved surface.

Tani (1962) was the first to demonstrate the existence of the longitudinal vortices in the turbulent boundary layer along a concave wall. According to Tani, the resultant wave amplitude of the vortices decreased as the radius of curvature of the surface was increased. More recently, Patel (1968b) found that the longitudinal vortices also appeared on the concave wall of his 180° channel, and suggested that before studying the influence of concave curvature on a two-dimensional turbulent boundary layer, one should examine these vortices in detail so as to determine the curvature parameter that would govern the appearance and strength of these vortices.

1.3 Present Objectives

A great many mathematical models of physical phenomena are very complicated and are highly nonlinear in nature. With the present knowledge of nonlinear equations, most of these models cannot be solved in full. Usually, simplifying assumptions are necessary to reduce these equations to a more manageable form. In so doing, the researcher is faced with the difficulty of deciding which effects or variables are more important. Experimental studies are designed to provide such information. Not only will the experimental results reveal the most significant features of a physical phenomenon (provided the experimental work is designed and carried out properly), they will also provide empirical correlations for the theoretical researcher, thus, enabling the researcher to make further simplifications of the

mathematical model and eventually obtain a solution to the particular problem.

In connection with this, Coles (1962) has pointed out that the most useful data are those in which one physical effect or parameter is varied at a time. Well designed experiments should be able to separate the various physical effects and isolate them for investigation, thus allowing the researcher to comprehend the significance of these various effects easily. Fully developed turbulent flows in pipes and channels and flat plate turbulent boundary layer with the pressure gradient carefully controlled, have led Clauser (1954, 1956) to the formulation of the concept of the equilibrium boundary layer.

In keeping with the idea that one variable should be varied at a time, the present experiments are so designed that curvature alone is isolated for investigation. Due to the presence of the pressure gradient across the boundary layer in flows along curved walls, it is hard to avoid the streamwise pressure gradient in the flow along a flat surface joining smoothly to a curved surface. However, the pressure change in the streamwise direction should be minimized, so that the flow can recover from the pressure effect in a relatively short distance. Means of doing this are incorporated in the boundary layer tunnel that is specially designed for the present investigation. (This will be discussed further in Chapter II.) Provisions are also made for the variation of streamwise pressure distribution along the curved wall, so that both constant pressure and pressure gradient data can be obtained. Because of the need to be able to establish constant pressure on both convex and concave surfaces, it is apparent that a single test section cannot provide such versatility. Therefore, separate test sections, one with convex curvature and one with concave curvature, are required. Again, provisions are made in the tunnel so that the test section can be changed without too much trouble. No attempt has been made to obtain data for several values of the curvature parameter, instead it has

been decided to study the flow phenomenon in more detail in addition to the usual velocity profile measurements.

Thus, the objective of the present investigation is to provide both empirical knowledge and physical understanding in the following areas. These areas are: (a) constant pressure flow along convex surface, (b) separating flow along convex surface, and (c) constant pressure flow along concave surface. In case (a), the curvature parameter is kept constant, but is varied along the flow in case (b). For both cases (a) and (b), velocity profiles were obtained from pitot measurements across the boundary layers while a rotating wire technique proposed by Fujita and Kovasznay (1968) was used to measure the various components of the Reynolds stress tensor.

In view of the fact that the flow along a concave surface is different from that along a convex surface, the system of longitudinal vortices that exists was mapped out first using fixed hot-wires. Then, the rotating-wire technique was used to measure the various components of the Reynolds stress tensor at both the positions of the crest and trough of the wave system.

Following a discussion of the various test equipment and their qualification in Chapter II, the results are examined and critically analyzed in Chapter III, and the Law of the Wall is established for flows along convex surfaces. In Chapter IV, a self-consistent set of equations for curved turbulent boundary layer flows is derived, together with an eddy viscosity which is modified to include curvature effects. The predictions by this model are then compared with the experimental results. Chapter V summarizes all the results and recommendations for future work are also given.

Chapter II
EXPERIMENTAL PROGRAM

2.1 Curved Wall Tunnel

2.1.1 Description of Tunnel

The construction of the curved wall tunnel used in the present investigation is described in detail in Appendix A. The diagrammatic layout of the tunnel is shown in Figure 1 and a picture of the curved wall tunnel is given in Figure 2. Briefly, the wind tunnel is of the open-return suction type and is powered by a two speed, 10 H.P. fan. The Reynolds numbers per unit length corresponding to these two speeds are 4.37×10^5 and 7.56×10^5 respectively. The wind tunnel is less quiet and the vibration due to the fan is more severe at the higher speed. As a result, all runs on both the convex and concave test walls were conducted at the lower Reynolds numbers. Originally the entry to the tunnel was made up of three layers of honey-comb flow straightener separated by screens. However, it was found that the unit cannot provide sufficient straightening effect to prevent unsteadiness in the flow. Later, through observation of tufts, the unsteadiness was shown to be due to the unsteady ingestion of vortices which formed on the floor of the room. To remedy the situation, two more layers of honey-comb straightener separated by screen together with a bell-mouth were added to the entrance of the tunnel. The traversing of tufts behind the last screen then showed that the entire unit has sufficient straightening effect to prevent unsteadiness in the flow, and that the flow is quite parallel.

A contraction section that has a contraction ratio of 6 to 1 is installed behind the flow straightener. The straight section that follows is 4 feet long and has a cross-section of 6 inches by 48 inches. The remainder of the tunnel consists of the curved test section which has a fixed test wall of varying curvature and an adjustable opposite

wall, the exit diffuser and the fan and motor housing. The adjustable wall allows the pressure distribution on the curved test wall to be adjusted to give any arbitrary pressure distribution.

Two curved test sections were made; one has a convex test wall, while the other has a concave test wall. The whole tunnel was so constructed that the test section could be connected to and disconnected from the straight section and the exit diffuser with relative ease. In order to accommodate the adjustable wall in the curved test section, the exit diffuser was constructed in such a manner that one movable wall was all that was required to fit the test section with either the convex or concave test walls. End wall jets were installed at the entrance to the curved test section to limit the secondary flow in the test section to small regions near the end walls. In addition, it was found necessary to have a side wall jet installed on the wall opposite the convex test wall. However, with a concave test wall, the side wall jet was found unnecessary. Further discussions of the significance of the side wall jet and the end wall jets will be given in Sections 2.3.2 and 2.3.3 respectively.

Wall static pressure taps made of .032 inches O.D. stainless tubing were installed in the walls of the tunnel. For the straight section where the wall is 9/16 inches thick, the tubings were cemented into slots milled into the walls of the tunnel. The extruded tubings were then sanded flush with the surface. For the curved test section where the walls are only 1/32 inches thick, it was found necessary to solder a square metal plate to the tubings. The tubings were then installed into holes drilled into the wall, and then secured in place by soldering the plate onto the wall. Again, the tubings were sanded flush with the surface. Thus, the resultant pressure taps were of the sharp edged, deep hole type.

2.1.2 Geometry of Curved Test Walls

In designing the curved wall, an original objective was to achieve

an equilibrium constant pressure profile characterized, however, by a constant value of the curvature parameter, δ^*/R . Using simple flat plate turbulent boundary layer theory, an estimate of $\delta^*(x)$ is obtained by assuming

$$\delta^*(x) = \frac{.037x}{Re_x^{1/5}} \quad (2.1.2-1)$$

The empirical relation provides values of $R(x)$ if the curvature parameter is maintained constant. For the convex wall, the constant is taken to be .01, while for the concave wall, the constant is assumed to be .007. The results are displayed in Figures 3 and 4 for the curved walls respectively.

2.2 Measurement Techniques and Instrumentations

2.2.1 Wall Static Pressure

A row of wall static pressure taps is provided on the tunnel center line in both the straight test wall and the curved test wall. In addition, two rows of pressure taps, 14 inches above and below the tunnel center line, are provided on the curved test walls. With the convex test wall, the pressure taps are spaced as follows. The first pressure tap in the tunnel center line is situated at $x = 4$ inches (see Figure 5), then every 10 inches until $x = 44$ inches, then every inch until $x = 58$ inches, then every 2 inches until $x = 78$ inches where the last pressure tap is situated. The off center line pressure taps are situated at $x = 51, 57, 62, 68, 72$ and 76 inches respectively. With the concave test wall, the pressure taps in the tunnel center line start at $x = 6$ inches (see Figure 6), then every 10 inches until $x = 46$ inches, then every 4 inches until $x = 54$ inches, then every inch until $x = 70$ inches, then every 2 inches until $x = 110$ inches where the last pressure tap is situated. The off center line pressure taps start at $x = 46$ inches and are spaced at 4 inches apart until $x = 110$ inches.

The pressure taps along the tunnel center line are used for the measurement of the potential velocity at the surface while the off center line pressure taps are used only for checking the pressure variation in the transverse direction. They also serve to indicate the influence of the secondary flow (see Section 2.3.3).

The wall static pressure taps are connected to the negative port of a Pace Model CP510-.1 PSID pressure transducer. The positive port of the pressure transducer is connected to a reference pressure which is provided by a pitot tube situated in the free stream near the tunnel entrance. The transducer output is connected to a DISA Model 55 D30 Digital DC Voltmeter which can be read to .001 volts. The transducer has a maximum output of 5 volts and this corresponds to a pressure of 3.51 inches of alcohol (sp. gr. = 0.791). Static calibration of the pressure transducer is carried out against a micro-manometer for the pressure range 0 - 1 inch of alcohol, and against a manometer which reads to within .02 inch of alcohol for the pressure range of 1 - 4 inches of alcohol. The calibration was checked from time to time and it was found that the calibration curve was quite repeatable.

2.2.2 Yaw Measurements

In the wall regions the centrifugal acceleration of the low velocity end-wall boundary layer flows cannot balance the pressure gradient impressed by the main stream. The resultant end-wall cross flows or secondary flows influence the flow near the tunnel center line and it may no longer be two-dimensional. Theoretically, if the aspect ratio of the channel is large enough, the secondary flow will be confined to a small region near the end walls, and the flow in the core will be essentially two-dimensional. The present tunnel has an aspect ratio of 8 in the straight section and varies to a minimum of 6.2 in the curved test section with the convex test wall (see Figure 3). In order to find out the extent of the secondary flow, yaw measurements inside the boundary

layers were made at the tunnel center line and at planes above and below the tunnel center line.

For the case of constant pressure flow along convex wall , yaw measurements were made at Stations 3, 4, 5, 10, 11 and 12. For the case of separating flow along convex wall , yaw measurements were made at Stations 3, 4, 5, 8, 9 and 10. The various locations of these stations are shown in Figure 5. For the case of constant pressure flow along concave wall , yaw measurements were made on the convex wall opposite the concave test wall. These measurements were made at $x = 70$ inches and $x = 96$ inches and at planes 16 inches above and below tunnel center line. The locations of these stations are shown in Figure 6.

A Conrad probe (used as a null direction probe) is used to measure flow directions inside the boundary layer. The particular probe geometry (see Figure 7) is chosen because of its high sensitivity and its zero scale effect (see Bryer, et.al. 1958). The probe has a stem of 1/8 inches O.D. stainless steel tube and a goose-neck (Figure 8) of .063 inches O.D. stainless steel tube. With this shape, the edge of the probe is in line with the axis of the probe. Therefore, by aligning the axis of the probe with the radial lines at the point of measurement, the traverse across the boundary layer will be perpendicular to the surface. The Conrad probe is inserted into the rotary device (Figure 9) which in turn is secured onto the probe carrier. The probe carrier is slid into a vertical stand and secured tightly in the level where the probe is to be introduced into the test section. The bottom of the stand is clamped to the floor of the tunnel and the top of the stand is also clamped to one of the ribs on the tunnel wall (see Figure 10). The probe is then introduced into the test section.

The introduction is through holes 7/16 inches diameter on the wall opposite the test wall. A plexiglass plug is machined to fit into the hole and flush with the wall. A hole just large enough to allow the probe to pass through is drilled onto the plug. The plug-probe assembly

is then taped onto the wall. When this probe is securely in place, it is traversed towards the test wall. An electrical circuit is arranged so that when the probe is touching the curved wall, a light goes on. When the probe is brought back to such a position that the light just goes off, the reading on the vernier mounted on the probe carrier is noted. This gives the zero reading for y . This way of positioning the probe has an accuracy in y of $\pm .001$ inches

The probe is rotated until the pressure is the same in the two openings. The pressure difference between the two openings is measured by a Pace Model CP51D-.1 PSID pressure transducer which is connected to a DISA 55D30 Digital Voltmeter, and is indicated by a zero reading on the voltmeter. However, due to pressure fluctuations, the voltmeter can be at best read to $\pm .01$ volts. The angle through which the probe has been rotated can be read from the dial on the rotary probe carrier (Figure 9). Depending on the mean flow velocity, this corresponds to an accuracy of $\pm 0.5^\circ$ in the determination of the flow direction. The sensitivity of the Conrad probe was determined for two different mean flow velocities in the fully developed pipe flow system and the result is given in Figure 8. Also, the null angle of the Conrad probe was determined in the pipe flow system. A more detailed explanation of the positioning of the probe, the accuracy of the yaw measurements, and the determination of the null angle is given in Appendix B.

2.2.3 Velocity Profiles

In most boundary layer measurements, the mean velocity is measured with a small pitot-static tube which is traversed in the direction perpendicular to the wall. The basis for these measurements is the incompressible, frictionless Bernoulli equation

$$P_t - P_s = \frac{1}{2} \rho U^2$$

The mean velocity thus measured depends on how accurate the pitot-static

tube measures the static pressure. The presence of this probe causes the streamlines to diverge as the leading edge of the probe is approached. This changes the curvature of the streamlines and as a result the local static pressure. The effect of the leading edge is felt many probe diameters downstream as the streamlines return to parallelism with those of the main flow. On the other hand, the disturbances created by the stem propagate upstream and produce a local variation from true static pressure. However, the two effects cause opposite changes in the stream pressure, and therefore a position can be found in the probe to locate the static pressure holes such that the effects of leading edge and stem cancel each other and again the true static pressure is measured.

Pitot-static probes of such design are commonly used in boundary layer measurements on flat surfaces where the probe is essentially parallel to the surface. For boundary layer flows along curved surfaces, the probe will no longer be parallel to the surface. As a result, the mean flow approaching the probe is at an angle of attack, and the probe will no longer register the true static pressure. In view of this, the conventional pitot-static probe was not used for velocity profile measurements. Rather, a total head probe was used to measure the local stagnation pressure, and the velocity was calculated from the incompressible frictionless Bernoulli equation together with the y momentum equation (see Section 2.4.1).

The stem of the total head probe is made from 1/8 inches O.D. stainless steel tube while the goose-neck is formed from .032 inches O.D. stainless steel tube flattened at the tip to an outside vertical dimension of .008 inches with an opening vertically of .004 inches (Figure 8). Rogers and Berry (1950) found that the response of such a flat nose probe was quite independent of yaw angle of 15 degrees and less. The accuracy of the present probe was checked against a standard pitot-static probe in a fully developed turbulent pipe flow system. The wall static pressure at the point of measurement was used as the reference for the

total-head probe. Assuming the static pressure to be constant across the pipe the probe gives the dynamic head directly. The measurements obtained using the pitot-static probe and the present probe were identical.

For the convex test section, velocity profile measurements were made at a total of twelve stations situated on both the straight and curved sections. Of the twelve stations, eight were situated along the tunnel center line, two were situated at a plane $1\frac{1}{4}$ inches above tunnel center line and the other two were situated at a plane $1\frac{1}{4}$ inches below tunnel center line. The locations of the center line stations together with the locations of the off center line stations are shown in Figure 5. For the case of constant pressure flow, the off center line stations were located directly above and below Stations 4 and 11, while for the separating flow case, they were located directly above and below Stations 4 and 9. This was because the flow was near separation at Station 11 for the separating flow case.

The positions of the various stations were measured from the entrance to the straight section. Since the constant pressure flow experiment was run first, the locations of the various stations on the test (inner) wall were selected and radial lines were marked on both the top and bottom walls of the tunnel at these locations. The adjustable (outer) wall was then installed and the correct pressure distribution was set up on the test wall (see Section 2.3.2). The intersection between the radial lines and the outer wall would then give the locations of the corresponding measuring stations on the outer wall. The total-head probe is introduced into the tunnel from the outer wall and is secured in place in much the same way as that used to secure the Conrad probe. The probe is carried by the probe carrier shown in Figure 10, and is positioned radially much the same way as that used to position the Conrad probe. The probe carrier is mounted in the same manner (see Figure 10). Again, the same electrical circuit is used to indicate whether the probe is just touching the wall. Since the surface of the

straight section was made of white panelite, it does not provide electrical connection. To remedy this, a thin coat of silver paint was painted on the tunnel center line of both side walls of the straight section.

The same outer wall was used for the separating flow experiment, but it was adjusted to give the correct pressure distribution on the test wall. Therefore, if the same holes were to be used to introduce the probe, their corresponding positions on the test wall will be different. The locations of these stations are also shown in Figure 5. It is seen that the positions of Stations 1 through 7 are not changed. The correct positioning of the probe radially depends on aligning the probe with the radial lines inscribed on both the top and bottom walls of the tunnel. However, with the separating flow case, there was only one set of radial lines inscribed on the lucite top. It was impossible to inscribe a corresponding set of radial lines on the bottom wall without taking the outer wall apart. This was not advisable once the correct pressure distribution has been set up.

The outlet of the total-head probe is connected to the negative port of a Pace Model CP51D-.1 psid pressure transducer. The positive port of the transducer is connected to a reference pressure which is provided by a pitot tube situated in the free stream near the tunnel entrance. The transducer output is connected to a DISA Model 55D30 Digital DC Voltmeter which can be read to .001 volts. The calibration of the transducer is described under Section 2.2.1.

At the time the velocity profile measurements were made on the convex wall with constant pressure distribution, the hot-wire equipment was not available. When the hot-wire equipment was ready, the velocity profile at Station 11 for the constant pressure flow case was made with the hot-wire equipment. The velocity profile calculated from the total-head probe measurement was then compared to the hot-wire measurement and the two profiles overlap each other (Figure 37). Because of its convenience,

the total-head probe was also used to measure the velocity profiles for the separating flow case. However, the total-head probe was not used to measure the velocity profiles in the case of the concave test wall. Rather, hot-wire was used. The hot-wire technique is described in Section 2.2.5.

Anticipating the fact that a system of longitudinal vortices would exit along the concave wall, the z positions of the locations where measurement was to be made could not be selected without a knowledge of the vortex system. The x positions of the stations were chosen at 24, 70 and 96 inches respectively. In order to determine the z positions, a hot-wire technique (see Section 2.2.6) was used to traverse the flow at $x = 24, 70$ and 96 inches respectively in the z direction. The z positions were then taken to be the tunnel center line or the positions of the trough and crest of a wave. The reason for this choice of z positions is discussed in Section 3.3. As a result of the these traverses, the positions of the five locations chosen are shown in Figure 6. Shown also are the z distance of these stations as measured from the tunnel center line. The hot-wire probe is introduced through the inner (adjustable) wall. The same method as before was used to secure the probe in place and the same technique as that used to position the Conrad probe radially was used to position the hot-wire probe. As to the y measurement, a description of the method used is given in Section 2.2.5.

2.2.4 Hot-Wire Equipment and Calibration

The hot-wire equipment used in the present experiment is shown in Figure 11. It consists of the following standard, commercially available units: one TSI Model 1010A Constant Temperature Anemometer, one DISA Model 55D10 Linearizer, one DISA 55D35 True RMS Voltmeter, two DISA 55D30 Digital Voltmeters, one Texas Instrument X-Y Plotter, one Pace Associates X-Y Plotter and one Techtronic Twin Beam Oscilloscope. The sensors and the probes were

obtained from Thermo System Inc. The sensors are tungsten wires and their characteristic dimensions are .00015 inches in diameter and .05 inches in sensitive length. Both ends of the sensor are copper plated. Throughout the whole experiment, factory mounted wires were used. The characteristic dimensions of the probe (see Figure 12) are: length of stem, 1.5 inches; diameter of stem, .059 inches; length of prongs, .25 inches; distance between tips of the prongs, .06 inches. The prongs are gold-plated.

A small portable calibration tunnel was built for hot-wire calibration. The tunnel is of the open-return type and is powered by a variable speed fan. A diagram of the calibration tunnel is shown in Figure 13. The air enters through a smooth bell-mouth which is followed by a layer of honey-comb straightener and a fine mesh screen. This is followed by a settling chamber that is three diameters long. A convergent nozzle accelerates the flow by a 4:1 ratio, and at the same time provides an axisymmetric contraction to the flow. The straight calibrating section is located behind the nozzle, and the station used for calibration is situated one diameter downstream of the nozzle exit. The air velocity in the tunnel can be varied continuously from zero to 100 ft/sec. The velocity at the calibrating station is monitored by a fixed pitot probe located on the center line upstream of the nozzle entrance and a wall static hole drilled diametrically opposite the calibrating station. The turbulence level was measured to be .2% when the air velocity in the tunnel was 90 ft/sec.

The relation between the output voltage of a constant temperature anemometer and the mean flow velocity is given by the equation

$$e^2 = A + BU^m \quad (2.2.4-1)$$

where A, B and m are constants to be determined by direct calibration. In arriving at this equation, free convection is neglected. Therefore,

in general A is not equal to the square of the zero flow voltage, and this complicates the calibration. The procedure finally adopted was to determine the constants A and B for different values of the exponent $1/m$ by least-square fitting the data to equation (2.2.4-1). The chosen value of m is the one that gives the minimum deviation which is defined as

$$\sigma^2(m) = \sum \{e_i^2 - A(m) - B(m) U_i^{\frac{1}{m}}\}^2 \quad (2.2.4-2)$$

All calibration
points

The data obtained showed no clear minimum for σ^2 . This means that the choice of m was not critical for the type of sensors used and the range of velocities considered. A plot of e^2 versus $U^{1/m}$ for different values of m is given in Figure 14. On the other hand, it was found that A/e_0 where e_0 is the zero flow voltage, correlates very well with m (Figure 15). As a result, $1/m$ was chosen to be .42 and A/e_0 was taken to be .89 according to the recommendation of DISA.

A diagrammatic layout of the hot-wire equipment is shown in Figure 16. For the present purpose, the linearizer which is connected in series with the constant temperature anemometer is just considered to be an analog computer having a well defined transfer function. A typical calibration curve of the linearizer output is given in Figure 17.

2.2.5 Hot-Wire Techniques

Mean Velocity Measurements

Once the hot-wire has been calibrated, it is a simple matter to use it to measure the mean flow velocity. The mean value of the linearized hot-wire signal follows the law

$$\bar{e}_L = hQf(\phi) \quad (2.2.5-1)$$

where Q is the magnitude of the velocity vector, ϕ is the angle between the normal to the sensor and the direction of the mean velocity, and h is the calibration constant. If the cross-flow is negligible compared to the mean flow U , (this is true for the two cases of constant pressure flow along convex and concave walls) then $Q = U$. The function f is symmetric with respect to its argument and is also normalized to 1 when its argument is zero, therefore by aligning the hot-wire so that its normal coincides with the flow direction,

$$\bar{e}_L = hU \quad (2.2.5-2)$$

which gives the mean velocity directly.

The straight hot-wire probe (figure 12) with a straight wire was introduced into the tunnel in the same manner as the Conrad and total-head probes and was carried by a rotating mechanism - probe carrier combination shown in Figure 10. Due to the fragility of the wire, a different method was used to determine the y position of the wire. First, a dummy probe (it can be a hot-wire probe with broken wire) is used. As before, an electrical circuit is used to indicate contact between the probe and the wall. The reading on the vernier is noted, and the probe is retracted until it is completely outside of the tunnel. Then the dummy probe is replaced by a hot-wire probe. Knowing the exact measurements of the hot-wire probe, the dummy probe and an average value of the backlash of the probe carrier, the y position of the wire can be determined to an accuracy of $\pm .008$ inches. A detailed description of this method is given in Appendix B.

Turbulence Measurements

The standard technique used in the measurements of turbulent stresses is the employment of an X-probe or a V-probe. However, this method requires accurate alignment of the probe, and this poses serious problems in the present investigations. In addition, if the longitudinal

vortex system does exist along the concave test wall, the flow will no longer be two-dimensional and the application of the X-probe or V-probe will be quite doubtful. For these reasons, a rotating-wire technique that is a modification of a technique proposed by Fujita and Kovasznay (1968) is selected. The method is essentially the same as the one used by Bissonnette (1970), therefore the method will not be discussed in detail here. Instead, the reader is referred to the thesis of Bissonnette.

The hot-wire probes used are the straight and the slanted probes shown in Figure 12. With the straight probes two types of wire are used; one is straight and the other is a 45° slanted hot-wire. With the slanted probe, only the straight wire is used.

The turbulent stresses can be determined by two sets of measurements, one set is given by the straight probe with the straight wire, while the other set is given either by the slanted probe with the straight wire or the straight probe with the slanted wire. For reasons that will be apparent later, the turbulent stresses in the case of constant pressure flow along convex wall were measured using straight wires on both the straight and slanted probes. For the other two cases, the turbulent stresses were measured using straight and 45° slanted wires on the straight probe only.

With the straight wire on either the straight probe or the slanted probe, the wire rotates in the xoz plane. The coordinate systems for both the straight wire and the slanted wire are shown in Figure 18. Both the straight probe and the slanted probe were introduced into the tunnel the same way as before, and the rotation was chosen to span approximately $-45^\circ < \phi < 45^\circ$. In order to minimize the backlash errors the recording of the linearized signal was always performed in the same direction of rotation. A sample recording of the mean value and the mean square value of the linearized signal versus the angle δ of rotation (straight-wire on straight probe) by means of X-Y plotters are shown in Figures 19 and 20 respectively. The recordings were performed

in both directions of rotation to account for the hysteresis due to the different time constants of the low pass filter and the RMS meter. The true signal was taken to be the average curve drawn between the two traces. Recording the signal in this manner was very time consuming (roughly about 15 minutes per experimental point) and in order to reduce this experimentation time, the two time constants were chosen to be approximately the same. Assuming comparable hysteresis in both cases, recording in only one direction was required, and results obtained were practically the same as those obtained by recording two traces.

With the 45° slanted wire on the straight probe, the wire generates a conical surface with axis parallel to the oy axis when the probe is rotated (Figure 18). In order to avoid the disturbance due to the longer prong, the probe is positioned in such a manner that the longer prong is always behind or parallel to the shorter prong during rotation.

For the case of constant pressure flow along convex wall, turbulence measurements were made at Stations 1, 7, 9 and 11, while for the case of separating flow along convex wall, turbulence measurements were made at Stations 1, 4, 9, 11 and 12. For the case of constant pressure flow along concave wall, turbulence measurements were made at all five stations.

2.2.6 Mapping of the Longitudinal Vortex System

In order to make meaningful measurements on the concave wall, the question of the existence of the longitudinal vortex system has to be resolved. From the data of Tani (1962) it can be seen that the vortex system is very likely to be stationary, otherwise Tani could not have detected it with a pitot traverse. For the present investigation, a hot-wire set at a constant distance away from the concave wall is used to traverse the flow in the z direction. The mechanism used to carry the hot-wire probe and drive it in the z direction is shown in Figure 21.

Briefly, the probe adaptor used in conjunction with the TSI miniature

hot-wire probe is firmly secured to a movable block which slides within two grooves on the strut of the probe carrier (Figure 22). The leads of the adaptor are connected to a co-axial wire which has a BNC connector on its other end. The straight hot-wire probe can then be plugged into the probe adaptor. A constant speed motor is used to drive the movable block along the strut. The speed of the motor can be varied by regulating the supplied voltage. The linear movement of the probe is translated into an electrical signal through a ten turn pot, so that its movement can be recorded on a X-Y plotter. The probe carrier is so constructed that the traverse in the z direction has a span of 21 inches, and is centrally located with respect to the tunnel center line. At both ends of the traverse, there is a limit-switch. When the movable block is located at either end, it triggers the switch and the motor is turned off. The pot, the motor and the gear assembly are located on top of the strut, and a piece of $\frac{1}{4}$ inches thick foam rubber is cemented on the bottom of the strut. The length of the strut including the piece of rubber is a bit longer than 4 feet.

With the straight hot-wire probe in position, the strut was introduced into the tunnel from the top. It was then fastened onto the lucite top by screws as shown in Figure 23. The three rectangular holes on the top wall of the tunnel at $x = 24, 70$ and 96 inches respectively were located in such manner that when there were no spacers in front of the probe carrier assembly, the hot-wire was exactly .2 inches away from the wall. By moving the spacers to the front, the hot-wire can be set at $y = .4, .6, .8$ and 1 inches away from the wall.

The straight hot-wire was positioned to give the maximum voltage output. The linearized signal was connected to one arm of the X-Y plotter. The X axis of the X-Y plotter was calibrated to indicate the z position of the probe. The origin of z is taken to be the tunnel center line, and z is positive when measured upward and negative downwards. The traverse was always in the same direction, i.e. from top downwards.

to bottom, and the speed of the motor was regulated to give a linear speed of approximately 6 in/min.

Since the purpose of this investigation was to detect and map out the longitudinal vortex system, no quantitative measurements of the vortices were made. Once the vortex system was mapped out, the locations of the stations where boundary layer measurements were to be made could be determined.

2.3 Qualification of Curved Wall Tunnel

2.3.1 Two-Dimensional Equilibrium Turbulent Flow in Straight Section

Uniformity and steadiness of the flow in the straight section of the tunnel was checked by observing tufts attached to the walls of the tunnel. The equilibrium nature and two-dimensionality of the flow were checked by actual measurements and comparison with Klebanoff's (1955) data under similar circumstances.

First, the boundary layer was checked to see if it was turbulent. To do this, velocity profile measurements were made at Station 1 and $x = 40$ inches. Results indicated that the flow was still laminar up to Station 1 and the boundary layer thickness at $x = 40$ inches was much less than 1 inch. The flow was then tripped a small distance downstream of the entrance to the straight section. The tripping was effected by a slightly stretched piano wire covered by electrical tape. The diameter of the wire was chosen to give a boundary layer thickness at $x = 40$ inches of approximately 1 inch. For the sake of symmetry, the flows on the other three walls were also tripped. With this arrangement, the flow was found to be turbulent at Station 1, and that the boundary layer thickness was approximately .6 inches. The total pressure profile at Station 1 was then measured using the flattened total-head probe and the velocity profile was calculated together with the skin friction at the wall (see Section 2.4.2). The defect plot of the velocity profile was then compared with the zero pressure gradient profile of Mellor

and Gibson (1966). The comparison is excellent and the result is shown in Figure 24. The calculated profile is given by the solid line in the figure. The result indicates that an equilibrium turbulent flow exists at Station 1.

The rotating-wire technique was used to measure the Reynolds stresses. First, the straight probe with the straight wire was used and this gives the following three Reynolds stresses, namely $\overline{u^2}$, \overline{uw} and $\overline{w^2}$ (see Section 2.4.3 for turbulence data reduction). Then the slanted probe with the straight wire was used. In order to get \overline{uv} and $\overline{v^2}$ with this probe, \overline{vw} has to be either known or assumed zero. In light of the fact that for two-dimensional flow, due to symmetry about the center line plane, the off-diagonal elements of the Reynolds stress tensor, except \overline{uv} , are necessary zero. Therefore, the assumption of $\overline{vw} = 0$ was made so that \overline{uv} and $\overline{v^2}$ could be calculated. In addition, if the measured \overline{uw} were indeed very small it would provide an independent check for the assumption, while at the same time, it would also serve to show the two-dimensional nature of the flow. To see if this is true, the measured \overline{uw} was plotted against the measured \overline{uv} at Station 1, and is given in Figure 25. It can be seen that nowhere inside the boundary layer was $(\overline{uw}/\overline{uv})$ greater than .05. This shows that the flow was relatively two-dimensional. To further substantiate this claim, the measured \overline{uv}/u^2_τ , u'/U_{pw} , v'/U_{pw} , w'/U_{pw} and $\overline{uv}/u'v'$ were plotted against y/δ and compared with the flat plate data of Klebanoff (1955). These are shown in Figures 26 to 30. In general, the measured data compare favorably with Klebanoff's data except near the wall. This is because the rotating-wire technique is not very accurate in region of high shear (see Bissonnette 1970). From these measurements, it can be concluded that the flow was in equilibrium and was indeed two-dimensional.

After the first set of experiments with the convex wall was finished, the pressure distribution on the test section was set up to give a

separating flow in the curved tunnel. In order to make sure that the same entrance flow exists in this case as in the constant pressure flow case, measurements at Station 1 were repeated again. Surprisingly, the measured velocity profile did not show any noticeable difference, but the measured $\bar{u}w$ was found to be much larger than before (at one point $\bar{u}w/\bar{u}v$ even amounts to $\sim .2$). Also, the measured $\bar{u}v/u_\tau^2$ was noticeably smaller than the previous data. After a long and tedious check on the equipment and the rotating-wire technique (including the test of the technique in the fully developed pipe flow) it was found that the flow was not transistiting properly. The improper transition of the flow was caused by the loosening of the tripping wire. As a result, the transition was not uniform along the walls, thus creating a certain skewness in the flow, and the off-diagonal elements of the Reynolds stress tensor was no longer zero. To correct for this, a tripping device proposed by Hama (1957) was used.

Briefly, the tripping device consists of isosceles triangles made of either electrical tap or aluminum sheet. These triangles are then cemented to the walls of the tunnel so that the vertices of the triangles are facing the flow. According to Hama, the device was very efficient, and anchored the transition right at the tripping device. With this modification, the measured $\bar{u}w/\bar{u}v$ was again found to be less than .08 across the boundary layer. However, the boundary layer at Station 1 was found to be approximately 20% thicker than the previous measurement. The measured velocity profile together with the various Reynolds stresses at Station 1 for the case of separating flow along convex wall are shown in Figures 24, and 26 to 30. Again the flow was in equilibrium and was two-dimensional.

When the test wall was changed to the concave wall, the same measurements were performed at Station 1. However, in this case, the wall opposite the previous test wall was the test wall. The results of these measurements are again plotted in Figures 24, and 26 to 30, and

they show that the flow was in equilibrium and two-dimensional. In addition, they show that the flow in the straight section was very uniform.

2.3.2 Pressure Distribution on Curved Test Section

In the course of setting up the wall static pressure distribution on the convex test wall it was found that the pressure decreased slowly as the flow approached the entrance to the curved section, and then steeply as the flow entered the curved section. The pressure drop amounts to more than 60% of the reference dynamic head. An effort was made to reduce this amount of pressure drop by increasing the cross-sectional area right at the entrance, but to no avail. Later it was found that the flow was separated on the adjustable wall and right at the entrance to the curved test section. Therefore, increasing the cross-section area at this section merely increased the separated region, and the flow on the test wall was undisturbed. To correct this, a side wall jet was installed on the adjustable wall and right at the entrance to the curved section. The jet is merely an opening, four feet high, on the side wall of the tunnel. The pressure difference between the outside and inside of the tunnel provides sufficient momentum to the jet. The opening of the jet is controlled by a flexible flap attached to the straight wall. The flap extends 8 inches into the straight section, thus providing some control on the flow approaching the curved section. The jet and flap control mechanism are shown in Figure 31. With this arrangement, it was found possible to reduce the pressure drop to about 30% of the reference dynamic head. However, the pressure drop cannot be eliminated completely. Because of this, the final constant pressure distribution set up on the convex wall was at a different level from that of the straight wall. Immediately after the pressure drop, there was a slight pressure increase. All these occurred within a distance of 6 inches, from $x = 46$ inches to 52 inches.

After that the adjustable wall was adjusted to give the minimum possible variation of wall static pressure on the convex wall. The above adjustment was done with no regard to the secondary flow in the tunnel.

Therefore, it was no surprise to find that the secondary flows measured at Stations 3 and 5 were quite appreciable. Means were introduced to control the secondary flow (this is discussed in Section 2.3.3) and this changed the pressure distribution. The secondary flows were adjusted to a minimum and the adjustable wall was again set to give the best pressure distribution. The final pressure distribution obtained for the case of constant pressure flow along convex wall is shown in Figure 32. The final setting of the adjustable wall is given in Figure 3. Finally, the wall static pressure at planes 14 inches above and below the tunnel center line were also measured. If these measurements were plotted on Figure 32, they would overlap the tunnel center line measurements. Therefore, for the sake of clarity, the off-center line wall static pressure measurements are not shown.

In setting up the pressure distribution on the convex wall for the separating flow case, the objective was to have a linear decelerating potential velocity at the wall (Figure 82). By pulling back the adjustable wall, this was relatively easy to set up in the curved section between $x = 50$ inches to 60 inches. After $x = 60$ inches, the pressure distribution began to level off. Again, the adjustable wall was pulled back, but there was relatively little change in the pressure distribution at the test wall. At this point, the flow was suspected to have separated, but the line of separation was not known. In an effort to locate the separation line, tufts were attached to the convex wall between $x = 60$ inches and 70 inches at an equal spacing of two inches apart. The effort proved to be futile, but it did seem to indicate that separation did not occur along a straight line from the top to the bottom of the tunnel. There was clear indication that the flow separated first near the top and bottom of the tunnel and further downstream along the central

portion of the tunnel.

Attempts were made to move the separation curve further downstream by readjusting the whole adjustable wall. The results was a non-linear distribution of decelerating potential velocity at the convex wall. After much trial and error, the original pressure distribution was set up. This is given in Figure 32. The final setting of the adjustable wall is shown in Figure 3. The linear distribution of decelerating potential velocity at the wall is displayed in Figure 81, together with the actual measured potential velocity at the wall. As far as can be made out from the tufts, separation occurred somewhere between $x = 66$ inches and 70 inches. Later measurements of the velocity profiles lend evidence to this. The secondary flows at Stations 3, 5, 8 and 10 were then measured, and the end-wall jets were adjusted to give the minimum secondary flow at these stations. The pressure distribution was measured again, but in this case no repeated adjustments were made as in the case of the constant pressure flow. The final results are those mentioned above. The secondary flow measurements are discussed in detail in the next section.

The wall static pressure at planes 14 inches above and below the tunnel center line was measured. The difference between these measurements and the tunnel center line measurements were very small at the leading section of the convex wall, and became noticeable near separation. However, for the sake of clarity, they are not shown in Figure 32.

For the concave test wall, the pressure at the wall increases as the flow enters the curved section. In order to reduce this pressure increase, the flow in the region upstream and downstream of the entrance to the curved section was accelerated by adjusting the adjustable wall. As a result, no side wall jet was necessary. The adjustable wall extends one foot into the straight section, and this provides sufficient adjustment for the region upstream of the entrance to the curved section. Again, after much trial and error, the final constant pressure distribution

set up on the concave wall is at a level about 22% higher than at the straight section. The pressure distribution is given in Figure 33, while the final setting of the adjustable wall is shown in Figure 4. In this case, the variation of the wall static pressure in the stream-wise direction is greater than the corresponding case with the convex test wall. Efforts were made to reduce these variations but to no avail. The wall static pressure at planes 14 inches above and below the plane of symmetry was also measured. Again, there were noticeable differences between these measurements and the tunnel center line measurements. To show the extent of these variations, the off center line wall static pressure measurements are also shown in Figure 33.

As in the case of the constant pressure flow along convex wall, the secondary flows at planes 16 inches above and below the tunnel center line were measured, and the end wall jets were adjusted to give the minimum secondary flow. The pressure distribution was then re-set and the secondary flow was again measured and readjusted if necessary. The whole procedure was repeated until a satisfactory pressure distribution was obtained together with a reasonable secondary flow at the stations where measurements were made. The secondary flow measurements are discussed in detail in the next section.

2.3.3 Secondary Flows in Curved Test Sections

As has been explained in Section 2.2.2, secondary flows exist near the end walls of the tunnel because of the longitudinal curvature of the test section. The influence of this end-wall flow can extend to the tunnel center line.

When the tunnel was first designed, it was thought that if it has a large aspect ratio, the secondary flows would be essentially confined to small regions near the end walls. However, initial yaw measurements at Stations 3, 5, 10 and 12 on the convex wall, with the constant pressure distribution along it, revealed that the measured yaw angles at Stations 3,

and 5 were approximately equal and were opposite in sign but they reached a maximum of $\sim 10^\circ$. The maximum reached at Stations 10 and 12 was about 20° . To reduce the secondary flows, end wall jets were installed on the top and bottom walls of the tunnel and right at the entrance to the curved section (Figure 31). A series of four tangential jets were installed on each end wall. The jets were made of 1/8 inches I.D. tube, and were supplied by a high enough pressure to give critical flow at the jet exits. Thus, the amount of mass flow added to the tunnel flow is quite small while the amount of momentum added is enough to compensate the momentum defect of the end wall boundary layers at the position of the jets. This additional momentum is sufficient to reduce the secondary flows considerably even at Stations 10 and 12.

With the end wall jets installed, yaw measurements were again made at Station 3, 5, 10 and 12. The maximum yaw angles at Stations 3 and 5 and 10 and 12 were found to be less than 2° and 4° respectively. By monitoring the yaw angles at Stations 3 and 5, repeated measurements of the pressure distribution along the convex wall and continually adjusting the adjustable wall to give the minimum variation in the streamwise pressure, it was possible to set up the best constant pressure distribution on the convex wall. The resultant yaw measurements at Stations 3, 4, 5, 10, 11 and 12 are shown in Figure 34. The flow in the tunnel was relatively two-dimensional. Later velocity profiles and turbulence measurements lend support to this claim.

Essentially the same end wall jets operating at the same conditions were used to control the secondary flows in the case of separating flow along convex wall. In this case, because of the added complexity in setting up the correct pressure distribution, the procedure followed was different from that adopted in the case of constant pressure flow along convex wall. The correct pressure distribution was set up with the end wall jets operating at the optimal conditions. Then, yaw measurements

were made at Stations 3, 4, 5, 8, 9 and 10. The results are shown in Figure 35, and for the sake of clarity, the yaw measurements at Stations 4 and 9 are not shown. The maximum yaw measured at Station 4 was less than 1° and that at Station 9 was less than 2° . Although the flow along the tunnel center line is quite symmetrical, the secondary flows at Stations 8 and 10 are considered large. Attempts were made to reduce this by installing larger jets to the end walls. This managed to reduce the secondary flows. However, the pressure distribution along the convex wall was disturbed, and it was not possible to obtain a linear decelerating potential velocity at the wall. After much trial, it was finally decided to go back to the original set up. Later velocity profile and off center line wall static pressure measurements seem to indicate that the flow was relatively two-dimensional up to $x \approx 60$ inches. Downstream of $x = 60$ inches, the influence of the secondary flow can no longer be discounted.

For the case with the concave test wall, secondary flow measurements were taken on the adjustable wall opposite the concave test wall. The reason for doing this is because of the existence of the system of longitudinal vortices. Under the influence of the longitudinal vortices, the secondary flow measurements would depend to a large extent on where the measurements were taken. As a result, the true influence of the end-wall secondary flows cannot be estimated.

From previous experiences, yaw measurements at tunnel center line were found to be unnecessary. For this reason yaw measurements were made at planes 16 inches above and below tunnel center line at $x = 70$ and 96 inches for the case of constant pressure flow along concave wall. The same end wall jets were used to limit the secondary flows to small regions near the end walls. The pressure distribution was set up on the concave wall, and yaw measurements were made at the off center line stations at $x = 70$ inches. The supplied pressure of the jets was then adjusted to give minimum yaw at the two stations where

measurements were made. The pressure distribution was measured again, and if considerable changes were noticed, the above procedure was repeated all over until a satisfactory pressure distribution on the concave test wall and a relatively small yaw profile across the boundary layer on the adjustable (convex) wall were obtained. The final yaw measurements at $x = 70$ and 96 inches are given in Figure 36.

2.4 Data Reduction

2.4.1 Calculation of Velocity Profiles

Assuming $\frac{\partial p}{\partial y} = \rho k U^2$, Bernoulli's equation may be written as

$$\frac{1}{2} \rho U^2 = P_t - P_r + \{P_r - P_{sw} - 2k \int_0^\infty (P_t - P_r) e^{2ky} dy\} e^{-2ky} \quad (2.4.1-1)$$

where the reference pressure P_r is here taken to be the total pressure in the potential core so that $P_t - P_r \rightarrow 0$ outside of the boundary layer. Therefore the potential velocity is given by

$$\frac{1}{2} \rho U_p^2 = \{P_r - P_{sw} - 2k \int_0^\infty (P_t - P_r) e^{2ky} dy\} e^{-2ky} \quad (2.4.1-2)$$

Within the boundary layer $ky < 0.1$ and it is possible to simply represent the potential velocity according to $U_p \propto U_{pw}(1-ky)$ (see Section 4.2). Furthermore, the integrals in equations (2.4.1-1) and (2.4.1-2), which represent the difference between the static pressure calculated from the actual velocity and the potential velocity, are small. Therefore it is possible to write

$$\frac{U^2}{U_{pw}^2} = \frac{P_t - P_r}{P_r - P_{sw}} + e^{-2ky} \quad (2.4.1-3)$$

and

$$\frac{U_p^2}{U_{pw}^2} = e^{-2ky} \quad (2.4.1-4)$$

where

$$\frac{1}{2} \rho U_{pw}^2 = P_r - P_{sw} \quad (2.4.1-5)$$

In Figure 37 the result of using equation (2.4.1-3) to reduce the data is compared with that of equation (2.4.1-1) which is also normalized with equation (2.4.1-5) instead of equation (2.4.1-2) after setting $y = 0$. The latter would be the consistent normalization if equation (2.4.1-1) were used, but then no distinction would be visible in Figure 37.

As discussed in Section 4.2, the present procedure is consistent with the boundary layer equations used to compute theoretical profiles. It should be noted that throughout this investigation $ky < 0.1$ and $e^{-ky} \approx 1 - ky$. However, it appears exceptionally convenient to retain the complete exponential form.

2.4.2 Skin Friction Deduction

The skin friction at the wall was not measured, but rather it was obtained from the Clauser plot (1956). For curved flow, the skin friction is defined as

$$\tau_w = \frac{1}{2} C_f \rho U_{pw}^2 \quad (2.4.2-1)$$

and since the Clauser plot is independent of the reference velocity chosen to make the velocity profile non-dimensional, the reference velocity is here chosen to be U_{pw} . The velocity profile was calculated and U/U_{pw} was plotted against $\log \frac{yU_{pw}}{v}$. On top of this was superimposed several plots of the Law of the Wall for different values of C_f . The line that passes through the most numbers of experimental points is taken to give the correct C_f for the measured profile. The correct C_f becomes a bit difficult to decide for the near separation profiles. Two sample plots of the velocity profiles for the determination of C_f are shown in Figure 38.

2.4.3 Calculation of the Reynolds Stresses

The general equations for analyzing the hot-wire signal were derived by Bissonnette (1970). However, they are recorded here for reference. These equations are specialized for the use of a linearizer with calibration constant h .

Straight Wire on Straight and Slanted Probes

$$\phi = \delta - \beta \quad (2.4.3-1)$$

$$\bar{e}_L = hQf(\phi) \quad (2.4.3-2)$$

$$\bar{e}'^2 = h^2 \{ f^2(\phi) \bar{u}^2^* - 2f(\phi)f'(\phi) \bar{u}\bar{w}^* + f'^2(\phi) \bar{w}^2^* \} \quad (2.4.3-3)$$

where

$$\begin{aligned} \bar{u}^2 &= \bar{z}^* \\ \bar{v}^2 &= \bar{v}^2^* \sin^2 \theta + 2\bar{v}\bar{w}^* \sin \theta \cos \theta + \bar{w}^2^* \cos^2 \theta \\ \bar{w}^2 &= \bar{v}^2^* \cos^2 \theta - 2\bar{v}\bar{w}^* \sin \theta \cos \theta + \bar{w}^2^* \sin^2 \theta \\ \bar{u}\bar{v} &= -\bar{u}\bar{v}^* \sin \theta + \bar{u}\bar{w}^* \cos \theta \\ \bar{u}\bar{w} &= -\bar{u}\bar{v}^* \cos \theta + \bar{u}\bar{w}^* \sin \theta \\ \bar{v}\bar{w} &= -\bar{v}\bar{v}^* \sin \theta \cos \theta + \bar{v}\bar{w}^* \sin^2 \theta \\ &\quad - \bar{v}\bar{w}^* \cos^2 \theta + \bar{w}\bar{w}^* \sin \theta \cos \theta \end{aligned} \quad (2.4.3-4)$$

θ is the angle between oz axis and the normal to the wire, and ϕ , δ and β are defined in Figure 18.

Slanted Wire on Straight Probe

$$\sin \phi = \sin \gamma \sin(\delta - \beta) \quad (2.4.3-5)$$

$$\bar{e}_L = hQf(\phi) \quad (2.4.3-6)$$

$$\bar{e}'^2 = h^2 \{ f^2(\phi) \bar{u}^2^* + \frac{\cos^2 \gamma}{\cos^2 \phi} f'^2(\phi) \bar{v}^2^* + \}$$

$$\begin{aligned}
& + \frac{\sin^2 \gamma}{\cos^2 \phi} \cos^2(\delta - \beta) f'^2(\phi) \overline{w^2}^* - 2 \frac{\cos \gamma}{\cos \phi} \\
& f(\phi) f'(\phi) \overline{uv}^* + 2 \frac{\sin \gamma \cos \gamma}{\cos^2 \phi} \cos(\delta - \beta) f'^2(\phi) \overline{vw}^* \\
& - 2 \frac{\sin \gamma}{\cos \phi} \cos(\delta - \beta) f(\phi) f'(\phi) \overline{uw}^* \}
\end{aligned} \tag{2.4.3-7}$$

where

$$\begin{aligned}
\overline{u^2} &= \overline{u^2}^* \cos^2 \beta - 2 \overline{uw}^* \sin \beta \cos \beta + \overline{w^2}^* \sin^2 \beta \\
\overline{v^2} &= \overline{v^2}^* \\
\overline{w^2} &= \overline{u^2}^* \sin^2 \beta + 2 \overline{uw}^* \sin \beta \cos \beta + \overline{w^2}^* \cos^2 \beta \\
\overline{uv} &= \overline{uv}^* \cos \beta - \overline{vw}^* \sin \beta \\
\overline{vw} &= \overline{uv}^* \sin \beta + \overline{vw}^* \cos \beta \\
\overline{uw} &= \overline{uw}^* (\cos^2 \beta - \sin^2 \beta) + (\overline{u^2}^* - \overline{w^2}^*) \sin \beta \cos \beta
\end{aligned} \tag{2.4.3-8}$$

The quantities with an asterisk refer to flow quantities defined in a frame of reference attached to the wire (wire coordinate system) while those without an asterisk refer to flow quantities defined in a frame of reference attached to the tunnel (tunnel coordinate system).

For the two cases where the test wall was convex, all measurements were made in the tunnel center line, therefore the cross-flow was very small (except near separation in the separating case) and $\beta \approx 0$. With the straight wire on the straight probe, $\theta = \pi/2$ and the wire coordinates coincide with the tunnel coordinates. As a result, equation (2.4.3-4) is much simpler and $\overline{u^2} = \overline{u^2}^*$, $\overline{v^2} = \overline{v^2}^*$, $\overline{uv} = \overline{uv}^*$, etc. With the straight wire on the slanted probe, $\theta \approx 46^\circ$ and the turbulent stresses are given by equation (2.4.3-4).

For the case of constant pressure flow along concave walls, measurements were taken at the position of the crest and trough of the wave system and it was argued that the cross-flows at those two positions were

very small, (for reason why refer to Section 3.3) hence $\beta \sim 0$. This again allows the equations for the signal analysis to be further reduced.

The x coordinate of each plot is calibrated to give the angle of rotation δ . Once δ and β are known, ϕ is given by either equations (2.4.3-1) or (2.4.3-5). The function $f(\phi)$ is normalized by the maximum on the trace, i.e. $\bar{e}_L(0)$ and is therefore given by

$$f(\phi) = \frac{\bar{e}_L(\phi)}{\bar{e}_L(0)} \quad (2.4.3-9)$$

For the sake of simplicity, the functional form proposed by Champagne et. al. (1967) for $f(\phi)$ is used, i.e.

$$f^2(\phi) = \cos^2 \phi + k^2 \sin^2 \phi \quad (2.4.3-10)$$

where k is a constant, and is determined for every run by fitting equation (2.4.3-10) to the experimental data. Taking k^2 to be the mean value over all data points, it is given by

$$k^2 = \frac{1}{N} \sum_{i=1}^N \frac{\bar{e}_L^2(\phi_i) / \bar{e}_L^2(0) - \cos^2 \phi_i}{\sin^2 \phi_i} \quad (2.4.3-11)$$

With the function $f(\phi)$ defined, the turbulence stresses $\overline{u^2}^*$, $\overline{w^2}^*$ and \overline{uw}^* can be obtained by least square fitting equation (2.4.3-3) to the experimental record of \bar{e}_L^2 . These values are then substituted into equation (2.4.3-7) and the other Reynolds stresses \overline{uv}^* , $\overline{v^2}^*$ and \overline{vw}^* are computed by a similar technique.

As explained earlier, the cross-flows are small for all cases of measurements and hence no corrections are necessary. Hence, in adapting Bissonnette's (1970) data reduction program for the present purpose β was set equal to zero. The accuracy of the rotating-wire technique was tested in a fully developed turbulent pipe flow experiment. From the measured axial pressure drop, the shear stress distribution across the

pipe can be calculated and this is used to check the measured shear stress profile. In general, the accuracy of the rotating-wire technique is very good except near the wall. This experiment is described in detail in Appendix C.

Chapter III
DISCUSSION OF RESULTS

In the following, the discussion is divided into three sections. The first deals with the results of the constant pressure flow along convex wall, the second concentrates on the results of separating flow along convex wall, while the third discusses the results of the constant pressure flow along concave wall. The discussion takes the following format. The mean flow data are analysed first and this is then followed by a discussion of the turbulence data. The results of these experiments are tabulated and are given in Tables 1 to 35. Tables 1 to 12 contain the results of the mean flow and turbulence measurements of the constant pressure flow along convex wall experiment. Tables 13 to 25 contain the data of the mean flow and turbulence measurements of the separating flow along convex wall experiment, and the mean flow and turbulence data of the constant pressure flow along concave wall experiment are given in Tables 26 to 35. For all three experiments, the free stream turbulence level in the straight section is less than .5%.

3.1 Constant Pressure Flow along Convex Wall

The end wall jets were installed for the sole purpose of controlling the secondary flows in the curved test section of the tunnel. Evidence that the flow was very nearly two-dimensional were the small yaw angles measured at Stations 3, 4, 5, 10, 11 and 12 (Figure 34), and the apparently identical pressure distributions at tunnel center line and planes above and below the tunnel center line. Besides, the velocity profiles measured at Stations 3 and 5 and 10 and 12 were no different from those measured at Stations 4 and 11 respectively (Figure 39). To further check the two-dimensionality of the flow, the von Karman momentum integral was integrated according to the method proposed by Coles (1958).

The von Karman momentum integral is derived in Section 4.2, and is given by equation (4.2-22). It can be written as

$$\frac{u_\tau^2}{U_{pw}^2} = \frac{d\theta}{dx} + (H+2) \frac{\theta}{U_{pw}} \frac{dU_{pw}}{dx} - q(x) \frac{dk}{dx}$$

where

$$q(x) = \int_0^\infty y \left(1 - \frac{U}{U_p}\right) dy + \int_0^\infty 2y \frac{U}{U_p} \left(1 - \frac{U}{U_p}\right) dy$$

Following Coles (1968) procedure, the equation can be written as

$$\int_{x_o}^x \frac{u_\tau^2}{(U_{pw}^2)_o} d\left(\frac{x}{\theta_o}\right) = \frac{\frac{2}{(U_{pw}^2)_o} \theta}{\frac{2}{(U_{pw}^2)_o}} - 1 + \frac{1}{2} \int_{x_o}^x \frac{\delta^*}{\theta_o} d\left(\frac{U_{pw}}{(U_{pw}^2)_o}\right) + \frac{1}{(U_{pw}^2)_o} \int_{x_o}^x \frac{U_{pw}}{R^2} q(x) dR(x) \quad (3.1-1)$$

where the subscript o denotes measurements in a reference station. To integrate this equation, values of δ^* , θ and u_τ at the various stations are required. The values of δ^* and θ are obtained by direct numerical integration of the measured profiles, which are shown in Figure 39, while the skin friction is obtained from the Clauser plot. The values thus obtained are plotted versus x in Figure 79, together with the shape factor (H) development. From these measured values, equation (3.1-1) is integrated numerically and the result is shown in Figure 40. It can be seen that all along the convex test wall PL (it denotes the quantity on the left hand side of equation (3.1-1)) is not too much different from PR (it denotes the quantities on the right hand side of equation 3.1-1)), hence the two-dimensional momentum integral is satisfied and the flow can be said to be relatively two-dimensional. Further evidence of two-dimensionality is provided by subsequent turbulence measurements, however, this will be discussed later.

Since the skin friction is not measured independently, the momentum balance calculation depends to a large extent on the validity of the Clauser plot to determine C_f for curved flow. To demonstrate the validity of this method it is necessary to show that the Law of the Wall holds even for turbulent flow along convex surfaces. The measured velocity profiles were plotted to show the Law of the Wall region using the u_τ determined from Clauser plot. If the Law of the Wall indeed holds for curved flows as well as for plane flows, then a straight line having a slope of 5.6 can be drawn through all the data points in the wall law region. The result is shown in Figure 41, where it can be seen that the measured profiles all show the existence of the wall law region. Also, all the profiles shown start to deviate at about the same point ($y u_\tau / \nu \approx 200$) where the flat plate profile (Station 1) begins to deviate from the Law of the Wall. Thus, it can be seen that the Law of the Wall, which is given by

$$\frac{U}{u_\tau} = 5.6 \log \frac{yu_\tau}{\nu} + B \quad (3.1-2)$$

also holds for flow along convex surfaces. However, this should come as no surprise, because in this region the mean flow streamlines are essentially parallel to the surface.

By comparison with plane flow, the Defect Law for convexly curved flow can be written as

$$\frac{U_p - U}{u_\tau} = F\left(\frac{y}{\Delta}\right) \quad (3.1-3)$$

where

$$\Delta = \int_0^\infty \frac{U_p - U}{u_\tau} dy$$

If the defect region overlaps with the wall law region, then the function

$F(y/\Delta)$ can be shown to be

$$F\left(\frac{y}{\Delta}\right) \sim -5.6 \log \frac{y}{\Delta} + A \quad (3.1-4)$$

Mellor and Gibson (1966) have pointed out that A is not truly a constant. Instead, it is a function of the equilibrium parameter $\beta = \frac{\delta^*}{\tau_w} \frac{dp}{dx}$, and for $\beta = 0$, which is the flat plate flow, $A \approx -0.6$. Since the Law of the Wall also holds for constant pressure flow along convex surface, therefore, the Defect Law as given by equation (3.1-3) should also hold. However, A should also be a function of some curvature parameter. A semi-log plot of $(U_p - U)/u_\tau$ verses y/Δ will indeed show that A depends on curvature. This is displayed in Figure 42. Therefore, it can be seen that $A = A(\delta/R, \beta)$.*

The assumption of an overlap region means that U can be described equally well by the Law of the Wall (3.1-2) or by the Defect Law (3.1-3). These equations may be added to give the skin friction equation

$$\left(\frac{2}{C_f}\right)^{\frac{1}{2}} = \frac{U_{pw}}{u_\tau} = 5.6 \log \frac{R_{\delta^*}}{\delta^*} + B + A \quad (3.1-5)$$

where $\Delta u_\tau = U_{pw} \frac{\delta^*}{\delta}$ is substituted to give the final equation and R_{δ^*} is the Reynolds number based on δ^* which is defined as

$$\overline{\delta^*} = \int_0^\infty \frac{U_p}{U_{pw}} \left(1 - \frac{U}{U_p}\right) dy \quad (3.1-6)$$

In obtaining equation (3.1-5), it is assumed that $U_p \sim U_{pw}$ as $y/\Delta \rightarrow 0$. The skin friction equation thus deduced is quite general. It applies to all types of boundary layer flows over plane or convex

* The reason for suggesting δ/R is because for the present experiment δ^*/R is constant. Besides, δ remains relatively constant along the convex wall, thus, rendering δ/R a very natural curvature parameter to use.

surfaces so long as $A(\delta/R, \beta)$ is known.

For convex curvature, A is positive, therefore, according to equation (3.1-5), C_f will decrease faster than the corresponding flat plate flow. This means that the flow is less "turbulent-like", and as a result, the flow cannot sustain as high a pressure gradient as the corresponding flat plate flow. In other words, under the action of the same adverse pressure gradient, the flow over a convex surface will separate first. This is a direct consequence of the reduced mixing activities between fluid layers, which can be seen from the following explanation.

For flows over convex surfaces, the centrifugal force on a fluid particle must be balanced by an inward pressure gradient. If a particle is moving too slowly, its centrifugal force is too small, and it moves inward. Hence, it can be seen that the fluid particles that move away from the surface carry with them the velocities at the points where they come from will have a smaller centrifugal force at their new locations*. As a result, they will be pushed inwards by the pressure gradient and hence the interchange of momentum, energy, etc., between the faster and the more slowly moving particles are hindered. Thus mixing of momentum in the boundary layer will be reduced. This is evident from the measurements. At Station 1, the boundary layer thickness, δ , is about 0.55 inches, and δ grows to about 1 inch at the entrance to the curved section. The boundary layer thickness at Station 2 is about 1 inch, and it remains constant up to Station 11 (Figure 39). Thus, it can be seen that the boundary layer has not grown at all under the influence of convex curvature.

By comparison with the flat plate equilibrium boundary layer,

* This is Prandtl's mixing length argument which says that the linear momentum of the fluid particle is conserved when it is displaced from layer y to a new location at layer $y \pm dy$.

$\Delta = \int_0^\infty \frac{U_p - U}{u_\tau} dy$ should be a characteristic length in the defect region of the boundary layer. Therefore, a plot of $\frac{U_p - U}{u_\tau}$ verses $\frac{y}{\Delta}$ would show whether the present flow has reached an equilibrium state or not. Such a plot is given in Figure 43. From this plot, it appears that the flow has reached equilibrium at Station 11. However, this condition is not sufficient to demonstrate the equilibrium nature of the flow. Further evidence should be obtained from the turbulence measurements. This point will be discussed again in the following.

The decrease in mixing activities is also evident from the turbulence measurements. The distribution of turbulence intensities and turbulence energy are shown in Figures 44, 45 and 46 respectively. It can be seen that there are significant decreases in turbulence intensities across the boundary layer. Of course, the results are influenced by the favourable pressure gradient at the entrance to the curved test section.

After the favourable pressure gradient, which only extends to Station 2, the only external force that acts on the fluid particles is the centrifugal force created by the convex curvature. In the absence of wall curvature, the boundary layer would recover from the favourable pressure gradient and flat plate equilibrium would again be reached at about Station 9 (later calculations lend evidence to this). This means that mixing between fluid layers and turbulent diffusion would bring the level of turbulence right back to the flat plate values*.

However, under the influence of convex curvature, the turbulence intensities are prevented from recovering. This is clearly evident from the measurements at Stations 7, 9 and 11 (Figures 44, 45 and 46). Convex curvature acts to prevent mixing and diffusion of fluid particles outward, therefore, after the decrease in turbulence activities caused

*As evidence by the fact that the turbulence measurements at Station 1 correlate well with Klebanoff's (1955) data. This shows that the distributions of u'/U_1 , v'/U_1 and w'/U_1 are the same for all equilibrium flat plate boundary layers.

by the favourable pressure gradient, the centrifugal force prevents any further increase in turbulence intensities. This is why the turbulence measurements at Stations 7, 9 and 11 are quite similar to each other. It should be pointed out that there are very little turbulence activity in the outer part of the boundary layer, i.e. $y/\delta > 0.4$. Instead of increasing from Stations 7 to 11, the turbulence intensities decrease. On the other hand, the turbulence intensities near the wall increase slightly from Stations 7 to 11. This indicates that the effect of curvature is much greater in the outer part of the boundary layer than near the wall. On the other hand, the similarity of the distribution of the turbulence intensities at Stations 7, 9 and 11 seems to indicate that the flow has reached a new equilibrium state. If this is so, then the shear stress profiles at Stations 7, 9 and 11 should also be similar. From examination of the measured shear stress profiles in Figure 47 it appears that the flow has not reached an equilibrium state.

The flow, after recovering from the initial favourable pressure gradient, settles into a kind of quasi-equilibrium state where an inner region of rotational mean flow and non-zero Reynolds stress ($y/\delta < 0.4$ in Figure 47) is embedded in a larger region ($y/\delta < 1$) of rotational mean flow but zero Reynolds stress. Presumably the inner region would slowly grow until it coincides with the mean rotational region. Only then will it be an equilibrium flow in the conventional sense. In the outer part of the boundary layer, it is clearly evident that the "curvature effects" counteract the usual shear stress producing mechanism.

Since the shear stress is not measured by a conventional method, there is always doubt as to the reliability of the data, especially the "inviscid like" nature of the flow in the outer part of the boundary layer. For the present case, a slanted probe with a straight wire is used to measure \bar{uv} , $\bar{v^2}$ and \bar{vw} . It was pointed out in Section 2.4.3 that in reducing the data for \bar{uv} and $\bar{v^2}$, \bar{vw} is assumed zero. This assumption is justified because of the relative two-dimensionality of

the flow*. As an independent check, the measured \bar{uw} (which can be obtained directly by rotating the straight probe with a straight wire in the u and w plane) is found to be very nearly zero. A plot of \bar{uw} and \bar{vw} measured at Stations 1 and 11 is given in Figure 25. It can be seen that nowhere is \bar{uw} greater than 5% of \bar{uv} . This not only serves to show the true two-dimensional nature of the flow in the curved test section, but also the reliability of the measured shear stress profiles and the fact that the stress vanishes when $y/\delta > 0.4$.

The distribution of shear correlation coefficient is given in Figure 48. For equilibrium flat plate boundary layer, the shear correlation coefficient is constant (.5) for a greater part of the boundary layer, but drops to zero rapidly near the edge of the boundary layer (measurements at Station 1). For flow over convex surfaces, the shear correlation coefficient also remains constant (the constant varies from Station to Station) for a greater part of the "shear thickness", but drops to zero rapidly near the edge of the shear stress profile. The constant reached by the shear correlation coefficient is .38 at Station 9 and .45 at Station 11.

The turbulent energy equation can be obtained by adding equations (E-14), (E-15) and (E-16). The result is

$$\begin{aligned} \frac{Dq^2/2}{Dt} &= -\bar{uv} \left(\frac{\partial U}{\partial y} - kU \right) + \left(\frac{\partial}{\partial y} + k \right) \left\{ (q\ell_3 + v) \frac{\partial q^2/2}{\partial y} \right\} \\ &+ \left(\frac{\partial}{\partial y} + k \right) \left\{ (q\ell_3 + v) \frac{\bar{v^2}}{\partial y} \right\} + \frac{2}{3} \frac{\partial}{\partial y} \left\{ q\ell_2 \frac{\partial q^2/2}{\partial y} \right\} - \frac{q^3}{\Lambda} \end{aligned} \quad (3.1-12)$$

From this equation and the three fluctuation components given by equations (E-14), (E-15) and (E-16) or equations (E-1), (E-2) and (E-3), the following

*For two-dimensional flow, because of symmetry about the center line plane, \bar{uw} and \bar{vw} are necessarily zero.

points can be noted. First, turbulent energy is not produced only in $\overline{u^2}$ as in the case of a plane flow but also in $\overline{v^2}$. Second, the transfer of energy between $\overline{u^2}$ and $\overline{v^2}$ is due both to the pressure fluctuation and also to the term $\frac{ku^2v}{1+ky}$ appearing in equations (E-1) and (E-2). Third, the total energy production on all fluctuation components is

$$- \overline{uv} \left(\frac{\partial U}{\partial y} - kU \right)$$

A plot of the energy production is given in Figure 49. The smaller turbulent energy production explains the smaller turbulence intensities. Finally, the influence of the $\overline{v^2}$ - production term, $(+2k \overline{uv} U)$ in equation (E-2) or (E-15) on the flow should be pointed out. For flows over convex surfaces, k is positive, therefore $2k \overline{uv} U$ is positive and this means a suppression of $\overline{v^2}$ production. Hence, the radial movement of a fluid particle is suppressed. As a result, mixing activities between fluid layer are reduced. This means that radial displacement of a fluid particle in flows over convex surfaces is stable. Eskinazi and Yeh (1956) were the first to point out that this is in agreement with the stability criterion put forward by Rayleigh.

The advection and the production by normal stresses are also calculated and shown in Figures 50 and 51 respectively. In flat plate boundary layer the advection is very much smaller than the production except in the outermost part of the layer. The present result shows that in the inner part of the layer ($y/\delta < 0.4$), the advection is one order of magnitude smaller than the production (Figure 50). As to the outer part of the layer, curvature counteracts to reduce turbulence. The result is that the advection is nearly zero in this part of the layer. The production of normal stresses has been evaluated (Figure 51) to show that it is always small in comparison to the production. For the present experiment, the production of normal stresses is about two orders of magnitude smaller than the production.

3.2 Separating Flow Along Convex Wall

The setting up of the adverse pressure gradient for this experiment has already been examined in detail in Section 2.3.2, therefore, this will not be discussed again. However, it should be pointed out that a separating flow was obtained on the convex test wall. Although it was not possible to locate exactly the separation line, indications are that separation occurred around Station 11, at $x = 66.0$ inches. In this connection, it should be mentioned that later boundary layer calculations predict separation to occur at $x = 67$ inches (see Section 4.6.1). Because of the disturbing influence of the secondary flows near the end walls of the curved section, most likely separation would not occur along a line parallel to the z axis. Yaw measurements at Stations 8 and 10 (Figure 35), indicate that there is significant cross-flow at $x = 62.5$ inches. This means that there is convergence in the flow at this plane, and as a result, the flow would most likely separate first near the end walls than along the tunnel center line. Velocity profile measurements at Stations 8 and 10 (Figure 52) lend evidence to this as do the measurements of wall static pressure at planes 14 inches above and below tunnel center line. Because of this, the flow in this region can no longer be said to be two-dimensional. This fact is borne out by the momentum balance calculation.

In order to make use of equation (3.1.1) for the momentum balance calculation, the skin friction C_f and the boundary layer integral parameters δ^* and θ have to be known. Since the Law of the Wall is independent of the free stream conditions, and has previously been verified for flow over convex surfaces, it is assumed to be valid for the present experimental flow. This means that C_f can again be determined from the Clauser plot. The velocity profiles are numerically integrated to give δ^* and θ . Because of the errors involved in the velocity profile measurements near separation (i.e. at Stations 9 and 11), the calculated δ^* and θ at these two stations would be smaller than

the true values. This should be borne in mind when examining the momentum balance calculation.

The results of the momentum balance calculation using equation (3.1-1) is given in Figure 40. It can be seen that up to $x = 59$ inches, the flow is fairly two-dimensional, but the flow begins to deviate from two-dimensionality after that. This is consistent with all other measurements.

The development of δ^* and θ is shown in Figure 83 and the development of C_f and H is given in Figure 84. It can be seen that δ^* and θ increase steeply towards separation. However, δ^* increases much faster than θ , resulting in an extremely large slope for H near separation. Again, this lends evidence to the fact that the flow separates around $x = 66$ inches. Because of the errors in the velocity profile measurements near separation, the C_f determined from the Clauser plot would also be in error. Since near separation, the measured velocity is higher than the true value, the C_f determined from Clauser plot would tend to be greater. This is borne out by the fact that the measured C_f at Stations 9 and 11 are greater than the calculated C_f (see Section 4.6.1 and Figure 84).

The measured velocity profiles are plotted in Figure 52, and the results show that the measurements near the wall at Stations 9, 11 and 12 are in error, because the measurements give a near constant velocity in this region. In actuality, this is not the case, especially at Station 12, where the flow is known to have separated. Also shown are the off center line velocity measurements at Stations 3, 5, 8 and 10. Again, the results substantiate the claim of two-dimensionality at Station 4, but not at Station 9.

The semi-log plot of the measured velocity profiles at Stations 4, 7, 9 and 11 is given in Figure 53. The friction velocity u_τ is calculated from the measured U_{pw} and C_f . Again, the velocity profiles show the existence of a wall law region, and that all the data points in this region fall on the Law of the Wall, thus giving support to the claim that

the Law of the Wall also applies to flow over convex surfaces in an arbitrary pressure gradient. This should come as no surprise, because for plane flow, the Law of the Wall has been shown to be independent of the free stream conditions.

By comparison with turbulent boundary layers over plane surfaces, it can be expected that the Defect Law also holds for boundary layers over convex surfaces in arbitrary pressure distribution. A semi-log plot of $(U_p - U)/u_T$ versus y/Δ is given in Figure 54. Again, the result shows that A is also a function of δ/R . Therefore, the skin friction relation as given in equation (3.1-5) is also applicable to convexly curved turbulent flows in adverse pressure gradient.

In previous experiment, the straight probe with a straight wire was used to measure $\bar{u^2}$, \bar{uw} and $\bar{w^2}$. The slanted probe with a straight wire was used to obtain \bar{uv} and $\bar{v^2}$, while \bar{vw} was assumed zero. However, for the present experiment, due to the disturbing side influence of the secondary flows at $x = 62.5$ inches, it was felt that the assumption of $\bar{vw} = 0$ may not be a good one. Therefore, a straight probe with a slanted wire was used to measure \bar{uv} , $\bar{v^2}$ and \bar{vw} (see Sections 2.2.5 and 2.4.3), while the same technique was used for the measurements of $\bar{u^2}$, \bar{uw} and $\bar{w^2}$. The results of the measurements at Stations 1, 4, 9, 11 and 12 are given in Figures 55 to 62. Since the flow separates around Station 11, not too much significance should be attached to the measurements near the wall at Station 12. This is because there is probably a small reverse flow region at Station 12. However, the measurements at the outer part of the boundary layer would provide some insight into the nature of separated flows, therefore the data at Station 12 should be examined in this light.

The measurements at Station 1 serve to establish the reliability of the slanted wire technique to measure \bar{uv} . At the same time, the measured \bar{vw} would also indicate the validity of the assumption $\bar{vw} = 0$ made in the measurements of the previous experiment. The measured \bar{uw}

and \overline{vw} are shown in Figures 55 and 56 respectively. In Figure 57 the distribution of $\overline{u^2}$ is shown. It can be seen that at Station 1, nowhere are \overline{uw} and \overline{vw} greater than 5% of $\overline{u^2}$. Also, the measured turbulence intensities and shear stress at Station 1 correlate well with the measurements at Station 1 of the previous experiment and with the data of Klebanoff (1955). This establishes the reliability of the slanted wire technique to measure \overline{uv} . It also provides evidence to support the claim that the flow is truly two-dimensional in the straight section.

As to the measured \overline{uw} and \overline{vw} in the curved test section, the results show that toward separation, \overline{uw} and \overline{vw} are as high as 20% of $\overline{u^2}$. This is particularly true near the edge of the boundary layer where $\overline{u^2}$ is relatively small as a result of the effect of convex curvature. At Station 4, \overline{uw} and \overline{vw} are about 10% of $\overline{u^2}$ for the greater part of the boundary layer. However, since the error of the rotating-wire method as determined in the fully developed pipe flow experiment (Appendix C) and the measurements at Station 1 is about 5%, the flow at Station 4 can still be considered to be fairly two-dimensional. At Stations 9, 11 and 12, even discounting the error of the rotating-wire method, \overline{uw} and \overline{vw} still amount to about 15% of $\overline{u^2}$. To the best of the author's knowledge, no measurements of \overline{uw} and \overline{vw} are available for boundary layers in an adverse pressure gradient. Therefore, it is hard to estimate whether the \overline{uw} and \overline{vw} are the result of the effect of convex curvature or the three-dimensional nature of the flow. However, from the results of the measurements of the constant pressure flow experiment, it is very likely that \overline{uw} and \overline{vw} arise as a result of the convergence of the flow towards separation.

From the flat plate experiment of Klebanoff (1955), it is known that the fluctuation velocities ($\overline{u^2}$, $\overline{v^2}$ and $\overline{w^2}$) reach their maximum very near to the wall. The separating flow experiment of Schubauer and Klebanoff (1951) showed that under the influence of an adverse pressure

gradient, these maxima slowly move away from the wall. The same phenomenon is observed in the present experiment, but the effect of convex curvature tends to reduce the maximum reached by the fluctuation velocities (see Figures 57-59). Again, this is due to the fact that convex curvature acts to reduce mixing, and hence suppresses turbulence activity. In spite of the large adverse pressure gradient (which promotes turbulent mixing) the turbulence intensities in the outer part of the boundary layer ($y/\delta > 0.4$) are still significantly smaller than the corresponding values at Station 1 (Figures 57, 58 and 59). Compared with the results of the constant pressure flow experiment, it can be said that the effect of convex curvature is very significant in the outer part of the boundary layer, and the data seem to indicate that the curvature effect is independent of the pressure gradient. This can be seen from a comparison of Figures 48 and 60. For the constant pressure flow, $q^2/u_{pw}^2 \approx .002$ at $y/\delta = .4$ and this drops slowly to zero towards the edge of the boundary layer. For the separating flow $q^2/u_{pw}^2 \approx .002$ at $y/\delta = .5$, and this too drops to zero in the same manner as in the case of the constant pressure flow. The fact that q^2 is approximately the same for Stations 4, 9 and 11 in the outer part of the boundary layer is an indication that the effect of curvature is far greater than the adverse pressure gradient effect.

The shear stress distributions for Stations 1, 4, 9, 11 and 12 are plotted in Figure 61. Under the action of an adverse pressure gradient, the point of maximum shear stress moves away from the wall. But, how far should the maximum point be away from the wall, and how great is the maximum in the absence of wall curvature cannot be determined, because of the lack of data for a corresponding plane flow. However, anticipating the results of the boundary layer calculations outlined in Chapter IV, a rough estimate can be obtained. The result of such a calculation is shown in Figure 86. It can be seen that convex curvature acts to reduce the maximum reached by the shear stress and prevent the point of maximum from

moving too far away from the wall. This will be discussed further in Section 4.6.1. In spite of the adverse pressure gradient, the shear stress again vanishes inside the boundary layer at $y/\delta \approx 0.5$. This is another indication that convex curvature in the outer part of the boundary layer has a much greater effect on the flow than the pressure gradient.

To provide a check for the measured shear stress profiles, the boundary layer equations (4.2-15) to (4.2-17) are numerically integrated using the measured velocity profiles and the C_f determined from the Clauser plot. The resultant shear stress profiles at Stations 4, 9 and 11 are then compared with the measured profiles. It was found that the resultant profiles were quite similar to those calculated by the present prediction method, and for the sake of clarity they were not shown.

From Figure 86, it can be seen that the measured shear stress is much lower than the shear stress calculated from the measured velocity profiles. The discrepancy could be explained by the fact that the flow is not quite two-dimensional, and by errors in measurements (it is pointed out by Bissonnette (1970) that in regions of very high velocity gradient, the rotating-wire method for the measurement of $-\bar{uv}$ becomes inaccurate).

Much the same discussion about turbulent energy production in the previous section also applies to the results of this experiment, and hence will not be repeated. However, it should be pointed out that although the flow is under the influence of a severe adverse pressure gradient, there is very little turbulent energy production after $y/\delta \approx 0.5$. Even in the region near the wall, energy production is severely curtailed by the effect of convex curvature. Since the shear stress measurements are in error, therefore, the energy production calculations are only qualitatively correct.

3.3 Constant Pressure Flow along Concave Wall

The z direction traverse at Station 1 serves two purposes. First, it serves to indicate the kind of disturbances created by the presence of

the traversing device in the tunnel, and second, it serves to provide a basis for comparison with subsequent traverses in the concave test section. Since the flow in the straight section is shown to be two-dimensional (see discussion in Section 2.3.1), the velocity inside the boundary layer and at a fixed distance away from the wall should be constant for all z planes. Therefore, if the traversing device (Figure 21) is set up properly inside the tunnel, the hot-wire would give a straight line on the X-Y plotter for the z direction traverses at Station 1. Indeed, this was the case, and the result of five different traverses at $y = 0.2, 0.4, 0.6, 0.8$ and 1.0 inches from the wall is shown in Figure 63. This substantiates the previous claim that the flow is two-dimensional in the straight section, and that the disturbances created by the presence of the traversing device do not disturb the nature of the flow. However, it does increase the local flow velocity because of the blockage effect it has on the flow. To estimate the amount of increase, the traversing device was set at two different positions at Station 1 such that the hot-wire was 0.2 and 1 inches away from the wall. The hot-wire was then moved down to the tunnel center line plane and the mean velocities at these two y positions were measured. Comparisons with the velocity profile measured in the same location show that the velocity increase varies from 1% to less than 5% of the free stream velocity, and that the increase is greater in the free stream than near the wall. The velocity increase is due to the relatively large cross-section of the strut (aerofoil shape with maximum thickness of $1/2$ inches and a chord of $2 1/2$ inches) in a tunnel of 6 inches wide. Due to the peculiar design of this traversing device, it is not possible to make a quantitative study of the increase in velocity across the boundary layer. As a result, all traverses obtained in the z direction can only be interpreted qualitatively.

The X-Y plotter trace of the z direction traverses at $x = 70$ and 96 inches are shown in Figures 64 and 65 respectively. Again, traverses

were taken at $y = 0.2, 0.4, 0.6, 0.8$ and 1.0 inches respectively. All five traces were plotted on the same graph. Compared to the traces obtained at Station 1 (Figure 63), the results given in Figures 64 and 65 clearly indicate that there is significant velocity variations in the z direction. These velocity variations can be explained by assuming the existence of a system of longitudinal vortices similar to the Taylor-Gortler type vortices inside the boundary layer. Then the positions of the high points (crests) in the trace could be taken to correspond to the positions between two vortices whose flow directions are directed towards the wall, and the positions of the low points (trough) could be taken to correspond to the positions between two vortices whose flow directions are directed away from the wall (see Figure 66). In the positions of the crests, faster moving fluid elements are being entrained into the boundary layer by the vortices, and as a result of the turbulent mixing process inside the boundary layer, the mean velocity becomes higher. On the other hand, in the positions of the troughs, the vortices sweep up slower moving fluid elements from the wall, and through mixing, the mean velocity becomes smaller. Thus, the "wave like" shape of the trace in the z direction.

The data also show that there are more than one pair of vortices inside the boundary layer. For the 21 inches traversed in the central core of the tunnel, there are about 10 pairs of vortices at $x = 70$ inches and 7 pairs at $x = 96$ inches. This indicates that the vortices spread in the z direction and some vortex pairs end at the end walls of the tunnel as the flow moves downstream. The mean half wave length at $x = 70$ inches is approximately 0.57 inches, and it is about 0.9 inches at $x = 96$ inches. In addition, it can be inferred that the positions of the crest and trough are quite stationary, and that they remain at the same z position across the boundary layer. These results substantiate Tani's (1962) findings that a system of Taylor-Gortler type vortices does occur in turbulent boundary layers over concave surfaces, and that the wave

amplitude does decrease as the radius of curvature increases.

It should be pointed out that the above data only manage to show the presence of the vortices up to $y = 1.0$ inch. No traverses were made above $y = 1.0$ inch at both $x = 70$ and 96 inches. This is most unfortunate because the maximum y position is limited by the width of the curved test section and the relatively large size of the traversing device. The traversing device is located outside the boundary layer for all the traverses at $x = 70$ inches, and partly inside the boundary layer at $x = 96$ inches. However, since the hot-wire is 2.75 inches away from the strut, the disturbances created by the strut will not be felt at the hot-wire, except that the flow between the strut and the wall will be slightly accelerated. This is certainly true at Station 1, and it is assumed to be true also at $x = 70$ and 96 inches respectively.

Since the mean output of the hot-wire only gives the normal component of the resultant velocity, and the flow direction inside the boundary layer is not known, it is not possible to construct a quantitative diagram of the vortex structure inside the boundary layer from the traces shown in Figure 64 and 65. As a result, only a qualitative diagram is given in Figure 66. The appearance of two layers of vortices at $x = 96$ inches will be explained later. From this simple-minded diagram, the z locations of the points of measurements can be determined. For Station 1, the measurements were taken at tunnel center line, i.e. $z = 0$, while for $x = 70$ and 96 inches, measurements were taken at the position of the crest and trough of the wave system. The reason for this is obvious. Assuming the presence of the vortex system, there is a minimum of cross flow at the positions of the crest and trough. Those positions that are nearest to the tunnel center line and lie above it are chosen to be the points of measurements, because at these locations, the variation of the positions of the crest and trough is a minimum across the boundary layer. The locations of the trough and crest are labelled Stations 2 and 3, 4 and 5 at $x = 70$ and 96 inches respectively. The distance

between Stations 2 and 3 is 0.672 inches and between Stations 4 and 5 is 1.092 inches. The x and z coordinates of the measuring stations are given in Figure 6.

The velocity profiles measured at Stations 2, 3, 4 and 5 are plotted in Figure 67. Since the cross-flow is a minimum at these locations the measured velocities are not corrected for cross-flow. Instead W is assumed to be zero at these locations. The measured velocities are not corrected for V , which can be significantly greater than the corresponding flat plate flow. However, the results show that δ/R varies between .07 and .18, and since V/U can be at most of the order of $(\delta/U)(\partial U/\partial x)$, therefore, the maximum resultant velocity $Q \approx 1.018U$. In this sense, the measured profiles can be considered as profiles of U .

From the measured profiles, it can be seen that the boundary layer is thicker at the position of the trough than at the position of the crest, and the growth rate at these two positions is approximately the same. The thicker boundary layer at the trough can be explained as follows. Concave curvature enhances mixing, so when a fluid particle is displaced from a position nearer the wall to a position further away from the wall, it will tend to move even further out under the action of the centrifugal force. At the position of the trough, the particle is pushed even further out by the vortex motion, and as a result, the boundary layer becomes thicker. At the position of the crest, the vortex motion acts in the opposite direction to that of the centrifugal force, thus the boundary layer becomes thinner compared to that at the trough. The results also show that the boundary layer thickness at the position of the trough is about twice that at the position of the crest.

To find out whether the Law of the Wall also holds for flow over concave surfaces, the velocity profiles are plotted in the Clauser form. The values of U_{pw} were obtained by extrapolating the measured profiles to $y = 0$. This is because no wall static pressure measurements were made at the positions of the crest and trough. A sample plot of the

velocity profiles at Stations 2 and 3 in the Clauser form is given in Figure 68. The plot shows the existence of a log region near the wall, but no Clauser lines match the data. The Clauser lines match the data points in the viscous region. However, this should not be taken as given the C_f at these locations. Therefore, the conclusion can be drawn that the Law of the Wall does not hold for flow along concave surfaces. As a result, the skin friction at the wall cannot be determined.

Since convex curvature suppresses mixing, therefore, concave curvature should enhance mixing. The result of this would be a significant increase in the fluctuation velocities inside the boundary layer.

Evidence to this fact is given by the turbulence measurements at Stations 1 to 5. The results are shown in Figures 69 to 72. In analysing these results, one point should be noted, and this is the effect of the adverse pressure gradient on the flow at the entrance to the curved section.

Bradshaw and Ferriss (1965) showed that in a relaxing boundary layer, the turbulence intensities decrease as the pressure gradient is removed. Also, in passing from a zero pressure gradient region into an adverse pressure gradient region, the turbulence intensities increase significantly. For the present case, if the concave curvature has no effect on the flow, then the turbulence intensities should increase from $x = 24$ inches to $x = 70$ inches and decrease significantly from $x = 70$ inches to $x = 96$ inches. The distribution of $\overline{u^2}/U_{pw}^2$ does show a decrease in the region near the wall from $x = 70$ inches to 96 inches, but remains relatively constant in the outer part of the boundary layer (Figures 69). This is consistent with the findings of the convex wall, i.e. wall curvature has very little effect in the region near the wall. However, the same trend is not noted in the distribution of $\overline{v^2}/U_{pw}^2$ and $\overline{w^2}/U_{pw}^2$ (Figures 70 and 71). There is no discernable decrease in $\overline{v^2}$ and $\overline{w^2}$ distribution across the boundary layer from $x = 70$ to 96 inches.

According to the $\overline{v^2}$ component of the turbulence energy equation (E-2), concave curvature promotes $\overline{v^2}$ production, and this is evident

from the distribution of $\overline{v^2}/U_{pw}^2$ (Figure 70). However, not all of the increase over that measured at Station 1 is due to the influence of concave curvature. Part of the increase is due to the adverse pressure gradient effect at the entrance to the curved section, and part of the increase is due to the effect of the vortex system. At Stations 2 and 4, the vortices have a resultant motion in the yz plane directed away from the wall. This contributes further to the outward radial movement of the fluid particles. At Stations 3 and 5, the vortices have a resultant motion in the yz plane directed towards the wall, thus any radial movement of fluid particles outward would be hindered by the vortices. As a result, the $\overline{v^2}$ at Stations 2 and 4 are greater than at Stations 3 and 5 respectively. This is particularly true at $x = 96$ inches. The reason is that there may be more than one layer of vortices at $x = 96$ inches. This point will be discussed again later. The same is true of the $\overline{w^2}/U_{pw}^2$ distribution (Figure 71). In other words, the system of longitudinal vortices contribute to the production of $\overline{v^2}$ and $\overline{w^2}$ fluctuations, but not $\overline{u^2}$. This is evident from the fact that near the wall, $\overline{u^2}$ drops from $x = 70$ to 96 inches, but not $\overline{v^2}$ and $\overline{w^2}$. As a result of this, the distribution of turbulence energy q^2/U_{pw}^2 does not change significantly from $x = 70$ to 96 inches (Figure 72). Note that the turbulence energy distribution is greater at Stations 2 and 4 than at Stations 3 and 5. This is especially true at $x = 96$ inches.

The shear stress profiles at $x = 70$ inches are given in Figure 73, while those at $x = 96$ inches are shown in Figure 74. The shear stress profile at Station 1 is also shown for purpose of comparison. The fact that the shear stress profiles at $x = 70$ inches show a maximum is due to the adverse pressure gradient effect at the entrance to the curved section. The maximum remains even at $x = 96$ inches. This indicates the influence concave curvature has on the mixing process. However, the shear stress profiles at $x = 96$ inches show two points of maximum.

This could be due to the fact that there is more than one layer of longitudinal vortices at $x = 96$ inches. Turbulence intensity measurements also seem to lend evidence to such a postulate. However, the strongest evidence comes from the profiles of \bar{uw} and \bar{vw} at $x = 70$ and 96 inches (Figures 75 and 76). Measurements of \bar{uw} and \bar{vw} at Stations 2 and 3 show that there is only one maximum (Figure 76), while the measurements at Stations 4 and 5 distinctly show two maximum points for both \bar{uw} and \bar{vw} . It can be postulated that at $x = 70$ inches, there is only one layer of longitudinal vortices, while at $x = 96$ inches, there are two layers. This is depicted in Figure 66. Also shown are the velocity traverse at a constant distance away from the wall and the boundary layer thickness distribution in the z direction. Of course, within each bigger vortex, there are smaller vortices, but these are not shown.

From previous discussion, the directions of rotation of the vortices at $x = 70$ inches can be postulated to be as shown in Figure 66. Based on the same evidence, the directions of rotation of the first layer of vortices (the layer nearer to the wall) at $x = 96$ inches are assumed to be the same as that at $x = 70$ inches. The directions of rotation of the second layer of vortices can be postulated after an examination of Figures 75 and 76. At Station 2, the distribution of \bar{uw} is positive across the boundary layer, while that of \bar{vw} is negative (Figure 75). At Station 4, the distribution of \bar{uw} is also positive across the whole boundary layer, while that of \bar{vw} is also negative (Figure 76). This seems to indicate that the second layer of longitudinal vortices would also have the same direction of rotation as the first layer. At Station 3, the \bar{uw} distribution is negative, and the \bar{vw} distribution is positive. The same is true at Station 5. This again lends evidence to support the postulate that the directions of rotation of the second layer of vortices at $x = 96$ inches are the same as the first layer. The fact that there are two layers of vortices at

$x = 96$ inches is very clear from Figure 76. However, the vortex structure at $x = 96$ inches is not stable. Therefore, further downstream, it may revert back to that of a single layer structure.

The distributions of \overline{uw} and \overline{vw} at Stations 4 and 5 all show the existence of two waves with the waves going to zero at the wall, at $y/5 \approx .6$ and at the edge of the boundary layer. Based on all these evidences, the resultant vortex structure as shown in Figure 66 is postulated for the boundary layer flow at $x = 70$ and 96 inches respectively.

Finally the shear correlation coefficient and the turbulent energy production are calculated and plotted in Figures 77 and 78. As expected, the shear correlation coefficient does not remain constant across the boundary layer. This is due to the effect of the longitudinal concave curvature which gives rise to the Taylor-Gortler type vortices. As to the peculiar behaviour of the turbulent energy production at $x = 96$ inches, this is probably due to the peculiar velocity profiles at Stations 4 and 5.

Chapter IV
THEORETICAL PREDICTIONS OF
CURVED TURBULENT BOUNDARY LAYERS

4.1 Introduction

The ultimate goal in boundary layer research is the understanding of the physics of such flow and at the same time to be able to develop a procedure for predicting, both quantitatively and easily, the practical features (e.g. H , C_f , and the shear stress) of boundary layers. In the past, investigators have been quite successful in the development of prediction methods for two-dimensional boundary layers. In these calculation methods, be they based on integral or differential equations, it has been assumed that the static pressure variation across the layer, due to either rapid boundary layer growth, flow injection at the surface, or surface curvature (when $|\delta/R| \ll 1$) has very little effect on the flow and hence can be neglected. Such an assumption neglects the effects of the curvature of the mean flow streamlines. These effects are shown to have a considerable influence on the mixing process in the flow. Convex curvature in the mean flow streamlines reduces the mixing between the fluid layers and this leads to an early cut off of the shear stress (see Fig. 59). In contrast, concave curvature enhances the mixing process, and the shear stress profile remains quite full until the edge of the boundary layer where it drops to zero steeply (see Figs. 73 and 74).

Thompson (1963) was the first author to point out the importance of incorporating a curvature parameter in calculation methods. In a critical review of existing two-dimensional calculation methods, he found that the small curvature that existed on most of the test surface where measurements were made, was not large enough to cause substantial difference between the measured velocity profiles and that calculated assuming the flow to be two-dimensional plane flow. However, there was a consistent difference between the measured and calculated shape factor

development in the streamwise direction. A well-known case was the measurements on an aerofoil by Schubauer and Klebanoff (1951). In their measurements, the curvature parameter δ/R , as defined by Thompson, was $\sim 1/150$ downstream of the pressure minimum. Most predictions methods gave fairly good correlation for the velocity profiles and the momentum thickness, but all predicted the shape factor too low. Thompson argued that the effect of curvature was on the entrainment process. He modified Head's entrainment function by the inclusion of an empirical factor which was assumed to be a simple function of the curvature parameter δ/R . This improved the agreement between the experimentally measured H and that predicted by his calculation method. Although the method used by Thompson was not very satisfactory, his results brought to light the very important conclusion, namely that the primary influence of the streamline curvature was on the mechanism of the turbulent motion and the entrainment of free stream fluid into the layer. Therefore, any attempt to extend existing two-dimensional calculation methods to include curvature effects should be directed to the modification of some parameter, e.g. Head's entrainment function or eddy viscosity, that will take the physics of the flow into account.

More recently, Bradshaw (1968) has drawn the analogy between the Richardson Number, which is a meteorological parameter, and a curved flow parameter "L" which describes the effect of streamline curvature on turbulent flow. Using this analogy to apply meteorological data to curved turbulent flows, Bradshaw showed that the apparent mixing length was affected appreciably even though $\delta/R \sim 1/300$. Incorporating this modified mixing length into the Bradshaw, Ferris and Atwell calculation method, Bradshaw managed to obtain better agreement between H , δ^* and C_f as measured by Schubauer and Klebanoff (1951) and that predicted by his calculations. Again, this points to the need to modify the eddy viscosity or mixing length function, such that the resultant form will be general enough to predict both curve and plane turbulent flows.

accurately.

Hence, the object of the present chapter is to seek a set of self consistent turbulent boundary layer equations for flows along curved surfaces, and the corresponding momentum integral. This is done in Section 2 and Appendix D.

In Section 3 a modified eddy viscosity function which consists of the product of the flat plate eddy viscosity and a factor that is a simple function of the curvature parameter is derived. This modified eddy viscosity approaches the eddy viscosity function put forward by Mellor and Gibson (1966) as the surface curvature becomes zero. A technique similar to that proposed by Mellor and Herring (1970) is adopted for the derivation of the modified eddy viscosity function.

Assumptions are made to simplify the turbulence energy equations of \bar{u}^2 , \bar{v}^2 , \bar{w}^2 and \bar{uv} for curved turbulent flows (for derivation of these equations see Appendix E) so that all terms in these equations, including the pressure-velocity correlations and the triple velocity correlations terms, can be expressed in terms of the double velocity correlations. These equations are further simplified by assuming the advection and diffusion terms to be small compared to the dissipation and production terms, and hence can be neglected. This is equivalent to assuming that energy production balances dissipation and that a state of equilibrium is reached as far as the energy distribution is concerned. This is a plausible assumption because existing flat plate (Klebanoff 1955) and pipe flow (Laufer 1954) data do indicate such a state of equilibrium for the flow near the wall. The resultant equations are algebraic and can easily be solved for the shear stress.

In relating the various terms in the turbulence energy equations to $\bar{u_i u_j}$, four length scales are introduced as proportionality constants. Therefore, in order that the shear stress be specified completely by mean flow quantities only, empirical statements for these length scales should be derived. Mellor and Herring (1970) have shown that the four

length scales are not truly independent and from experimental correlation two relations can be found for the four length scales. This leaves two length scales to be specified. If the eddy viscosity function for curved turbulent flow as derived in Section 3 is truly a general one, then the length scales appearing in the expression should be independent of curvature and pressure gradient. Hence, it is sufficient to obtain empirical statements for the length scales by only considering the plane flow turbulence energy equation and the Law of the Wall. This is done in Section 4.

The boundary layer equations together with the eddy viscosity function are then solved using a finite difference method adopted by Herring and Mellor (1970). Reduction of the set of equations to an ordinary differential equation is given in Section 5. The calculations are then compared with the measurements on both the convex and concave surfaces. Finally, a brief discussion of the calculation method and the comparisons are given in Section 6.

4.2 Boundary Layer Equations for Curved Flow and the Momentum Integral

The Navier-Stokes equations for a constant density incompressible flow can be written as:

$$\nabla \cdot \bar{q} = 0 \quad (4.2-1)$$

$$\frac{\partial \bar{q}}{\partial t} + \bar{q} \cdot \nabla \bar{q} = -\frac{1}{\rho} \nabla p + \nu \nabla^2 \bar{q} \quad (4.2-2)$$

Consider a flow over a two dimensional curved surface. Use general orthogonal coordinates with x measured along the surface, y normal to the surface and z at right angles to the x - y plane which is the plane of the motion. If $k(x) = 1/R(x)$ is the curvature of the surface, (k is taken to be positive for convex curvature, and negative for concave curvature) the elements of length along the parallel curves and along the normal are $h_1 = 1 + ky$ and $h_2 = 1$. The element of length along

the z direction is $h_3 = 1$. Taking u , v , and w to be the velocity components along the x , y and z directions respectively, and working out the components of the vector equation of motion (see Owczarek 1964), the following equations for u , v and w are obtained:

$$\begin{aligned} \frac{\partial u}{\partial t} + \frac{1}{1+ky} u \frac{\partial u}{\partial x} + v \frac{\partial u}{\partial y} + w \frac{\partial u}{\partial z} + \frac{k}{1+ky} uv \\ = - \frac{1}{1+ky} \frac{\partial p}{\partial x} + \frac{1}{1+ky} \frac{\partial T_{xx}}{\partial x} + \frac{\partial T_{xy}}{\partial y} + \frac{\partial T_{xz}}{\partial z} \\ + \frac{2k}{1+ky} T_{xy} \end{aligned} \quad (4.2-3)$$

$$\begin{aligned} \frac{\partial v}{\partial t} + \frac{1}{1+ky} u \frac{\partial v}{\partial x} + v \frac{\partial v}{\partial y} + w \frac{\partial v}{\partial z} - \frac{k}{1+ky} u^2 \\ = - \frac{\partial p}{\partial y} + \frac{1}{1+ky} \frac{\partial T_{xy}}{\partial x} + \frac{\partial T_{yy}}{\partial y} + \frac{\partial T_{yz}}{\partial z} \\ - \frac{k}{1+ky} (T_{xx} - T_{yy}) \end{aligned} \quad (4.2-4)$$

$$\begin{aligned} \frac{\partial w}{\partial t} + \frac{1}{1+ky} u \frac{\partial w}{\partial x} + v \frac{\partial w}{\partial y} + w \frac{\partial w}{\partial z} = - \frac{\partial p}{\partial z} \\ + \frac{1}{1+ky} \frac{\partial T_{xz}}{\partial x} + \frac{\partial T_{yz}}{\partial y} + \frac{\partial T_{zz}}{\partial z} + \frac{k}{1+ky} T_{yz} \end{aligned} \quad (4.2-5)$$

where

$$T_{xx} = 2v \left(\frac{1}{1+ky} \frac{\partial u}{\partial x} + \frac{k}{1+ky} v \right)$$

$$T_{yy} = 2v \frac{\partial v}{\partial y}$$

$$T_{zz} = 2v \frac{\partial w}{\partial z}$$

are the viscous normal stresses and

$$T_{xy} = \nu \left\{ (1 + ky) \frac{\partial}{\partial y} \left(\frac{u}{1+ky} \right) + \frac{1}{1+ky} \frac{\partial v}{\partial x} \right\}$$

$$T_{yz} = \nu \left\{ \frac{\partial v}{\partial z} + \frac{\partial w}{\partial y} \right\}$$

$$T_{xz} = \nu \left\{ \frac{\partial u}{\partial z} + \frac{1}{1+ky} \frac{\partial w}{\partial x} \right\}$$

are the shearing stresses. It should be pointed out that the pressure p and the stresses T_{ij} have the dimension of velocity square in these equations. The continuity equation can be written

$$\frac{\partial u}{\partial x} + \frac{\partial}{\partial y} \{ (1+ky)v \} + \frac{\partial}{\partial z} \{ (1+ky)w \} = 0 \quad (4.2-6)$$

Consider a turbulent flow that is two dimensional in the mean.

Therefore, the mean flow in the z direction is zero, and all $\frac{\partial}{\partial z}$ of mean flow quantities vanish. The field equations of motion for such a flow when decomposed into ensemble mean velocities U, V plus fluctuating velocities u, v, w and their concomitant pressure P and p are:

$$\frac{\partial U}{\partial x} + \frac{\partial}{\partial y} \{ (1+ky)V \} = 0 \quad (4.2-7)$$

$$\begin{aligned} \frac{\partial U}{\partial t} + \frac{1}{1+ky} U \frac{\partial U}{\partial x} + V \frac{\partial U}{\partial y} + \frac{k}{1+ky} UV &= - \frac{1}{1+ky} \frac{\partial P}{\partial x} + \frac{1}{1+ky} \frac{\partial}{\partial x} (\bar{u}^2 + T_{xx}) \\ &+ \frac{\partial}{\partial y} (-\bar{u}v + T_{xy}) + \frac{2k}{1+ky} (-\bar{u}v + T_{xy}) \end{aligned} \quad (4.2-8)$$

$$\begin{aligned} \frac{\partial V}{\partial t} + \frac{1}{1+ky} U \frac{\partial V}{\partial x} + V \frac{\partial V}{\partial y} - \frac{k}{1+ky} U^2 &= - \frac{\partial P}{\partial y} + \frac{1}{1+ky} \frac{\partial}{\partial x} (-\bar{u}v + T_{xy}) + \frac{\partial}{\partial y} (-\bar{v}^2 + T_{yy}) \\ &- \frac{k}{1+ky} ((\bar{u}^2 + T_{xx}) - (\bar{v}^2 + T_{yy})) \end{aligned} \quad (4.2-9)$$

$$\frac{\partial u}{\partial x} + \frac{\partial}{\partial y} \{ (1+ky)v \} + \frac{\partial}{\partial z} \{ (1+ky)w \} = 0 \quad (4.2-10)$$

$$\begin{aligned}
\frac{\partial u}{\partial t} + \frac{1}{1+ky} \frac{\partial}{\partial x} (2uU + u^2 - \bar{u}^2) + \frac{\partial}{\partial y} (vU + uV + uv - \bar{uv}) \\
+ \frac{\partial}{\partial z} (wU + uw - \bar{uw}) + \frac{2k}{1+ky} (vU + uV + uv - \bar{uv}) \\
= - \frac{1}{1+ky} \frac{\partial p}{\partial x} + \frac{1}{1+ky} \frac{\partial \tau_{xx}}{\partial x} + \frac{\partial \tau_{xy}}{\partial y} + \frac{2k}{1+ky} \tau_{xy} + \frac{\partial \tau_{xz}}{\partial z} \quad (4.2-11)
\end{aligned}$$

$$\begin{aligned}
\frac{\partial v}{\partial t} + \frac{1}{1+ky} \frac{\partial}{\partial x} (vU + uV + uv - \bar{uv}) + \frac{\partial}{\partial y} (2vV + v^2 - \bar{v}^2) \\
+ \frac{\partial}{\partial z} (wV + vw - \bar{vw}) - \frac{k}{1+ky} (2uU - 2vV + u^2 - v^2 - \bar{u}^2 + \bar{v}^2) \\
= - \frac{\partial p}{\partial y} + \frac{1}{1+ky} \frac{\partial \tau_{xy}}{\partial x} + \frac{\partial \tau_{yy}}{\partial y} - \frac{k}{1+ky} (\tau_{xx} - \tau_{yy}) + \frac{\partial \tau_{yz}}{\partial z} \quad (4.2-12)
\end{aligned}$$

$$\begin{aligned}
\frac{\partial w}{\partial t} + \frac{1}{1+ky} \frac{\partial}{\partial x} (wU + uw - \bar{uw}) + \frac{\partial}{\partial y} (wV + vw - \bar{vw}) \\
+ \frac{\partial}{\partial z} (w^2 - \bar{w}^2) + \frac{k}{1+ky} (wV + vw - \bar{vw}) = - \frac{\partial p}{\partial z} \\
+ \frac{1}{1+ky} \frac{\partial \tau_{xz}}{\partial x} + \frac{\partial \tau_{yz}}{\partial y} + \frac{k}{1+ky} \tau_{yz} + \frac{\partial \tau_{zz}}{\partial z} \quad (4.2-13)
\end{aligned}$$

The τ_{ij} are the fluctuating viscous stresses given by the same expressions as T_{ij} except that all velocities in T_{ij} are now replaced by the fluctuating velocities.

The only component of vorticity that is non-zero is that normal to the x-y plane and is given by:

$$\zeta = \frac{1}{1+ky} \frac{\partial v}{\partial x} - \frac{\partial U}{\partial y} - \frac{k}{1+ky} U \quad (4.2-14)$$

With the field equations of motions given by equations (4.2-7) to (4.2-9) and the vorticity defined by equation (4.2-14), the next step is to simplify these equations to obtain a set of self-consistent boundary layer equations for a turbulent flow that is two-dimensional in the mean along a curved surface. The assumptions to be made are that the boundary layer thickness δ is very small compared to the x dimension and the radius of curvature R of the surface is of the same order as the x dimension. Therefore, δ/R is very much smaller than 1. The geometry of the surface is specified by $R(x)$. The function $R(x)$ has to be smooth but otherwise it can be a general one.

Recently, Mellor (1970) has demonstrated that the method of matched asymptotic expansion can also be applied to turbulent boundary layers. Two small parameters, $\epsilon = u_t/U_0$ and $\epsilon^2 \hat{\epsilon} = \nu/U_0 \ell$, (where u_t is any characteristic turbulent velocity, U_0 is any characteristic free stream velocity and ℓ is a characteristic length) appear as a result of making the equations non-dimensional with respect to u_t , U_0 and ℓ . However, Mellor (1970) has shown that expansion in one parameter, ϵ , is sufficient and that $(\hat{\epsilon}/\epsilon^n) \sim 0$ as $\hat{\epsilon} \rightarrow 0$ for arbitrary n . Unlike the case of laminar boundary layers, three layers exist, (an outer layer, a middle layer and an inner layer) due to the presence of the two small parameters. Also, the Law of the Wall is shown to be a consequence of the matching between the inner and the middle layers. In view of this, the set of boundary layer equations for a curved flow is obtained through the method of matched asymptotic expansion instead of through dimensional argument. This is carried out in Appendix D for equations (4.2-7) to (4.2-9) and equation (4.2-14). The resultant set of equations in dimensional form is given by equations (D-22) to (D-25) and equation (D-26), which is

$$\frac{\partial U}{\partial x} + \frac{\partial V}{\partial y} + kV = 0 \quad (4.2-15)$$

$$U \frac{\partial U}{\partial x} + V \frac{\partial U}{\partial y} + kUV = - \frac{1}{\rho} \frac{\partial P}{\partial x} + \frac{\partial}{\partial y} \left(\frac{\tau}{\rho} \right) + 2k \frac{\tau}{\rho} \quad (4.2-16)$$

$$k \frac{U^2}{\rho} = \frac{1}{\rho} \frac{\partial P}{\partial y} \quad (4.2-17)$$

$$\zeta = - \frac{\partial U}{\partial y} - kU \quad (4.2-18)$$

$$\frac{\tau}{\rho} = \nu_e \left(\frac{\partial U}{\partial y} - kU \right) \quad (4.2-19)$$

where U_p is the potential velocity which is, as yet, undefined.

The inner boundary condition is given by the no slip condition.

The outer boundary condition can be defined so that the velocity approaches the free stream velocity as $y \rightarrow \delta$. The free stream velocity is obtained from the Bernoulli equation and the condition of zero vorticity. This immediately gives the free stream velocity distribution as:

$$U_p(x, y) = U_{pw}(x) e^{-ky} \quad (4.2-20)$$

where $U_p(x, y)$ is the potential velocity and $U_{pw}(x)$ is the potential velocity at the surface.

It should be noted that, inserting (4.2-20) into (4.2-19) shows that τ/ρ does not vanish as $y \rightarrow \infty$ if ν_e is maintained constant. On the other hand, the terms $\frac{\partial}{\partial y} \left(\frac{\tau}{\rho} \right) + 2k \frac{\tau}{\rho} \sim 0$ as $y \rightarrow \infty$. This circumstance is identical to that obtained in laminar flow. This is pointed out because, later on, an eddy viscosity model where ν_e does stay constant for large y is assumed. This is, of course, not particularly realistic but it is known that predicted velocity profiles are insensitive to the detailed behavior of ν_e at large y .

Equation (4.2-17) must be used together with the other approximations of the boundary layer equations (see Appendix D). If $\frac{1}{\rho} \frac{\partial P}{\partial y} = k \frac{U^2}{\rho}$ is used instead, the pressure term will not balance the advective terms in equation (4.2-16) when it is integrated over the whole layer. Thus,

integrating equation (4.2-17) and then differentiate the resultant expression with respect to x it can be shown that

$$\frac{1}{\rho} \frac{\partial P}{\partial x} = - \frac{1}{2} \frac{\partial}{\partial x} \{ U_{pw}^2 e^{-2ky} \} \quad (4.2-21)$$

Substitute $\frac{1}{\rho} \frac{\partial P}{\partial x}$ into equation (4.2-16) and then integrate from 0 to ∞ ^{*}, the momentum integral, thus obtained, can be written as follows:

$$\begin{aligned} \frac{1}{2} C_f &= \frac{d\theta}{dx} + (H + 2) \frac{\theta}{U_{pw}} \frac{dU_{pw}}{dx} - \frac{dk}{dx} \int_0^\infty y \left(1 - \frac{U}{U_p} \right) dy \\ &\quad - \frac{dk}{dx} \int_0^\infty 2y \frac{U}{U_p} \left(1 - \frac{U}{U_p} \right) dy \end{aligned} \quad (4.2-22)$$

where C_f , δ^* and θ are defined as:

$$C_f = \frac{\tau_w}{\frac{1}{2} \rho U_{pw}^2} \quad (4.2-23)$$

$$\delta^* = \int_0^\infty \left(1 - \frac{U}{U_p} \right) dy \quad (4.2-24)$$

$$\theta = \int_0^\infty \frac{U}{U_p} \left(1 - \frac{U}{U_p} \right) dy \quad (4.2-25)$$

^{*}The integration is somewhat complicated. It is helpful to first rewrite the shear stress terms in equation (4.2-16) as $\rho^{-1} e^{-2ky} \frac{\partial(e^{2ky}\tau)}{\partial y}$ and then set $U = e^{-ky} u(x, y)$ where $k = k(x)$ and $u \sim U_{pw}$ as $y \rightarrow \infty$. Solving the continuity equation gives

$$V = e^{-ky} \left[- \int_0^\infty \frac{\partial u}{\partial x} dy + \frac{dk}{dx} \int_0^\infty y u dy \right]$$

Substituting the above U , V terms and equation (4.2-21) into equation (4.2-16) the integration may be performed and the result cleared of exponential functions. Finally, noting that $u = U_{pw} (U/U_p)$, the result can be written in the form of equation (4.2-22).

Note that the two integrals in equation (4.2-22) are finite since $U/U_p \rightarrow 1$ at the edge of the boundary layer. If $\frac{1}{\rho} \frac{\partial P}{\partial y} = kU^2$ had been used instead of equation (4.2-17), a term would be introduced which would blow up as the limit of integration approached infinity.

The set of equations (4.2-15), (4.2-16), (4.2-17) and (4.2-18) together with the eddy viscosity ν_e to be derived in Section 3 form a closed set, and can be solved when the appropriate initial and boundary conditions are specified. The boundary conditions are given by:

$$U(x,0) = V(x,0) = 0 \quad (4.2-26)$$

at the wall, and

$$U(x,y) = U_p(x,y) = U_{pw}(x)e^{-ky} \quad (4.2-27)$$

at the edge of the boundary layer. To solve this set of equations, the method of Herring and Mellor (1970) is used. The reduction of these equations to a single ordinary differential equation is given in Section 5.

4.3 The Eddy Viscosity Hypothesis

As pointed out by Mellor and Herring, an expression for the shear stress ($-\bar{uv}$) can be obtained from the turbulence energy equations when further assumptions are made to simplify the equations to a set of algebraic equations. Invoking the assumptions that in the region near a wall, the advection and diffusion of turbulence energy are very much smaller than the production and dissipation of turbulence energy, the advection and diffusion terms in equations (E-14) to (E-17), as derived in Appendix E, can be neglected. The result is

$$\frac{1}{3} \frac{q}{\ell_1} (\bar{u}^2 - \frac{1}{3} q^2) + \frac{2}{3} \frac{q^3}{\Lambda} + 2 \bar{uv} \frac{\partial U}{\partial y} + 2k \bar{uv} U = 0 \quad (4.3-1)$$

$$\frac{1}{3} \frac{q}{\ell_1} (\bar{v}^2 - \frac{1}{3} q^2) + \frac{2}{3} \frac{q^3}{\Lambda} - 4k \bar{uv} U = 0 \quad (4.3-2)$$

$$\frac{1}{3} \frac{q}{\ell_1} (w^2 - \frac{1}{3} q^2) + \frac{2}{3} \frac{q^3}{\Lambda} = 0 \quad (4.3-3)$$

$$\frac{1}{3} \frac{q}{\ell_1} (\bar{uv}) + \bar{v^2} \frac{\partial U}{\partial y} - k(2 \bar{u^2} - \bar{v^2})U = 0 \quad (4.3-4)$$

where Λ and ℓ_1 are length scale as defined in equation (E-6) and (E-7) respectively.

The equations are correct to order δ because of the inclusion of the curvature terms. Since the objective of the present Section is to find an eddy viscosity function that includes curvature, this purpose will not be served if the curvature terms in the turbulence energy equations are excluded.

Omitting all the algebra, the result of solving equations (4.3-1) to (4.3-4) for $(-\bar{uv})$ is

$$(-\bar{uv}) = (\ell_1 \Lambda^{1/3})^{3/2} (1 - \frac{6\ell_1}{\Lambda})^{3/2} \left\{ 1 - \frac{72(\ell_1/\Lambda)}{1-6(\ell_1/\Lambda)} x \right. \\ \left. \frac{(1 + \frac{kU}{\partial U/\partial y}) \frac{kU}{\partial U/\partial y}}{(1 - \frac{kU}{\partial U/\partial y})^2} \right\}^{3/2} \quad (4.3-5)$$

It should be noted that in deriving this expression for $(-\bar{uv})$, isotropy is not assumed. If isotropy is assumed, the same expression will still be obtained, except that the factor $(1 - 6\ell_1/\Lambda)^{3/2}$ becomes 1. In this case, when curvature is assumed zero, the expression.

$$(-\bar{uv}) = (\ell_1 \Lambda^{1/3})^{3/2} \left| \frac{\partial U}{\partial y} \right| \frac{\partial U}{\partial y}$$

is obtained. Immediately, it can be recognized that the eddy viscosity can be identified with the expression $(\ell_1 \Lambda^{1/3})^{3/2} \frac{\partial U}{\partial y}$. Similarly, one can identify $(\ell_1 \Lambda^{1/3})^{3/2} (1 - 6\ell_1/\Lambda)^{3/2} \frac{\partial U}{\partial y}$ as the eddy viscosity in a

plane flow when isotropy is not assumed. Denoting the latter expression by ν_{eF} and after some rearrangement, equation (4.3-5) can be written as

$$(-\bar{u}\bar{v}) = \nu_{eF} \left\{ 1 - \beta \frac{\left(\frac{\partial U}{\partial y} + kU \right) kU}{\left(\frac{\partial U}{\partial y} - kU \right)^2} \right\}^{3/2} \left| 1 - \frac{kU}{\partial U / \partial y} \right| \left(\frac{\partial U}{\partial y} - kU \right) \quad (4.3-6)$$

where

$$\beta = \frac{72(\ell_1/\Lambda)}{1 - 6(\ell_1/\Lambda)}$$

The shear stress is given by equation (4.2-19)

$$\frac{\tau}{\rho} = \nu_e \left(\frac{\partial U}{\partial y} - kU \right)$$

where ν_e is the eddy viscosity. Comparing equation (4.3-6) with equation (4.2-19) ν_e can be written

$$\nu_e = \nu_{eF} \left\{ 1 - \beta \frac{kU(\partial U / \partial y + kU)}{(\partial U / \partial y - kU)^2} \right\}^{3/2} \left| 1 - \frac{kU}{\partial U / \partial y} \right| \quad (4.3-7)$$

This then is the desired eddy viscosity function. Note that for convex curvature k is positive, and the modifying factor within the curly brackets is always smaller than 1, except at the wall. Hence, the physics of convexly curved flow, which in simple terms can be characterized by the decreased mixing, is embedded in the eddy viscosity function. For flow over concave surfaces, the present investigation has demonstrated that a system of longitudinal vortices exists inside the boundary layer. As a result, the flow is no longer two-dimensional, and the present approach to characterize the flow by a scalar eddy

viscosity function is in doubt. However, the eddy viscosity function as given in equation (4.3-7) affords the practical engineer a simple approach to estimate, though approximately, the various features of the turbulent boundary layer on a concave surface. This would involve some kind of assumptions about the flow or the prediction method (This will be discussed in detail in Section 4.2-6). For the present, it is enough just to point out the limitation of the eddy viscosity function. Now, it remains to define β which involves the ratio (ℓ_1/Λ) , and this is given in the next section.

4.4 Determination of (ℓ_1/Λ)

The eddy viscosity for a turbulent flow along any smooth curved surface is completely defined by equation (4.3-5). Theoretically, ν_e can be computed once the variation of ℓ_1 and Λ across the boundary layer is known. This requires emperical statements for ℓ_1 and Λ very near the wall, which at present cannot be obtained with certainty due to the lack of reliable turbulence data in this region. Since the present objective is to find a modifying function that includes curvature for the flat plate eddy viscosity, it suffices to identify

$$\nu_{eF} = (\ell_1 \Lambda^{1/3})^{3/2} (1 - 6 \frac{\ell_1}{\Lambda})^{3/2} \left| \frac{\partial U}{\partial y} \right|$$

with the eddy viscosity hypothesis put forward by Mellor and Gibson (1966). Therefore, only the ratio (ℓ_1/Λ) remains to be determined in the expression for ν_e .

From the emperical statements of ℓ_1 and Λ given by Mellor and Herring (1970), it can be seen that (ℓ_1/Λ) is practically constant in the overlap and defect regions of the boundary layer. Due to the fact that the flow near the wall is predominantly viscous in nature, the curvature, according to Van Dyke (1962), is a second order effect in this region. Hence, it is sufficient only to determine the ratio (ℓ_1/Λ) in the outer

part of the boundary layer, and this can be obtained, most conveniently, by considering the Law of the Wall region only.

Near the wall, Mellor and Herring (1970) assume that

$$\ell_1 = f_n(y, q, \nu)$$

or

$$\frac{\ell_1 q}{\nu} = \phi_{\ell_1}(x) ; \quad x = \frac{qy}{\nu}$$

Similarly

$$\frac{\Lambda q}{\nu} = \phi_{\Lambda}(x)$$

As yet, the functions $\phi_{\ell_1}(x)$ and $\phi_{\Lambda}(x)$ are undefined. For the Law of the Wall region, it is further assumed that these functions can be approximated by a power law namely

$$\frac{\ell_1 q}{\nu} = A \left(\frac{qy}{\nu} \right)^n \quad (4.4-1)$$

$$\frac{\Lambda q}{\nu} = B \left(\frac{qy}{\nu} \right)^m \quad (4.4-2)$$

where A and B are constants and n and m are integers to be determined.

The eddy viscosity function should be applicable to both curved and plane flows with arbitrary pressure distribution. Therefore, it is necessary only to determine ℓ_1 and Λ for the flow along a flat plate. The turbulence energy equations for $\overline{u^2}$, $\overline{v^2}$, $\overline{w^2}$ and \overline{uv} , neglecting the diffusion and advection terms are:

$$\frac{1}{3} \frac{q}{\ell_1} (\overline{u^2} - \frac{1}{3} q^2) + \frac{2}{3} \frac{q^3}{\Lambda} + 2 \overline{uv} \frac{\partial U}{\partial y} = 0 \quad (4.4-3)$$

$$\frac{1}{3} \frac{q}{\ell_1} (\bar{v}^2 - \frac{1}{3} q^2) + \frac{2}{3} \frac{q^3}{\Lambda} = 0 \quad (4.4-4)$$

$$\frac{1}{3} \frac{q}{\ell_1} (\bar{w}^2 - \frac{1}{3} q^2) + \frac{2}{3} \frac{q^3}{\Lambda} = 0 \quad (4.4-5)$$

$$\frac{1}{3} \frac{q}{\ell_1} \bar{u}\bar{v} + \bar{v}^2 \frac{\partial U}{\partial y} = 0 \quad (4.4-6)$$

In this region, the Law of the Wall also hold and

$$\frac{\partial U}{\partial y} = \frac{u_\tau}{\kappa y} \quad (4.4-7)$$

where $u_\tau^2 = \frac{\tau_w}{\rho}$ is the friction velocity and κ is the von Karman constant. Making the velocities non-dimensional with respect to u_τ and with the substitution of equations (4.4-1), (4.4-2) and (4.4-7), equations (4.4-3) to (4.4-6) can be written as

$$\begin{aligned} \frac{u_\tau}{A} \left(\frac{q u}{\nu} \right)^{-n} \frac{q^{+2}}{\nu} (\bar{u}^{+2} - \frac{1}{3} q^{+2}) + \frac{2u_\tau}{B} \left(\frac{q y}{\nu} \right)^{-m} \frac{q^{+4}}{\nu} \\ - 6 \left(-\bar{u}\bar{v}^+ \right) \frac{1}{\kappa y} = 0 \end{aligned} \quad (4.4-8)$$

$$\frac{u_\tau}{A} \left(\frac{q y}{\nu} \right)^{-n} \frac{q^{+2}}{\nu} (\bar{v}^{+2} - \frac{1}{3} q^{+2}) + \frac{2u_\tau}{B} \left(\frac{q y}{\nu} \right)^{-m} \frac{q^{+4}}{\nu} = 0 \quad (4.4-9)$$

$$\frac{u_\tau}{A} \left(\frac{q y}{\nu} \right)^{-n} \frac{q^{+2}}{\nu} (\bar{w}^{+2} - \frac{1}{3} q^{+2}) + \frac{2u_\tau}{B} \left(\frac{q y}{\nu} \right)^{-m} \frac{q^{+4}}{\nu} = 0 \quad (4.4-10)$$

$$- \frac{u_\tau}{A} \left(\frac{q y}{\nu} \right)^{-n} \frac{q^{+2}}{\nu} (-\bar{u}\bar{v}^+) + 3 \bar{v}^{+2} \frac{1}{\kappa y} = 0 \quad (4.4-11)$$

where

$$\begin{aligned}\bar{u}^{+2} &= \frac{\bar{u}^2}{u_\tau^2}, & \bar{v}^{+2} &= \frac{\bar{v}^2}{u_\tau^2}, & \bar{w}^{+2} &= \frac{\bar{w}^2}{u_\tau^2} \\ \bar{q}^{+2} &= \frac{\bar{q}^2}{u_\tau^2}, & \bar{uv}^+ &= \frac{\bar{u}\bar{v}}{u_\tau^2}\end{aligned}$$

It is further assumed that the shear stress is constant, i.e. $(-\bar{u}\bar{v}^+) = 1$, in the Law of the Wall region, and the function ϕ_{ℓ_1} and ϕ_Λ are universal, hence, $v\phi_{\ell_1}$ and $v\phi_\Lambda$ are independent of viscosity. This necessary implies that $n = m = 1$. With these simplifications, equations (4.4-8) to (4.4-11) reduce to:

$$Bq^+ (\bar{u}^{+2} - \frac{1}{3} \bar{q}^{+2}) + 2Aq^{+3} - 6 \frac{AB}{\kappa} = 0 \quad (4.4-12)$$

$$B(\bar{v}^{+2} - \frac{1}{3} \bar{q}^{+2}) + 2Aq^{+2} = 0 \quad (4.4-13)$$

$$B(\bar{w}^{+2} - \frac{1}{3} \bar{q}^{+2}) + 2Aq^{+2} = 0 \quad (4.4-14)$$

$$-q^+ (-\bar{u}\bar{v}^+) + \frac{3Av}{\kappa} = 0 \quad (4.4-15)$$

Solving these equations give:

$$-\frac{2A}{B} = \frac{\bar{v}^{+2} + \bar{w}^{+2}}{2\bar{q}^{+2}} - \frac{1}{3} \quad (4.4-16)$$

$$B = \kappa q^{+3} \quad (4.4-17)$$

$$\kappa^4 = A^3 B (1 - 6 \frac{A}{B})^3 \quad (4.4-18)$$

A value of ℓ_1/Λ which gives the best agreement in C_f between the calculated values and the measured values for the case of constant pressure flow along convex wall is chosen and used for calculations of the other two cases. However, whatever value one chooses for ℓ_1/Λ , it should

satisfy equation (4.4-18), so that the von Karman constant can always be recovered.

4.5 Reduction of the Set of Boundary Layer Equations to an Ordinary Differential Equation

The set of equations (4.2-15), (4.2-16), (4.2-17) and (4.2-18) together with boundary conditions (4.2-26) and (4.2-27) can be reduced to an ordinary differential equation through the following substitutions. Following Herring and Mellor (1970), assume

$$\frac{\partial f}{\partial \eta} = f'(x, \eta) = \frac{U_p - U}{U_p} \quad (4.5-1)$$

where

$$\eta = \frac{y}{\delta^*}$$

Differentiate equation (4.5-1) with respect to x and y and integrate the continuity equation (4.2-15) to obtain V , it can be shown that

$$\begin{aligned} U \frac{\partial U}{\partial x} &= e^{-2a\eta} [U_{pw} U'_{pw} (1-f')^2 - U_{pw}^2 (1-f') \frac{\partial f'}{\partial x} \\ &+ \frac{U_{pw}^2}{\delta^*} \{a\delta^{*'} - a'\delta^*\} \eta (1-f')^2 \\ &+ U_{pw}^2 \frac{\delta^{*'}}{\delta^*} (1-f') \eta f''] \end{aligned} \quad (4.5-2)$$

$$\begin{aligned} V \left(\frac{\partial U}{\partial y} + kU \right) &= e^{-2a\eta} [U_{pw} U'_{pw} (\eta-f) f'' + \frac{U_{pw}^2}{\delta^*} \{a\delta^{*'} - a'\delta^*\} x \\ &+ (\frac{1}{2} - \eta f + G) f'' - U_{pw}^2 f'' \frac{\partial f}{\partial x} + \frac{U_{pw} \delta^{*'}}{\delta^*} (\eta f' - f) f''] \end{aligned} \quad (4.5-3)$$

where $a = k\delta^*$ and $G = \int_0^\eta f d\eta$. The primes in a , δ^* and U_{pw} refer

to ordinary differentiation with respect to x .

The pressure term can be obtained by differentiating the integral of equation (4.2-17). The result is:

$$-\frac{1}{\rho} \frac{\partial P}{\partial x} = e^{-2a\eta} \left[U_{pw}^2 + \frac{U_{pw}^2}{\delta^*} (a\delta^{*'} - a'\delta^{*})\eta \right] \quad (4.5-4)$$

Bearing in mind that $1 + ky$ is taken to be 1 only whenever it appears as a coefficient and noting that v_e is a function of η , the shear stress terms can be written as

$$\begin{aligned} \frac{\partial}{\partial y} \left(\frac{\tau}{\rho} \right) + 2k \left(\frac{\tau}{\rho} \right) &= e^{-2a\eta} \frac{U_{pw}^2}{\delta^*} \left[-e^{a\eta} (\phi f'') \right. \\ &\quad \left. + e^{a\eta} a(\phi f'') - e^{a\eta} a(2\phi' + a\phi)(1 - f') \right] \end{aligned} \quad (4.5-5)$$

where

$$\phi = \frac{v_e}{U_{pw} \delta^*}$$

Substitute equations (4.5-2) to (4.5-5) into equation (4.2-16) and after some rearrangement, the following equation for f is obtained, namely:

$$\begin{aligned} (\phi f'')' &= -e^{-a\eta} \left\{ \left(\frac{\delta^* U'}{U_{pw}} + \delta^{*'} \right) (\eta - f) + (a\delta^{*'} - a'\delta^{*}) \right. \\ &\quad \left. \left(\frac{1}{2}\eta^2 - \eta f + G \right) f'' - e^{-a\eta} \left\{ \frac{\delta^* U'}{U_{pw}} + (a\delta^{*'} - a'\delta^{*})\eta \right\} \right. \\ &\quad \left. (f' - 2)f' + e^{-a\eta} \delta^* (1 - f') \frac{\partial f}{\partial x} + e^{-a\eta} \delta^* f'' \frac{\partial f}{\partial x} \right. \\ &\quad \left. + a(\phi f'') - a(2\phi' + a\phi)(1 - f') \right\} \end{aligned} \quad (4.5-6)$$

This equation (4.5-6) can be further reduced to an ordinary differential

equation through the use of the identities

$$\frac{\partial f}{\partial x} = \frac{f_i - f_{i-1}}{\Delta x}$$

$$\frac{\partial f'}{\partial x} = \frac{f'_i - f'_{i-1}}{\Delta x}$$

for the differential with respect to x .

The resultant equation as function at x_i can be written as

$$\begin{aligned} -(\phi f'')_i' &= -\tau_b' + c_1(f''_i + f''_{i-1}) + c_2(f'_i + f'_{i-1}) \\ &+ c_3(f'_i - f'_{i-1}) - c_4(f_i - f_{i-1}) - c_5 - c_6 \end{aligned} \quad (4.5-7)$$

where

$$\begin{aligned} \tau_b' &= -(\phi f'')_{i-1}' \\ c_1 &= e^{-a\eta} \left(\frac{\delta^* U'}{U_{pw}} + \delta^* \right) \left(\eta - \frac{f_i + f_{i-1}}{2} \right) + e^{-a\eta} \\ &\quad (a\delta^* - a' \delta^*) \left(\frac{1}{2} \eta^2 - \eta \frac{f_i + f_{i-1}}{2} + \frac{G_i + G_{i-1}}{2} \right) \\ c_2 &= e^{-a\eta} \left\{ \frac{\delta^* U'}{U_{pw}} + \eta (a\delta^* - a' \delta^*) \right\} \left(\frac{f_i + f_{i-1}}{2} - 2 \right) \quad (4.5-8) \\ c_3 &= e^{-a\eta} \frac{\delta_i^* + \delta_{i-1}^*}{\Delta x} \left(1 - \frac{f'_i + f'_{i-1}}{2} \right) \\ c_4 &= e^{-a\eta} \frac{\delta_i^* + \delta_{i-1}^*}{\Delta x} \left(\frac{f''_i + f''_{i-1}}{2} \right) \\ c_5 &= a \{ (\phi f'')_i + (\phi f'')_{i-1} \} \\ c_6 &= 2a \left(2\phi' + a\phi \right) \left(1 - \frac{f'_{i-1} + f'_i}{2} \right) \end{aligned}$$

The overbar denotes average value and the C_i 's are all calculated from the previous iteration. Rearranging the equation further, the final equation to be solved can be written as:

$$(b_5 f'')_i^1 = b_4 + b_3 f''_i + b_2 f'_i + b_1 f_i \quad (4.5-9)$$

and

$$b_5 = -\phi_i$$

$$b_4 = -\tau_b' + C_1 f''_{i-1} + (C_2 + C_3) f'_{i-1} + C_4 f_{i-1} - C_5 + C_6$$

$$b_3 = C_1 \quad (4.5-10)$$

$$b_2 = C_2 - C_3$$

$$b_1 = -C_4$$

The boundary conditions at the wall are:

$$\begin{aligned} f'(x,0) &= 1 \\ f(x,0) &= 0 \end{aligned} \quad (4.5-11)$$

and the free stream boundary condition is

$$\lim_{\eta \rightarrow \infty} f'(x,\eta) = 0 \quad (4.5-12)$$

The unknown function b_5 is given by equation (4.3-6). In terms of f , it can be written as

$$\phi = \phi_F \left\{ 1 + \beta \frac{a f''(1-f')}{[f''+2a(1-f')]^2} \right\}^{3/2} \left| \frac{(f''+2a(1-f'))}{(f''+a(1-f'))} \right| \quad (4.5-13)$$

where $\phi_F = \frac{v_{eF}}{U_{pw}\delta^*}$ is the flat plate eddy viscosity function.

The equations (4.5-9) and (4.5-13) together with boundary conditions (4.5-11) and (4.5-12) are solved using as initial conditions the measured data at Station 1 of the three experimental cases, namely: (1) constant pressure flow along convex wall, (2) separating flow along convex wall and (3) constant pressure flow along concave wall. The results are then compared with the present data. A discussion of this comparison is given in the next section.

4.6 Comparison with Present Data

The boundary layer program of Herring and Mellor (1968) is used to numerically integrate the ordinary differential equation (4.5-9) with the set of boundary conditions (4.5-11) and (4.5-12). The program uses a fourth order Runge-Kutta technique for the numerical integration. Although such a technique works well for all types of boundary layer development on a flat surface, it fails to give a solution that converges to the required accuracy on both f and f' when the surface is curved. The difficulties occur at the point where curvature begins, and in part is due to the fact that the shear stress vanishes at about half the boundary layer thickness at this point. In order to overcome this shortcoming, another integration technique is used. The method is discussed in Richmeyer and Morton (1964). Essentially, it reduces the ordinary differential equation to a set of algebraic equations and these are then solved for f' simultaneously with the boundary conditions. Instead of shooting out from the wall, the method proceeds inward, thus eliminating completely the initial guess on $f''(x,0)$ which is required in the case of the Runge-Kutta technique. The shear stress is then obtained by differentiating f' numerically. The whole calculation is repeated until f and f' converge to the required accuracy.

Initially, $\ell_1/\Lambda = .0136$ (obtained by setting $q^+ = 3$) is used. However, this gives a C_f that is too high compared to the data of constant

pressure flow along convex wall. Various values of (ℓ_1/Λ) are tried until one (ℓ_1/Λ) is found such that the calculated C_f and the measured C_f for the case of constant pressure flow along convex wall correlate with each other. Such a value of (ℓ_1/Λ) is found to be .0417 and this is used for the boundary layer predictions of the other two cases.

4.6.1 Turbulent Boundary Layers along Convex Surfaces

The results for the case of constant pressure flow are given in Figures 79 to 81. The agreement among the various integral parameters θ , δ^* and H are very good (Figure 79). In order to show more explicitly the curvature effect, two more calculations are made. One is without curvature, i.e. $R_o \rightarrow \infty$, while the curvature for the second calculation is halved, i.e. $R_o = 20$ inches. For both calculations, the same initial condition and the same distribution of potential velocity at the wall are used. It can be seen that the result of convex curvature is to reduce θ and increase δ^* , hence H is very much different from the corresponding flow along a flat plate. The calculation with no curvature shows that $H = 1.35$ when the flow is in equilibrium again after passing through the favorable pressure gradient. However, with the designed curvature ($R_o = 10$ inches) H still keeps on increasing and this is an indication that the flow is not in equilibrium even at $x = 75$ inches. On the other hand, with the curvature halved, H approaches a constant at $x = 75$ inches. The prediction of C_f is of course excellent, since ℓ_1/Λ is chosen so that the calculated and measured C_f matched each other at $x = 71$ inches, i.e. Station 11. For the corresponding flat plate flow, C_f is about 13% higher than the measured C_f . This strongly indicates that turbulent flows along convex surface cannot support as high an adverse pressure gradient as the same flow over a flat surface. This fact will again be borne out in the separating flow case. Calculated velocity profiles at Stations 2, 7, 9 and 11 are shown in Figure 80 together with the measured profiles.

In general, agreement is good, and the present method predicts the velocity profile quite well even at Station 2 which locates downstream of the strong favourable pressure gradient. For purpose of clarity, the velocity profiles from the other two calculations are not shown.

The present method also predicts the shear stress profile very well (Figure 81), especially the point where the shear stress vanishes. Near the wall, the agreement is off, but in this region, the measurements are in error because the rotating-wire method is not accurate in region of high shear as pointed out in Appendix D. Aside from this region which is about one displacement thickness, the agreement is very good. At Station 7, the shear stress profiles of the zero wall curvature ($R_o \rightarrow \infty$), and half wall curvature ($R_o = 20$ in.) are also shown. This shows clearly the effect of convex curvature in "cutting off" turbulence. With no curvature, the shear stress vanishes at the edge of the boundary layer ($\eta \approx 11$), with $R_o = 20$ inches, the shear stress vanishes at $\eta \approx 5$, while with $R_o = 10$ inches (the designed curvature), the shear stress vanishes at $\eta \approx 4$. Hence it can be seen that even if the surface has a very small curvature, the point of zero shear will be somewhere inside the boundary layer (the boundary layer is assumed to have been established previously).

In the calculation of the separating flow case, instead of using the measured distribution of potential velocity at the wall all the way up to $x = 75$ inches, the extrapolated velocity distribution from $x = 62.5$ inches to $x = 75$ inches is used (Figure 82). This gives a linear decelerating potential velocity distribution at the wall, and this is the desired velocity distribution to be set on the convex surface (see Section 2.3.2). The results are shown in Figures 83 to 86. As in the case of constant pressure flow, two more calculations (one with $R_o \rightarrow \infty$ and the other with $R_o = 20$ in.) are made for the sake of parametric study of the curvature effect. The calculated and measured θ and δ^* are given in Figure 83. Under the influence of adverse pressure gradient,

the differences in the development of θ is unnoticeable. The development for the case of $R_o = 20$ inches is practically the same as that of $R_o \rightarrow \infty$, hence not shown on the graph. However, the differences in δ^* are discernable, especially near separation.

Although the location of the point of separation is not known, it can be said with confidence that the flow separates somewhere between $x = 66$ inches and $x = 69.5$ inches. If separation is defined as the point where $C_f \rightarrow 0$, then the separation point as calculated by the present method falls right within the range of $x = 66$ inches to $x = 69.5$ inches, and is at $x \approx 67$ inches (Figure 84). With $R_o = 20$ inches, separation occurs at $x \approx 73$ inches, and for zero wall curvature, the flow does not separate until $x \approx 80$ inches. This supports the previous conclusion that under the same distribution of potential velocity at the wall, the flow separates earlier when the surface has a convex curvature.

The calculated C_f agrees well with the measured C_f up to $x = 59$ inches, and after this the calculated value is generally lowered. The reason is that in the actual flow, the inviscid-viscous interaction causes the velocity distribution to level off, and therefore has a delaying effect on separation. This is borne out by the fact that if the measured velocity distribution is used instead of the linear decelerating velocity distribution, the present method gives good agreement with C_f up to $x = 66$ inches. However, separation is predicted to be at $x = 78$ inches, and no separation is predicted for the other two cases. This points out one of the difficulties in trying to predict near separation flow. Unless a way can be found to account for the inviscid-viscous interaction near separation, the difficulty remains.

The agreement between calculated and measured velocity profiles at stations 4, 7, 9 and 11 is excellent (Figure 85). However, the agreement is poor between calculated and measured shear stress profiles at stations 4 and 7 (Figure 86). In spite of the poor agreement, the point

where $\tau \rightarrow 0$ is accurately predicted. Even though the flow is under the influence of a strong adverse pressure gradient, τ still vanishes at about half the boundary layer thickness, and that by decreasing the curvature to half, it pushes the point where $\tau \rightarrow 0$ by about the same amount as in the case of the constant pressure flow. This seems to indicate that curvature operates independently of the pressure gradient and this may also be the reason why the value of (ℓ_1/Λ) , obtained by considering flat plate data, works so well in this case. The designed convex curvature not only causes C_f to decrease by about 25% (Figures 79 and 84), it also causes the maximum shear stress reached inside the boundary layer to decrease by the same amount (Figure 86).

In conclusion, the value of (ℓ_1/Λ) so obtained is also good for pressure gradient flow and that the present method can be considered rather successful in the prediction of boundary layer developments along convex walls with arbitrary pressure gradient.

4.6.2 Turbulent Boundary Layers along Concave Surfaces

The present experimental investigation has shown that the turbulent boundary layer on a concave surface is different from that on a convex surface because of the presence of a system of longitudinal vortices. However, it is most desirable, from the practical engineer's point of view, that turbulent boundary layers over concave surfaces can be predicted by simple method like that discussed above. This would be possible and therefore some approximations of the boundary layer growth could be obtained if the following assumptions were made about the flow. Firstly, assume the vortex pairs that constitute the vortex system are similar. (This can be evident from Figures 64 and 65). Secondly, assume the flow to be completely characterized by parameters which are obtained by averaging over any one vortex pair. Finally, assume the eddy viscosity function given by equation (4.3-7) is capable of describing the resultant "average" flow. That this assumption is feasible can be seen from

equation (4.3-7). For concave curvature, κ is negative, so the factor within the curly brackets in equation (4.3-7) is always positive. In simple terms, this can be taken to characterize the increased mixing of flows over concave surfaces.

It is only in this sense that the present calculations are compared with the measurements on the concave surface. Since only two measurements at two different z planes in a vortex pair are made, the averages of the various integral parameters can at best represent approximately the "average" flow.

Having established the premise for the comparison between the present calculations and the measured data, the results are presented in Figures 87 to 90. As a result of the vortex system, the Law of the Wall does not hold. Since direct measurements on the skin friction have not been made, the wall shear stresses at the four measuring stations are not known. Because of this, no comparisons between C_f are made.

The results for the velocity profiles are given in Figures 87 and 89. Presented in Figure 87 is the results at the $x = 70$ inches position. The average values of δ^* , θ and H are included and these compared quite favourable with the calculated values. The shape of the profile is also quite similar. However, the calculated boundary layer thickness is not the same as the average boundary layer thickness. At the $x = 96$ inches position, the calculated values of δ^* and θ are approximately 45% greater than the mean values between Stations 4 and 5, but the shape factor H agrees to within 10% (Figure 89). This apparent difference in δ^* and θ is probably due to the presence of more than one system of vortices at this position.

The calculated shear stress profiles at $x = 70$ inches and 96 inches are given in Figures 88 and 90 respectively. The calculated shear stress at the wall at both these locations seem to agree well with the measured profiles, and at $x = 70$ inches the calculated profile and the average of the measured profiles correlated very well near the wall (Figure 88).

Even the maximum reached and the position where this maximum occurs are predicted quite correctly by the calculated profile. However, far away from the wall, substantial difference between the calculated and the average of the measured profiles begin to show. The difference increases towards the edge of the boundary layer, and become constant in the free stream. At $x = 96$ inches, the average of the measured profiles show a rather constant shear stress across the boundary layer, and towards the edge, the shear stress decreases steeply. However, the calculated profile does not display such a shape at all (Figure 90). It has the same shape as that at $x = 70$ inches with the maximum shear stress located away from the wall. (The appearance of the shear maximum away from the wall under a zero pressure gradient is due to the memory of the adverse pressure gradient which the flow has gone through at the entrance to the concave wall). Although the calculated value compares favourably with the average of the measured values near the wall, the calculated value is generally much lower than the average of the measured values far away from the wall. However, this difference decreases towards the edge of the boundary layer. Even then the calculated profile does not vanish but approaches a constant in the free stream. The fact that the calculated shear stress does not vanish can be accounted for by the shear stress relation (4.2-19). As explained in Section 4.2, τ/ρ approaches the value of $\nu(-2k U_{pw} e^{-2ky})$ in the free stream when ν_e is taken to be ν outside of the layer. This is a small viscous stress, and in the actual flow, the shear stress would probably approach this value. On the other hand, in the present method, no provision is made to allow the eddy viscosity to slowly decrease to ν , the molecular viscosity, as the edge of the boundary layer is reached. As a result, the value of ν_e approaches $2 \nu_{eF}$ (see eq. (4.5-13)). For flows along flat plates, the condition of zero vorticity in the free stream implies zero shear stress too. Therefore, it is immaterial what value ν_{eF} takes. For flow along convex surfaces, the shear stress goes

negative somewhere inside the boundary layer, and although vanishing vorticity does not imply vanishing shear in the free stream, the eddy viscosity at the point where the shear stress goes negative is taken to be ν so that the shear stress will again approach $\nu(-2k U_{pw} e^{-2ky})$ in the free stream. Hence, in this case ν_e adjusts itself. This is evident from equation (4.5-10), since the quantity inside the curly bracket decreases as η increases. However, the same quantity increases with η if the curvature is concave, and this is the reason why the calculated shear stress remains large towards the edge of the boundary layer. This points to the need of modifying (ℓ_1/Λ) in such a way that it will effect a rapid decrease in ν_e towards the edge of the boundary layer.

It can be argued that the condition of small viscous shear can be satisfied by writing:

$$\frac{\tau}{\rho} = -\bar{uv} = \nu_e \left(\frac{\partial U}{\partial y} + kU \right)$$

in accordance with Prandtl's (1929) mixing length argument. With this expression for $(-\bar{uv})$, the eddy viscosity hypothesis becomes:

$$\nu_e = \nu_{eF} \left\{ 1 - \beta \frac{kU(\partial U / \partial y + kU)}{(\partial U / \partial y - kU)^2} \right\}^{3/2} \left| \frac{(\partial U / \partial y - kU)^2}{\partial U / \partial y (\partial U / \partial y + kU)} \right|$$

Such an expression for ν_e is undesirable because of the singular behavior of ν_e as $\partial U / \partial y \rightarrow 0$ inside the boundary layer and $(\partial U / \partial y + kU) \rightarrow 0$ towards the free stream. Therefore, in spite of the fact that the condition of small viscous shear cannot be satisfied for the flow over concave walls, the present approach is adopted.

In closing, it can be said that the present method can be quite useful in predicting the mean characteristics of flows over concave walls if (ℓ_1/Λ) is modified so that the condition of small viscous shear in the free stream is satisfied.

Chapter V
CONCLUDING REMARKS

5.1 Conclusions

As a result of this investigation, the following conclusions can be drawn. For the sake of clarity, attempts are made to divide the conclusions into the following three categories. The first two categories are concerned with the experimental investigation and the first one is limited to turbulent boundary layers along convex surfaces, while the second one dwells only on constant pressure turbulent boundary layers along concave surfaces. The third and final category includes those conclusions that are drawn as a result of the theoretical investigation.

5.1.1 Turbulent Boundary Layers along Convex Surfaces

(i) In spite of the secondary flow which arises as a result of the longitudinal curvature of the test wall, a nearly two dimensional flow is established along the central plane of the convex test section. However, due to the rapid growth of the boundary layer thickness near separation in the case of separating flow, the secondary flow becomes quite significant.

(ii) The Law of the Wall holds for turbulent flows along convex surfaces. Its validity can also be demonstrated through the method of matched asymptotic expansion applied to the curved turbulent boundary layer equations. The skin friction obtained from Clauser's plot of the velocity profiles correlates well with the momentum integral.

(iii) A skin friction relation in which A is both a function of $(\frac{\delta^*}{\tau_w} \frac{\partial P}{\partial x})$ and δ/R is obtained. The relation reduces back to the flat plate skin friction relation as $\delta/R \rightarrow 0$. It is applicable to turbulent boundary layers over plane or convex surfaces with arbitrary pressure gradient so long as $A(\delta/R, \frac{\delta^*}{\tau_w} \frac{\partial P}{\partial x})$ is known.

(iv) Measurements in the case of constant pressure flow show that the flow towards the end of the convex test section is not quite in equilibrium although separately the velocity profile and the shear stress profiles at the last two stations are quite similar. Also, the measurements indicate that even if equilibrium is reached, the defect part of the profile will be quite different from that of the corresponding flat plate profile.

(v) The initial decrease in the intensities of turbulence is due partly to the favourable pressure gradient and partly to curvature. The inability of the intensities to increase further downstream is a clear indication of the effectiveness of convex curvature in reducing mixing between fluid layers.

(vi) As a result of the reduced mixing, the boundary layer growth is retarded on convex surfaces.

(vii) Also the ability of the flow to support adverse pressure gradient is reduced, hence, under the same wall static pressure distribution, the flow would separate earlier than the corresponding plane flow.

(viii) Turbulence energy production is drastically reduced and is quite small at about half the boundary layer thickness.

(ix) For the case with zero pressure gradient, the shear stress decreases steeply outside the viscous region and approaches zero at about half the boundary layer thickness. However, under the influence of strong adverse pressure gradient, the maximum shear stress occurs at some distance away from the wall, but it still goes to zero at about half the boundary layer thickness.

(x) For the case with no pressure gradient, the shear correlation coefficient again remains constant for the greater part of the shear thickness, but drops to zero steeply towards the edge of the shear stress profile.

5.1.2 Turbulent Boundary Layers along Concave Surfaces

(i) A system of longitudinal vortices similar to the Taylor-Gortler type vortices exists. For a given geometry of the concave surface and a given Reynolds number per unit length of the flow, the system of longitudinal vortices is stationary and does not depend on the upstream conditions.

(ii) The limited data lends evidence to the fact that there are more than one system of vortices. At least two such systems are detected at stations 4 and 5, $x = 96.0$ inches.

(iii) The boundary layer at the position of the trough of the wave is approximately twice as thick as the boundary layer at the position of the crest of the wave. Initial evidence also indicates that the growth rate of the boundary layer is the same in both these positions.

(iv) Instability of the fluid particles, as a result of the concave curvature, promotes mixing between fluid layers, hence a substantial increase in the turbulence energy all across the boundary layer.

(v) The shear stress profiles at stations 4 and 5, $x = 96.0$ inches show two peaks, one near the wall and one far away from the wall. The location of these peaks for the measurements at the position of the crest are different from that at the position of the trough. The existence of two peaks indicates the existence of two systems of vortices.

(vi) The Reynolds stress \overline{uw} is positive when measured at the position of the trough and negative when taken at the position of the crest. The opposite is true for \overline{vw} . However, at $x = 96.0$ inches, the distributions of \overline{uw} and \overline{vw} are definitely wave like and show two peaks. Again this indicates that there are at least two systems of longitudinal vortices at this stream position.

(vii) Unlike the case of convex curvature, there is no region inside the boundary layer where the shear correlation coefficient is constant. This is another indication of the three dimensional nature

of the flow.

(viii) For a concavely curved turbulent flow, turbulence energy production is not confined to the region very close to the wall, rather it extends nearly to the edge of the boundary layer.

5.1.3 Theoretical Predictions

(i) The set of equations (4.2-15) to (4.2-18) is a self consistent set of curved turbulent boundary layer equations.

(ii) The eddy viscosity hypothesis as proposed by Mellor and Gibson is generalized to include the effect of curvature.

(iii) The value .0417 for the ratio (λ_1/Λ) is found to give excellent correlation for all three cases including the concave curvature case.

(iv) The results of the present calculations supports the assumption that the value of (λ_1/Λ) obtained by just considering the Law of the Wall region can be used for the whole layer.

(v) For convex surfaces, the present method predicts the boundary layer growth and the point of zero shear stress accurately. The present method also predicts the separation point fairly well.

(vi) The present method can be used to predict the mean boundary layer development on a concave surface.

(vii) For concave surfaces, because of the existence of the longitudinal vortices, the constant B in the Law of the Wall is no longer a constant. Although a certain log region still exists, the skin friction deduced differs considerably from that predicted by the present method.

(viii) With convex curvature in the mean flow stream lines, the maximum reached by the shear stress is about 75% of the corresponding flow over a flat surface.

5.2 Recommendations for Future Work

The following extensions of the present investigation are recommended for future work.

(i) In view of the similarity of the equations that govern curved turbulent boundary layers and those that describe stratified flows, a frequency corresponding to the Brunt-Vaisala frequency may exist inside the boundary layer. Both Eskinazi and Yeh's findings and a preliminary measurements by the author do not seem to indicate the existence of such a frequency. However, due to the limited time available, this was not pursued in depth, but the author believes that this aspect of the flow should be investigated further.

(ii) Efforts should be devoted to establish a formal analogy between the centrifugal force effect and the buoyancy effects in stratified flow.

(iii) Spectral measurements should be made in order to better understand the detail structure of curved turbulent boundary layers, and the results compared with the data of Eskinazi and Yeh.

(iv) The system of longitudinal vortices should be studied in more detail, so that its effect on the turbulence structure can be better understood.

(v) Measurements of shear stress at the wall are necessary for the clarification of the question of the validity of the Law of the Wall in concavely curved turbulent boundary layers.

(vi) More measurements should be made in the transverse plane to see if similarity of the flow exists. Also, more measurements are required between the crest and the trough of the wave to establish the fact that in the mean, such a flow can still be treated assuming two-dimensionality. No doubt, this will be of value to the practical engineer.

(vii) Parametric study of the curvature affect using the present calculation method will help improve design of such things as aerofoils, turbine blades, etc.

APPENDIX A

CONSTRUCTION DETAILS OF THE CURVED WALL TUNNEL

The curved wall tunnel used for the present investigations is an open-return, suction type wind tunnel. It is powered by a two speed, 10 H.P. fan. The lower speed is capable of giving a flow with a Reynolds number per unit length of 4.37×10^5 while the higher speed gives a corresponding Reynolds number of 7.56×10^5 . Since all the runs on both the convex and concave test walls are conducted with the lower Reynolds number, the higher speed capacity of the fan was never used. The tunnel consists of six different units, and these are: (1) the entrance section (2) the contraction section, (3) the straight section, (4) the curved test section, (5) the exit section, and (6) the composite unit of the 90° bend, the diffuser, the fan and its housing. The tunnel is assembled by bolting these six units together as shown in Figure 1. With this arrangement, the curved test section can be changed with relative ease. The entire top wall and floor of the tunnel, from the inlet screen to the diffuser, is flat, thus giving the tunnel a rectangular cross-section. The depth of the tunnel is 4 feet and this gives a nearly two dimensional flow on the side walls of the tunnel. The quality of this two dimensional flow has already been commented on in both Sections 2.3 and 3.1.

The entrance section of the tunnel consists of five individual compartments 3 feet wide by 4 feet deep. Each has one layer of $2\frac{1}{2}$ inches thick Hexcel aluminum honey-comb of $1/4$ inches cell size, and each compartment is separated by a single layer of 18-mesh screen. These compartments are bolted together with two more layers of screen, one in front of the first honey-comb and one downstream of the last honey-comb. This entire unit is then bolted on to the contraction section.

The contraction section is designed to give a contraction ratio of 6:1. The side walls of this section are made of $1/8$ inches thick masonite, bent to the required curvature and kept in place by five ribs of 1 inch thick fir equally spaced on each wall. The top and bottom

walls of the tunnel are made of $1/2$ inches thick paper faced fir plywood, and are bolted on to the ribs on the side walls. Both side walls are lined with $1/16$ inches thick white panelite to give the required smooth surface.

The straight section is 4 feet long and has a cross-section of 6 inches by 48 inches. This cross-sectional geometry leads to nearly two dimensional flow everywhere on the two side walls. The side walls are made of $1/2$ inches thick paper faced fir plywood lined with $1/16$ inches thick white panelite. In order that the joint between the contraction section and the straight section be smooth, the white panelite lining is of one piece. This can be accomplished by cementing the lining on to the side walls after the straight section has been bolted on to the contraction section, thus making these two sections a composite unit. One side wall of the straight section is hinged to the contraction section, thus rendering it adjustable. The adjustment is $1/2$ inches at the end of the straight section. The original intent was to achieve added control on the free stream velocity distribution especially at the entrance to the convex test section. Later, it was found that the free stream velocity remained rather constant up to about 8 inches to the exit end of the straight section, and a flexible flap installed in the last 8 inches will provide the necessary control. A diagram showing the flap and its control mechanism is given in Figure 31. With the installation of the flap, there is no need for the wall to be adjustable any more. Therefore, it is positioned to give a uniform width of 6 inches with the fixed wall and then securely clamped to the top and bottom wall of the straight section. Except for a section of 1 feet wide, $1/2$ inches thick paper faced fir plywood are installed as the top and bottom walls of this section. The side walls are strengthened with five ribs of 1 inch thick fir equally spaced between the top and bottom to prevent them from wobbling. A $1/2$ inches thick by 1 feet wide lucite is placed mid-way between the entrance and exit end of the straight section, so that flow

observation can be made.

Together two curved test sections are made, one has a convex test wall while the other has a concave test wall. The geometry of these curved walls have already been discussed in Section 2.1.2 and their specifications given in Figures 3 and 4. Hence, only the details of their construction will be described.

The convex test wall is made of cold rolled steel $1/32$ inches thick, with surface finish specified as 63 micro inches. The wall is rolled to the specified curvature and its shape is maintained by four ribs of 1 inch thick fir also cut to the same curvature (see Figure 2). It is then bolted to the straight section and to the fixed wall of the exit section. The wall opposite the convex test wall is also made of the same material. Since it is necessary to be able to control the shape of the outer wall so that the desired pressure distribution on the convex wall can be obtained, three rolls of struts, with six in each roll, are installed. The linear adjustment is large enough to give both a constant velocity distribution and a linear decelerating velocity distribution on the convex wall. Details of the control mechanism is shown in Figure 91. As explained in Section 2.3.3, end wall jets are required for control of the secondary flow. Four tangential jets of $1/8$ inches I.D. are installed at the entrance to the curved test section on both the top and bottom walls of the tunnel. Two pressure regulators graduated to 1 psig are used to regulate the air supply which is from the shop's main compressed air supply. The large fluctuation of the main compressed air supply made the installation of the pressure regulators necessary. The details of the end wall jets together with the side wall jet and the flap are shown in Figure 31. The side wall jet has already been discussed in Section 2.2.3. Due to the presence of the side wall jet, the entrance end of the adjustable wall is secured to the straight section frame. The exit end is then screwed onto the adjustable wall of the exit section.

For no other reason but the availability of material in the shop, the concave wall is rolled out of $1/32$ inches thick stainless steel with a surface finish specified to 32 micro inches. The shape of the wall is maintained by two ribs of $1/2$ inches thick aluminum alloy spaced 28 inches apart. The opposite wall is made adjustable through two rolls of struts, with nine struts in each roll. It is bolted to the straight section and the fixed wall of the exit section. The details of the adjustable inner wall is shown in Figure 92. The same number of tangential wall jets are installed at the entrance to the curved section. However, no side wall jet is required because the inner wall is adjusted to minimize flow deceleration at the entrance to the concave test section. Because of this, the entrance end of the adjustable inner wall can be bolted to the straight section. Again, the exit end is screwed onto the adjustable wall of the exit section.

The bottom wall of the curved test section is the base which also serves as the support for the tunnel, while the top wall is made of $1/2$ inches thick lucite. The lucite top is not clamped or bolted onto the side walls. The pressure difference between the ambient air and the flowing stream will press the top onto the side walls. Leakage can be prevented when rubber seals are cemented onto the side walls as shown in Figures 91 and 92.

The exit section is so constructed that one adjustable wall is all that is required to accommodate both the convex and concave test sections. Then come the 90° bend, exit diffuser and the fan and housing unit which are all bolted together to form one composite unit. The support for the whole tunnel can be adjusted to give a level bottom wall.

APPENDIX B

POSITIONING AND ACCURACY OF THE VARIOUS PROBES

1) Conrad Probe

The Conrad probe is used as a nulled direction probe. The null angle can be found by aligning the probe in the direction of flow in the pipe flow system (Figure 93). The Conrad probe is carried by a rotary probe carrier (Figure 9) which in turn is fixed to the probe carrier (Figure 10). The whole unit is then mounted on a horizontal platform, and the Conrad probe introduced into the pipe flow horizontally. Every-time the Conrad probe is introduced into the rotary probe carrier, it is set into the same position by a set screw with a conical tip that fits right into the conical dent in the probe. This arrangement allows a reference for the null angle measurement to be established, and does not depend on the relative location of the whole unit as long as the probe carrier is always mounted horizontally. Once the null angle is found, the whole unit is then transferred to the curved wall tunnel.

The Conrad probe is introduced into the test section from the wall opposite the test wall, and the probe carrier is mounted as shown in Figure 10. In order that the axis of the probe be normal to the wall where measurements are to be taken, radial lines are inscribed on the bottom wall and the lucite top of the tunnel. The probe axis is then aligned with these radial lines by sighting with a telescope placed on the lucite top. The Conrad probe is shaped like a goose-neck (Figure 8) so that the edge of the probe is aligned with the axis of the probe. Hence, once the axis of the probe is aligned with the radial lines, the edge of the probe will traverse along the normal to the wall. Since both the curved wall and the Conrad probe are made of metal, an electrical circuit can be so arranged that when the probe is touching the curved wall, a light goes on. When the probe is brought back to such a position that the light just goes off, the reading on the vernier mounted on the

probe carrier is noted. This gives the zero reading for y . This way of positioning the probe has an accuracy in y of the order of ± 0.001 inches. Since the traverse is towards the free stream, and because of the small uncertainty in the measurement of y , the measurements near the wall will be much less accurate than those far away from the wall. The rotation of the Conrad probe is controlled by a set of gears so arranged that the smallest angle which can be measured accurately on the dial is one tenth of a degree.

The reason for choosing this particular probe (see Figure 7 for probe geometry) for the yaw measurements is because of its high sensitivity and its zero scale effect (see Bryer, Walshe and Garner 1958). The pressure difference between the two openings is measured by a Pace Model CP51D-1PSID pressure transducer and the read out is on a DISA Digital Voltmeter. Because of the pressure fluctuations, the Conrad probe can be rotated to read to $\pm .01$ volts only. The sensitivity of the probe decreases with the free stream velocity (see Figure 7), therefore the accuracy of the yaw measurement decreases as the wall is approached. To determine the effect of the free stream velocity, the null angle of the probe is measured for two different velocities in the pipe flow. For a velocity of 72.6 ft/sec., it was found possible to determine the null angle to $\pm .2^\circ$, and when the velocity is reduced to 28.9 ft/sec., it was only possible to determine the null angle to $\pm 0.5^\circ$. Even though the turbulent fluctuating velocities in the curved tunnel are not the same as that in the pipe flow, much the same accuracy would be expected when the Conrad probe is used to measure the secondary flow.

2) Total Head-Probe

The total-head probe is also shaped like a goose-neck with the edge of the probe aligned with the axis of the probe (Figure 7). With this configuration, the total-head probe can be positioned in the tunnel in the same manner as the Conrad probe, therefore, the same accuracy in the measurement of y .

The major source of errors of a total-head probe used for measurement on a low velocity stream are the effect of turbulence, the effect of yawing and the effect of a wall. The errors due to the effect of turbulence on total-pressure readings are not well understood. However, assuming the frontal part of the probe to be a stagnation point, Goldstein (1936) found theoretically that the total-head probe measured the total head of the total velocity vector, i.e.,

$$P_{t_1} = P_s + \frac{1}{2} \rho \{ (\bar{U} + \bar{u})^2 + \bar{v}^2 + \bar{w}^2 \}$$

This expression is correct only if the frontal area can be considered a true point. However, due to the finite size of the total-head-tube hole, deviations from the above expression may be expected. Aside from the lateral velocity gradient effect, which is neglected in the above expression, there is also the lateral velocity fluctuations effect. This may not produce an impact pressure as given by Goldstein's expression, but rather appreciably smaller. Hinze and Van der Hegge Zijnen (1949) neglected the effect of the lateral turbulence velocities and arrived at

$$P_{t_1} = P_s + \frac{1}{2} \rho \bar{U}^2 + \frac{1}{2} \rho \bar{u}^2$$

If P_t is the true total pressure, then

$$\frac{P_{t_1} - P_t}{\frac{1}{2} \rho \bar{U}^2} = \frac{\bar{u}^2}{\bar{U}^2}$$

Hence, for a turbulence level less than 10%, the error in total-pressure measurement will be less than 1% of the dynamic pressure. For the present investigations, the turbulence level in the flow along convex surfaces is always less than 10%, therefore the readings of the total-head probe are not corrected for turbulence effect. As for the velocity profile measurements on concave surfaces, hot-wires are used, thus eliminating the need to correct for turbulence effect, since in this

case, the turbulence level is expected to be higher than the corresponding flow along convex surface.

Gracey, et.al. (1951) found that most simple total-head probes are rather insensitive to yaw. They presented their data in terms of the "critical angle" of a given probe. The "critical angle" is defined as that angle at which the error in reading the total pressure amounts to 1% of the indicated dynamic head. They found that for all simple probes, ranging from cylindrical heads to ogive heads, the critical angles are of the order of $\pm 15^\circ$ in subsonic flow. Rogers and Berry (1950) also found that the critical angles for a round nose probe and a flat nose probe are of the order of $\pm 15^\circ$. Therefore, the flat nose total-head probe used in the present investigation is quite insensitive to yaw. Although there is a certain amount of secondary flow in the test section due to the longitudinal curvature of the test wall, the flow in the plane of symmetry is not expected to deviate too much away from the stream direction. Yaw measurements show that the angle of deviation is less than a degree. Again, there is no need to correct the total pressure measurements to account for probable yaw of the flow.

Very little work has been done to investigate the probe-wall effect. By observing the response of a one-sided rectangular tube with the wall as the bottom surface, in a known laminar profile, Stanton, et.al. (1920) were able to plot "effective position of tube" against "opening of tube" and used this plot as a calibration curve in interpreting measurements near the wall in turbulent profiles. The correction for wall effect was found to be in the form of an "effective displacement" of the probe centre. Corrections to the measurements near the wall are made using the curve of Stanton, et.al., but the corrections are found to be negligible. In using the curve of Stanton, et.al., the assumption was made that the effective displacement was equal in the calibrated laminar boundary layer and in the measured turbulent layer. However, this assumption does not hold even in the viscous sub-layer of the turbulent boundary

layer. As a result, the wall effect is not fully accounted for by the curve of Stanton, et.al. On top of this, the transverse velocity gradient effect is also important. These two effects together would account for the observed shifts of the measurements near the wall.

3) Hot-Wire Probes

The hot-wire probe is introduced into the tunnel much the same way as the Conrad probe and the total-head probe. However, in this case, the distance between the hot-wire and the wall cannot be measured by the same method. This is due to the fact that the hot-wire probe, unlike the Conrad probe or the total-head probe, is very fragile, hence the hot-wire will break once it touches the wall. To remedy this, a less accurate method for determining y is used.

A broken hot-wire probe is used as a dummy probe. The length (from the tip of the prongs to the edge of the adaptor) of this dummy probe is measured accurately (to one tenth of one thousand of an inch) using a telescope. The length (from the hot-wire to the edge of the adaptor) of the hot-wire probe is also measured to the same accuracy. First the dummy probe is used and the probe is traversed inwards towards the test wall until the tip of the prongs touches the wall. This closes the electric circuit and the light goes on. The probe is then brought back until the light just goes off. The reading on the vernier in the probe carrier is noted. The whole probe is then retracted until it is outside of the tunnel. The dummy probe is removed from the adaptor and the hot-wire probe is put in its place. Knowing the backlash of the probe carrier, the length of the dummy probe, the length of the hot-wire probe and the vernier reading at the point where the dummy probe just touches the wall, the hot-wire probe can be set at any distance away from the wall by moving the probe towards the test wall. With this arrangement, the boundary layer is traversed inward from the edge and not outward from the wall.

The miniature TSI hot-wire probe has a mark on it so that every

time it is snapped into the adaptor, good contact is ensured only when the mark on the probe is flushed with the edge of the adaptor. This also ensures that the length between the hot-wire and the edge of the adaptor is always the same. This fact is borne out by repeated measurement of the length when the miniature hot-wire probe is snapped in and out of the adaptor. The maximum variation between five different measurements is less than 0.001". The backlash of the probe carrier is measured by a dial gauge to 0.001". Repeated measurements show that the backlash varies between 0.006" and 0.010". The backlash was also checked from time to time and in no case was it found to exceed 0.010". A mean value of 0.008" is used for all hot-wire measurements.

With this arrangement, it is possible to determine y to an accuracy of $\pm 0.008"$. Since the accuracy of the hot-wire measurement near the wall depends on the size of the wire other than the velocity gradient, heat transfer to the wall, etc., it is not very meaningful to try to measure the turbulence velocities any closer to the wall than the length of the hot-wire. The miniature TSI hot-wire has a sensitive length of 0.050", therefore an error in y of $\pm 0.008"$ will not contribute very much to the overall error of the turbulence velocities measurements. Besides, the measurements at Station 1 serve as a check not only in the two dimensionality of the flow, but also in the accuracy of the above arrangement for the determination of the position of the probe away from the wall.

The various effects associated with the rotating-wire method that affect the accuracy of the hot-wire measurements have been discussed by Bissonnette (1970), therefore they will not be repeated here. As for the reliability and the overall accuracy of the rotating-wire method, Appendix C discusses this in some detail.

APPENDIX C

FULLY DEVELOPED TURBULENT PIPE FLOW EXPERIMENT

In order to test the accuracy of the rotating-wire method, a fully developed pipe flow experiment is set up. The pipe assembly has a convergent nozzle at the entrance. This is then followed by a diffusor and two layers of 2 1/2 inches thick Hexcel aluminum honey-comb flow straighteners of 1/2 inches cell size. The flow straighteners are preceded and followed by two 18-mesh screens. This is followed by two 18 feet long aluminum pipes of 6.005 inches I.D. The working section is downstream of the aluminum pipes and is made up of one 3 feet long lucite tubing which is machine bored to 6.005 inches I.D. Downstream of the lucite tubing is another aluminum pipe of 3 feet long. In order to minimize vibration in the flow in the working section, the exit diffuser - fan housing unit is connected to the aluminum pipe by a bellow. The pipe flow tunnel is of the open-return, suction type and the air is drawn in by an axial flow fan driven by a variable speed d.c. motor. A picture of the pipe flow tunnel together with the hot-wire equipment is presented in Figure 93.

Fully developed turbulent flow is obtained at about 60 diameters downstream of the entrance. The axial pressure gradient for the next 18 diameters is plotted in Figure 94. The friction velocity can be calculated from the measured pressure gradient and is given by:

$$u_{\tau}^2 = \frac{r_i}{2} \frac{1}{\rho} \frac{dp}{dx} \quad (C-1)$$

where r_i is the inner radius of the pipe and $\frac{dp}{dx}$ is the axial pressure gradient. If the flow is fully developed turbulent flow, the Reynolds stress $\bar{u}v$ is related to the friction velocity u_{τ} by the expression:

$$\bar{u}v = u_{\tau}^2 \left(\frac{r}{r_i} \right) \quad (C-2)$$

However, very close to the wall, this does not hold.

The measured \bar{uv} is compared with the theoretical prediction as given by equations (C-1) and (C-2). The comparison is shown in Figure 95 and the general agreement is good. The measured normal stresses \bar{u}^2 , \bar{v}^2 and \bar{w}^2 are shown in Figures 96, 97 and 98. Together with the present data is also plotted the data of Laufer (1954), Sandborn (1955), and Patel (1963 and 1968) for comparison purposes. It is seen that the present data falls well within the evident scatter between the various sets of data.

If the flow were truly axisymmetric and fully developed, then the off-diagonal stress components \bar{uw} and \bar{vw} are zero. The values \bar{uw} and \bar{vw} as measured by the rotating-wire method are less than 5% of the local \bar{u}^2 . Also, these values are randomly distributed across the pipe.

The above comparison shows that the rotating-wire method is rather reliable. It also indicates that, in similar flow conditions, the rotating-wire method will permit the determination of each component of the Reynolds stress tensor to about 5% of the locally measured turbulence energy per unit mass. This estimate will no longer be true in regions of very high shear such as boundary layer measurements very close to the wall.

The above work on the verification of the rotating-wire method was performed in cooperation with Mr. Luc Bissonnette, who is also a graduate student in the Department of Aerospace and Mechanical Sciences.

APPENDIX D

CURVED BOUNDARY LAYER EQUATIONS

THROUGH METHOD OF MATCHED ASYMPTOTIC EXPANSIONS

Equations (4.2-7) to (4.2-9) are made non-dimensional by dividing all velocities by U_0 , all coordinates and the radius of curvature R by ℓ and the pressure by ρU_0^2 . The Reynolds stresses are made non-dimensional by u_t^2 where u_t can be any velocity characteristic of the turbulence field. After some algebra the equations can be written as:

$$\frac{\partial U}{\partial X} + \frac{\partial}{\partial Y} \{(1 + KY)V\} \quad (D-1)$$

$$\begin{aligned} \frac{1}{1+KY} U \frac{\partial U}{\partial X} + V \frac{\partial U}{\partial Y} + \frac{K}{1+KY} UV &= - \frac{1}{1+KY} \frac{\partial P}{\partial X} + \\ \frac{1}{1+KY} \frac{\partial}{\partial X} \{ \epsilon^2 T_{XX} + \epsilon^2 \hat{\epsilon} \left(\frac{2}{1+KY} \frac{\partial U}{\partial X} + \frac{2K}{1+KY} V \right) \} \\ + \frac{\partial}{\partial Y} \{ \epsilon^2 T_{XY} + \epsilon^2 \hat{\epsilon} \left[(1+KY) \frac{\partial}{\partial Y} \left(\frac{U}{1+KY} \right) + \frac{1}{1+KY} \frac{\partial V}{\partial X} \right] \} \\ + \frac{2K}{1+KY} \{ \epsilon^2 T_{XY} + \epsilon^2 \hat{\epsilon} \left[(1+KY) \frac{\partial}{\partial Y} \left(\frac{U}{1+KY} \right) + \frac{1}{1+KY} \frac{\partial V}{\partial X} \right] \} \end{aligned} \quad (D-2)$$

$$\begin{aligned} \frac{1}{1+KY} U \frac{\partial V}{\partial X} + V \frac{\partial V}{\partial Y} - \frac{K}{1+KY} U^2 &= - \frac{\partial P}{\partial Y} \\ + \frac{1}{1+KY} \frac{\partial}{\partial X} \{ \epsilon^2 T_{XY} + \epsilon^2 \hat{\epsilon} \left[(1+KY) \frac{\partial}{\partial Y} \left(\frac{U}{1+KY} \right) + \right. \\ \left. \frac{1}{1+KY} \frac{\partial V}{\partial X} \right] \} + \frac{\partial}{\partial Y} \{ \epsilon^2 T_{YY} + \epsilon^2 \hat{\epsilon} \left[2 \frac{\partial V}{\partial Y} \right] \} - \\ \frac{K}{1+KY} \{ [\epsilon^2 T_{XX} + \epsilon^2 \hat{\epsilon} \left(\frac{2}{1+KY} \frac{\partial U}{\partial X} + \frac{2K}{1+KY} V \right)] - \\ [\epsilon^2 T_{YY} + \epsilon^2 \hat{\epsilon} \left[2 \frac{\partial V}{\partial Y} \right]] \} \end{aligned} \quad (D-3)$$

$$\zeta = \frac{1}{1+KY} \frac{\partial V}{\partial X} - \frac{\partial U}{\partial Y} - \frac{K}{1+KY} U \quad (D-4)$$

where T_{ij} are the non-dimensional components of the Reynolds stress tensor and

$$\epsilon^2 = \frac{u_t^2}{U_o^2}, \quad \epsilon^2 \hat{\epsilon} = \frac{\nu}{U_o \ell}$$

Mellor (1970) has shown that $\frac{\hat{\epsilon}}{\epsilon^n} \sim 0$ as $\epsilon \rightarrow 0$ for arbitrary n . Therefore, the technique of matched asymptotic expansion in terms of ϵ is applied to equations (D-1) to (D-4) for the sole purpose of seeking a set of self-consistent second order boundary layer equations.

Due to the presence of the two small parameters ϵ and $\hat{\epsilon}$, three regions exist in the flow field and these are: (1) the Outer or Inviscid Region where the length scale is ℓ , (2) the Middle or Defect Region where the characteristic length is $\Delta_t = \epsilon \ell$, and (3) the Inner or Viscous Region where the length scale is $\hat{\epsilon} \Delta_t = \hat{\epsilon} \epsilon \ell$. Since the radius of curvature is assumed to be of the same order as ℓ , $K(X) = O(1)$. Mellor's (1970) procedure is followed closely in the subsequent derivation of the boundary layer equations.

Outer or Inviscid Layer

In this region the free stream turbulence and the free stream vorticity are assumed to be zero, hence $T_{ij} = 0$, $\zeta = 0$ and the following expansions are assumed

$$\begin{aligned} U &= U_1(X, Y) + \epsilon U_2(X, Y) + \epsilon^2 U_3(X, Y) + \dots \\ V &= V_1(X, Y) + \epsilon V_2(X, Y) + \epsilon^2 V_3(X, Y) + \dots \\ P &= P_1(X, Y) + \epsilon P_2(X, Y) + \epsilon^2 P_3(X, Y) + \dots \end{aligned} \quad (D-5)$$

Substitute (E-5) into equations (D-1) to (D-3) and collecting terms, the following is obtained,

to first order

$$\begin{aligned}\frac{\partial U_1}{\partial X} + \frac{\partial}{\partial Y} \{(1+KY)V_1\} &= 0 \\ \frac{1}{1+KY} U_1 \frac{\partial U_1}{\partial X} + V_1 \frac{\partial U_1}{\partial Y} + \frac{K}{1+KY} U_1 V_1 &= - \frac{1}{1+KY} \frac{\partial P_1}{\partial X} \quad (D-6) \\ \frac{1}{1+KY} U_1 \frac{\partial V_1}{\partial X} + V_1 \frac{\partial V_1}{\partial Y} - \frac{K}{1+KY} U_1^2 &= - \frac{\partial P_1}{\partial Y}\end{aligned}$$

to second order

$$\begin{aligned}\frac{\partial U_2}{\partial X} + \frac{\partial}{\partial Y} (1+KY)V_2 &= 0 \\ \frac{1}{1+KY} \{U_1 \frac{\partial U_2}{\partial X} + U_2 \frac{\partial U_1}{\partial X}\} + \{V_1 \frac{\partial U_2}{\partial Y} + V_2 \frac{\partial U_1}{\partial Y}\} + \frac{K}{1+KY} (U_1 V_2 + U_2 V_1) &= - \frac{1}{1+KY} \frac{\partial P_2}{\partial X} \\ \frac{1}{1+KY} \{U_1 \frac{\partial V_2}{\partial X} + U_2 \frac{\partial V_1}{\partial X}\} + \{V_2 \frac{\partial V_1}{\partial Y} + V_1 \frac{\partial V_2}{\partial Y}\} - \frac{K}{1+KY} 2U_1 U_2 &= - \frac{\partial P_2}{\partial Y} \quad (D-7)\end{aligned}$$

to third order

$$\begin{aligned}\frac{\partial U_3}{\partial X} + \frac{\partial}{\partial Y} \{(1+KY)V_3\} &= 0 \\ \frac{1}{1+KY} \{U_1 \frac{\partial U_3}{\partial X} + U_2 \frac{\partial U_2}{\partial X} + U_3 \frac{\partial U_1}{\partial X}\} + \{V_1 \frac{\partial U_3}{\partial Y} &\\ V_2 \frac{\partial U_2}{\partial Y} + V_3 \frac{\partial U_1}{\partial Y}\} + \frac{K}{1+KY} (U_1 V_3 + U_2 V_2 + U_3 V_1) &= - \frac{1}{1+KY} \frac{\partial P_3}{\partial X} \\ \frac{1}{1+KY} \{U_1 \frac{\partial V_3}{\partial X} + U_2 \frac{\partial V_2}{\partial X} + U_3 \frac{\partial V_1}{\partial X}\} + \{V_1 \frac{\partial V_3}{\partial Y} + V_2 \frac{\partial V_2}{\partial Y} + V_3 \frac{\partial V_1}{\partial Y}\} - \frac{K}{1+KY} (U_2^2 + 2U_1 U_3) &= - \frac{\partial P_3}{\partial Y} \quad (D-8)\end{aligned}$$

Middle or Defect Layer

In this region, the length scale is $\Delta_t = \epsilon \ell$, therefore $Y = \epsilon y$ where y is the normal coordinate in this region. In addition, the following expansions are assumed

$$\begin{aligned} u &= u_1(x, y) + \epsilon u_2(x, y) + \epsilon^2 u_3(x, y) + \dots \\ v &= \epsilon \{ v_1(x, y) + \epsilon v_2(x, y) + \epsilon^2 v_3(x, y) + \dots \} \\ p &= p_1(x, y) + \epsilon p_2(x, y) + \epsilon^2 p_3(x, y) + \dots \\ t_{ij} &= t_{1ij}(x, y) + \epsilon t_{2ij}(x, y) + \epsilon^2 t_{3ij}(x, y) + \dots \end{aligned} \tag{D-9}$$

Hence

$$1 + KY = 1 + \epsilon Ky$$

and

$$(1 + \epsilon Ky)^{-1} = 1 - \epsilon Ky + \epsilon^2 (Ky)^2 - \epsilon^3 (Ky)^3 + \epsilon^4 (Ky)^4 \dots$$

Rewrite equations (D-1) to (D-3) in terms of X and y . Substitute (D-9) into the resultant equations and collecting terms, (since $\hat{\epsilon} = O(\epsilon^n)$, all terms that have $\hat{\epsilon}$ as coefficient can be neglected) the following is obtained:

to first order

$$\begin{aligned} \frac{\partial u_1}{\partial X} + \frac{\partial v_1}{\partial y} &= 0 \\ u_1 \frac{\partial u_1}{\partial X} + v_1 \frac{\partial u_1}{\partial y} &= - \frac{\partial p_1}{\partial X} \\ 0 &= \frac{\partial p_1}{\partial y} \end{aligned} \tag{D-10}$$

to second order

$$\begin{aligned}
 \frac{\partial u_2}{\partial x} + \frac{\partial v_2}{\partial y} + \frac{\partial(Kyv_1)}{\partial y} &= 0 \\
 u_1 \frac{\partial u_2}{\partial x} + v_1 \frac{\partial u_2}{\partial y} + u_2 \frac{\partial u_1}{\partial x} + v_1 \frac{\partial u_1}{\partial y} + \\
 Ky(u_1 + y \frac{\partial u_1}{\partial y}) &= - \frac{\partial p_2}{\partial x} + \frac{\partial t_{1xy}}{\partial y} \\
 Ku_1^2 &= \frac{\partial p_2}{\partial y}
 \end{aligned} \tag{D-11}$$

to third order

$$\begin{aligned}
 \frac{\partial u_3}{\partial x} + \frac{\partial v_3}{\partial y} + \frac{\partial(Kyv_2)}{\partial y} &= 0 \\
 u_1 \frac{\partial u_3}{\partial x} + v_1 \frac{\partial u_3}{\partial y} + u_3 \frac{\partial u_1}{\partial x} + v_3 \frac{\partial u_1}{\partial y} + u_2 \frac{\partial u_2}{\partial x} \\
 + v_2 \frac{\partial u_2}{\partial y} + Ku_2 v_1 + Ku_1 v_2 + \\
 Ky \{ v_1 \frac{\partial u_2}{\partial y} + v_2 \frac{\partial u_1}{\partial y} - \frac{\partial t_{1xy}}{\partial y} \} &= - \frac{\partial p_3}{\partial x} \\
 + \frac{\partial t_{1xx}}{\partial x} + \frac{\partial t_{2xy}}{\partial y} + 2Kt_{1xy} \\
 u_1 \frac{\partial v_1}{\partial x} + v_1 \frac{\partial v_1}{\partial y} - Ku_1(2u_2 - Kyu_1) &= - \frac{\partial p_3}{\partial y} + \frac{\partial t_{1xy}}{\partial y}
 \end{aligned} \tag{D-12}$$

Inner or Viscous Layer

In this region, the length scale is $\hat{\epsilon}\Delta_t$, hence $y = \hat{\epsilon}\hat{y}$ or $Y = \epsilon\hat{\epsilon}\hat{y}$, and

$$\frac{1}{1+KY} = 1 - \epsilon\hat{\epsilon} (Ky) + (\epsilon\hat{\epsilon})^2 (Ky)^2 \dots$$

The following expansion is assumed:

$$\begin{aligned}
 U &= \hat{u}_1(x, \hat{y}) + \epsilon \hat{u}_2(x, \hat{y}) + \epsilon^2 \hat{u}_3(x, \hat{y}) + \dots \\
 V &= \epsilon \hat{v}_1(x, \hat{y}) + \epsilon \hat{v}_2(x, \hat{y}) + \epsilon^2 \hat{v}_3(x, \hat{y}) + \dots \\
 P &= \hat{p}_1(x, \hat{y}) + \epsilon \hat{p}_2(x, \hat{y}) + \epsilon^2 \hat{p}_3(x, \hat{y}) + \dots \\
 T_{ij} &= \hat{t}_{1ij}(x, \hat{y}) + \epsilon \hat{t}_{2ij}(x, \hat{y}) + \epsilon^2 \hat{t}_{3ij}(x, \hat{y}) + \dots
 \end{aligned} \tag{D-13}$$

Rewrite the equations (D-1) to (D-3) in inner variables. Substitute (D-13) into the resultant equations and collect terms, the following is obtained:

to first order

$$\begin{aligned}
 \frac{\partial \hat{u}_1}{\partial x} + \frac{\partial \hat{v}_1}{\partial \hat{y}} &= 0 \\
 0 &= \frac{\partial^2 \hat{u}_1}{\partial \hat{y}^2} \\
 0 &= \frac{\partial \hat{p}_1}{\partial \hat{y}}
 \end{aligned} \tag{D-14}$$

to second order

$$\begin{aligned}
 \frac{\partial \hat{u}_2}{\partial x} + \frac{\partial \hat{v}_2}{\partial \hat{y}} &= 0 \\
 0 &= \frac{\partial}{\partial \hat{y}} \left\{ \hat{t}_{1xy} + \frac{\partial \hat{u}_2}{\partial \hat{y}} \right\} \\
 0 &= - \frac{\partial \hat{p}_2}{\partial \hat{y}}
 \end{aligned} \tag{D-15}$$

to third order

$$\frac{\partial \hat{u}_3}{\partial x} + \frac{\partial \hat{v}_3}{\partial \hat{y}} = 0$$

$$0 = \frac{\partial}{\partial \hat{y}} \{ \hat{t}_{2xy} + \frac{\partial \hat{u}_3}{\partial \hat{y}} \}$$

$$0 = - \frac{\partial \hat{p}_3}{\partial \hat{y}} + \frac{\partial \hat{t}_{1yy}}{\partial \hat{y}} \quad (D-16)$$

The aim here is to obtain a set of first order curved boundary layer equations, therefore the solutions of these various equations will not be discussed. Instead, the reader is referred to the paper by Mellor (1970). The boundary conditions for the three layers are very well discussed in Mellor's (1970) article and these will not be repeated here. However, it should be pointed out that the conditions of zero vorticity in the free stream is satisfied by matching the vorticity in the middle layer as $y \rightarrow \infty$ to that of the outer layer as $Y \rightarrow 0$.

This gives:

to first order

$$\lim_{y \rightarrow \infty} \frac{\partial u_1}{\partial y} = 0 \quad (D-17)$$

to second order

$$\lim_{y \rightarrow \infty} \left\{ - \frac{\partial u_2}{\partial y} - K u_1 \right\} = 0 \quad (D-18)$$

The set of second order boundary layer equations is given by the sets (D-11) and (D-15). The free stream velocity is given by (D-17) and (D-18). Since the first order equations in the Middle and Inner layers are the same as that for a flat plate (see Mellor 1970), the solutions to u_1 and v_1 are:

$$u_1 = u_1(x, 0)$$

$$v_1 = - y u_{1x}(x, 0)$$

With these substitutions, the boundary layer equations become

$$\frac{\partial u_2}{\partial x} + \frac{\partial v_2}{\partial y} = 2 K y \frac{\partial U_1}{\partial x} \quad (D-19)$$

$$U_1 \frac{\partial u_2}{\partial x} + (u_2 - y \frac{\partial u_2}{\partial y}) \frac{\partial U_1}{\partial x} = - \left\{ \frac{d}{dx} (K U_1^2) - K U_1 \frac{dU_1}{dx} \right\} y + \frac{\partial}{\partial y} \left(\frac{\tau}{\rho} \right) \quad (D-20)$$

$$K U_1^2(x,0) = \frac{\partial p_2}{\partial y} \quad (D-21)$$

where

$$\frac{\tau}{\rho} = - \bar{u}\bar{v} + \nu \frac{\partial u_2}{\partial y}$$

and

$$\lim_{y \rightarrow \infty} \left(\frac{\partial u_2}{\partial y} + K U_1 \right) = 0$$

The rather surprising result is that equations (D-19), (D-20) and (D-21) are linear. It is believed that they are the self consistent turbulent boundary layer equations (also for the plane case obtained by simply setting $K = 0$). However, turbulent boundary layer researchers have long been accustomed to making some of the approximations involved in these equations (and justified consistently in a laminar like boundary layer approximation), but not others. Notably the non-linear terms in the x -momentum equation are retained. For the present working equations, the same practice is adopted here. This is to conform to convention and hopefully to improve accuracy although in the light of the present asymptotic analysis this practice means that some higher order terms are being reinstated while other terms of the same higher order are being left out. Thus, reinstating some terms found in the original equations,

the set of boundary layer equations become:

$$\frac{\partial U}{\partial x} + \frac{\partial V}{\partial y} + kV = 0 \quad (D-22)$$

$$U \frac{\partial U}{\partial x} + V \frac{\partial U}{\partial y} + kUV = - \frac{1}{\rho} \frac{\partial P}{\partial x} + \frac{\partial}{\partial y} \left(\frac{\tau}{\rho} \right) + 2k \frac{\tau}{\rho} \quad (D-23)$$

$$k \frac{U^2}{\rho} = \frac{1}{\rho} \frac{\partial P}{\partial y} \quad (D-24)$$

$$\lim_{y \rightarrow \infty} \left(\frac{\partial U}{\partial y} + kU \right) = 0 \quad (D-25)$$

Here the full non-linear advective terms in the x -momentum equation are reinstated. Also, in order to satisfy equation (D-25), i.e.

$U \sim U_p \equiv U_{pw} e^{-ky}$ as $y \rightarrow \infty$, it is necessary to include both viscous terms in equation (D-23) where

$$\frac{\tau}{\rho} = \nu_e \left(\frac{\partial U}{\partial y} - kU \right) \quad (D-26)$$

In this way the combined viscous term will limit to zero and the outer boundary condition can be satisfied even if ν_e approaches constant as $y \rightarrow \infty$. The constant may be the actual molecular viscosity or it can be the eddy viscosity artificially maintained constant for large y . In the case of plane flow it is well established that whether ν_e maintains a constant value or decreases for large y makes little difference in the results.

As explained in the text, it is necessary to keep the term kU_p^2 on the left of equation (D-24) rather than replace it with kU^2 , for example. Otherwise, the pressure term will not quite balance out the advective terms and the integral of equation (D-23) will not exist. This is not only uncomfortable with regard to the von Karman integral, but is equally uncomfortable in the process of numerical integration of the full equations.

APPENDIX E

DERIVATION OF THE TURBULENCE ENERGY EQUATIONS FOR
CURVED BOUNDARY LAYERS

The equations for \bar{u}^2 , \bar{v}^2 and \bar{w}^2 can be obtained by multiplying equation (4.2-11) by u , equation (4.2-12) by v and equation (4.2-13) by w . Similarly the equation for \bar{uv} is obtained by adding v times equation (4.2-11) to u times equation (4.2-12). Making use of both the continuity equations for the mean and fluctuating quantities, and taking the time average of the equations, the results are:

$$\begin{aligned}
 \frac{\partial \bar{u}^2}{\partial t} + \frac{1}{1+ky} \frac{\partial}{\partial x} \{ \bar{u}^2 U + \bar{u}^3 + 2\bar{u}(\bar{p} - \bar{\tau}_{xx}) \} \\
 + \frac{\partial}{\partial y} \{ \bar{u}^2 V + \bar{u}^2 v - 2\bar{u} \bar{\tau}_{xy} \} + \frac{\partial}{\partial z} \{ \bar{u}^2 w - 2\bar{u} \bar{\tau}_{xz} \} \\
 + \frac{k}{1+ky} \{ 2\bar{u}\bar{v}U + 3\bar{u}^2 V + 3\bar{u}^2 v \} = - \frac{2\bar{u}^2}{1+ky} \frac{\partial U}{\partial x} \\
 - 2\bar{u}\bar{v} \frac{\partial U}{\partial y} + \frac{2}{1+ky} \bar{p} \frac{\partial u}{\partial x} - \frac{2}{1+ky} \bar{\tau}_{xx} \frac{\partial u}{\partial x} \\
 - 2\bar{\tau}_{xy} \frac{\partial u}{\partial y} + \frac{4k}{1+ky} \bar{u}\bar{\tau}_{xy} - 2\bar{\tau}_{xz} \frac{\partial u}{\partial z} \tag{E-1}
 \end{aligned}$$

$$\begin{aligned}
 \frac{\partial \bar{v}^2}{\partial t} + \frac{1}{1+ky} \frac{\partial}{\partial x} \{ \bar{v}^2 U + \bar{u}\bar{v}^2 - 2\bar{v}\bar{\tau}_{xy} \} \\
 + \frac{\partial}{\partial y} \{ \bar{v}^2 V + \bar{v}^3 + 2\bar{v}(\bar{p} - \bar{\tau}_{yy}) \} + \frac{\partial}{\partial z} \{ \bar{v}^2 w - 2\bar{v}\bar{\tau}_{yz} \} \\
 - \frac{k}{1+ky} \{ 4\bar{u}\bar{v}U - \bar{v}^2 V + 2\bar{u}^2 v - \bar{v}^3 \} = - \frac{2\bar{u}\bar{v}}{1+ky} \frac{\partial V}{\partial x} \\
 - 2\bar{v}^2 \frac{\partial V}{\partial y} + 2\bar{p} \frac{\partial v}{\partial y} - \frac{2\bar{\tau}_{xy} \bar{\partial} v}{1+ky \bar{\partial} x} - 2\bar{\tau}_{yy} \frac{\partial v}{\partial y} - 2\bar{\tau}_{yz} \frac{\partial v}{\partial z} - \frac{2k}{1+ky} \bar{v}(\bar{\tau}_{xx} - \bar{\tau}_{yy}) \tag{E-2}
 \end{aligned}$$

$$\begin{aligned}
& \frac{\partial \bar{w}^2}{\partial t} + \frac{1}{1+ky} \frac{\partial}{\partial x} \{ \bar{w}^2 \bar{u} + \bar{u} \bar{w}^2 - 2 \bar{w} \bar{\tau}_{xz} \} + \\
& \frac{\partial}{\partial y} \{ \bar{w}^2 \bar{v} + \bar{v} \bar{w}^2 - 2 \bar{w} \bar{\tau}_{yz} \} + \frac{\partial}{\partial z} \{ \bar{w}^3 + 2 \bar{w} (\bar{p} - \bar{\tau}_{zz}) \} \\
& + \frac{k}{1+ky} \{ \bar{w}^2 \bar{v} + \bar{v} \bar{w}^2 \} = 2p \frac{\partial \bar{w}}{\partial z} - \frac{2\bar{\tau}_{xz}}{1+ky} \frac{\partial \bar{w}}{\partial x} \\
& - 2 \bar{\tau}_{yz} \frac{\partial \bar{w}}{\partial y} + \frac{2k}{1+ky} \bar{w} \bar{\tau}_{yz} - 2 \bar{\tau}_{zz} \frac{\partial \bar{w}}{\partial z}
\end{aligned} \tag{E-3}$$

$$\begin{aligned}
& \frac{\partial \bar{u} \bar{v}}{\partial t} + \frac{1}{1+ky} \frac{\partial}{\partial x} \{ \bar{u} \bar{v} \bar{u} + \bar{u}^2 \bar{v} - \bar{u} \bar{\tau}_{xy} + \bar{v} (\bar{p} - \bar{\tau}_{xx}) \} + \frac{\partial}{\partial y} \{ \bar{u} \bar{v} \bar{v} + \bar{u} \bar{v}^2 - \bar{v} \bar{\tau}_{xy} \\
& + \bar{u} (\bar{p} - \bar{\tau}_{yy}) \} + \frac{\partial}{\partial z} \{ \bar{u} \bar{v} \bar{w} - \bar{u} \bar{\tau}_{yz} - \bar{v} \bar{\tau}_{xz} \} \\
& + \frac{k}{1+ky} \{ (\bar{v}^2 - 2\bar{u}^2) \bar{u} + \bar{u}^2 \bar{v} - \bar{u}^3 + \bar{u} \bar{v}^2 + 2\bar{u} \bar{v} \bar{v} \} = - \frac{\bar{u}^2}{1+ky} \frac{\partial \bar{v}}{\partial x} - \bar{u} \bar{v} \frac{\partial \bar{v}}{\partial y} \\
& - \frac{\bar{u} \bar{v}}{1+ky} \frac{\partial \bar{u}}{\partial x} - \bar{v}^2 \frac{\partial \bar{u}}{\partial y} + \frac{p}{\partial y} + \frac{1}{1+ky} \frac{p}{\partial x} \\
& - \frac{\bar{\tau}_{xy}}{1+ky} \frac{\partial \bar{u}}{\partial x} - \bar{\tau}_{yy} \frac{\partial \bar{u}}{\partial y} - \bar{\tau}_{yz} \frac{\partial \bar{u}}{\partial z} - \frac{\bar{\tau}_{xx}}{1+ky} \frac{\partial \bar{v}}{\partial x} - \bar{\tau}_{xy} \frac{\partial \bar{v}}{\partial y} \\
& - \bar{\tau}_{xz} \frac{\partial \bar{v}}{\partial z} + \frac{2k}{1+ky} \bar{v} \bar{\tau}_{xy} - \frac{k}{1+ky} \bar{u} (\bar{\tau}_{xx} - \bar{\tau}_{yy})
\end{aligned} \tag{E-4}$$

In accordance with the mean turbulence field closure scheme of Mellor and Herring (1970), assumptions are made to relate all terms in equations (E-1) to (E-4) in terms of $\bar{u}_i \bar{u}_j$. For the sake of completeness, these assumptions are:

$$\bar{u}_i \bar{\tau}_{kj} + \bar{u}_j \bar{\tau}_{ki} = \nu \left\{ \frac{\partial \bar{u}_j \bar{u}_k}{\partial x_i} + \frac{\partial \bar{u}_i \bar{u}_k}{\partial x_j} + \frac{\partial \bar{u}_i \bar{u}_j}{\partial x_k} \right\} \tag{E-5}$$

$$\overline{\tau_{kj} \frac{\partial \overline{u}_i}{\partial x_k} + \tau_{ki} \frac{\partial \overline{u}_j}{\partial x_k}} = \frac{2}{3} \frac{q}{\Lambda} q^3 \delta_{ij} \quad (E-6)$$

$$\overline{p \frac{\partial \overline{u}_i}{\partial x_j}} = - \frac{1}{6} \frac{q}{\ell_1} \{ \overline{u_i u_j} - \frac{\delta_{ij}}{3} q^2 \} \quad (E-7)$$

$$\overline{p u_i} = - \frac{q \ell_2}{3} \frac{\partial q^2}{\partial x_i} \quad (E-8)$$

$$\overline{u_i u_j u_k} = - q \ell_3 \{ \frac{\partial \overline{u_j u_k}}{\partial x_i} + \frac{\partial \overline{u_i u_k}}{\partial x_j} + \frac{\partial \overline{u_i u_j}}{\partial x_k} \} \quad (E-9)$$

With these simplifications and after much algebra, equations (E-1) to (E-4) reduce to

$$\begin{aligned} \overline{\frac{D\overline{u}}{Dt}} &= - \frac{1}{3} \frac{q}{\ell_1} (\overline{u^2} - \frac{1}{3} q^2) - \frac{2}{3} \frac{q^3}{\Lambda} - \frac{2\overline{u^2}}{1+ky} \frac{\partial \overline{u}}{\partial x} \\ &\quad - 2 \overline{u v} \frac{\partial \overline{U}}{\partial y} - \frac{2k}{1+ky} \{ \overline{u v U} + \overline{u^2 V} \} \\ &\quad + \frac{1}{1+ky} \frac{\partial}{\partial x} \{ 3(q \ell_3 + v) \frac{1}{1+ky} \frac{\partial \overline{u^2}}{\partial x} + \frac{2}{3} q \ell_2 \frac{1}{1+ky} \frac{\partial q^2}{\partial x} \} \quad (E-10) \\ &\quad + \frac{\partial}{\partial y} \{ (q \ell_3 + v) (\frac{2}{1+ky} \frac{\partial \overline{u v}}{\partial x} + \frac{\partial \overline{u^2}}{\partial y}) \} + \frac{2k}{1+ky} \{ (q \ell_3 + v) (\frac{2}{1+ky} \frac{\partial \overline{u v}}{\partial x} + \frac{\partial \overline{u^2}}{\partial y}) \} \\ &\quad + \frac{\partial}{\partial z} \{ (q \ell_3 + v) (\frac{2}{1+ky} \frac{\partial \overline{u w}}{\partial x} + \frac{\partial \overline{u^2}}{\partial z}) \} + \frac{k}{1+ky} \{ q \ell_3 (\frac{2}{1+ky} \frac{\partial \overline{u v}}{\partial x} + \frac{\partial \overline{u^2}}{\partial y}) \} \end{aligned}$$

$$\begin{aligned} \overline{\frac{D\overline{v}}{Dt}} &= - \frac{2\overline{u v}}{1+ky} \frac{\partial \overline{V}}{\partial x} - \frac{\overline{v^2}}{2} \frac{\partial \overline{V}}{\partial y} - \frac{1}{3} \frac{q}{\ell_1} (\overline{v^2} - \frac{1}{3} q^2) - \frac{2}{3} \frac{q^3}{\Lambda} + \frac{4k}{1+ky} \overline{u v U} \\ &\quad + \frac{1}{1+ky} \frac{\partial}{\partial x} \{ (q \ell_3 + v) (\frac{1}{1+ky} \frac{\partial \overline{v^2}}{\partial x} + 2 \frac{\partial \overline{u v}}{\partial y}) \} + \frac{\partial}{\partial y} \{ 3(q \ell_3 + v) \frac{\partial \overline{v^2}}{\partial y} + \frac{2}{3} q \ell_2 \frac{\partial q^2}{\partial y} \} \\ &\quad + \frac{\partial}{\partial z} \{ (q \ell_3 + v) (2 \frac{\partial \overline{v w}}{\partial y} + \frac{\partial \overline{v^2}}{\partial z}) \} - \frac{k}{1+ky} \{ (q \ell_3 + v) (\frac{2}{1+ky} \frac{\partial \overline{u v}}{\partial x} \end{aligned}$$

$$+ \frac{\partial \bar{u}^2}{\partial y} - 3 \frac{\partial \bar{v}^2}{\partial y}) \} - \frac{k}{1+ky} \{ q \ell_3 \left(\frac{2}{1+ky} \frac{\partial \bar{u}\bar{v}}{\partial x} + \frac{\partial \bar{u}^2}{\partial y} \right) \} \quad (E-11)$$

$$\begin{aligned} \frac{\partial \bar{w}^2}{\partial t} = & - \frac{1}{3} \frac{q}{\ell_1} \left(\bar{w}^2 - \frac{1}{3} \bar{q}^2 \right) - \frac{2}{3} \frac{\bar{q}^3}{\Lambda} + \frac{1}{1+ky} \frac{\partial}{\partial x} \{ (q \ell_3 + \nu) \left(\frac{1}{1+ky} \frac{\partial \bar{w}^2}{\partial x} + 2 \frac{\partial \bar{v}\bar{w}}{\partial z} \right) \} \\ & + \frac{\partial}{\partial y} \{ (q \ell_3 + \nu) \left(\frac{\partial \bar{w}^2}{\partial y} + 2 \frac{\partial \bar{v}\bar{w}}{\partial z} \right) \} + \frac{\partial}{\partial z} \{ 3(q \ell_3 + \nu) \frac{\partial \bar{w}^2}{\partial z} + \frac{2}{3} q \ell_2 \frac{\partial \bar{q}^2}{\partial z} \} \\ & + \frac{k}{1+ky} \{ (q \ell_3 + \nu) \left(\frac{\partial \bar{w}^2}{\partial y} + 2 \frac{\partial \bar{v}\bar{w}}{\partial z} \right) \} \end{aligned} \quad (E-12)$$

$$\begin{aligned} \frac{\partial \bar{u}\bar{v}}{\partial t} = & - \frac{1}{3} \frac{q}{\ell_1} \bar{u}\bar{v} - \frac{\bar{u}^2}{1+ky} \frac{\partial \bar{v}}{\partial x} - \bar{u}\bar{v} \frac{\partial \bar{v}}{\partial y} - \bar{u}\bar{v} \frac{\partial \bar{u}}{\partial x} - \bar{v}^2 \frac{\partial \bar{u}}{\partial y} + \frac{k}{1+ky} \\ & \{ (2\bar{u}^2 - \bar{v}^2) \bar{u} - \bar{u}\bar{v}\bar{v} \} + \frac{k}{1+ky} q \ell_3 \left(\frac{2}{1+ky} \frac{\partial \bar{u}\bar{v}}{\partial x} + \frac{\partial \bar{u}^2}{\partial y} \right) \\ & + \frac{1}{1+ky} \frac{\partial}{\partial x} \{ (q \ell_3 + \nu) \left(\frac{2}{1+ky} \frac{\partial \bar{u}\bar{v}}{\partial x} + \frac{\partial \bar{u}^2}{\partial y} \right) + \frac{1}{3} q \ell_2 \frac{\partial \bar{q}^2}{\partial y} \} \\ & + \frac{\partial}{\partial y} \{ (q \ell_3 + \nu) \left(\frac{1}{1+ky} \frac{\partial \bar{v}^2}{\partial x} + 2 \frac{\partial \bar{u}\bar{v}}{\partial y} \right) + \frac{1}{3} \frac{q \ell_2}{1+ky} \frac{\partial \bar{q}^2}{\partial x} \} + \frac{\partial}{\partial z} \\ & \{ (q \ell_3 + \nu) \left(\frac{1}{1+ky} \frac{\partial \bar{v}\bar{w}}{\partial x} + \frac{\partial \bar{u}\bar{w}}{\partial y} + \frac{\partial \bar{u}\bar{v}}{\partial z} \right) \} + \frac{k}{1+ky} \{ (q \ell_3 + \nu) \\ & \left(\frac{1}{1+ky} \frac{\partial \bar{v}^2}{\partial x} + 2 \frac{\partial \bar{u}\bar{v}}{\partial y} \right) \} - \frac{3}{2} \frac{k}{1+ky} \{ (q \ell_3 + \nu) \frac{1}{1+ky} \frac{\partial \bar{u}^2}{\partial x} \} \\ & + \frac{k}{1+ky} \nu \left\{ \frac{1}{2} \frac{1}{1+ky} \frac{\partial \bar{v}^2}{\partial x} + \frac{\partial \bar{u}\bar{v}}{\partial y} \right\} - \frac{3}{2} \frac{k}{1+ky} \frac{q \ell_3}{1+ky} \frac{\partial \bar{u}^2}{\partial x} \end{aligned} \quad (E-13)$$

Invoking the two dimensional boundary layer approximations, and in addition, the boundary layer thickness is assumed to be very much smaller than the radius of curvature of the surface, such that $\delta/R(x) \ll 1$, then the coefficient $1 + ky$ can be approximated by 1. With these

simplifications, equations (E-10) to (E-13) reduce to

$$\begin{aligned}
 \frac{\bar{D}^2}{Dt} &= \frac{\partial}{\partial y} \left\{ \left(q\ell_3 + \nu \right) \frac{\bar{u}^2}{\partial y} \right\} + 2k \left\{ \left(q\ell_3 + \nu \right) \frac{\bar{u}^2}{\partial y} \right\} \\
 &+ k \left\{ q\ell_3 \frac{\bar{u}^2}{\partial y} \right\} - \frac{1}{3} \frac{q}{\ell_1} \left(\bar{u}^2 - \frac{1}{3} \bar{q}^2 \right) - \frac{2}{3} \frac{q^3}{\Lambda} \\
 &- 2 \bar{u} \bar{v} \frac{\partial \bar{U}}{\partial y} - 2k \bar{u} \bar{v} \bar{U} \tag{E-14}
 \end{aligned}$$

$$\begin{aligned}
 \frac{\bar{D}^2}{Dt} &= \frac{\partial}{\partial y} \left\{ 3 \left(q\ell_3 + \nu \right) \frac{\bar{v}^2}{\partial y} + \frac{2}{3} q\ell_2 \frac{\bar{q}^2}{\partial y} \right\} - k \left(q\ell_3 \frac{\bar{u}^2}{\partial y} \right) \\
 &- k \left\{ \left(q\ell_3 + \nu \right) \left(\frac{\bar{u}^2}{\partial y} - \frac{1}{3} \frac{\bar{v}^2}{\partial y} \right) \right\} - \frac{1}{3} \frac{q}{\ell_1} \left(\bar{v}^2 - \frac{1}{3} \bar{q}^2 \right) \\
 &- \frac{2}{3} \frac{q^3}{\Lambda} + 4k \bar{u} \bar{v} \bar{U} \tag{E-15}
 \end{aligned}$$

$$\begin{aligned}
 \frac{\bar{D}^2}{Dt} &= \frac{\partial}{\partial y} \left\{ \left(q\ell_3 + \nu \right) \frac{\bar{w}^2}{\partial y} \right\} + k \left\{ \left(q\ell_3 + \nu \right) \frac{\bar{w}^2}{\partial y} \right\} \\
 &- \frac{1}{3} \frac{q}{\ell_1} \left(\bar{w}^2 - \frac{1}{3} \bar{q}^2 \right) - \frac{2}{3} \frac{q^3}{\Lambda} \tag{E-16}
 \end{aligned}$$

$$\begin{aligned}
 \frac{\bar{D}uv}{Dt} &= \frac{\partial}{\partial y} \left\{ 2 \left(q\ell_3 + \nu \right) \frac{\bar{u}\bar{v}}{\partial y} \right\} + 2k \left(q\ell_3 + \nu \right) \frac{\bar{u}\bar{v}}{\partial y} + k \left(q\ell_3 \right) \frac{\bar{u}^2}{\partial y} \\
 &+ k\nu \frac{\partial \bar{u}\bar{v}}{\partial y} - \frac{1}{3} \frac{q}{\ell_1} \bar{u}\bar{v} - \bar{v}^2 \frac{\partial \bar{U}}{\partial y} + k \left(2\bar{u}^2 - \bar{v}^2 \right) \bar{U} \tag{E-17}
 \end{aligned}$$

REFERENCES

- Bissonnette, L. (1970), "An Experimental Study of the Development of a Three-Dimensional Turbulent Boundary Layer Under Rapidly Changing Rate of Strain", Ph.D. Thesis, Princeton University.
- Bradshaw, P. (1969), "The Analogy Between Streamline Curvature and Bouyance in Turbulent Shear Flow", J. Fluid Mech., Vol. 36, Part 1, pp. 177-191.
- Bradshaw, P. and Ferriss, D. H. (1965), "The Response of a Retarded Equilibrium Turbulent Boundary Layer to the Sudden Removal of Pressure Gradient", MPL Aero. Report 1145, Great Britain.
- Bryer, D. W., Walshe, D. E. and Garner, H. C. (1958), "Pressure Probes Selected for Three-Dimensional Flow Measurement", A.R.C. R & M 3037.
- Champagne, F. H., Sleicher, C. A. and Wehrman, O. H. (1967), "Turbulence Measurements with Inclined Hot-Wires", J. Fluid Mech., Vol. 28, Part 1, pp. 153-175.
- Clauser, F. H. (1954), "Turbulent Boundary Layers in Adverse Pressure Gradient", J. Aero. Sci., Vol. 21, No. 1, pp. 91-108.
- Clauser, F. H. (1956), "The Turbulent Boundary Layer", Advances in Applied Mechanics, Vol. IV, Academic Press, New York.
- Coles, D. C. (1962), "The Turbulent Boundary Layer in a Compressible Fluid", The Rand Corp., Rept. R-403-PR.
- Coles, D. C. (1968), Proceedings, Computation of Turbulent Boundary Layers, 1968, AFSOR-1FP, Stanford Conference, Vol. 2.
- Eskinazi, S. and Yeh, H. (1956), "An Investigation on Fully Developed Turbulent Flows in a Curved Channel", J. Aero. Sci., Vol. 23, No. 1, pp. 23-35.
- Fugita, H. and Kovasznay, S. G. (1968), "Measurements of Reynolds Stress by a Single Rotated Hot Wire Anemometer", Review Sci. Inst., Vol. 39, No. 9, pp. 1351-1355.
- Goldstein, S. (1936), "A Note on the Measurement of Total Head and Static Pressure in a Turbulent Stream", Proc. Roy. Soc., Series A, Vol. 155, No. 886, pp. 570-75.
- Gortler, H. (1941), "Über eine dreidimensionale Instabilität laminarer Grenzschichten an konkaven Wänden", ZAMM, Vol. 21, pp. 250-252.

Gortler, H. (1959), "Über eine Analogie zwischen der Instabilität laminarer Grenzschichtstromungen an konkaven Wänden und an erwärmten Wänden", Ingr. Arch., Vol. 28, pp. 71-78.

Gracey, W., Letko, W. and Russel, W. R. (1951), "Wind Tunnel Investigations of a Number of Total Pressure Tubes at High Angles of Attack-Subsonic Speeds", NACA TN2331.

Hama, F. R. (1957), "An Efficient Tripping Device", J. Aero. Sci., Vol. 24, No. 3, pp. 236.

Herring, H. J. and Mellor, G. L. (1968), "A Computer Program to Calculate Incompressible Laminar and Turbulent Boundary Layer", NASA CR-1564.

Hinze, J. O. and van der Hegge Zijnen, B. C. (1949), Appl. Sci. Research, Vol. 1A, pp. 435.

Klebanoff, P. S. (1955), "Characteristics of Turbulence in a Boundary Layer with Zero Pressure Gradient", NACA Rept. 1247.

Laufer, J. (1954), "The Structure of Turbulence in Fully Developed Pipe Flow", NACA Rept. 1174.

Mellor, G. L. and Gibson, D. M. (1966), "Equilibrium Turbulent Boundary Layers", J. Fluid Mech., Vol. 24, Part 2, pp. 225-253.

Mellor, G. L. (1967), "Incompressible, Turbulent Boundary Layers with Arbitrary Pressure Gradients and Divergent or Convergent Cross Flows", AIAA J. Vol. 5, No. 9, pp. 1570-79.

Mellor, G. L. (1971), "The Large Reynolds Number Asymptotic Theory of Turbulent Boundary Layers", Princeton Univ. AMS Rept. 989.

Mellor, G. L. and Herring, H. J. (1970), "A Study of Turbulent Boundary Layer Models, Part II - Mean Turbulent Field Closure", Sandia Rept. SR-CR-70-6125B.

Owczarek, J. A. (1964), Fundamentals of Gas Dynamics, International Textbook Co., Pennsylvania.

Patel, R. P. (1963), "Measurements of the Reynolds Stresses in a Circular Pipe as a Means of Testing a DISA Constant Temperature Hot Wire Anemometer", Mech. Eng. Res. Lab., McGill University, Tech. Note 63-6.

Patel, R. P. (1968), "Reynolds Stresses in Fully Developed Turbulent Flow Down a Circular Pipe", Mech. Eng. Res. Lab., McGill University, Rept. 68-7.

Patel, V. C. (1968a), "The Effects of Curvature on the Turbulent Boundary Layer", ARC-30427, Great Britain.

Patel, V. C. (1968b), "Measurements of Secondary Flow in the Boundary Layers of a 180° Channel", ARC-30428, Great Britain.

Prandtl, L. (1929), "Einfluss Stabilisierender Kräfte auf die Turbulenz", Reprinted in Vortrage aus dem Gebiete der Aerodynamik und Verwandter Gebiete, (Translated as NACA TM 625).

Richmeyer, R. D. and Morton, K. W. (1967), Difference Methods for Initial Value Problems, Interscience Publishers, 2nd ed., pp. 198.

Rogers, E. W. and Berry, C. J. (1950), "Tests on the Effect of Incidence on some Pressure Heads at High Subsonic Speeds", A.R.C., CP41, Arc. 13, 263.

Sandborn, V. A. (1955), "Experimental Evaluation of Momentum Terms in Turbulent Pipe Flow", NACA TN 3266.

Stanton, T. E., Marshall, D. and Bryant, C. N., (1920), "On the Conditions at the Boundary of a Fluid in Turbulent Motion", Proc. Roy. Soc., Series A, No. 97, pp. 413.

Schmidbauer, H. (1936), "Behavior of Turbulent Boundary Layers on Curved Convex Wall", NACA, TM, No. 791.

Schneider, W. G. and Wade, J.H.T. (1967), "Flow Phenomena and Heat Transfer Effects in a 90° Bend", Canadian Aero. and Space Journal, Vol. 13, No. 2, pp. 73-89.

Schraub, F. A. and Kline, S. J. (1965), "A Study of the Structure of the Turbulent Boundary Layer with and without Longitudinal Pressure Gradients", Report MD-12, Thermosciences Division, Dept. of Mech. Eng., Stanford University.

Schubauer, G. B. and Klebanoff, P. S. (1951), "Investigation of Separation of the Turbulent Boundary Layer", NACA Report 1030.

Tani, I. (1962), "Production of Longitudinal Vortices in the Boundary Layer along a Concave Wall", J. Geophysical Research, Vol. 67, No. 8, pp. 3075-80.

Taylor, G. I. (1923), "Stability of a Viscous Liquid Contained Between Two Rotating Cylinders", Phil. Trans., A223, pp. 289.

Taylor, G. I. (1936), "Fluid Friction Between Rotating Cylinders. Part I: Torque Measurements, Part II: Distribution of Velocity Between Concentric Cylinders when Outer one is Rotating and Inner one is at Rest", Proc. Roy. Soc., 157A, pp. 546-78.

Thompson, B. G. J. (1963), Ph.D. Thesis, Cambridge University.

Van Dyke, Milton (1962), "Higher Approximations in Boundary-Layer Theory, Part I: General Analysis", J. Fluid Mech., Vol. 14, pp. 481-495.

Wattendorf, F. L. (1935), "A Study of the Effect of Curvature on Fully Developed Turbulent Flow", Proc. Roy. Soc., 148A, pp. 565-98.

Wilcken, H. (1930), "Turbulence Grenzschichten an gewolbten Flächen", Ing.-Arch. 1. Band, 4. Heft, S 358-76.

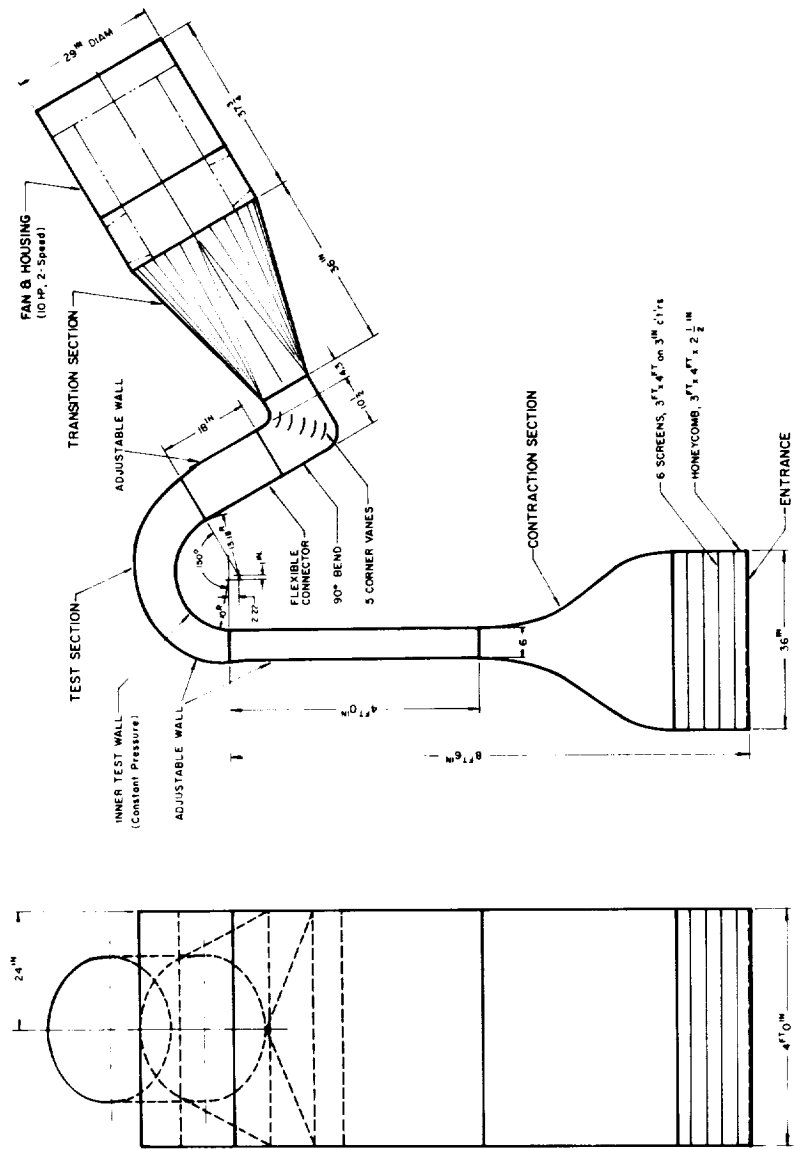


Figure 1. Curved wall tunnel.

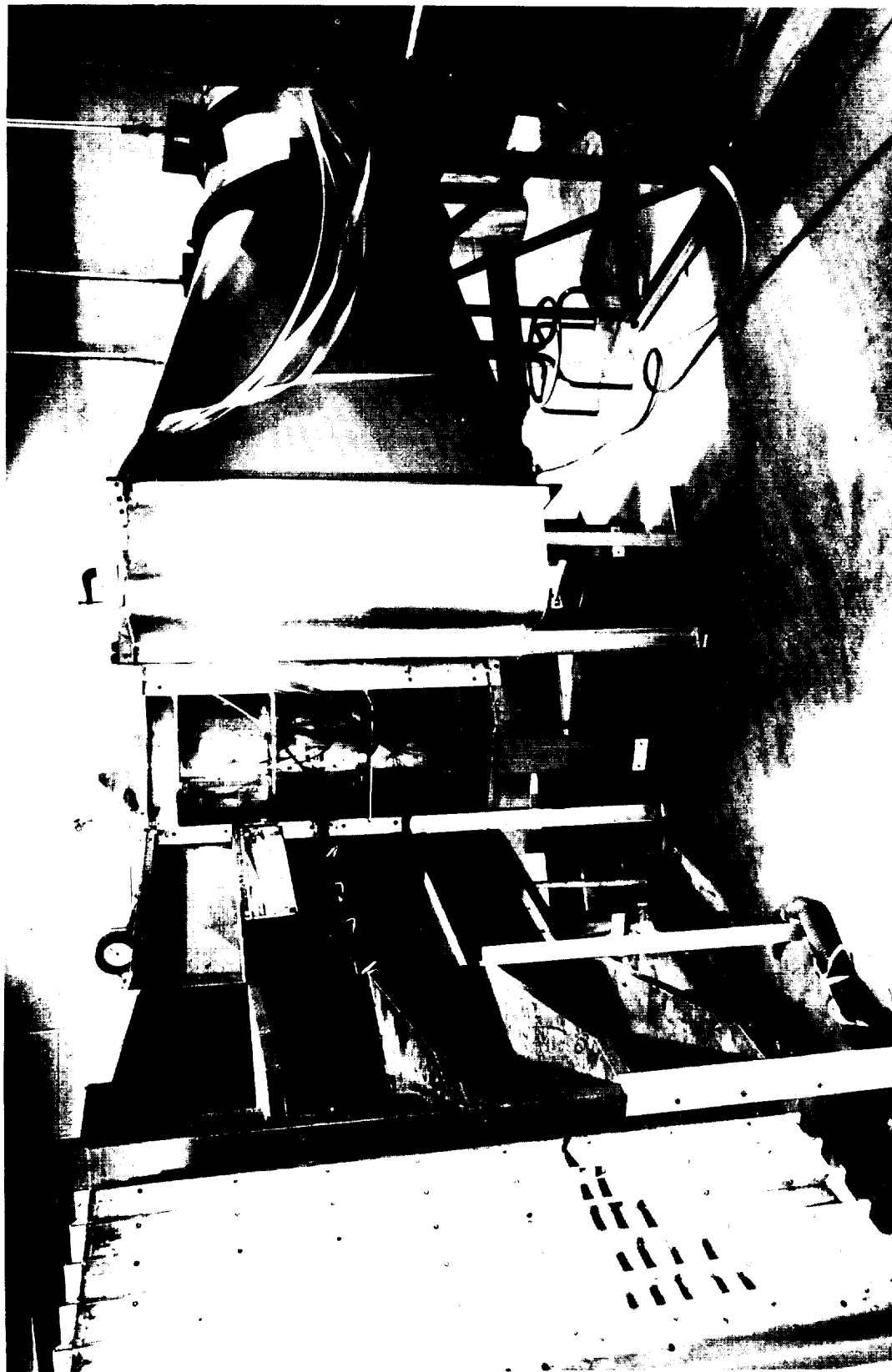


Figure 2. Photograph of curved wall tunnel.

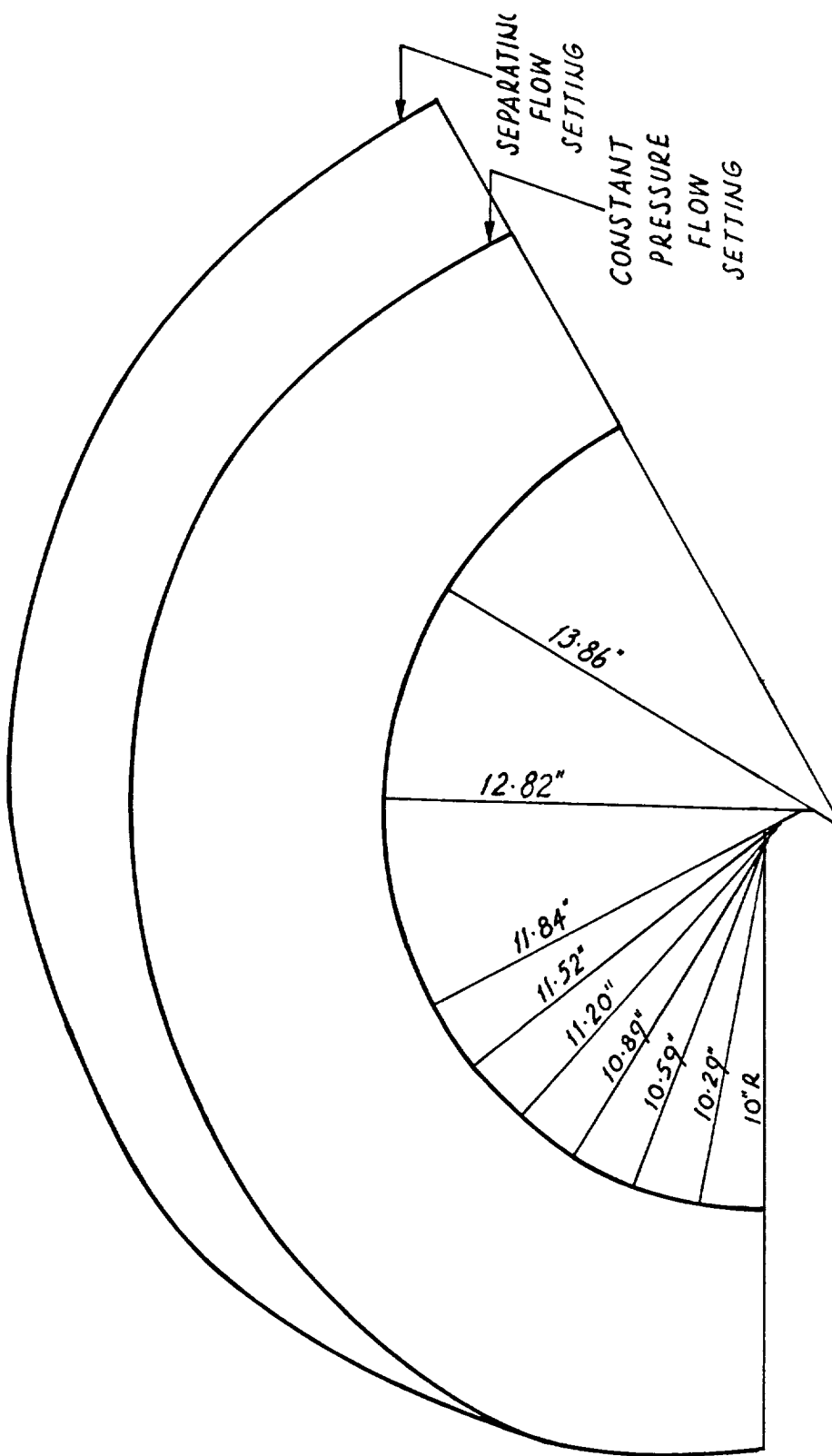


FIGURE 3 GEOMETRY OF CONVEX TEST SECTION (SCALE $1'' = 4''$)

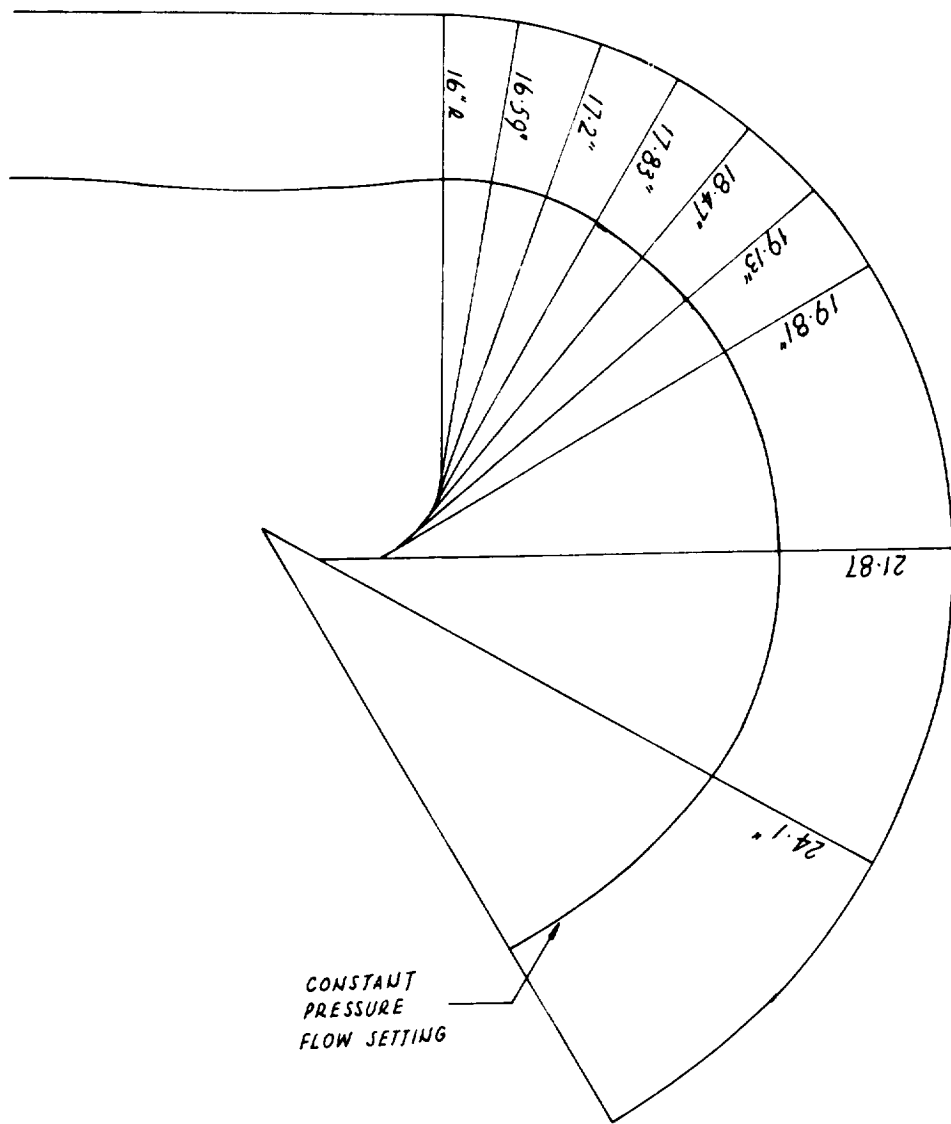
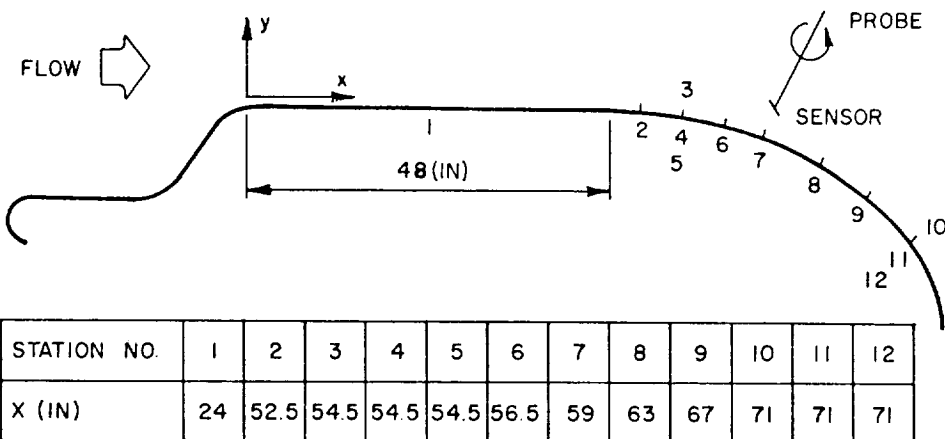


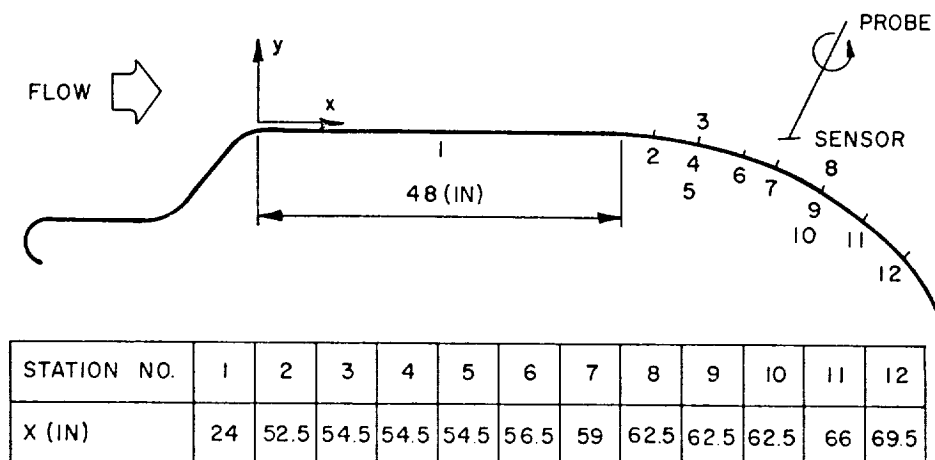
Figure 4. Geometry of concave test section. (Scale 1" = 4")



STATIONS 3 AND 10 ARE 14 (IN) ABOVE PLANE OF SYMMETRY

STATIONS 5 AND 12 ARE 14 (IN) BELOW PLANE OF SYMMETRY

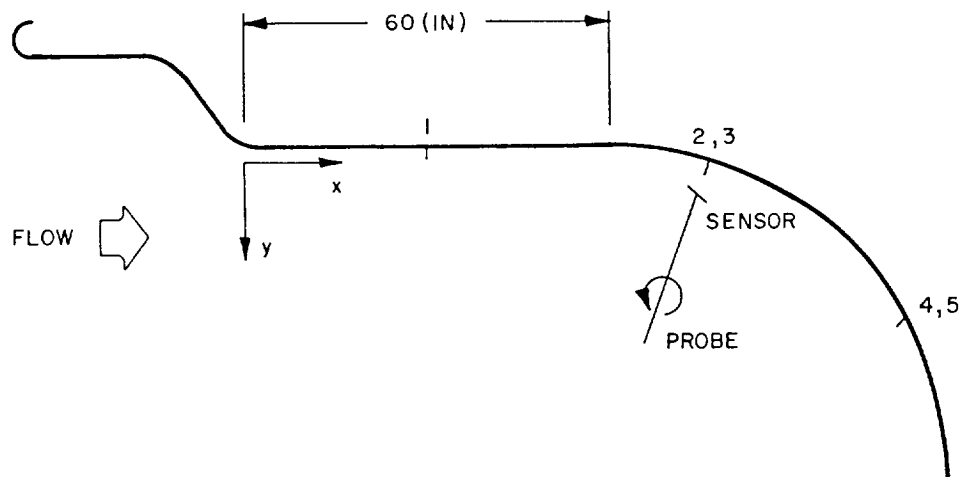
FIG. 5a. LOCATION OF MEASURING STATIONS FOR CONSTANT PRESSURE FLOW ALONG CONVEX WALL



STATIONS 3 AND 8 ARE 14 (IN) ABOVE PLANE OF SYMMETRY

STATIONS 5 AND 10 ARE 14 (IN) BELOW PLANE OF SYMMETRY

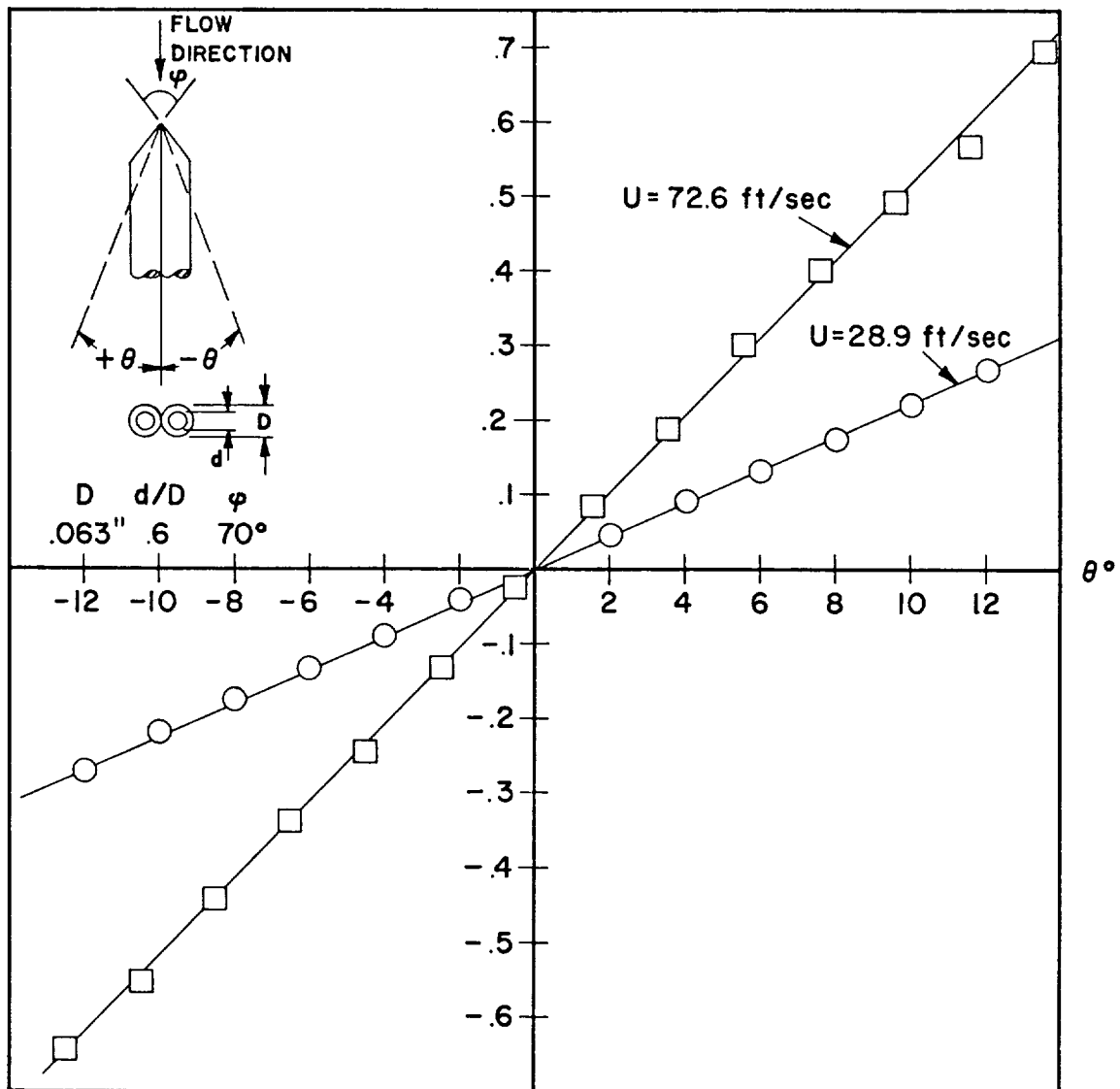
FIG. 5b. LOCATION OF MEASURING STATIONS FOR SEPARATING FLOW ALONG CONVEX WALL



STATION NO.	1	2	3	4	5
X (IN)	24	70	70	96	96
Z (IN) AS MEASURED FROM $\frac{C}{4}$	0	.672	1.344	1.008	2.100
		TRough	CREST	TRough	CREST

FIG. 6. LOCATION OF MEASURING STATIONS FOR CONSTANT PRESSURE FLOW ALONG CONCAVE WALL

$$\frac{\Delta p}{1/2 \rho U^2}$$



EFFECT OF YAWING OF CONRAD PROBE AT ZERO PITCH.
FIG. 7

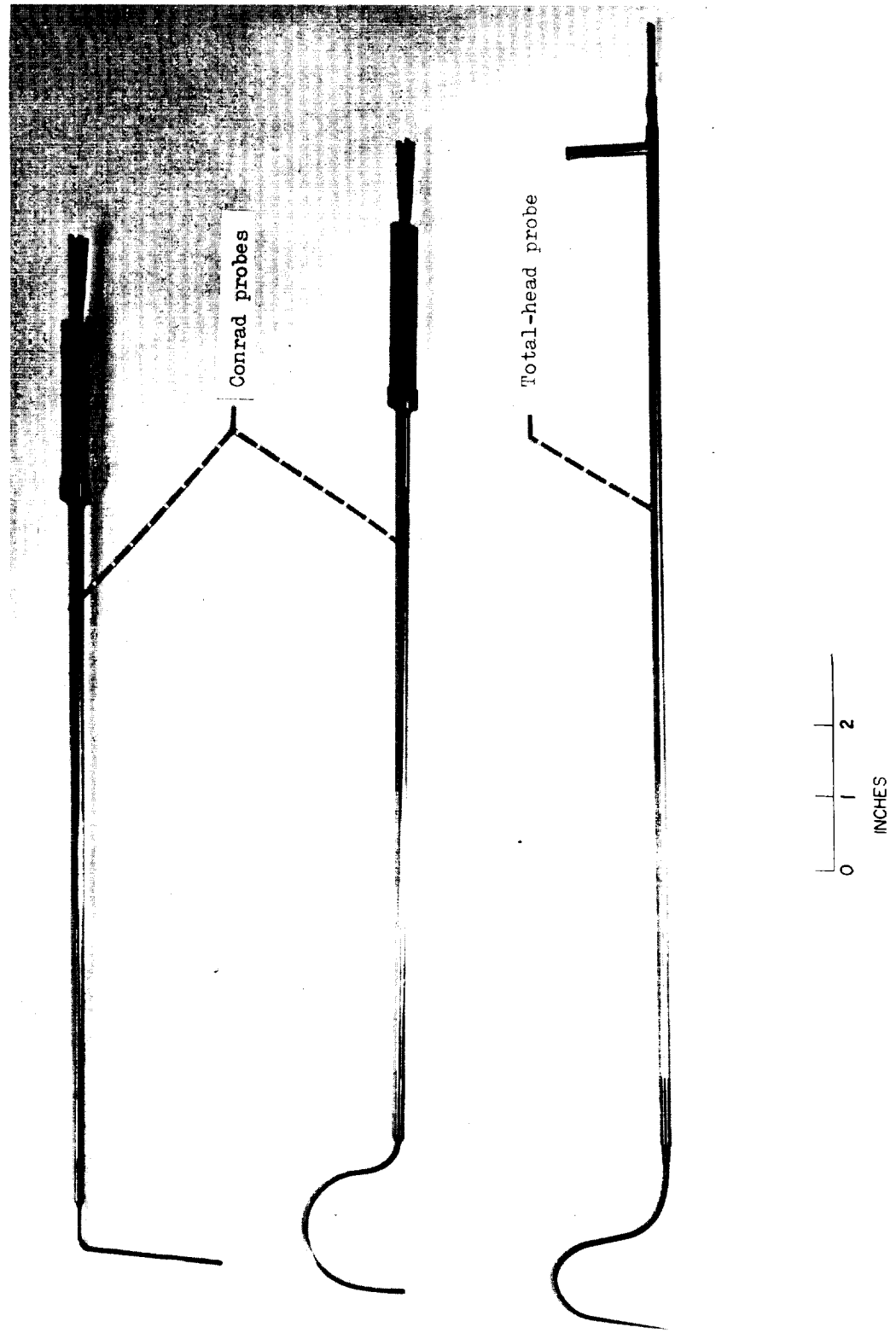


Figure 8. Total-head probe and Conrad probe.

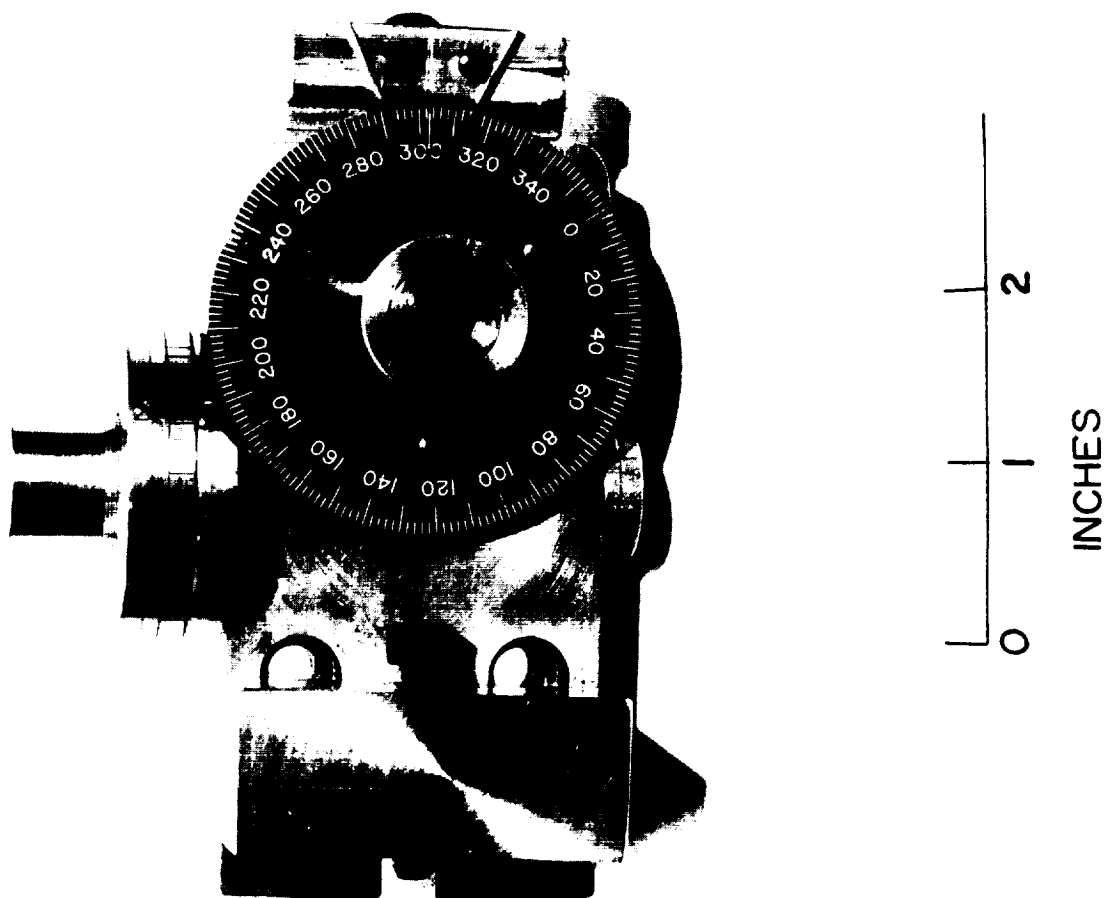


Figure 9. Rotary probe carrier.

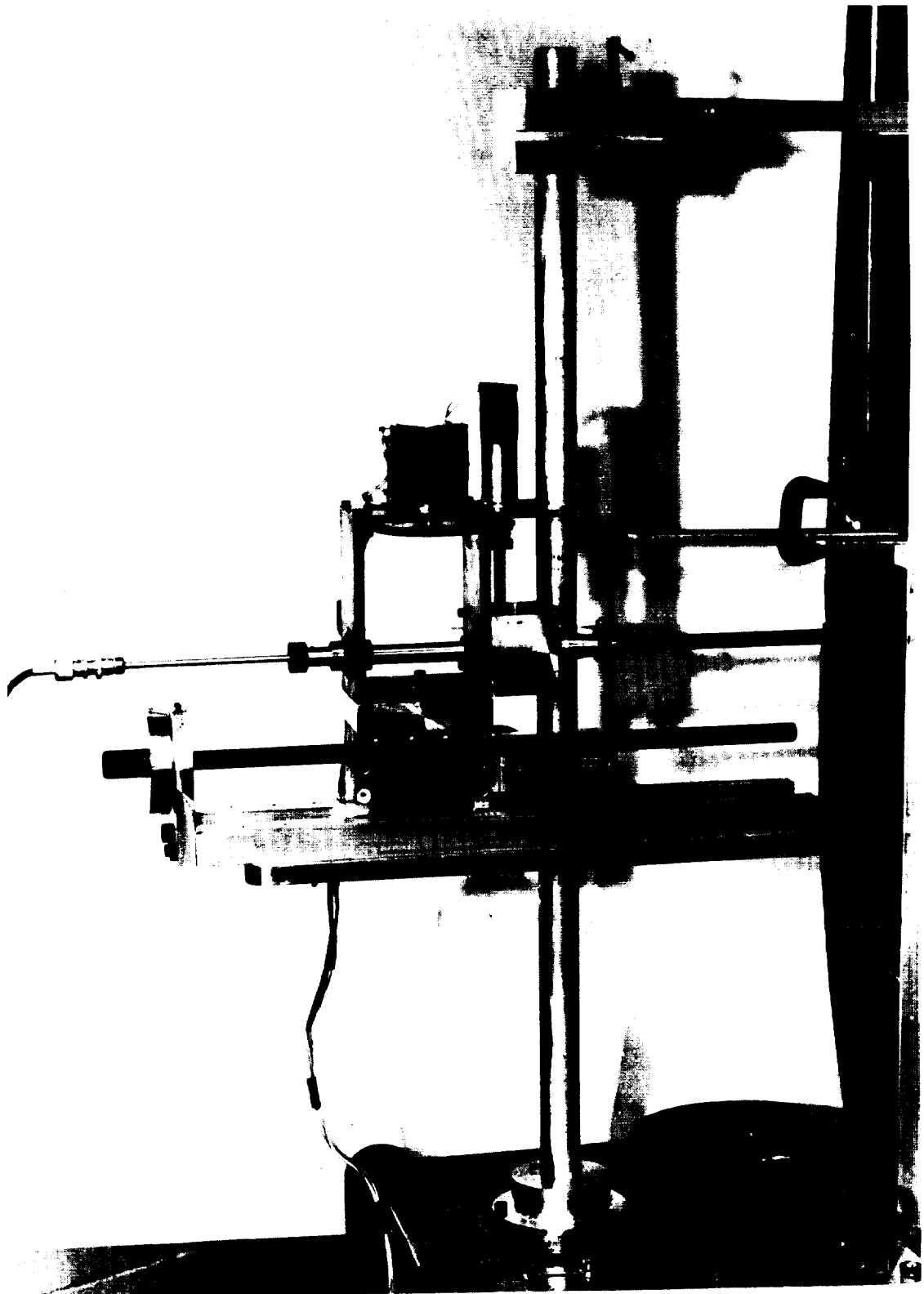


Figure 10. Probe carrier with attached rotary device.

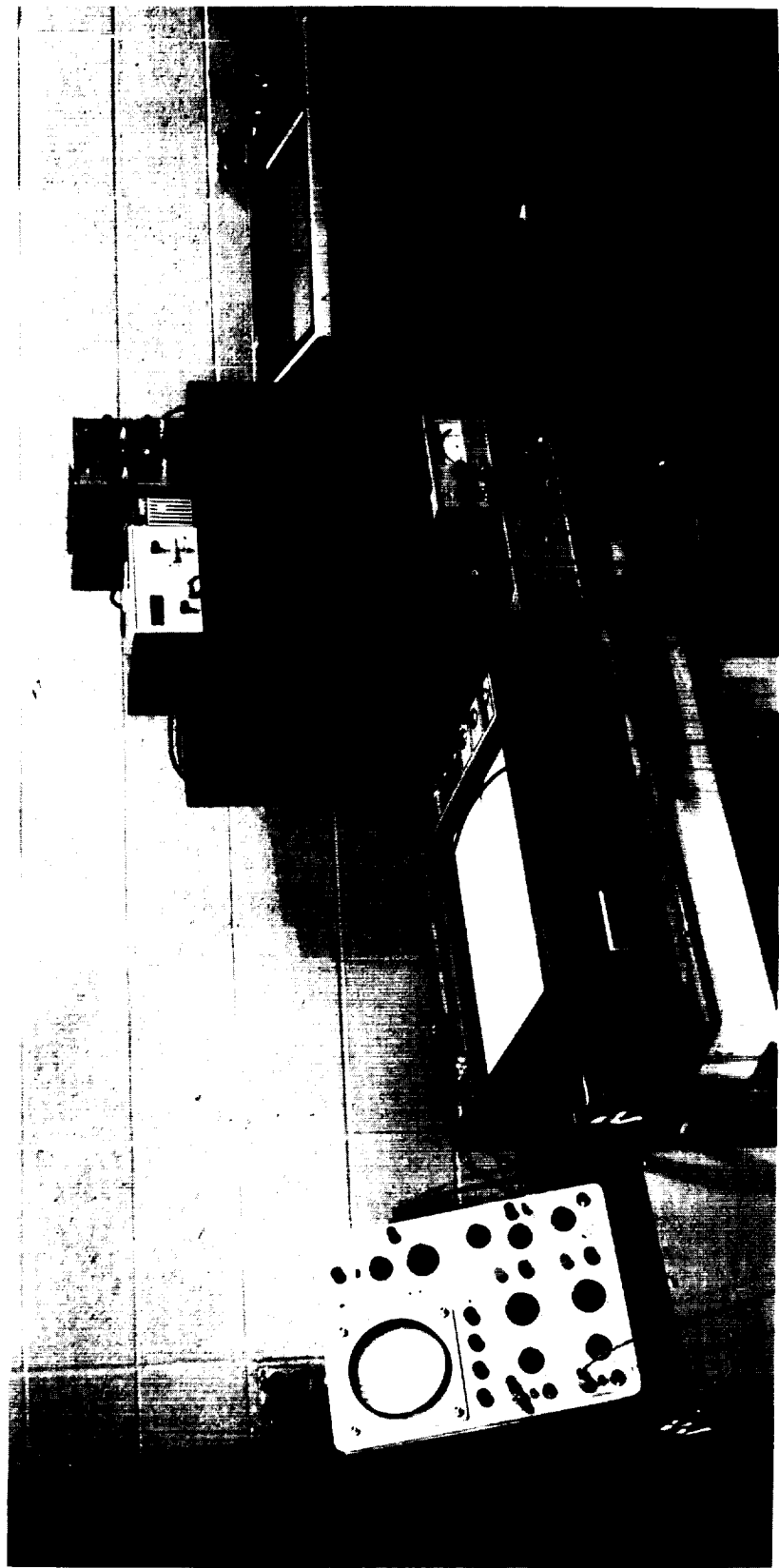


Figure 11. Photograph of hot-wire equipment.

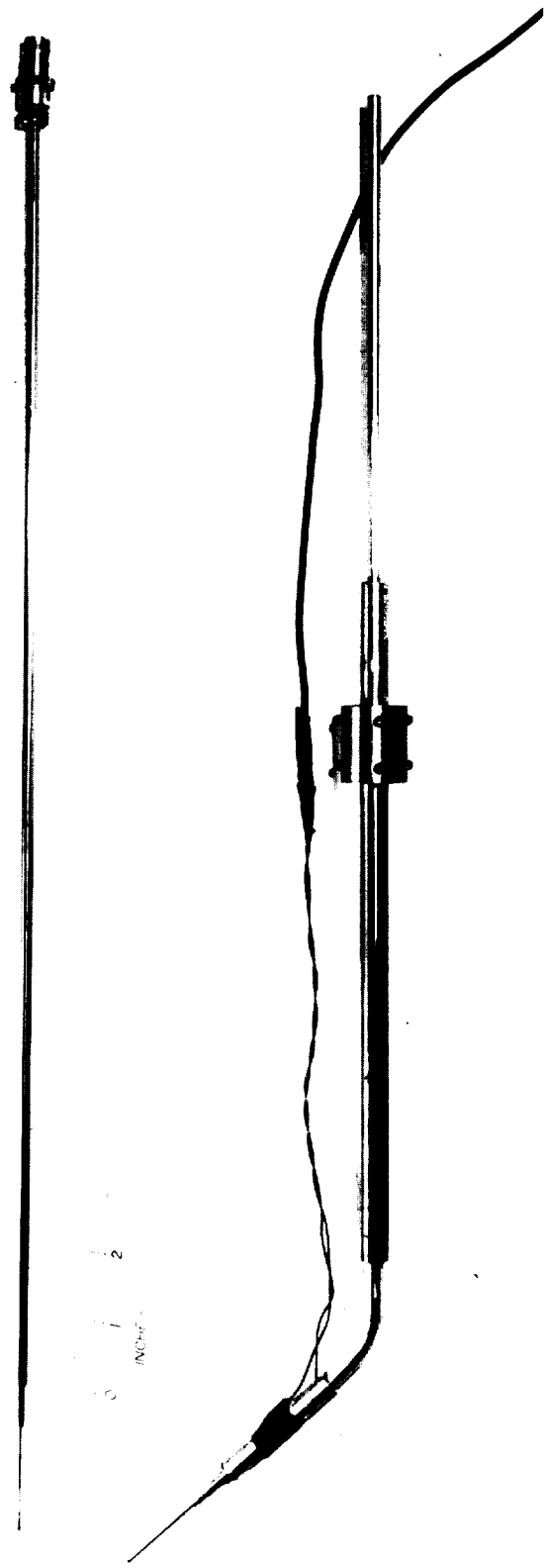
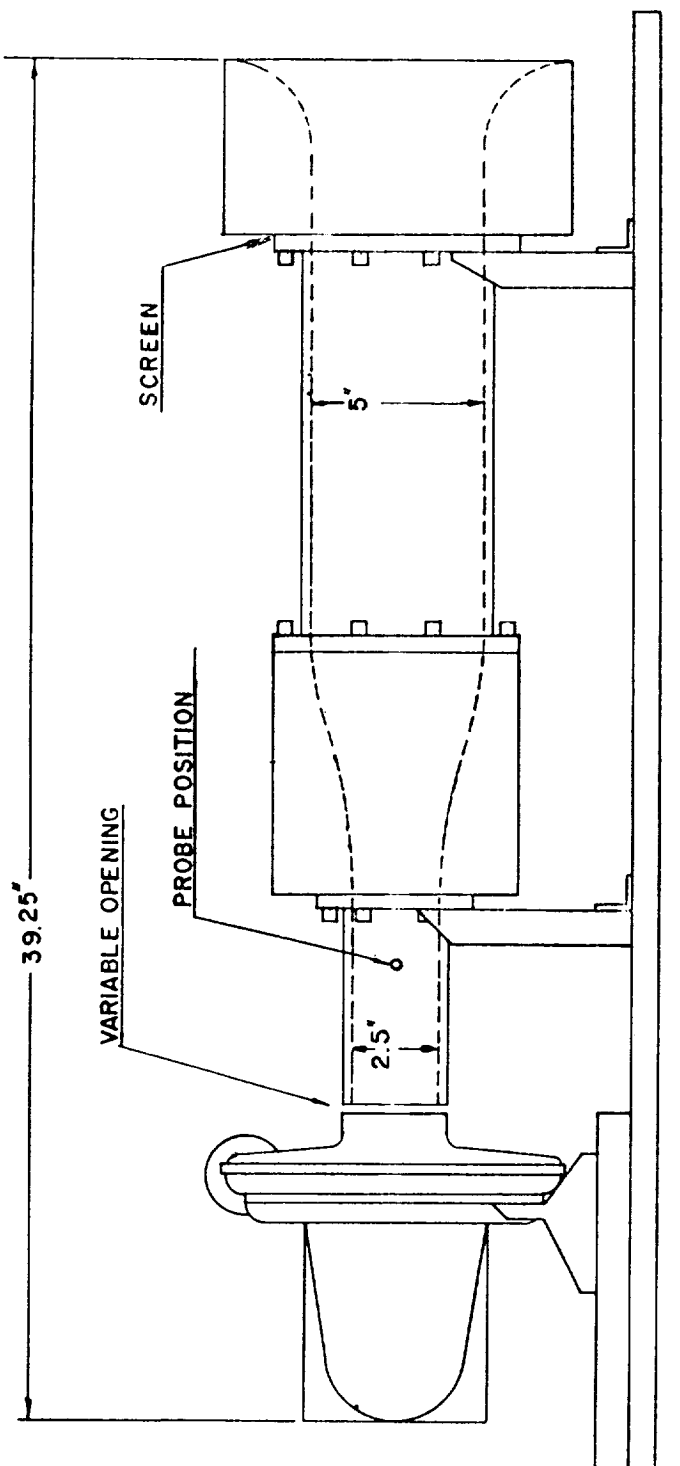


Figure 12. Straight and slanted hot-wire probes.



CALIBRATING TUNNEL

FIG. 13

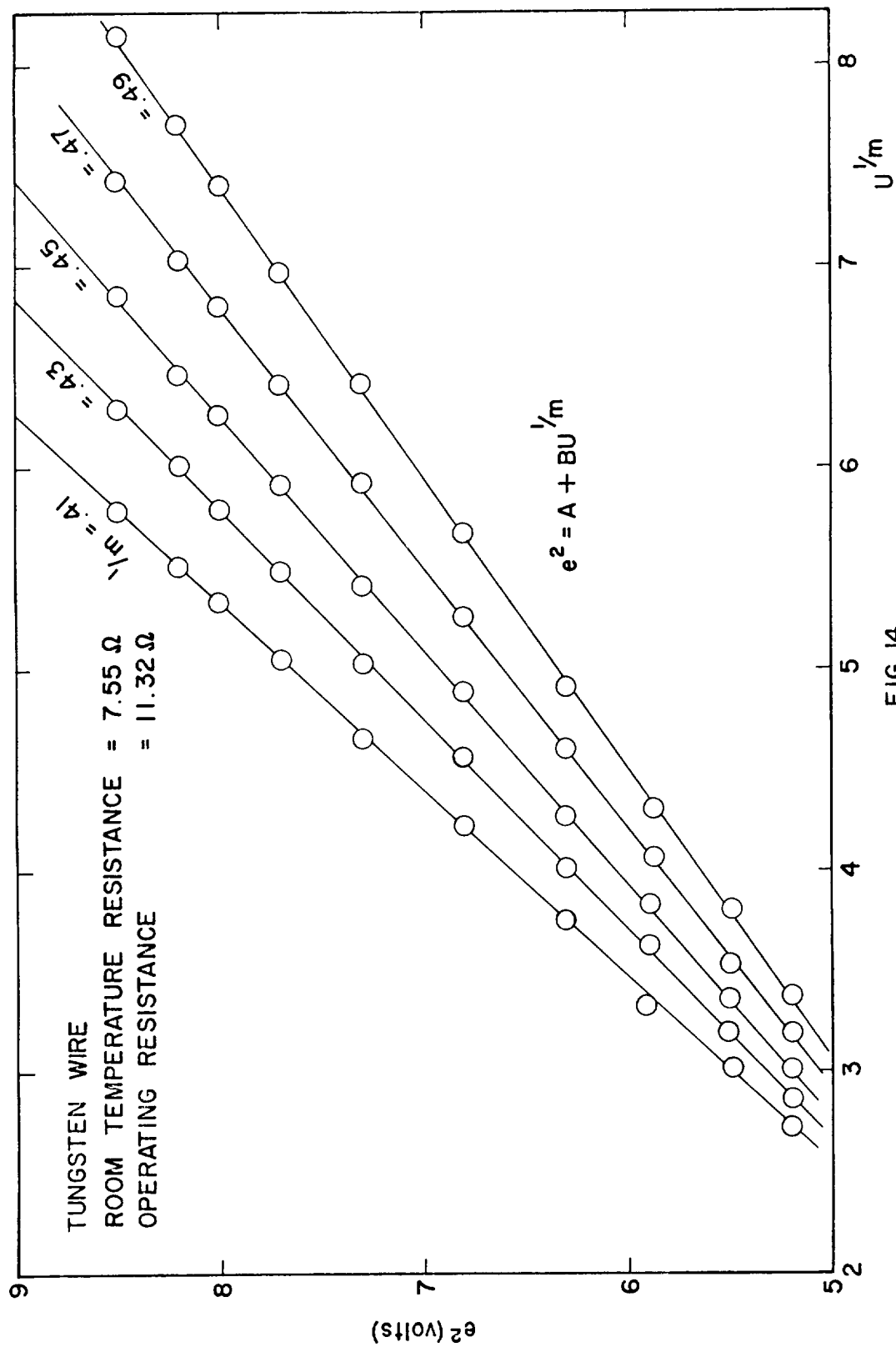
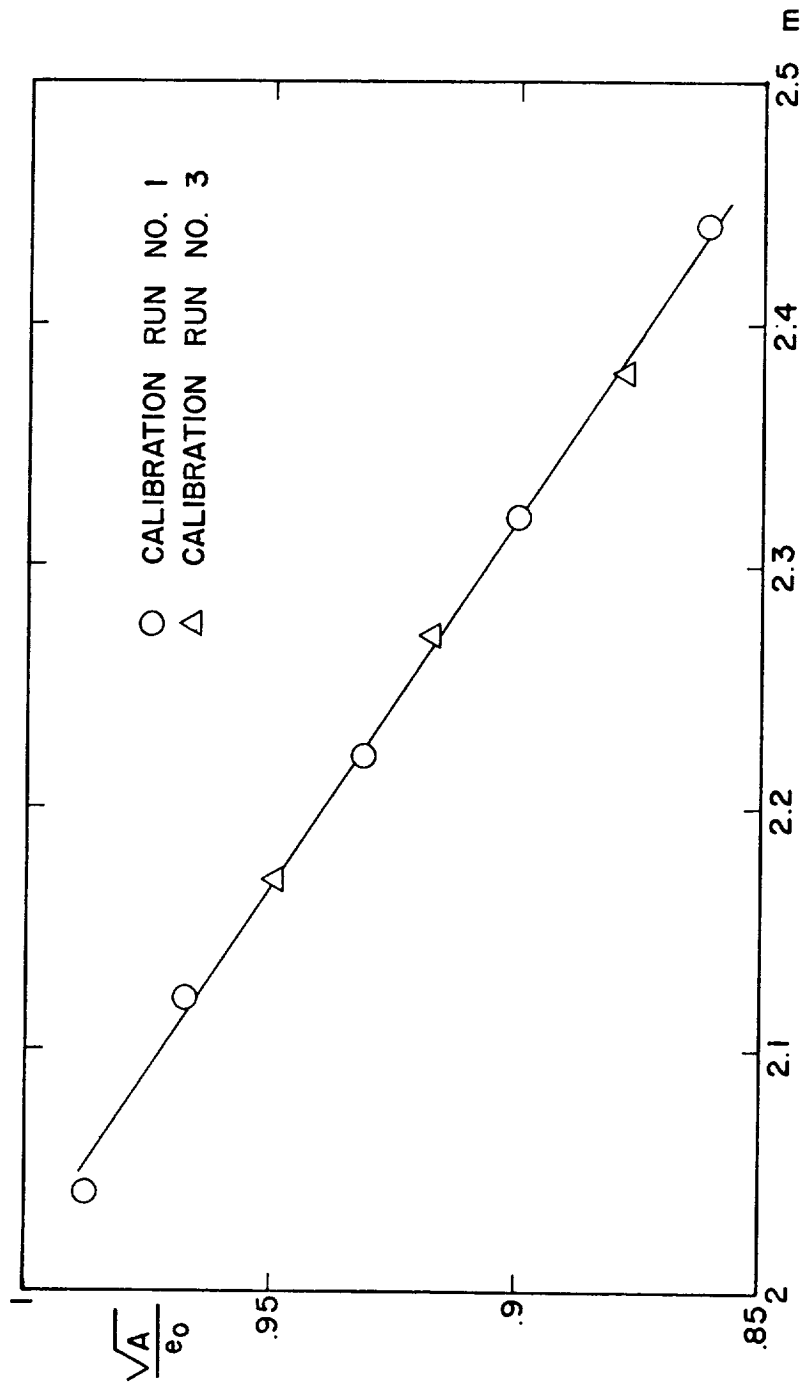


FIG. 14
 A SAMPLE SET OF CALIBRATION CURVES FOR CONSTANT TEMPERATURE ANEMOMETER.



CORRELATION BETWEEN ZERO VOLTAGE e_0 AND CONSTANT A IN EQUATION (2.2.4-1)

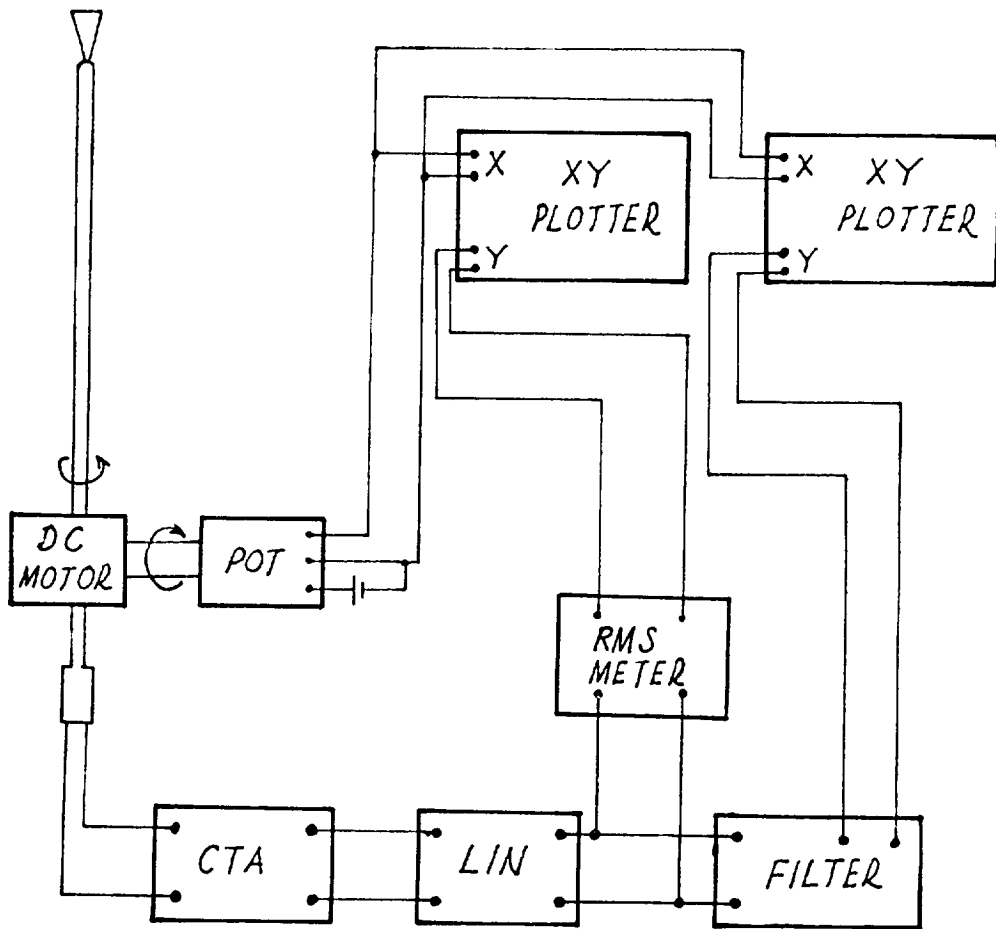
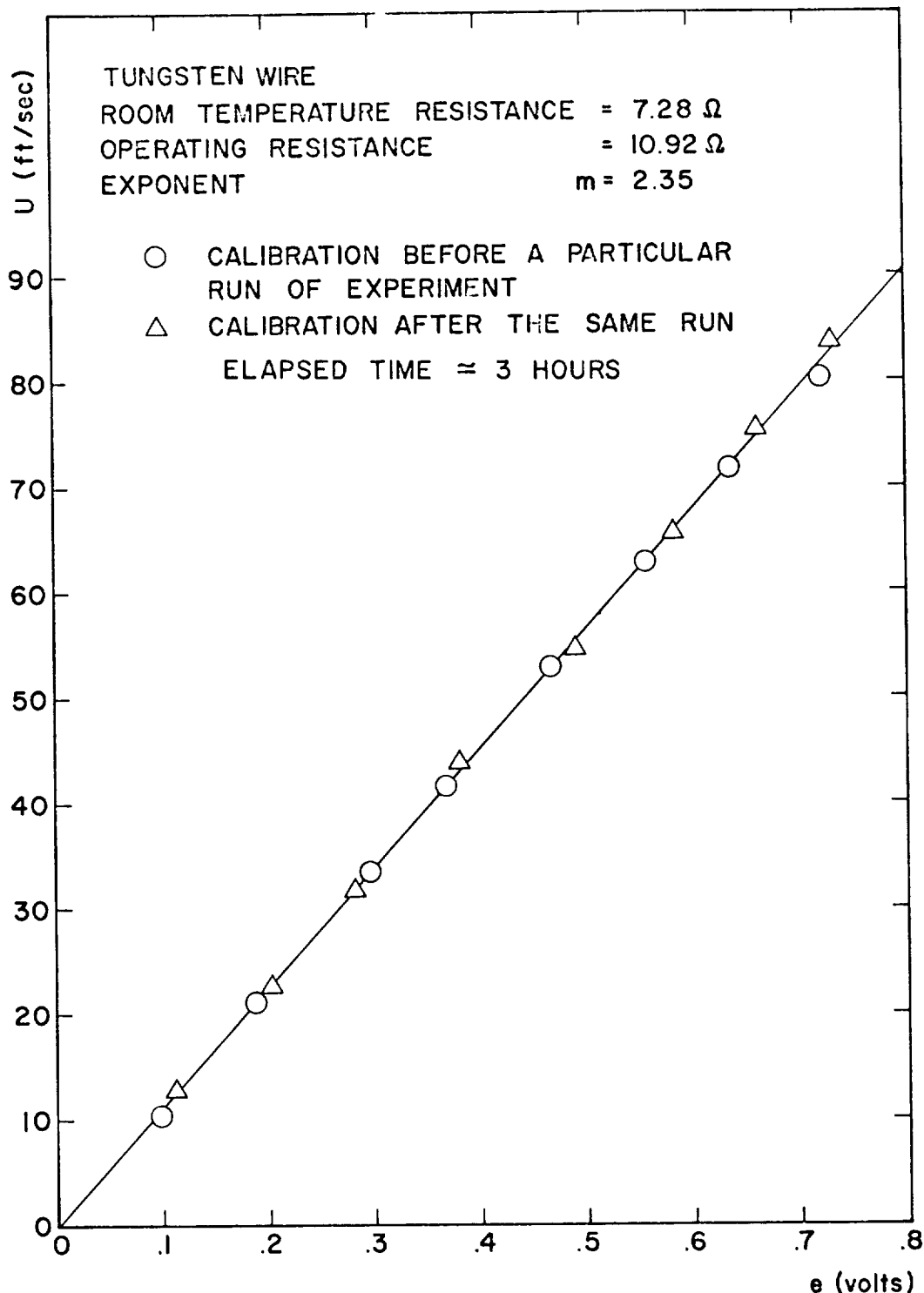


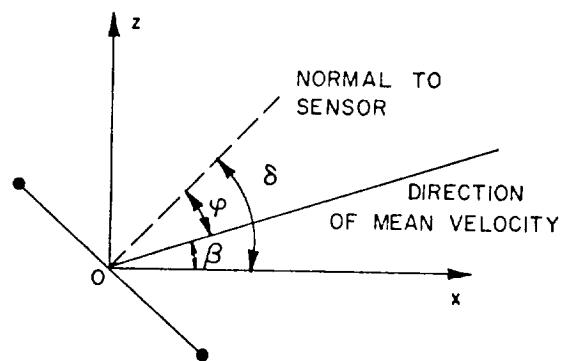
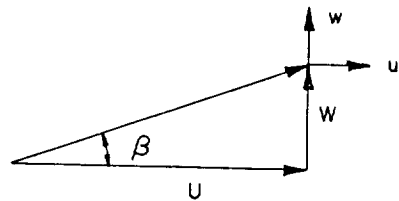
FIGURE 16
DIAGRAMATIC LAYOUT OF HOT-WIRE
EQUIPMENT



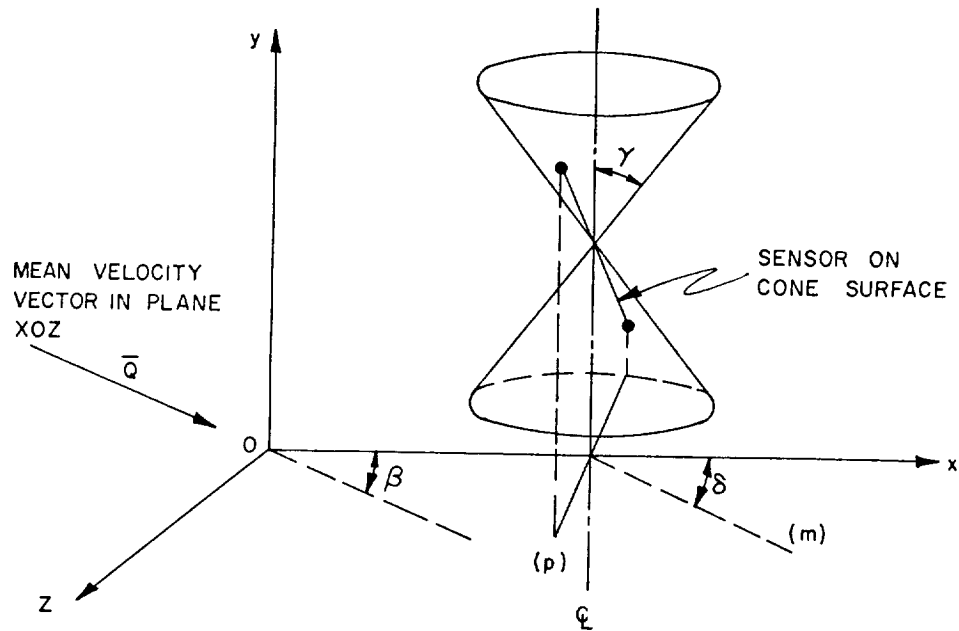
A SAMPLE CALIBRATION CURVE FOR LINEARIZER OUTPUT

FIG. 17

STRAIGHT - WIRE



SLANTED - WIRE



(p) PROJECTION OF SENSOR IN PLANE XOZ

(m) NORMAL TO LINE (p) IN PLANE XOZ

FIG. 18. COORDINATE SYSTEM FOR THE ROTATING STRAIGHT - WIRE AND SLANTED - WIRE PROBE

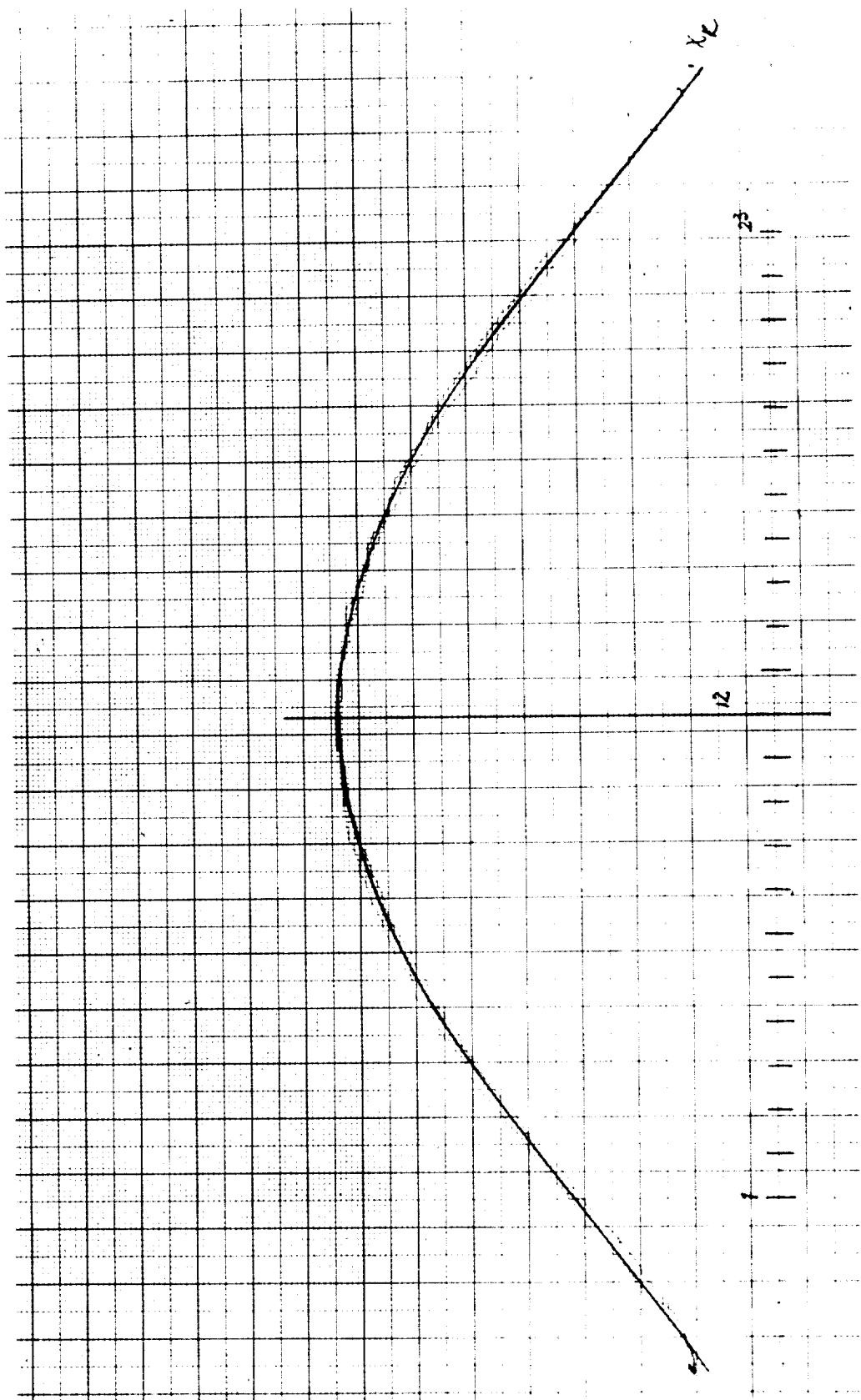


Figure 19. Sample X-Y plotter trace of linearized mean square voltage output.

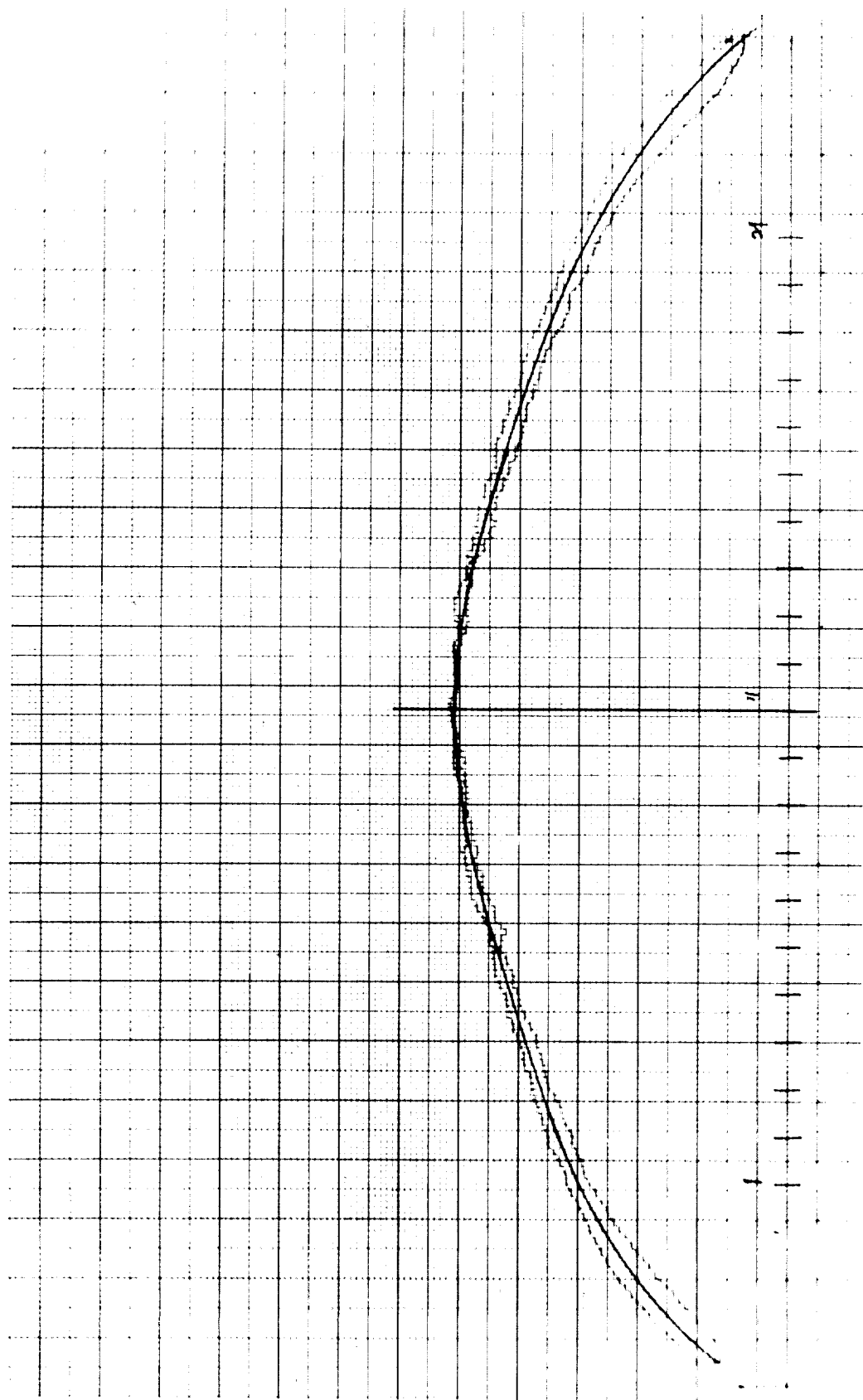
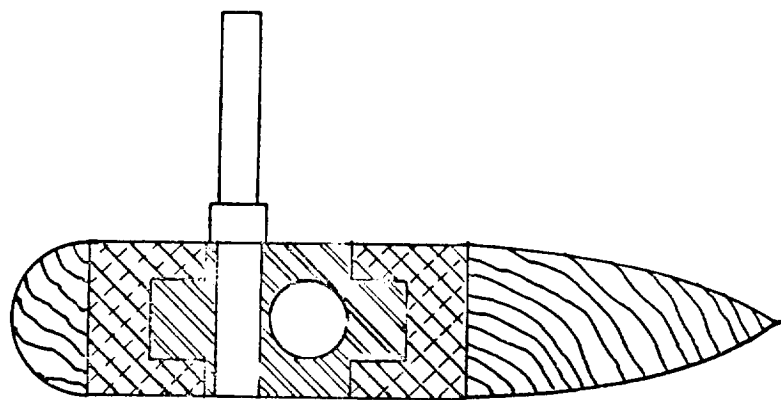


Figure 20. Sample X-Y plotter trace of linearized mean square voltage output.

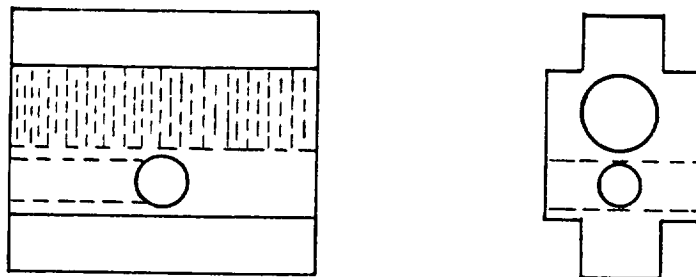


Figure 21. Photograph of probe carrier for traverse in Z direction.



PROBE STRUT CROSS-SECTION

SCALE : 2 x FULL SIZE



PROBE CARRIER

FIGURE 22 CROSS-SECTIONAL DRAWING OF STRUT
AND PROBE CARRIER

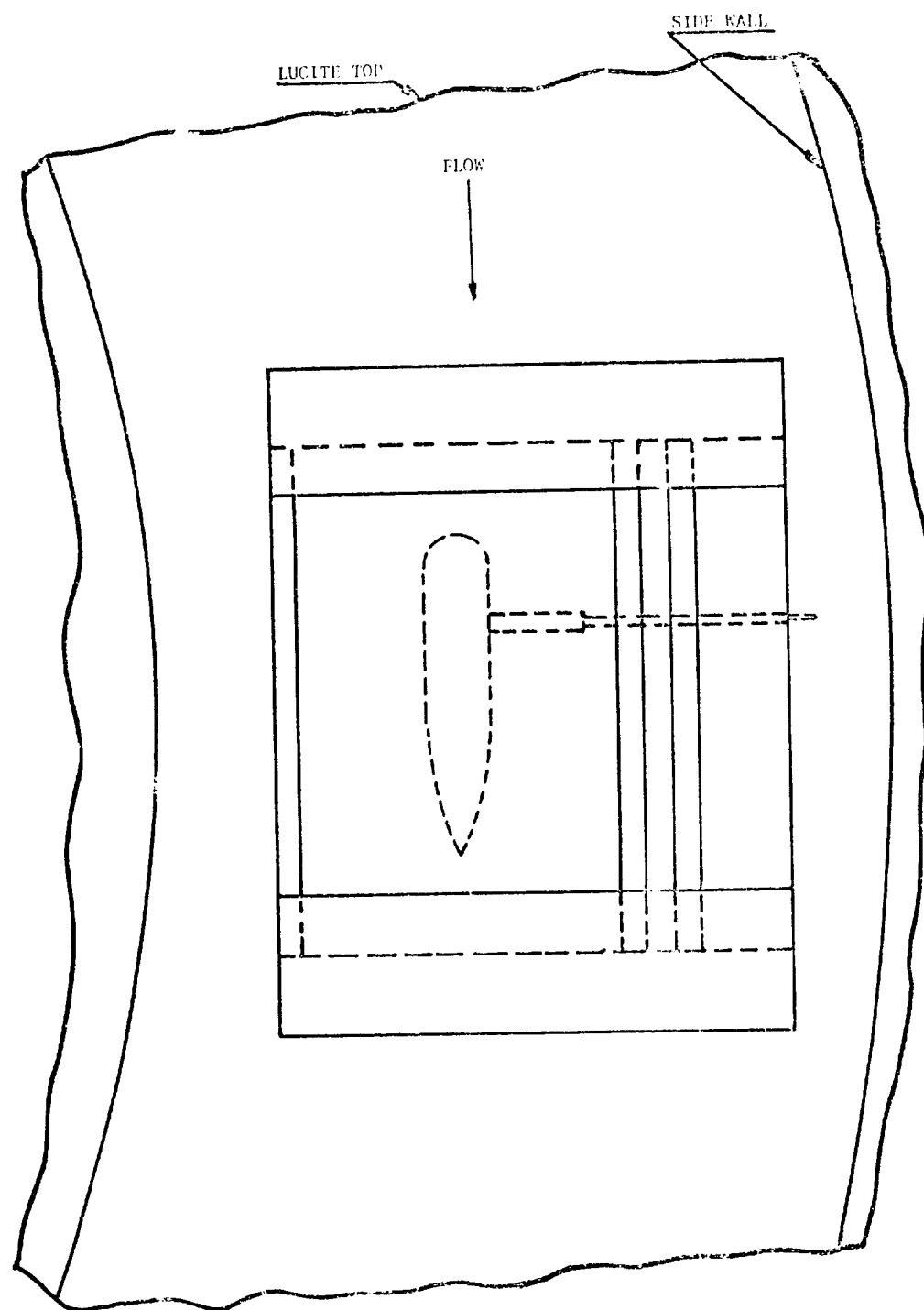


FIGURE 23

PROBE POSITION

SCALE : FULL SIZE

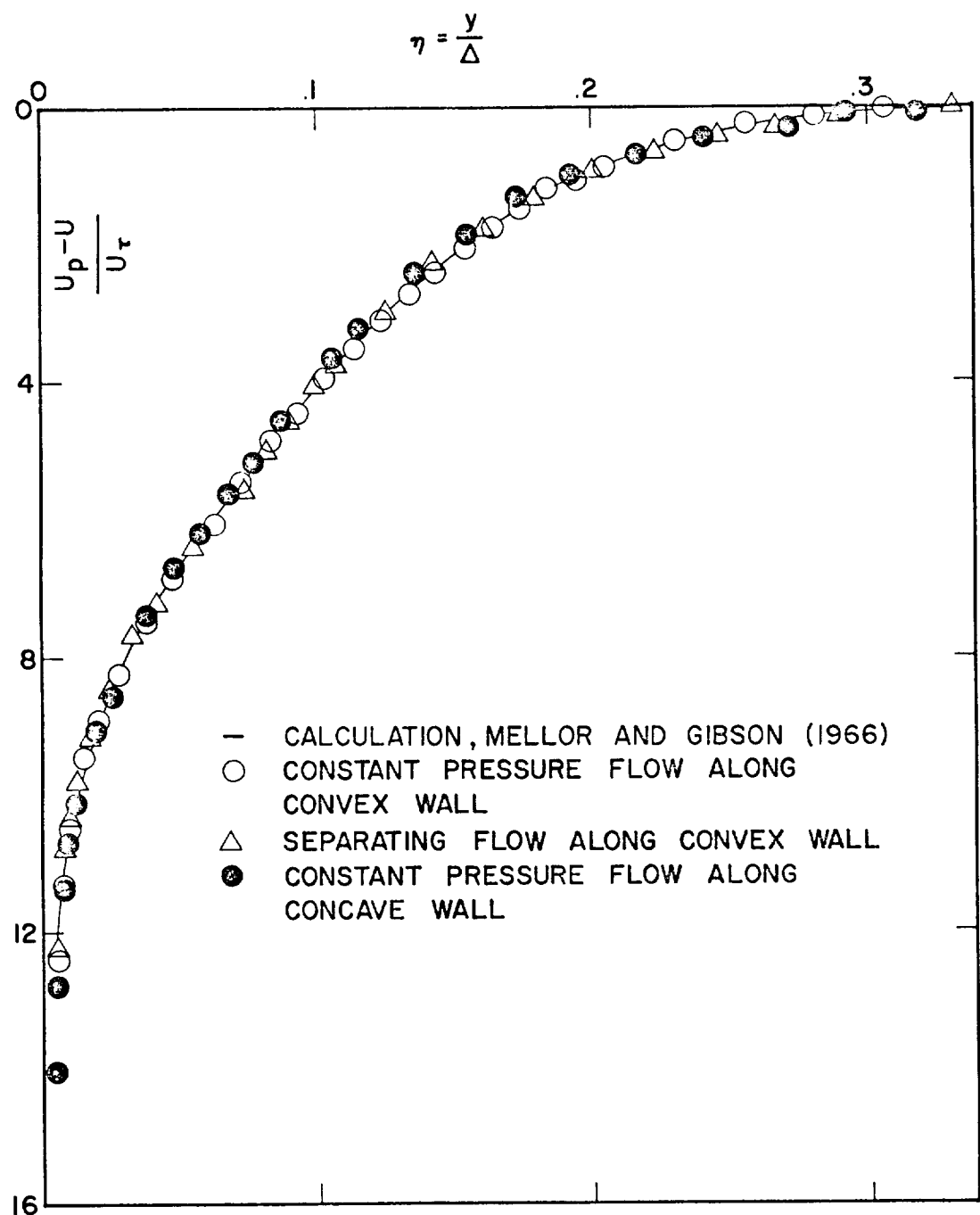


FIG. 24
DEFECT PLOT OF VELOCITY PROFILES AT STATION
NO. 1, $X(\text{IN})=24$.

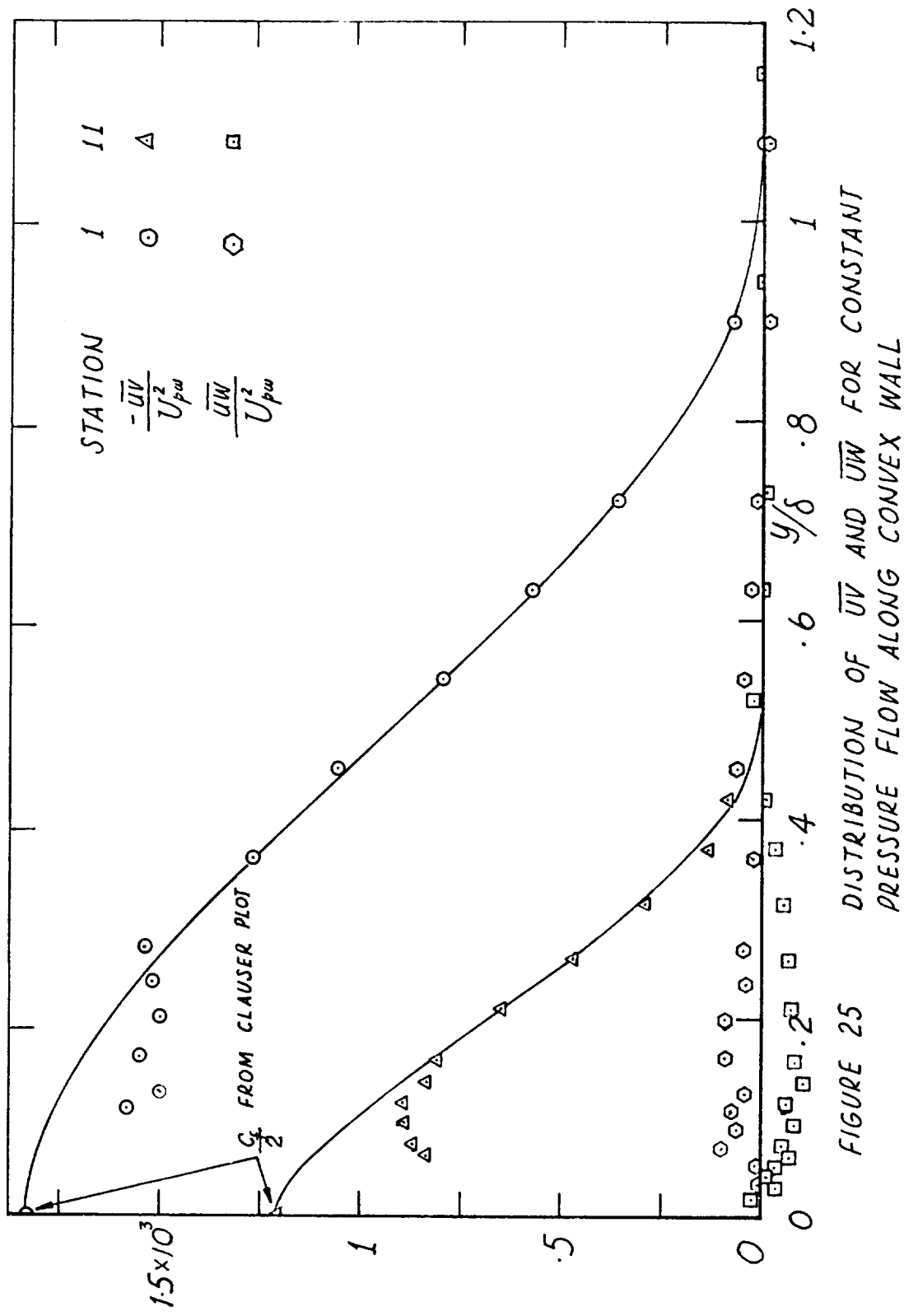
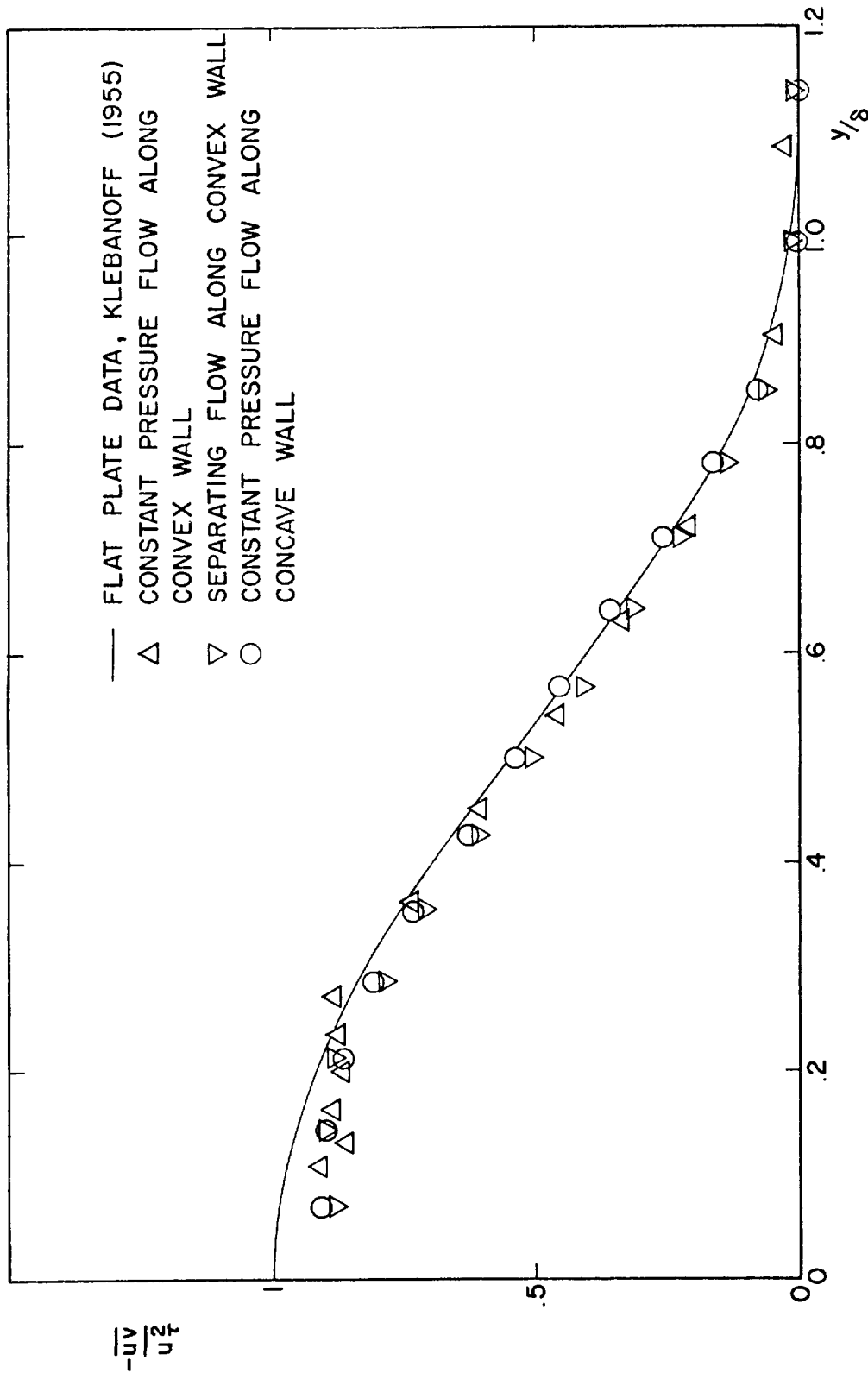


FIGURE 25 DISTRIBUTION OF $\bar{U}V$ AND $\bar{U}W$ FOR CONSTANT PRESSURE FLOW ALONG CONVEX WALL



SHEAR STRESS DISTRIBUTION AT STATION NO. 1, $X(IN)=24$.
FIG. 26

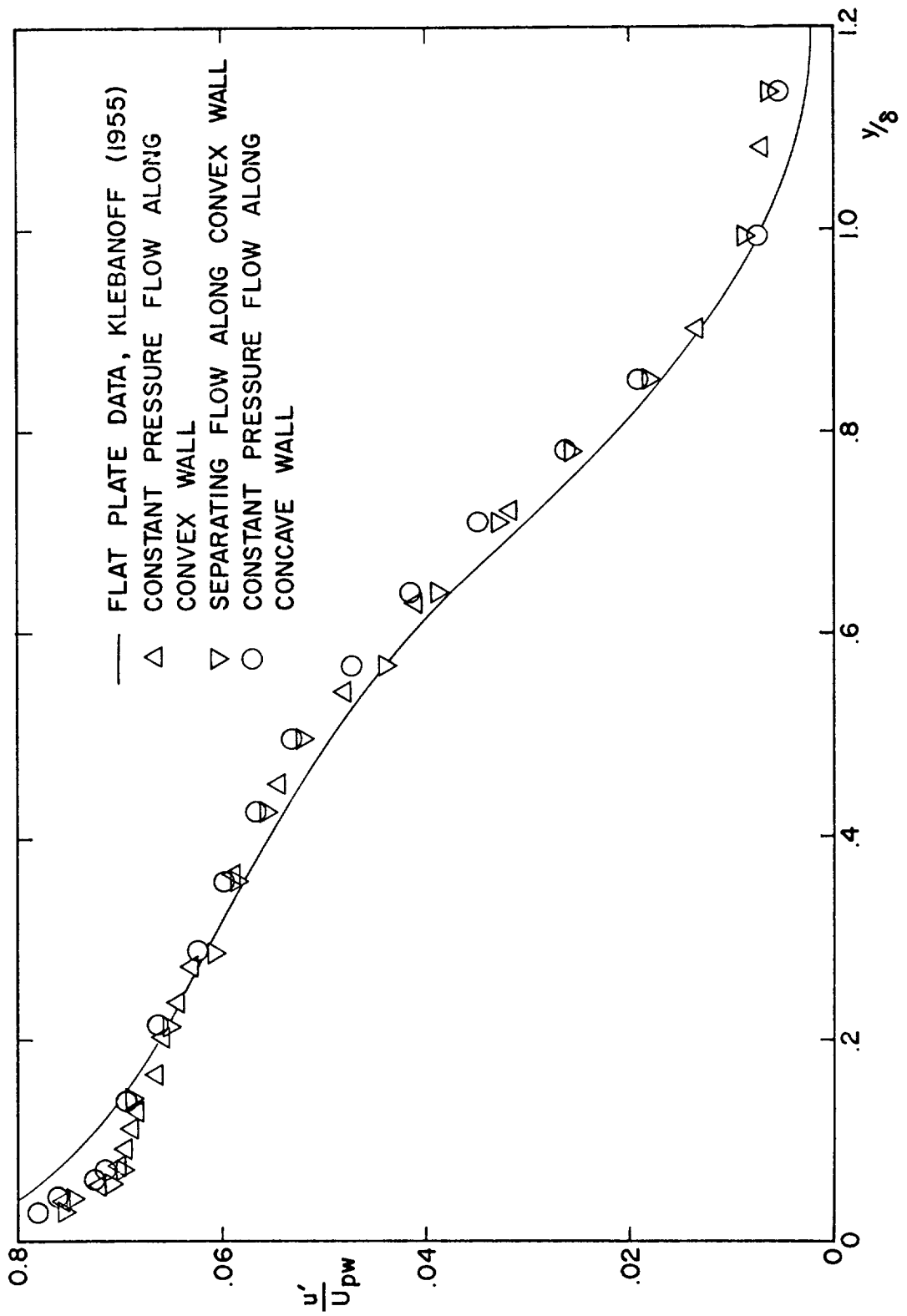


FIG. 27. DISTRIBUTION OF u'/U_{pw} AT STATION NO. 1, $X(1N)=24$.

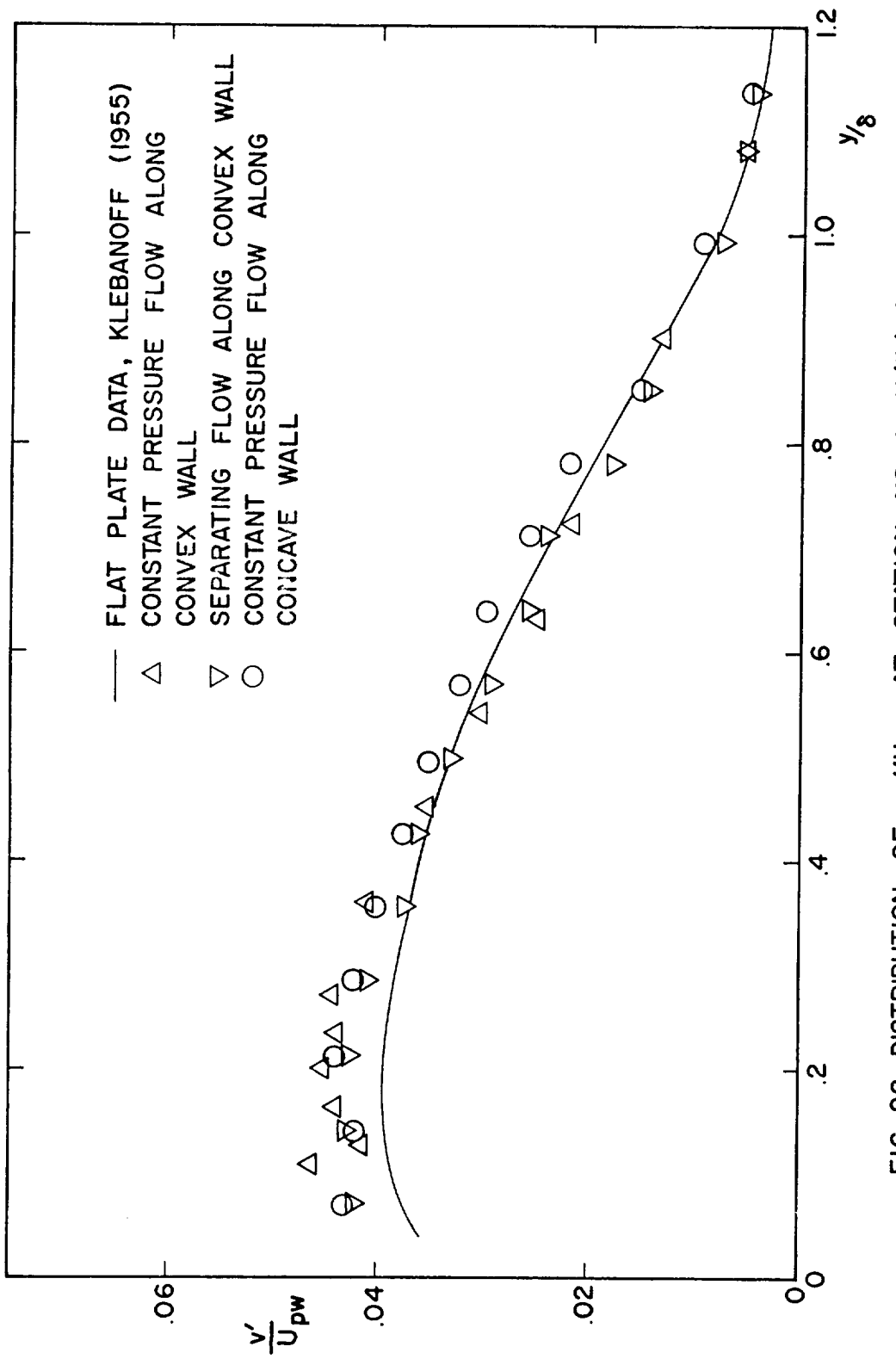


FIG. 28. DISTRIBUTION OF v'/U_{pw} AT STATION NO. 1, $X (IN) = 24$.

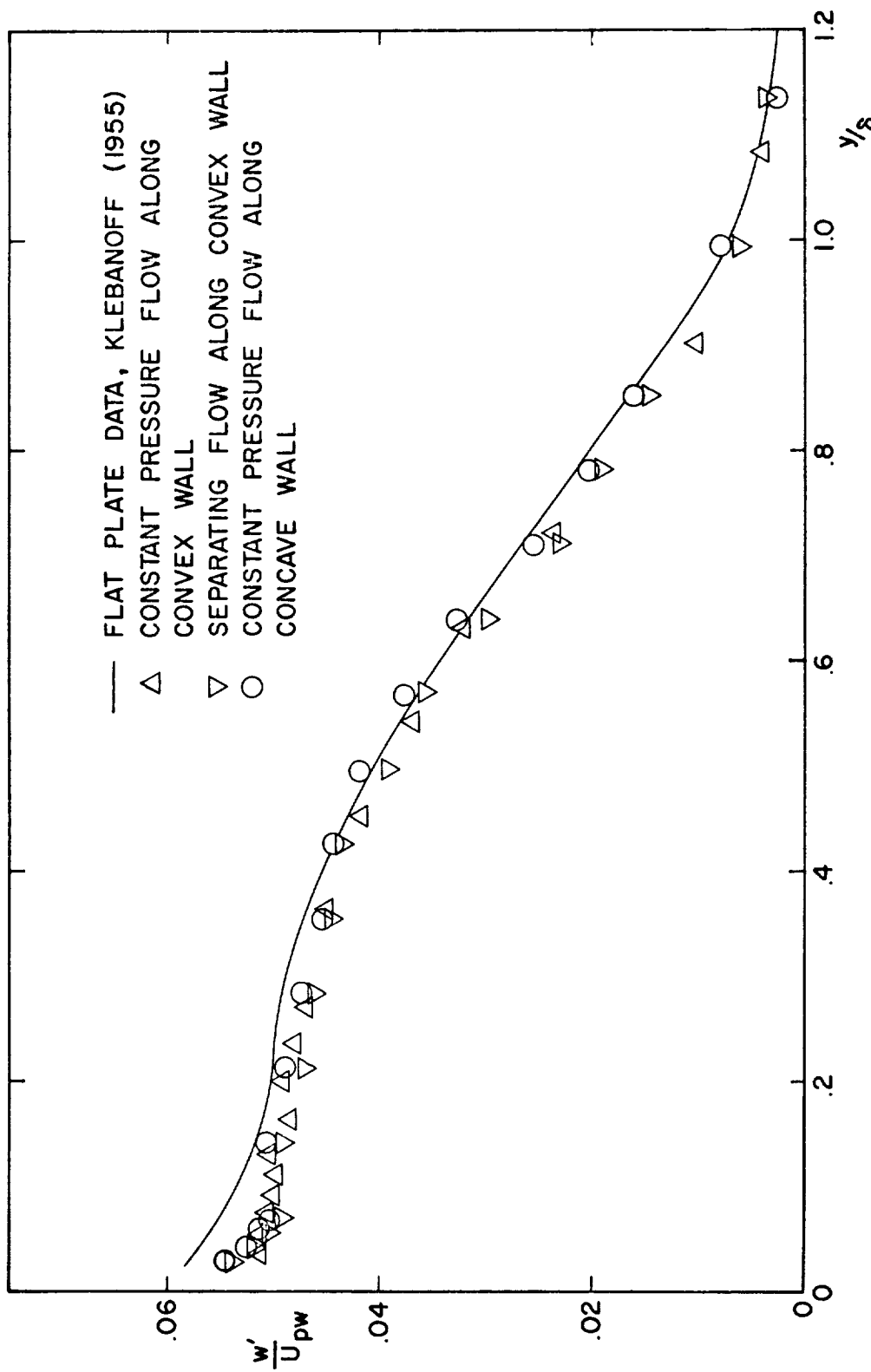


FIG. 29. DISTRIBUTION OF w'/U_{pw} AT STATION NO. 1, $X(IN)=24$.

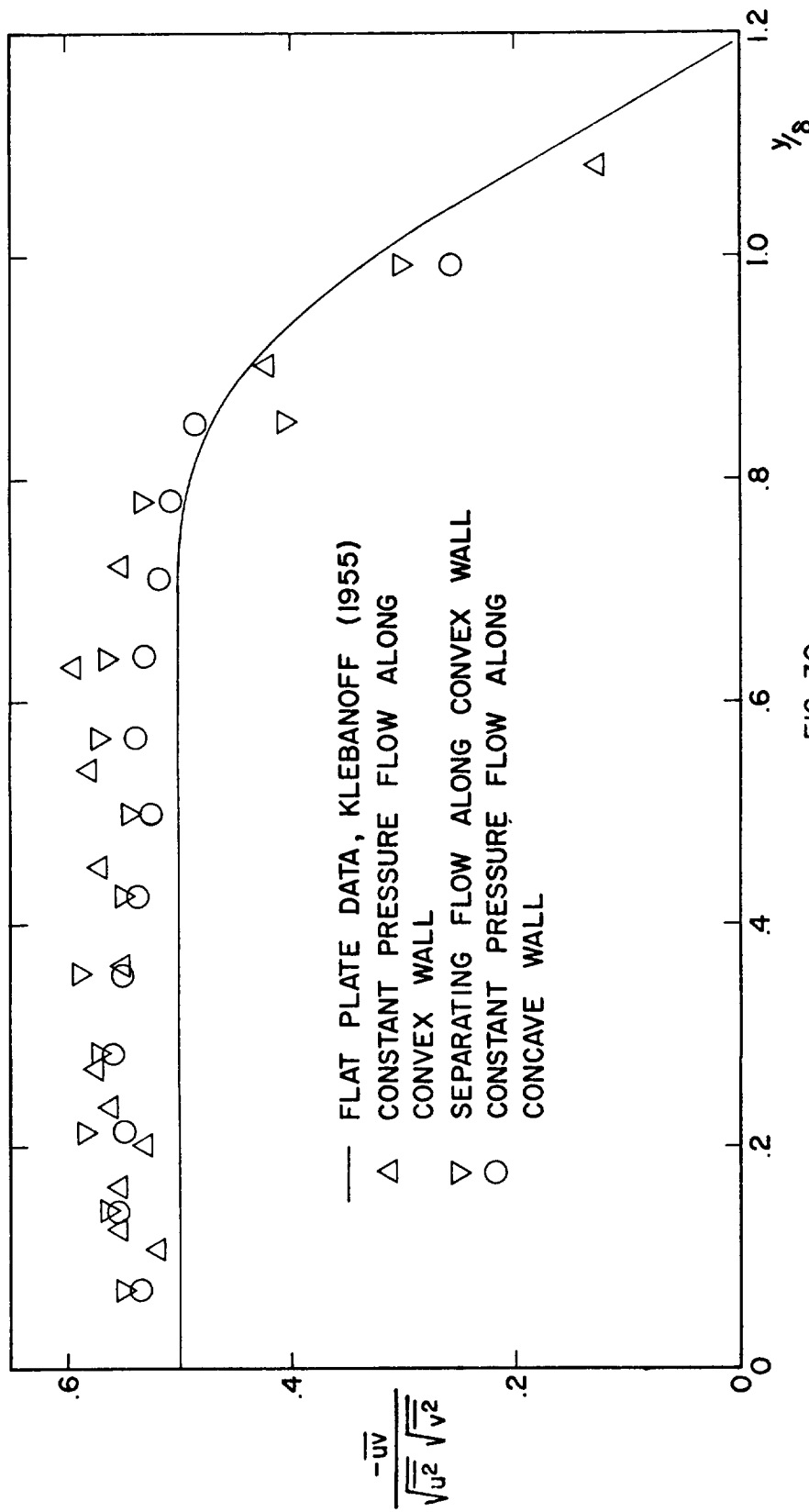


FIG. 30
DISTRIBUTION OF SHEAR CORRELATION COEFFICIENT AT STATION NO. 1, $X (IN) = 24$

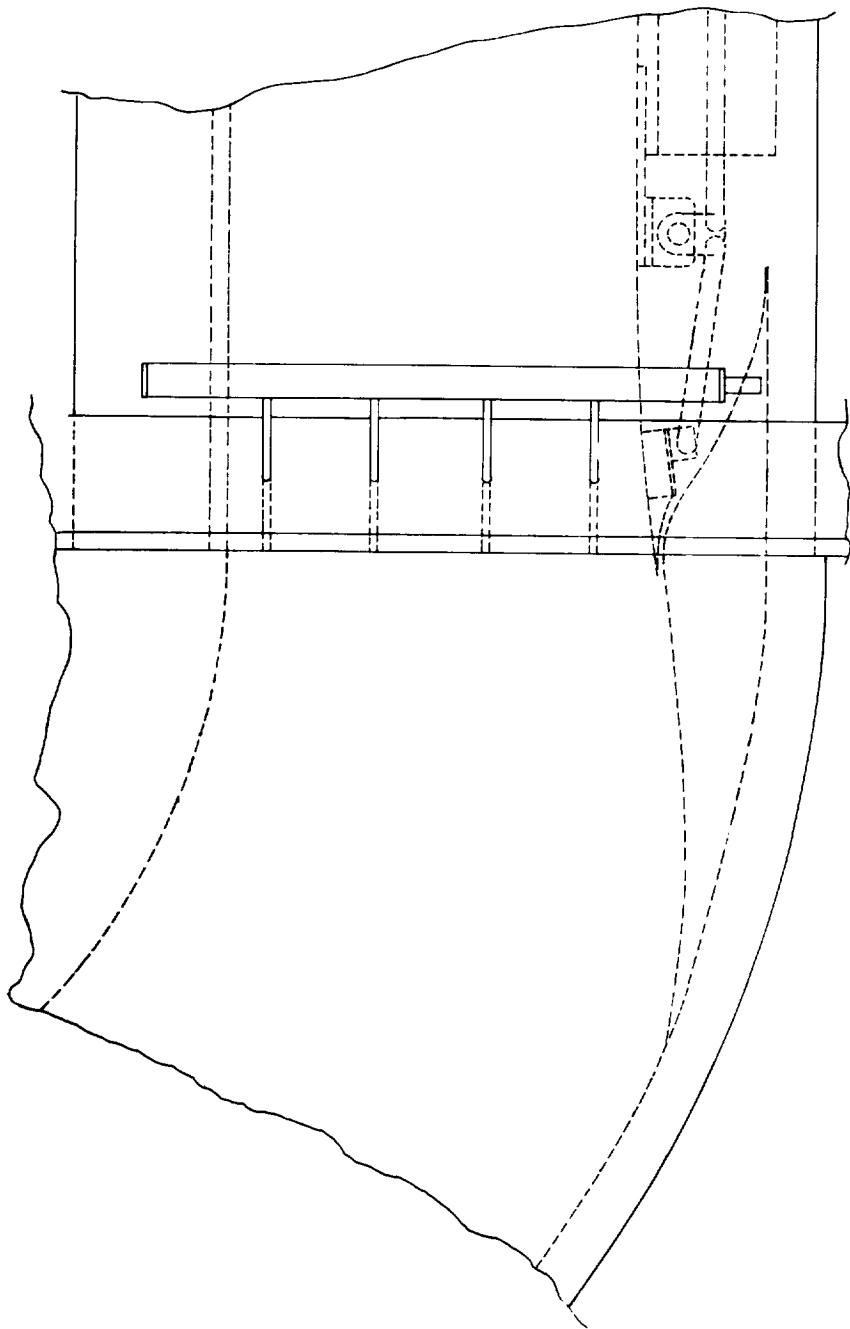


Figure 31. Flowing and flap control mechanisms.

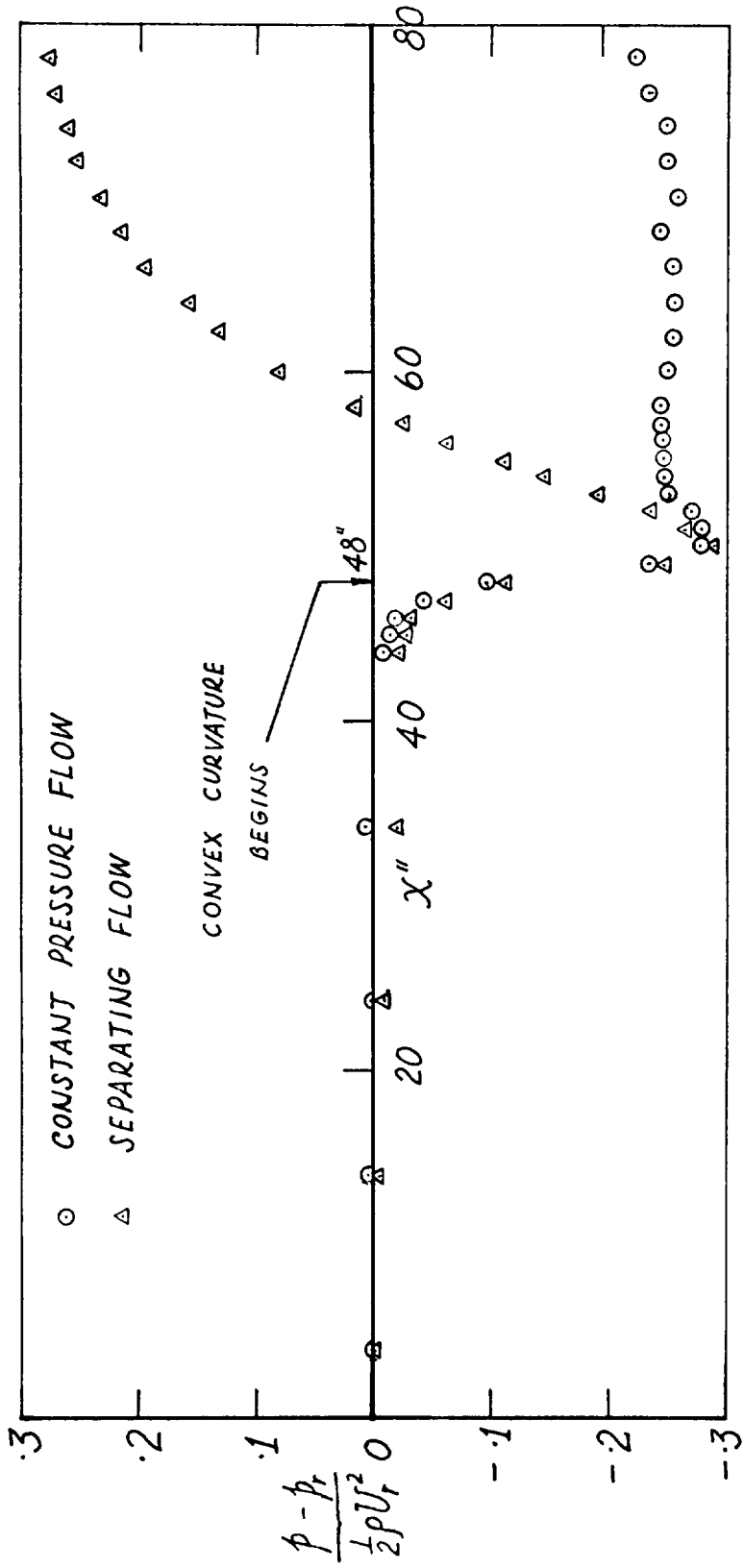


FIGURE 32 WALL STATIC PRESSURE DISTRIBUTION ALONG CONVEX WALL

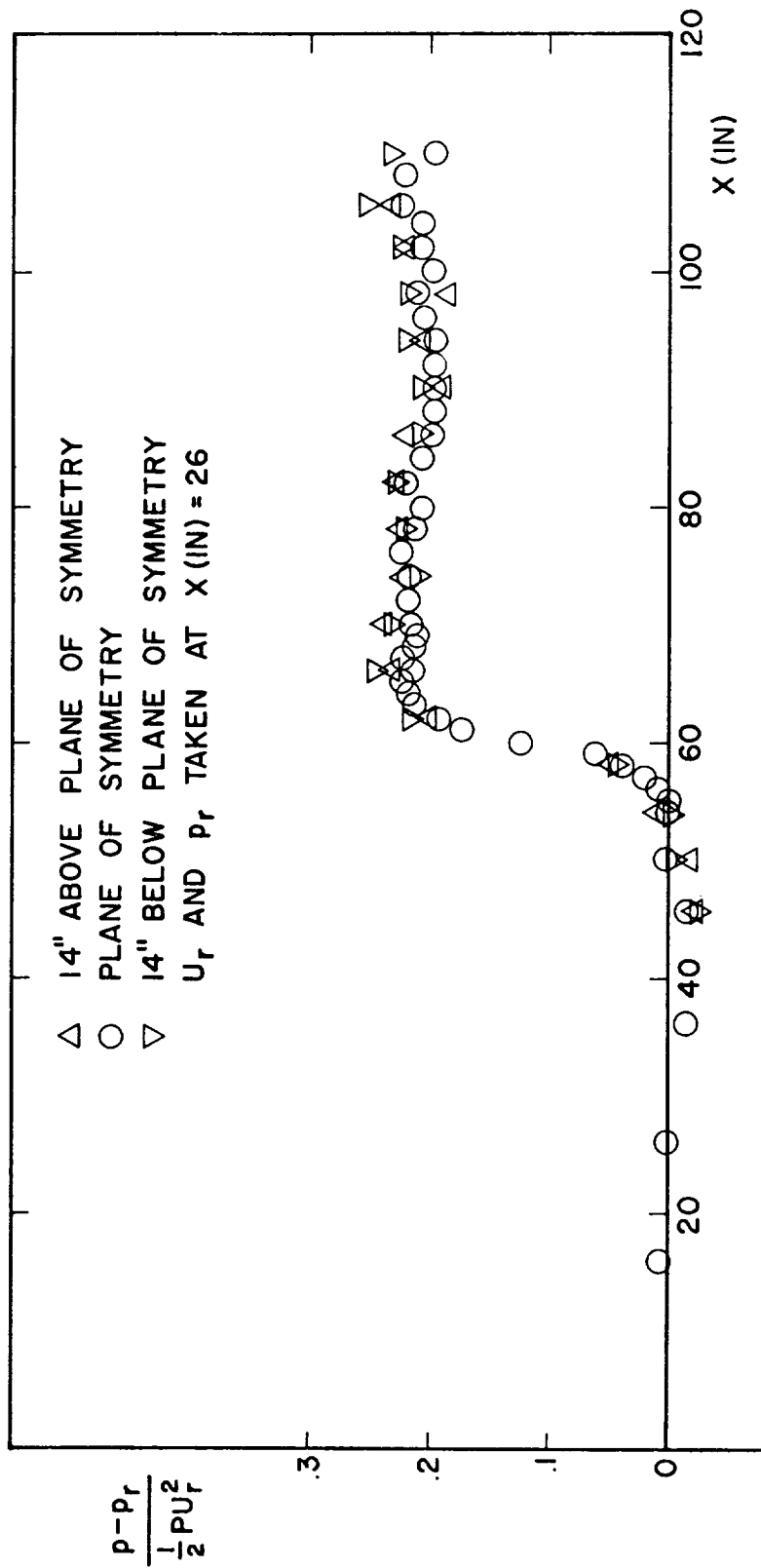


FIG. 33
WALL STATIC PRESSURE DISTRIBUTION FOR CONSTANT PRESSURE FLOW ALONG CONCAVE WALL

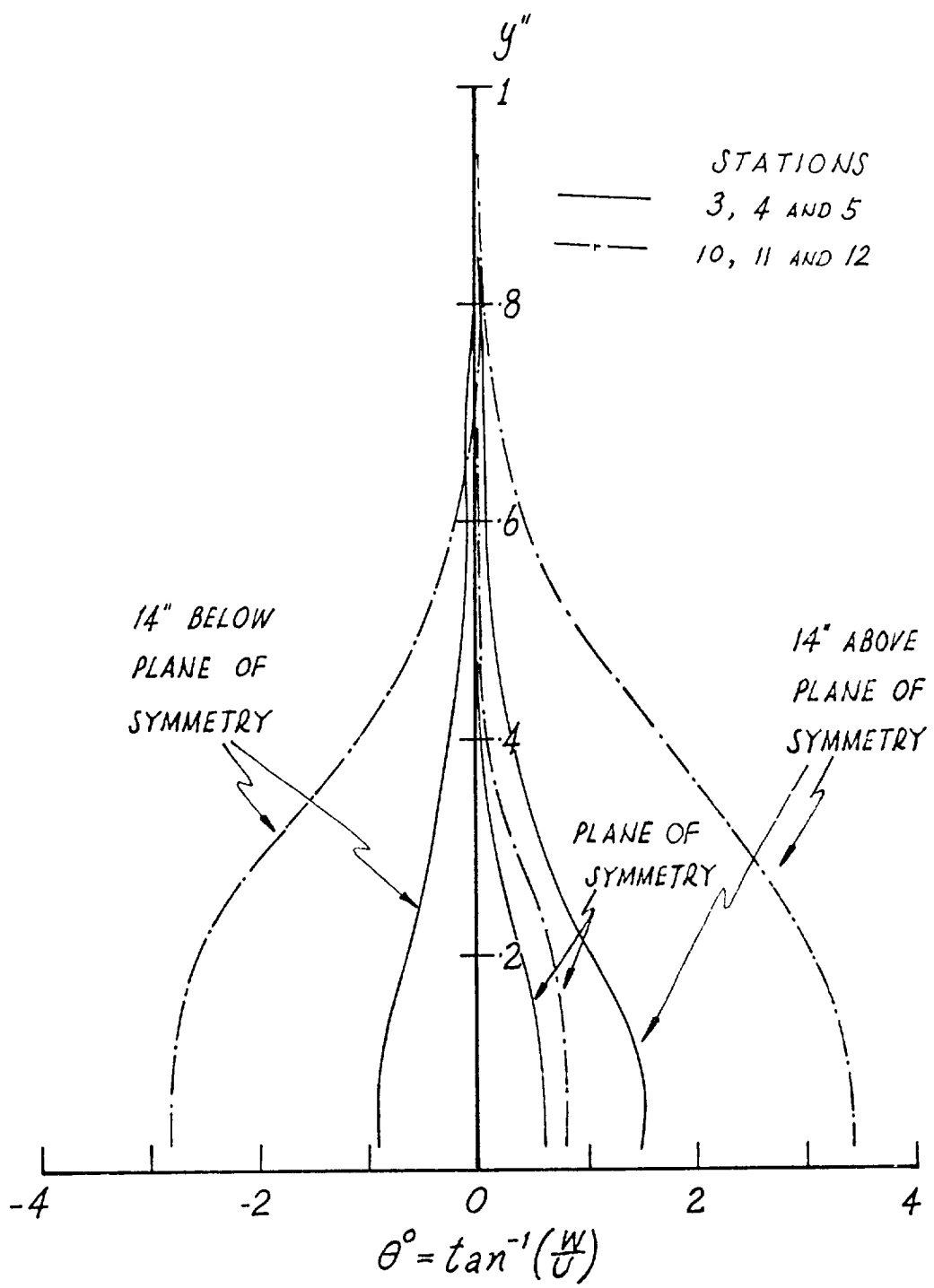


FIGURE 34 YAW DISTRIBUTION FOR CONSTANT PRESSURE FLOW ALONG CONVEX WALL

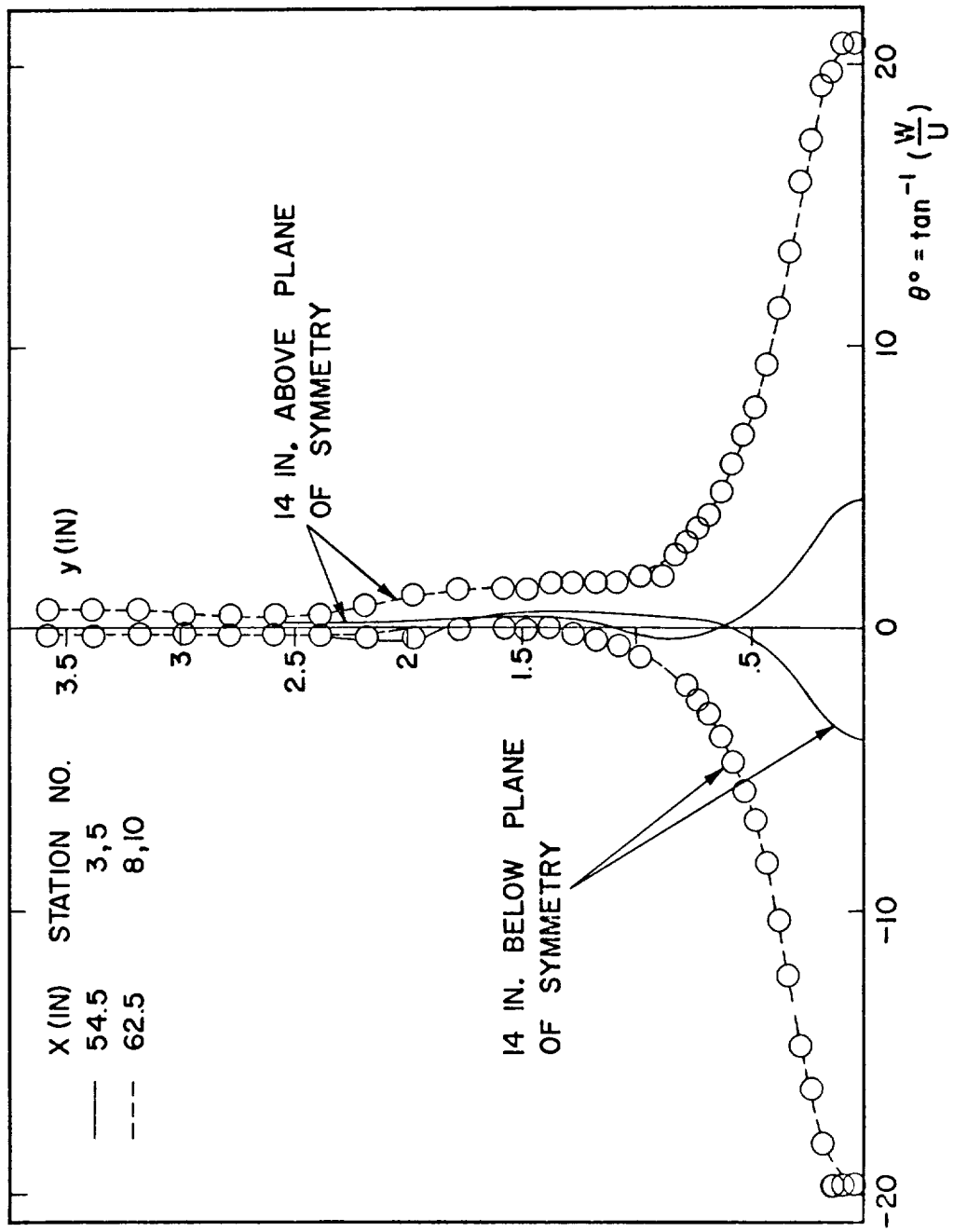
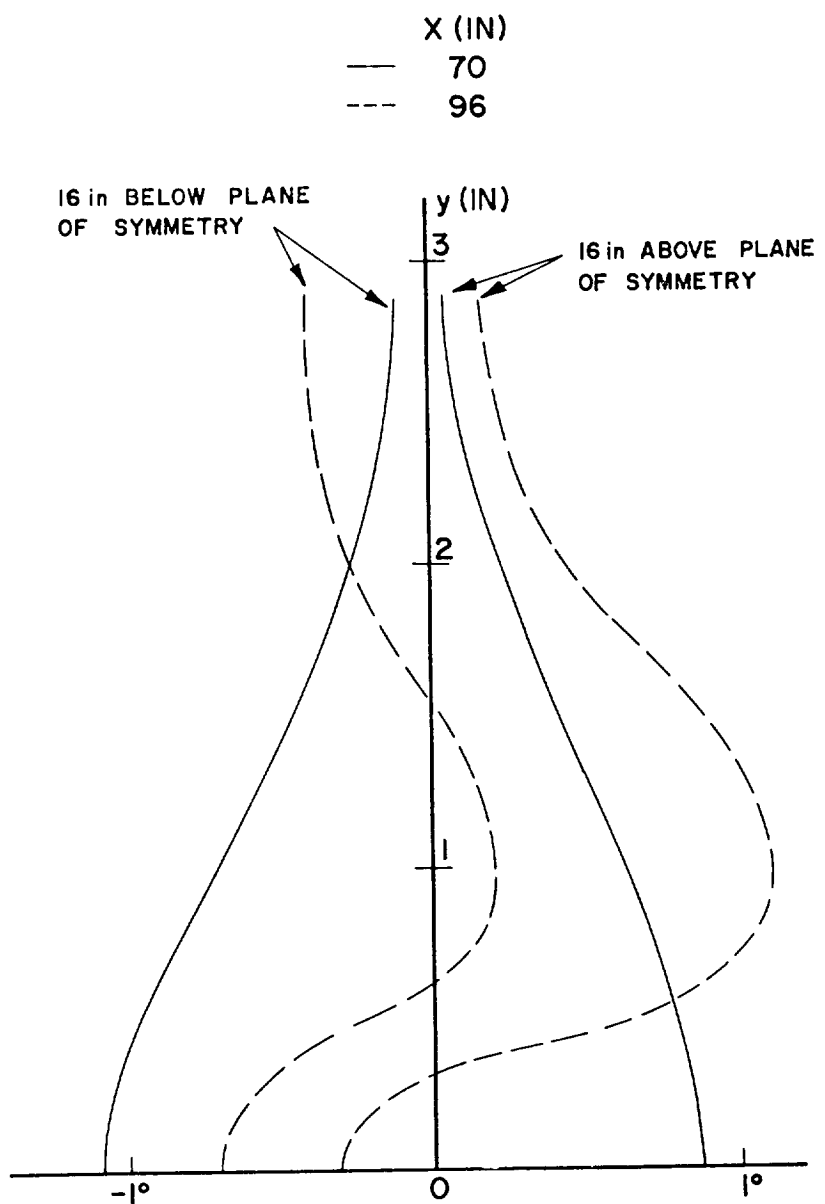


FIG. 35. YAW DISTRIBUTION FOR SEPARATING FLOW ALONG CONVEX WALL.



$$\theta = \tan^{-1} \left(\frac{W}{U} \right)$$

FIG. 36. YAW DISTRIBUTION TAKEN ON WALL OPPOSITE CONCAVE WALL.

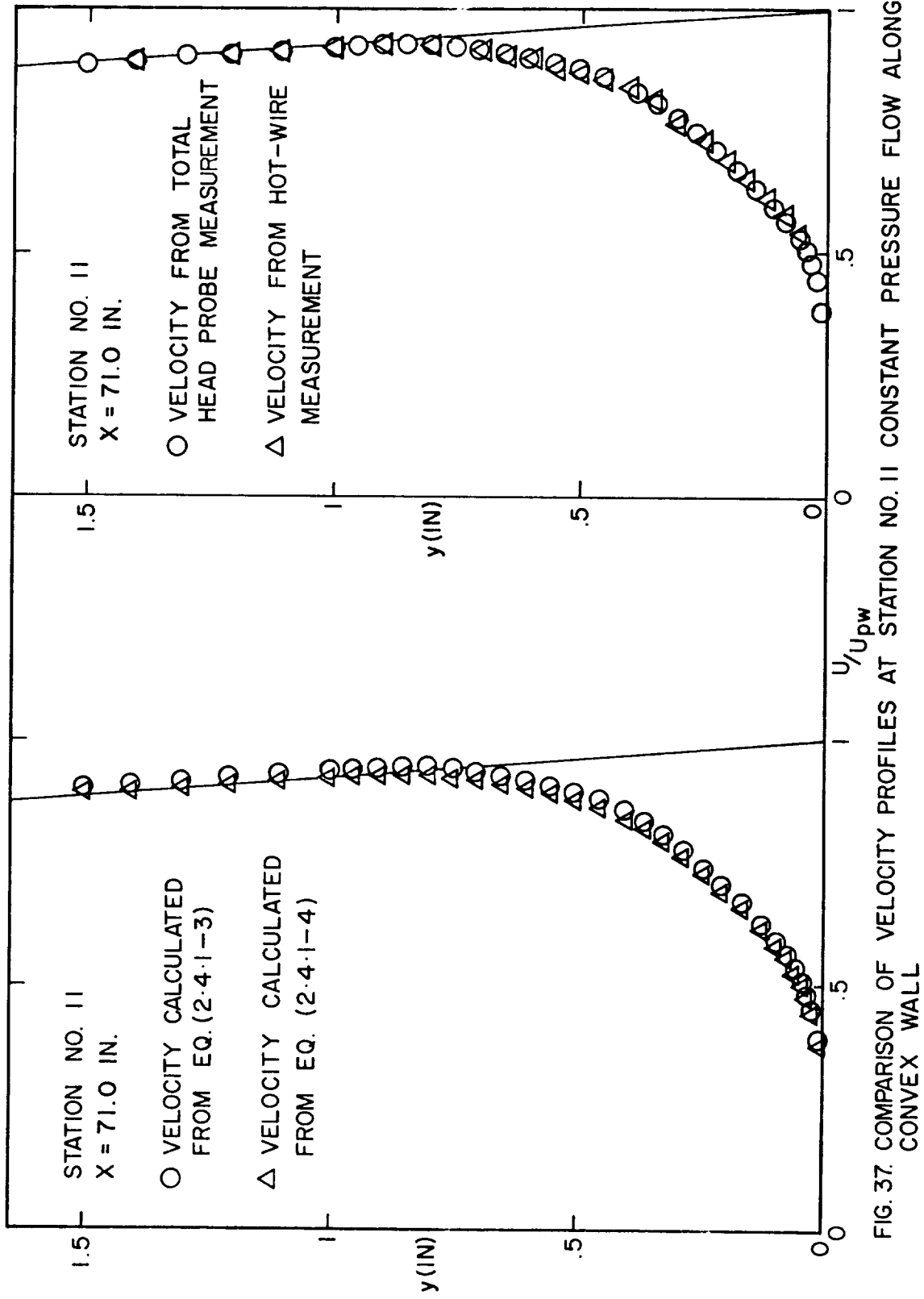


FIG. 37. COMPARISON OF VELOCITY PROFILES AT STATION NO. II CONSTANT PRESSURE FLOW ALONG CONVEX WALL

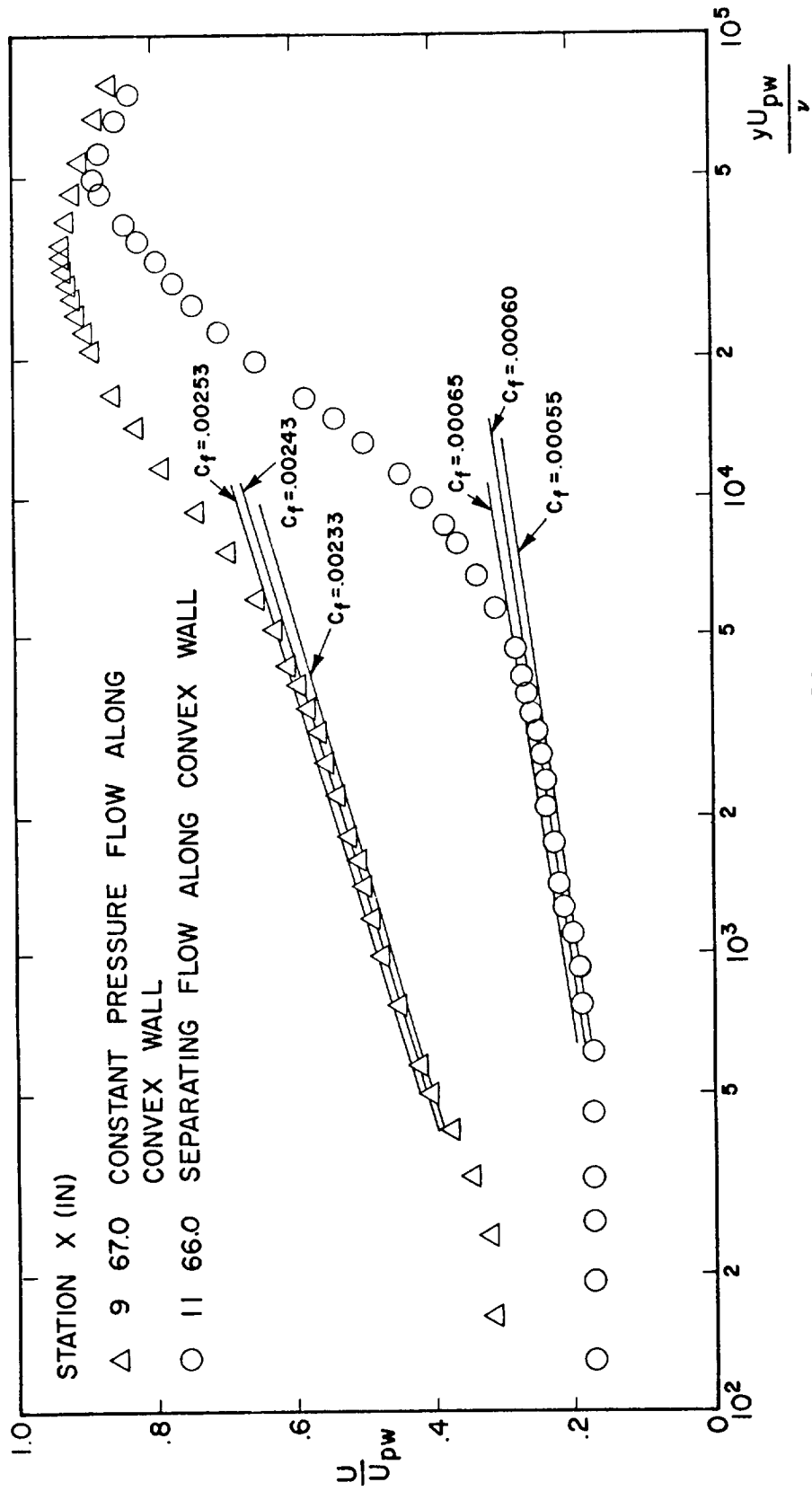


FIG. 38
SEMI-LOG PLOT OF VELOCITY PROFILES FOR THE DETERMINATION OF SKIN FRICTION

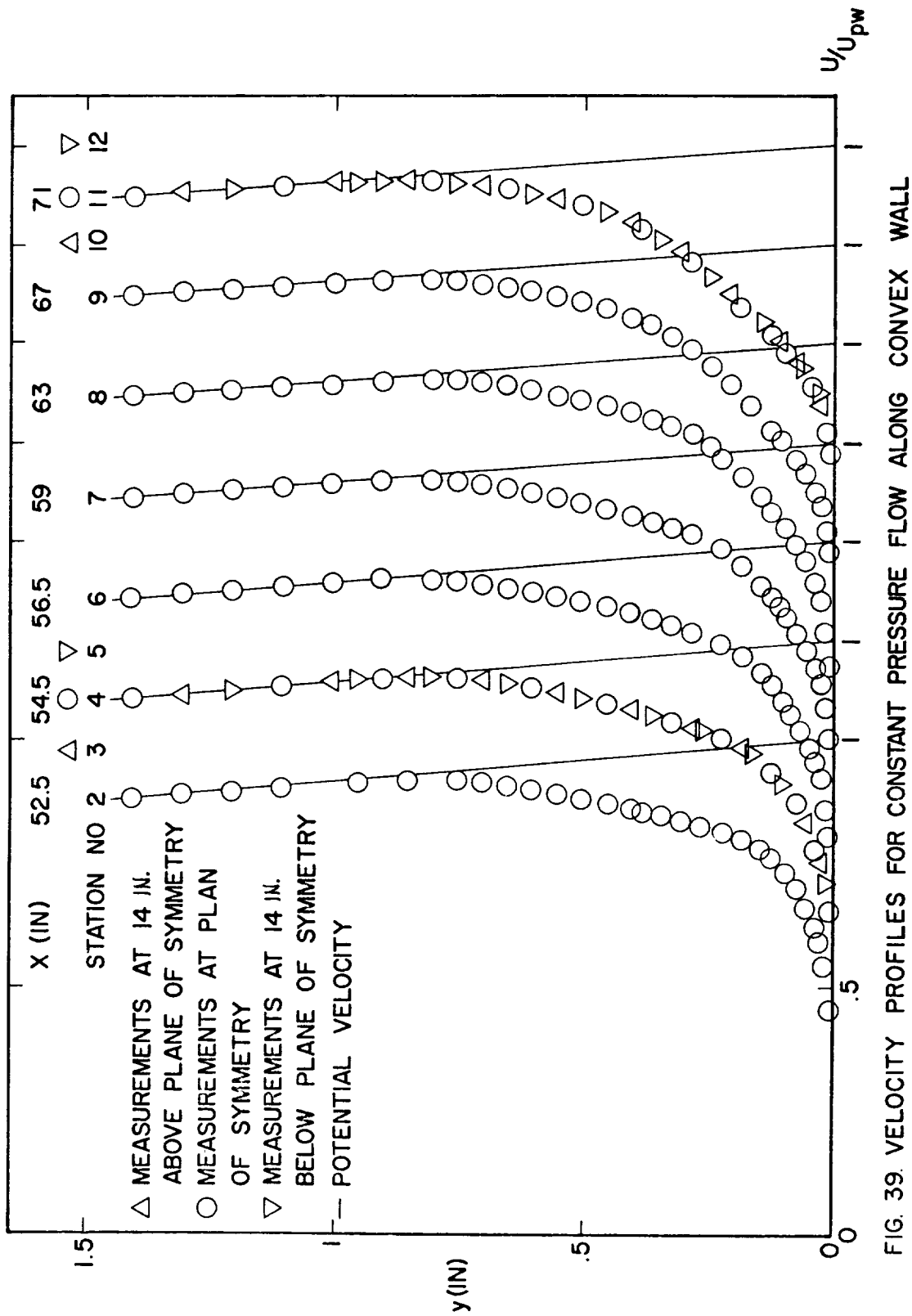


FIG. 39. VELOCITY PROFILES FOR CONSTANT PRESSURE FLOW ALONG CONVEX WALL

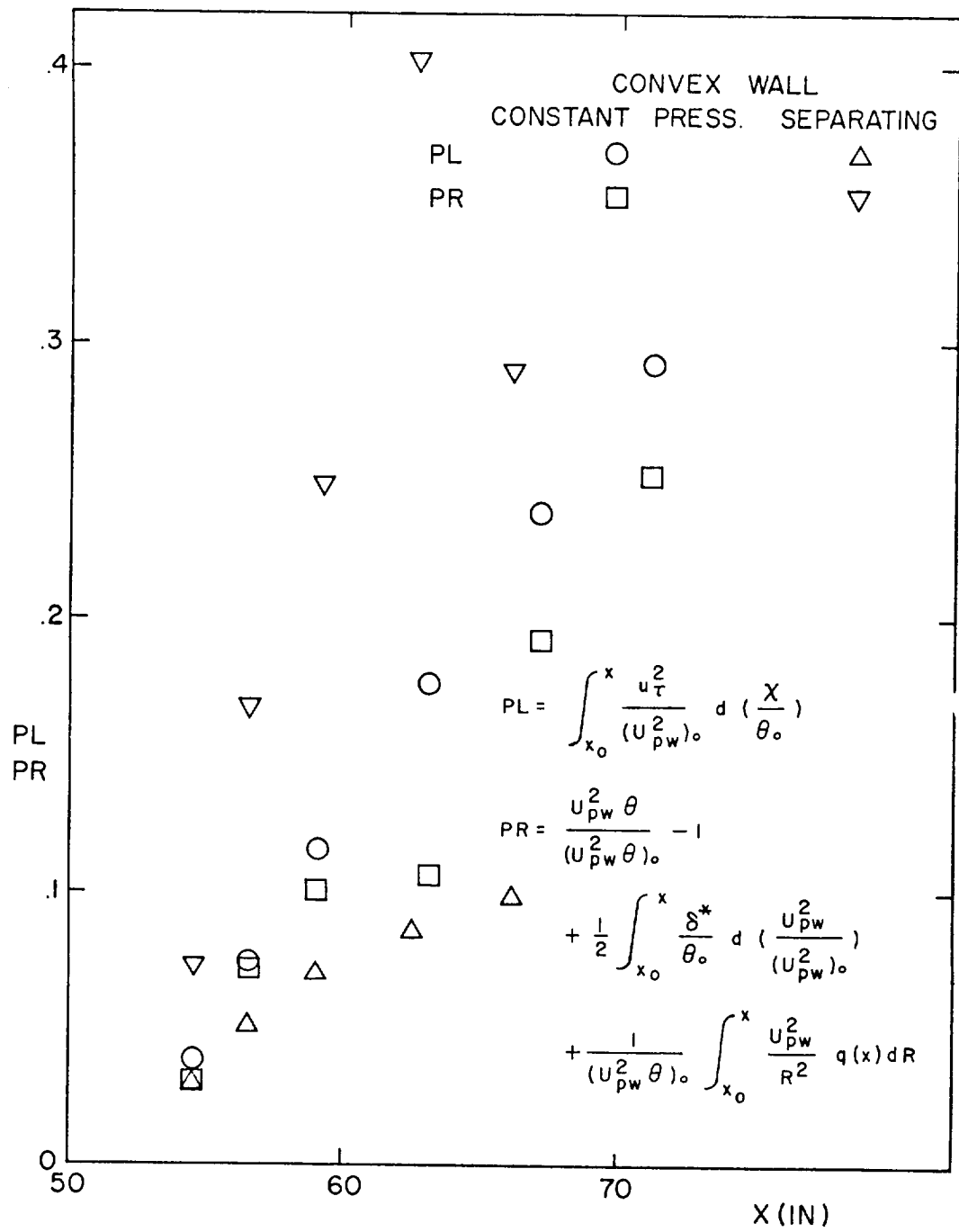


FIG. 40. MOMENTUM BALANCE FOR FLOW ALONG CONVEX SURFACES

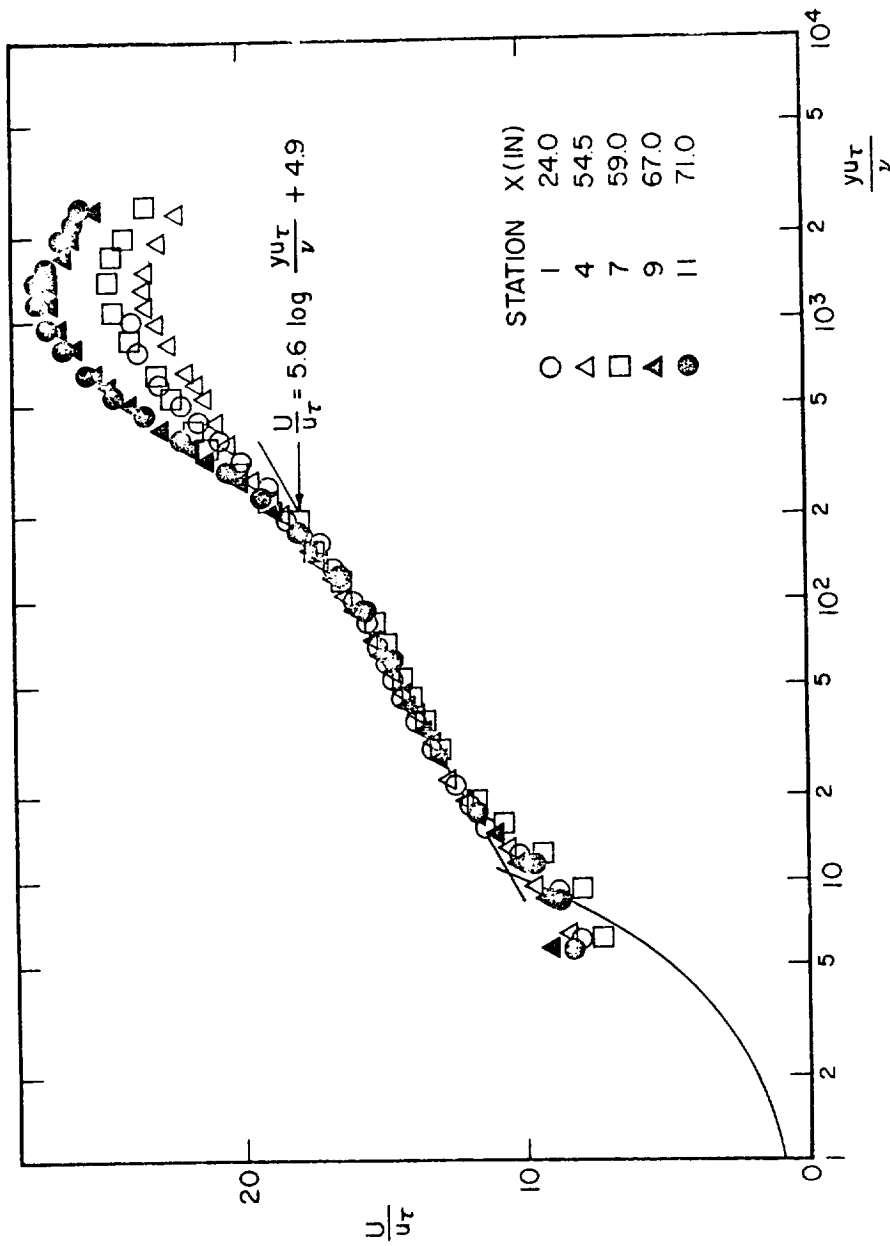


FIG 41. SEMI-LOG PLOT OF VELOCITY PROFILES TO SHOW THE LAW OF THE WALL REGION FOR CONSTANT PRESSURE FLOW ALONG CONVEX WALL.

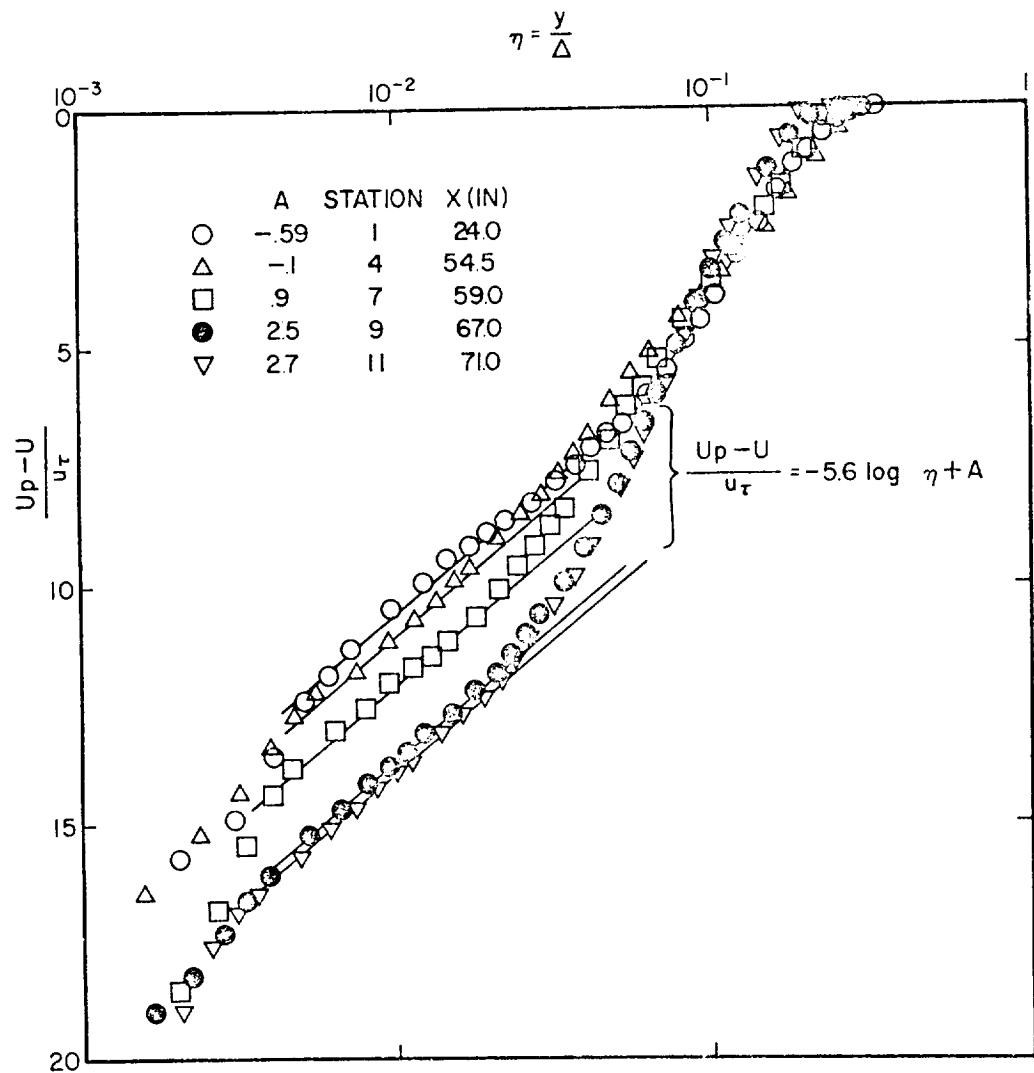


FIG. 42 SEMI-LOG PLOT OF VELOCITY DEFECTS TO SHOW DEPENDENCE OF A ON CURVATURE FOR CONSTANT PRESSURE FLOW ALONG CONVEX WALL.

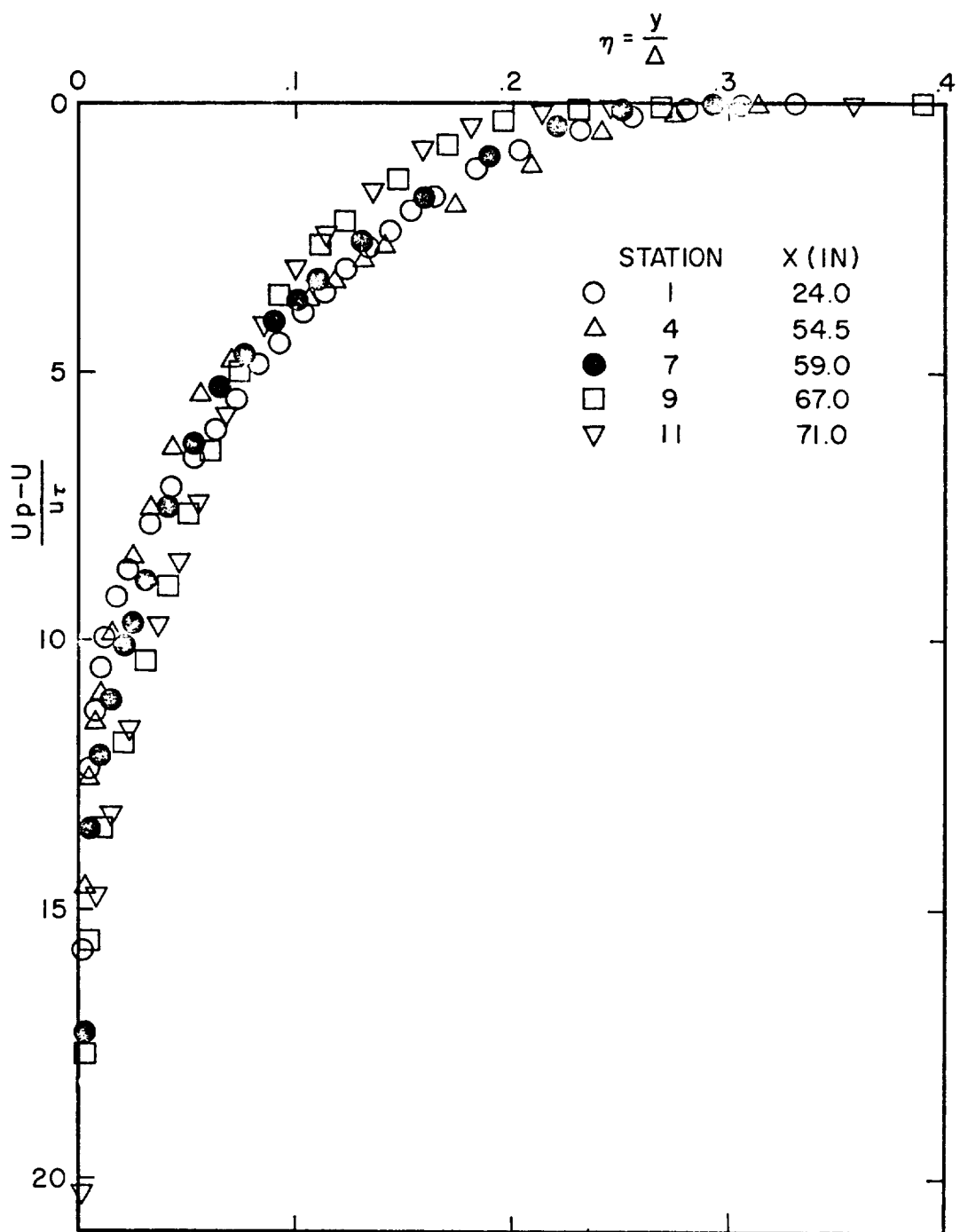


FIG. 43 DEFECT PLOT OF VELOCITY PROFILES FOR CONSTANT PRESSURE FLOW ALONG CONVEX WALL

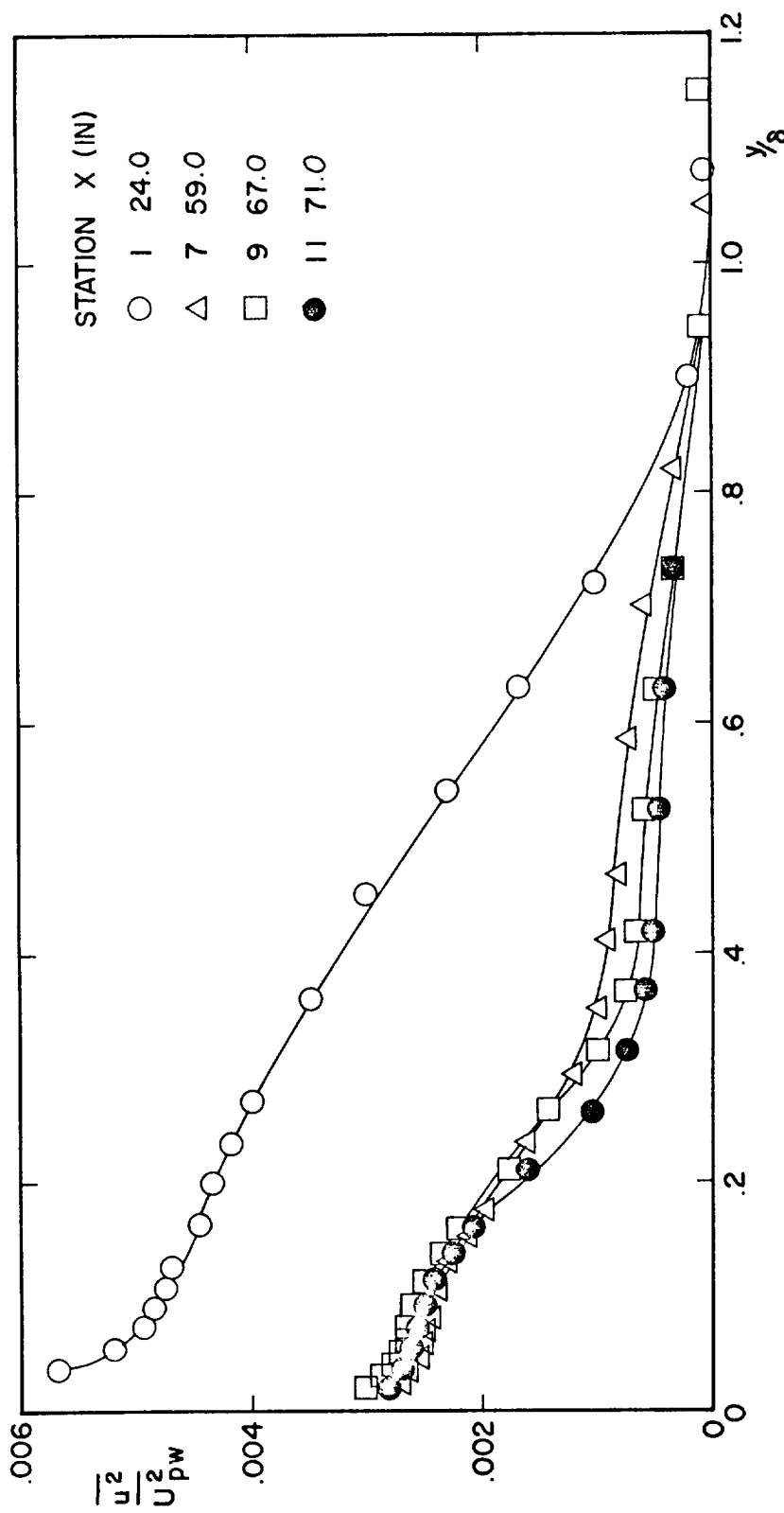


FIG. 44
DISTRIBUTION OF $\sqrt{\bar{u}^2/u_{pw}^2}$ FOR CONSTANT PRESSURE FLOW ALONG CONVEX WALL

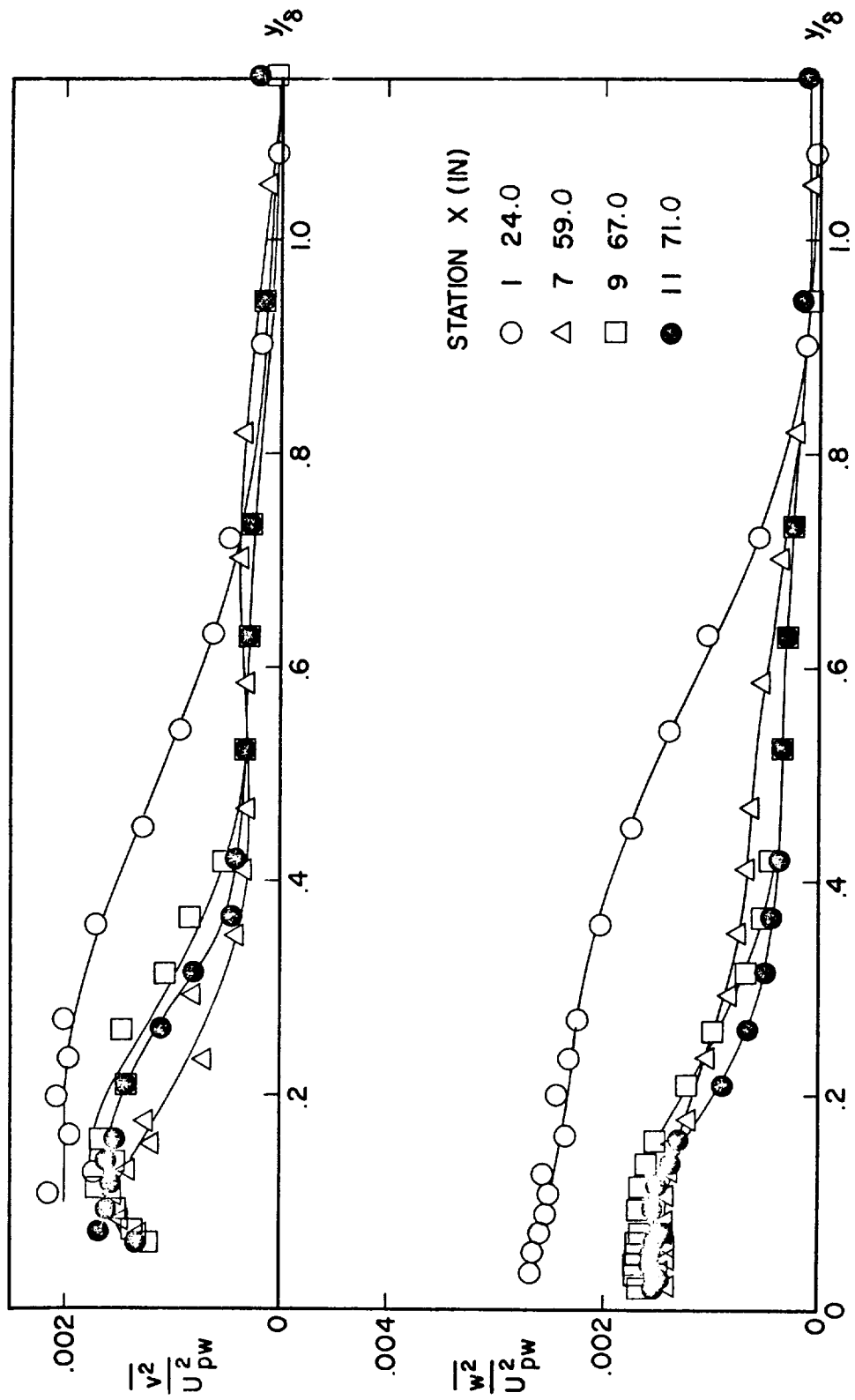


FIG. 45 DISTRIBUTION OF \bar{v}^2/U_{pw}^2 AND \bar{w}^2/U_{pw}^2 FOR CONSTANT PRESSURE FLOW ALONG CONVEX WALL.

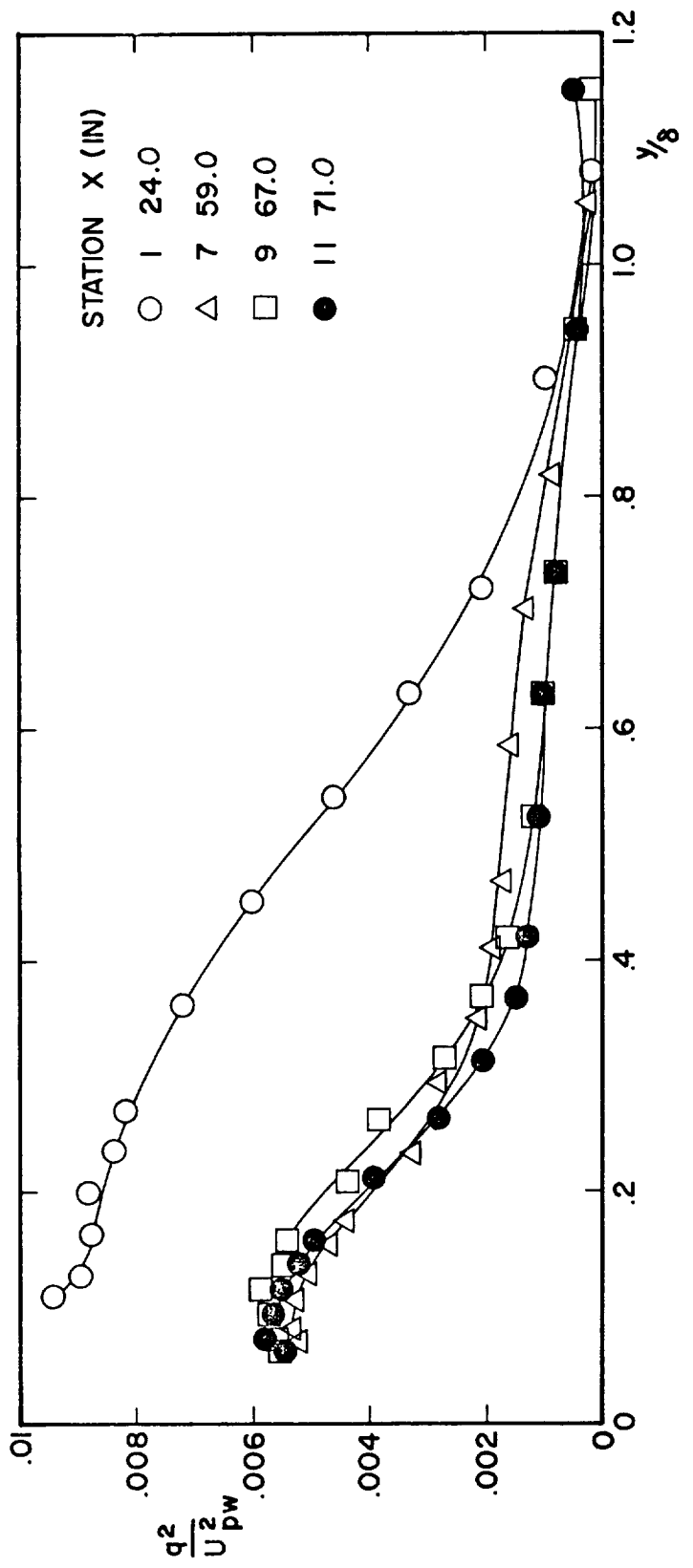


FIG. 46 DISTRIBUTION OF TURBULENCE ENERGY FOR CONSTANT PRESSURE FLOW ALONG CONVEX WALL.

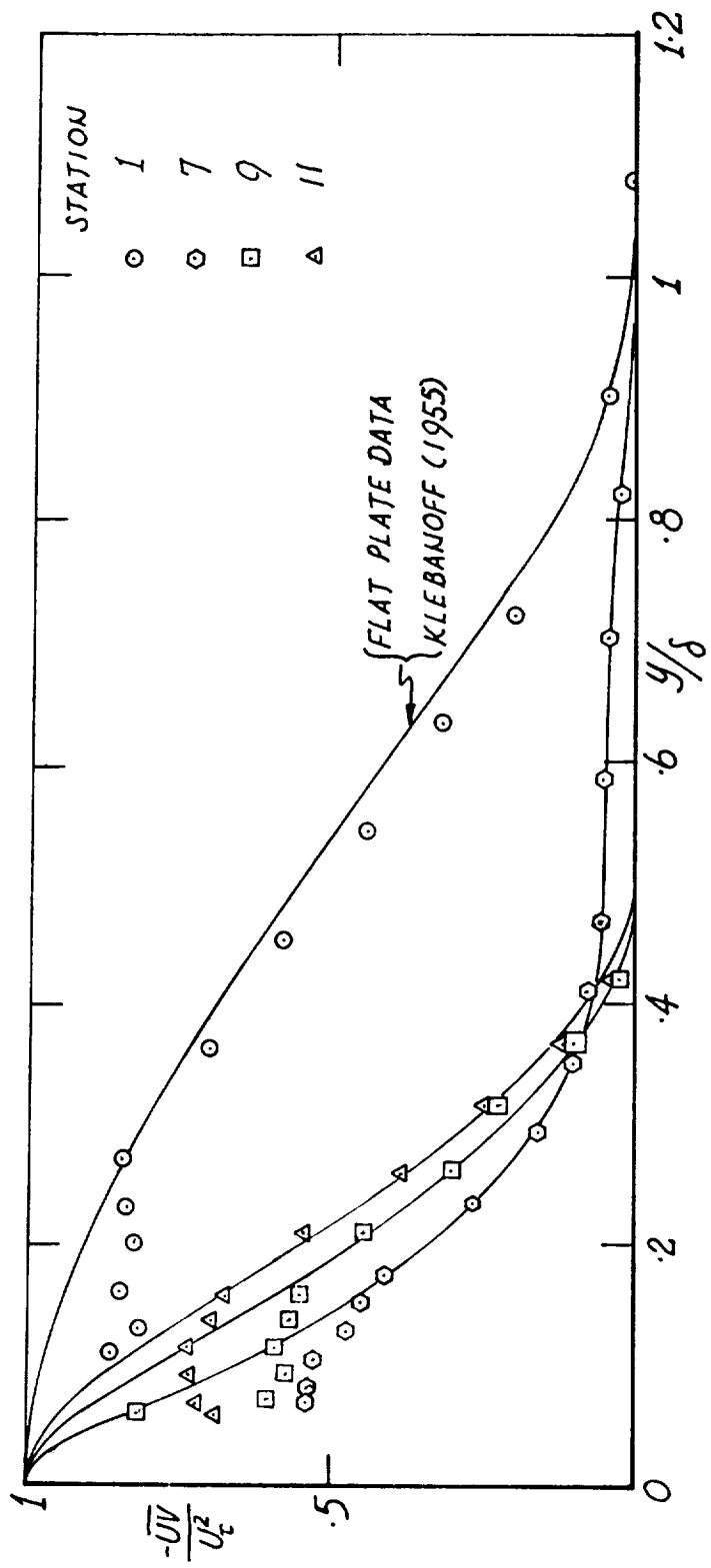


FIGURE 47 DISTRIBUTION OF SHEARING STRESS FOR CONSTANT PRESSURE FLOW ALONG CONVEX WALL

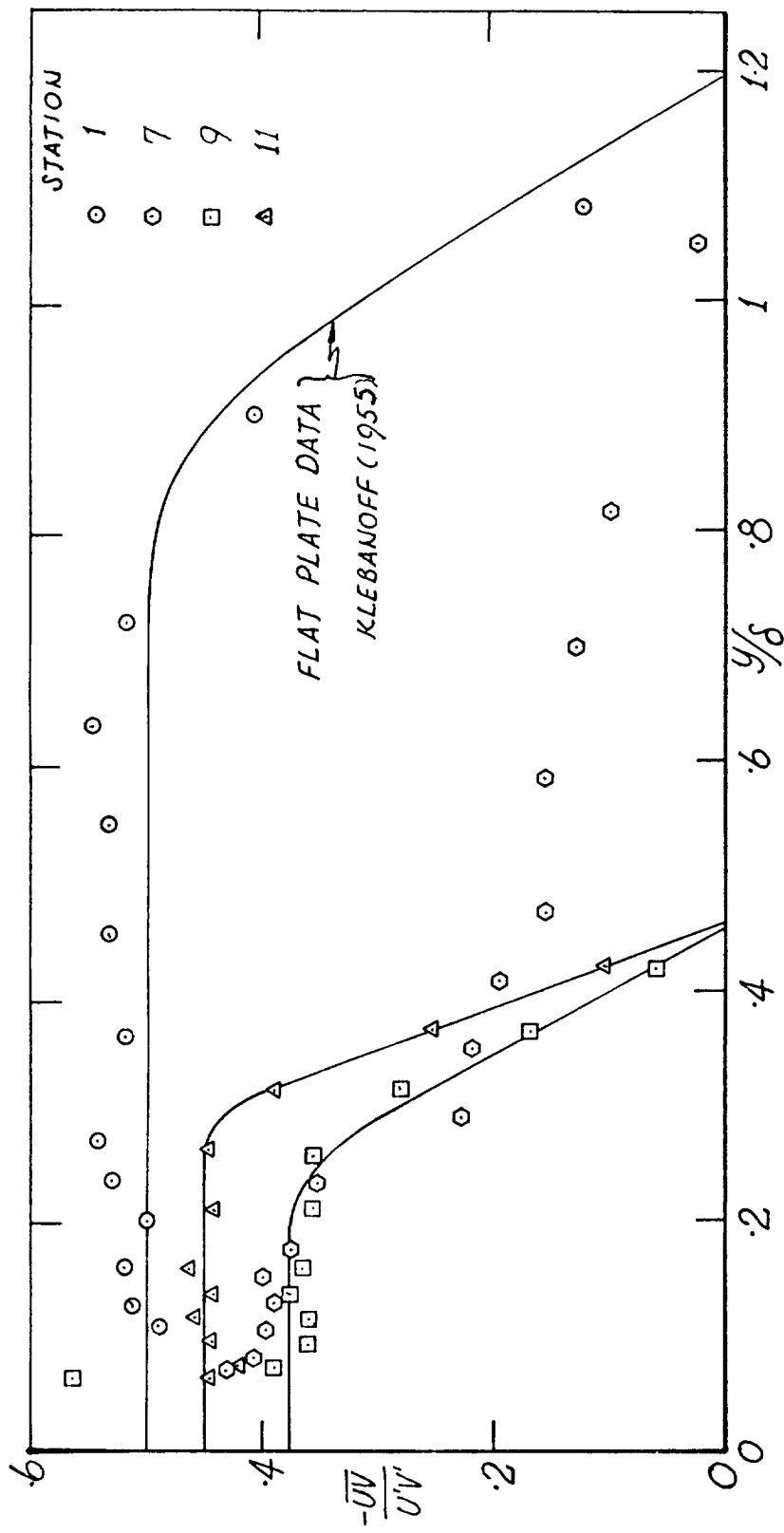


FIGURE 48 DISTRIBUTION OF SHEAR CORRELATION COEFFICIENT FOR CONSTANT PRESSURE FLOW ALONG CONVEX WALL

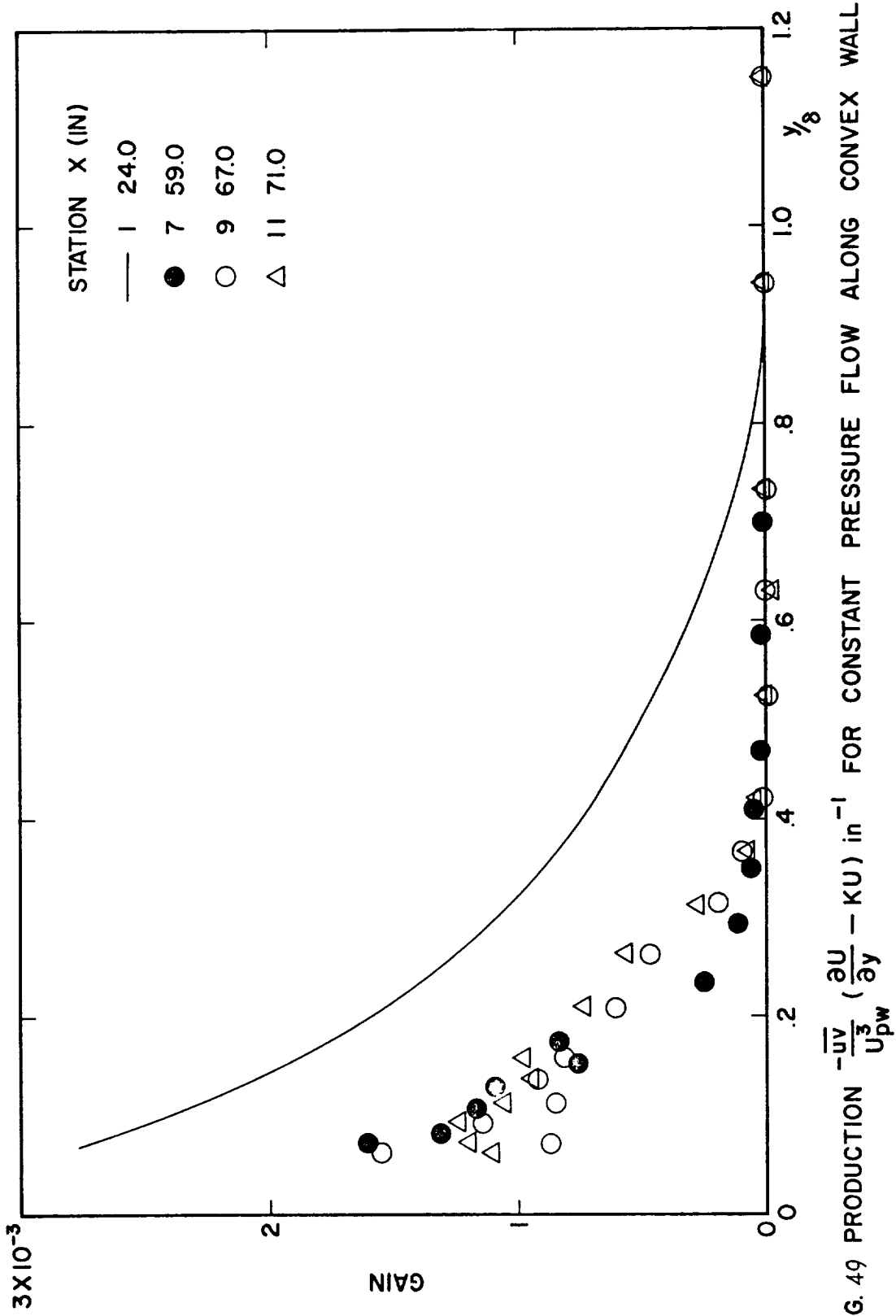


FIG. 49 PRODUCTION $-\frac{\bar{u}v}{U_{pw}^3} \left(\frac{\partial U}{\partial y} - KU \right) \text{ in}^{-1}$ FOR CONSTANT PRESSURE FLOW ALONG CONVEX WALL

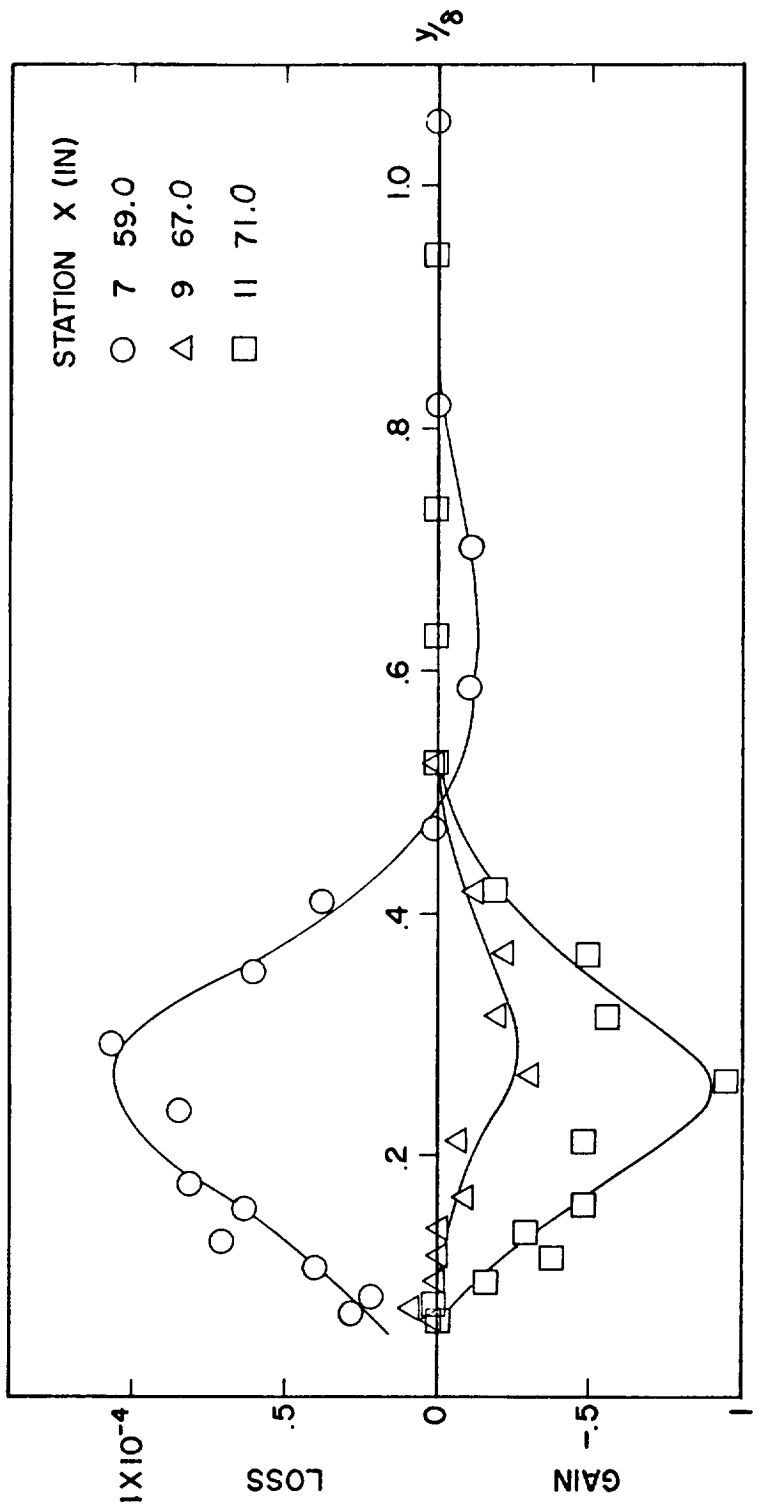


FIG. 50 ADVECTION $\frac{1}{U^3} \left(U \frac{\partial q^2/2}{\partial x} + V \frac{\partial q^2/2}{\partial y} \right) \text{ in}^{-1}$ FOR CONSTANT PRESSURE FLOW ALONG CONVEX WALL.

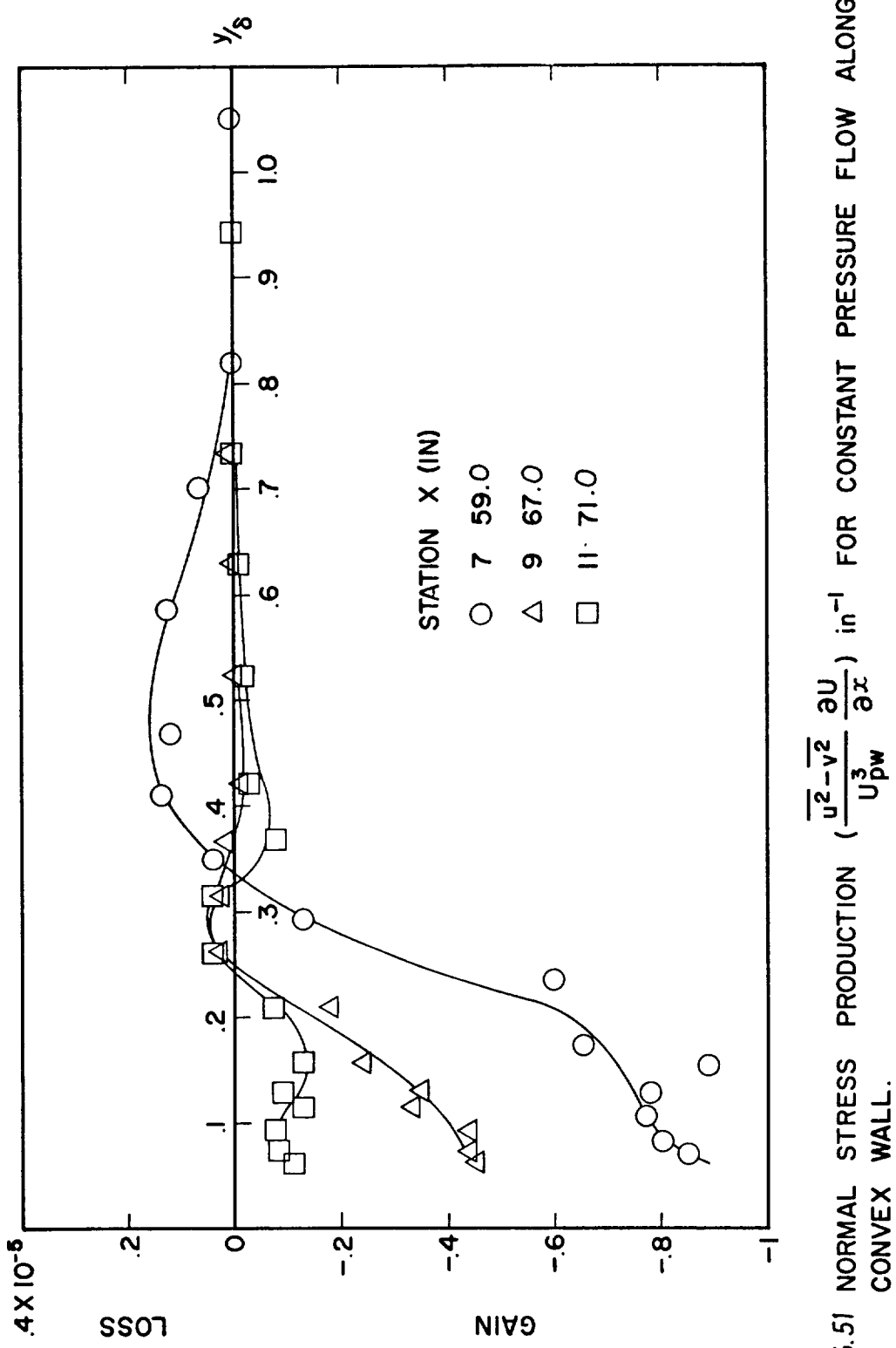


FIG.51 NORMAL STRESS PRODUCTION $(\frac{\bar{u}^2 - \bar{v}^2}{U_{pw}^3} \frac{\partial U}{\partial x}) \text{ in}^{-1}$ FOR CONSTANT PRESSURE FLOW ALONG CONVEX WALL.

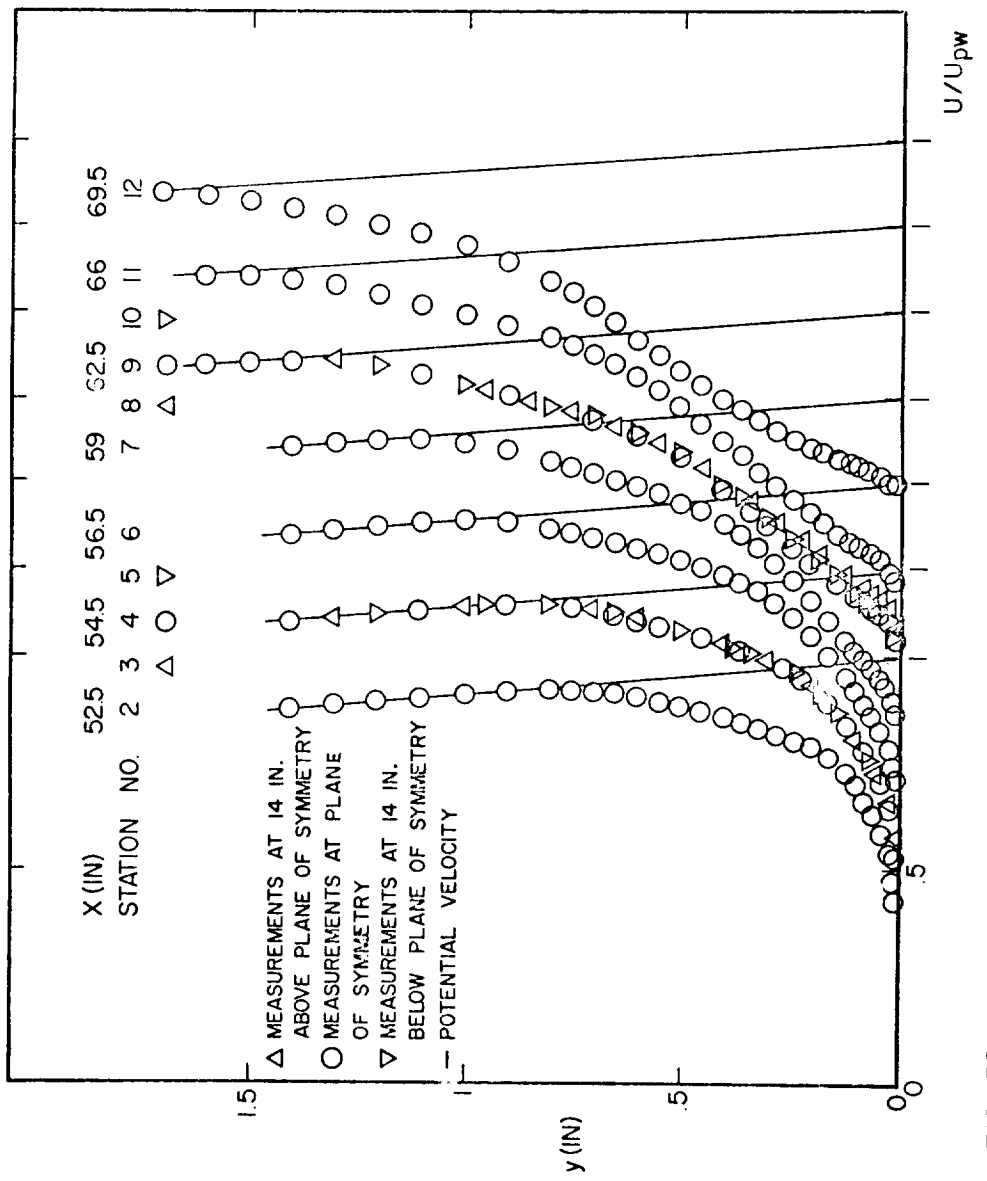


FIG. 52. VELOCITY PROFILES FOR SEPARATING FLOW ALONG CONVEX WALL.

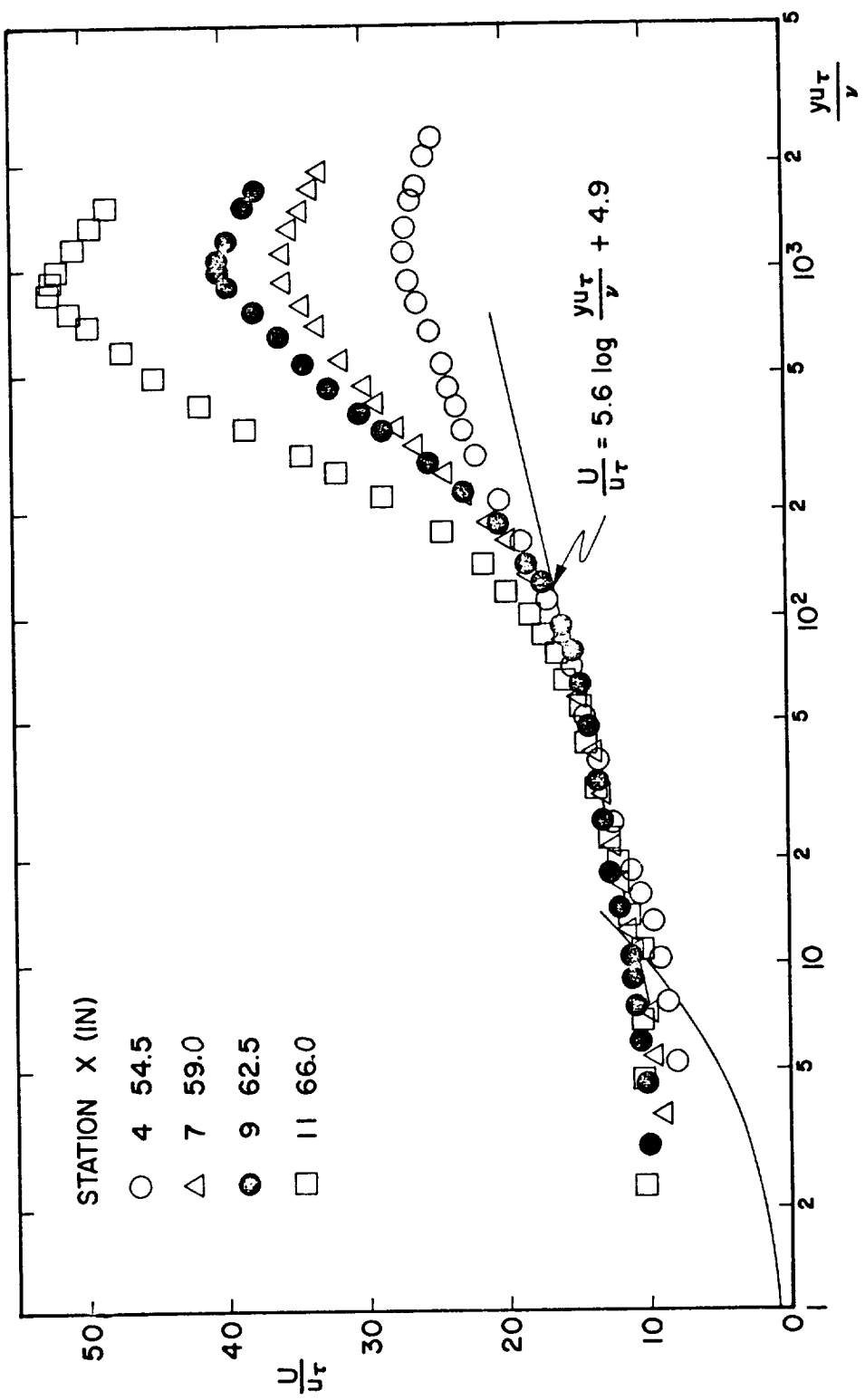


FIG. 53. SEMI-LOG PLOT OF VELOCITY PROFILES TO SHOW THE LAW OF THE WALL REGION FOR SEPARATING FLOW ALONG CONVEX WALL

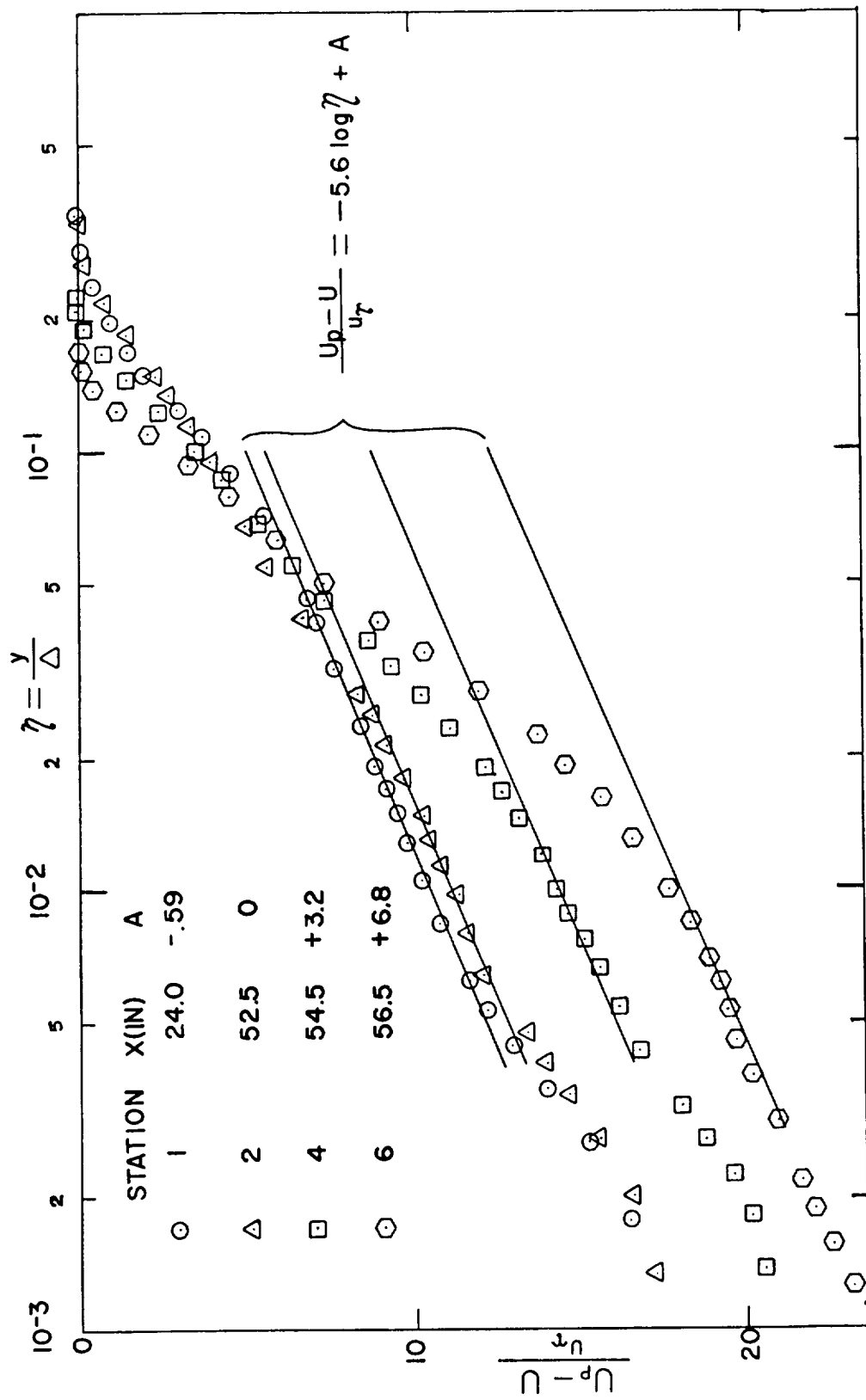


FIG. 54 SEMI-LOG PLOT OF VELOCITY PROFILES TO SHOW DEPENDENCE OF A ON CURVATURE FOR SEPARATING FLOW ALONG CONVEX WALL

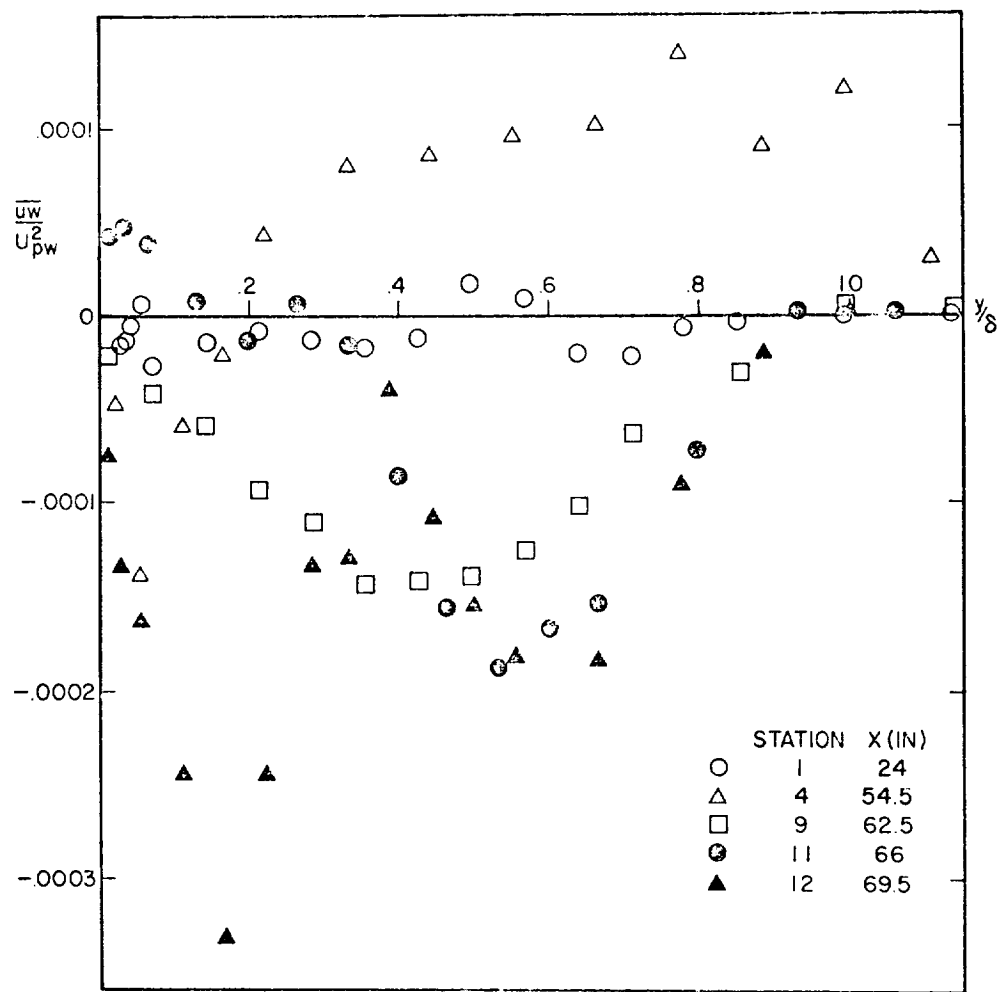
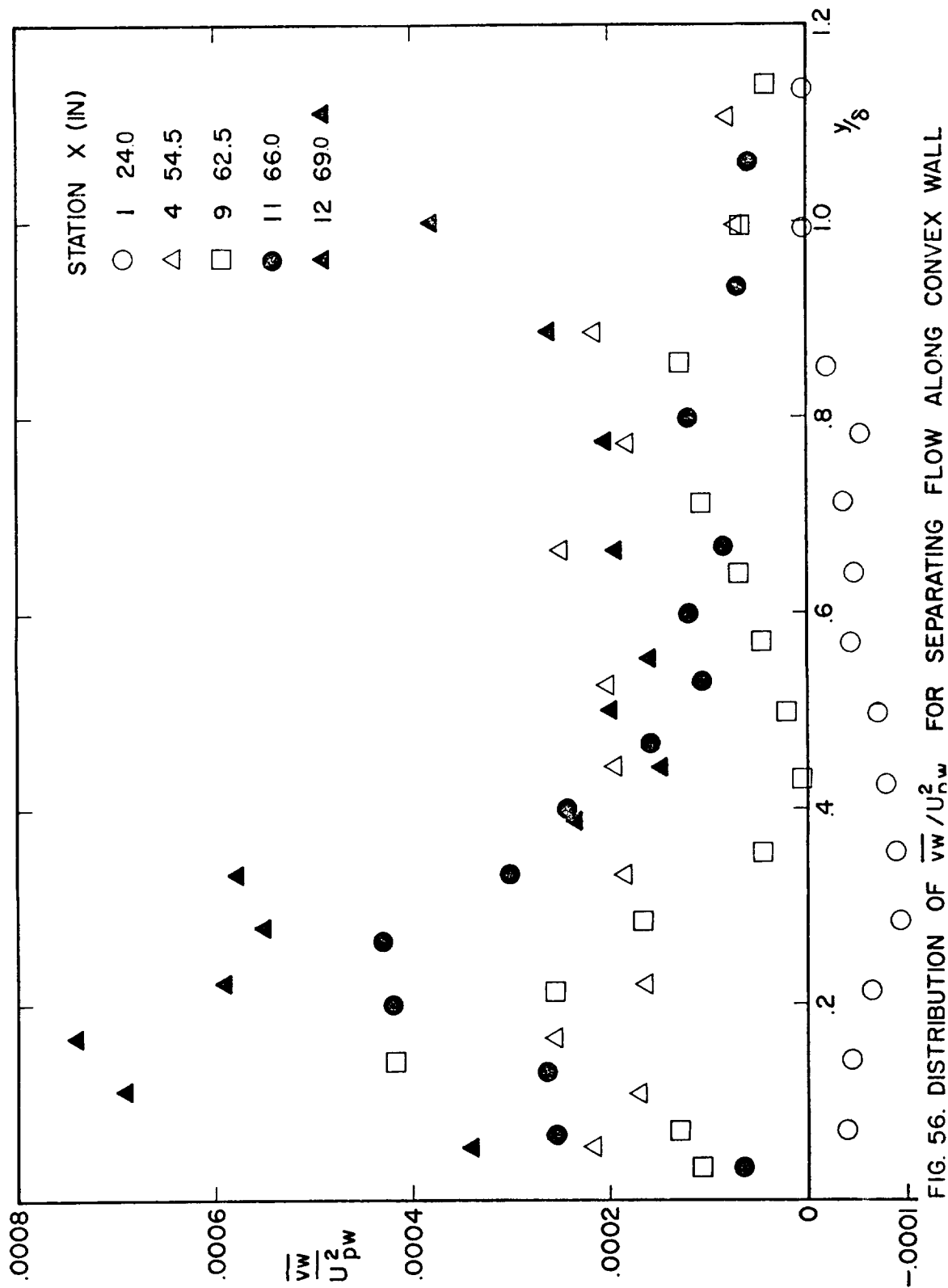


FIG. 55. DISTRIBUTION OF $\bar{u}w/U_{pw}^2$ FOR SEPARATING FLOW ALONG CONVEX WALL.



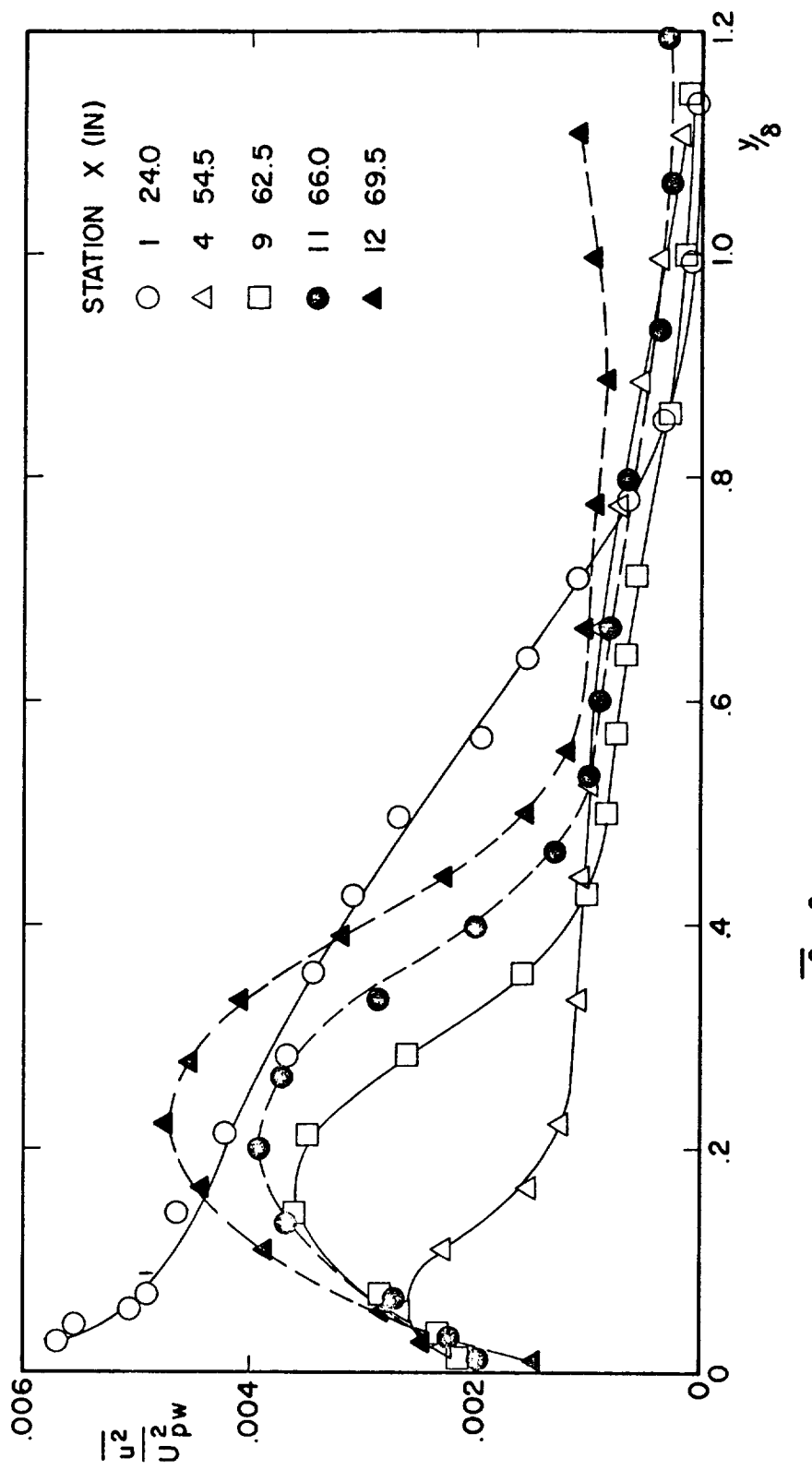


FIG. 57. DISTRIBUTION OF $\overline{u^2}/U_{pw}^2$ FOR SEPARATING FLOW ALONG CONVEX WALL

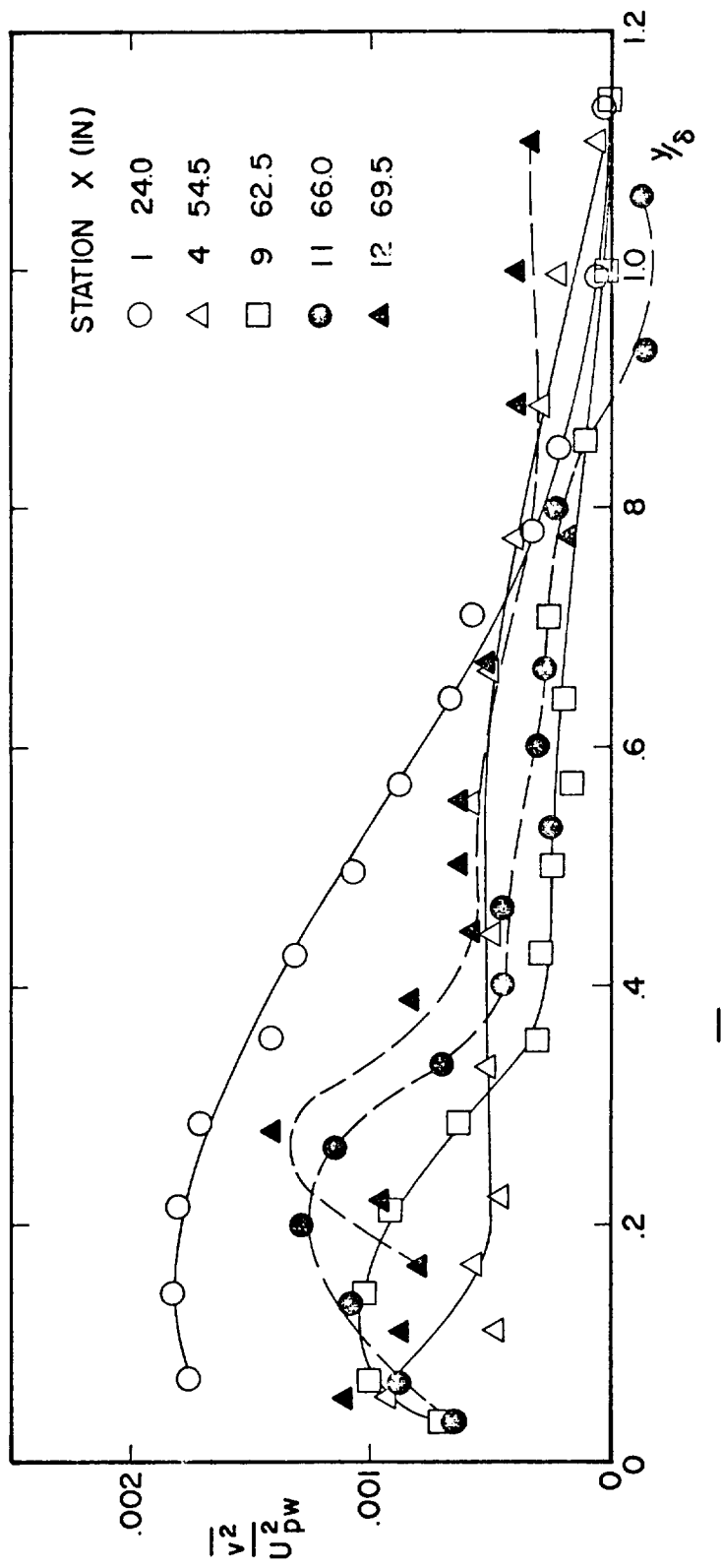


FIG. 58. DISTRIBUTION OF \bar{v}^2/U_{pw}^2 FOR SEPARATING FLOW ALONG CONVEX WALL

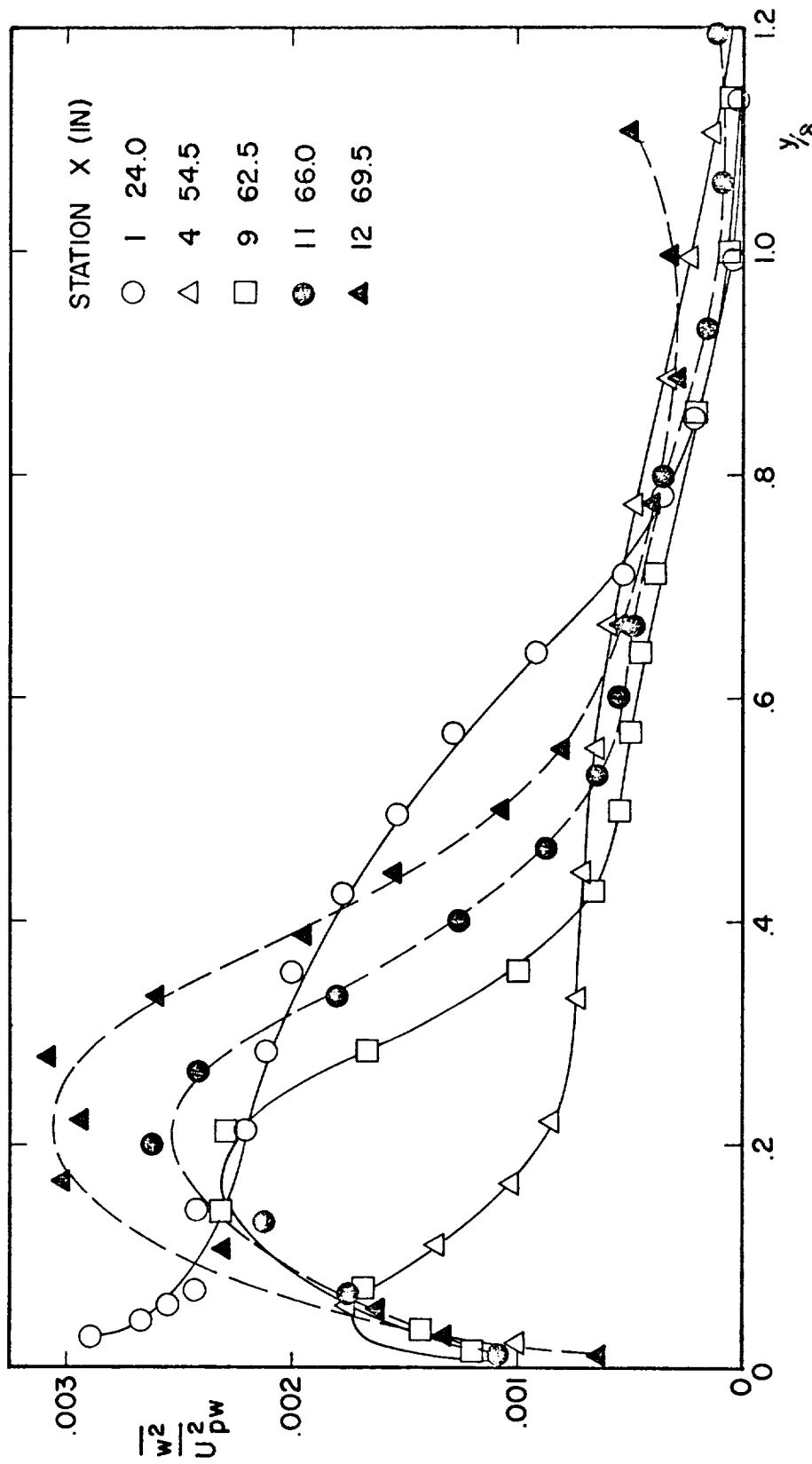


FIG. 59. DISTRIBUTION OF \bar{w}^2/U_{pw}^2 FOR SEPARATING FLOW ALONG CONVEX WALL

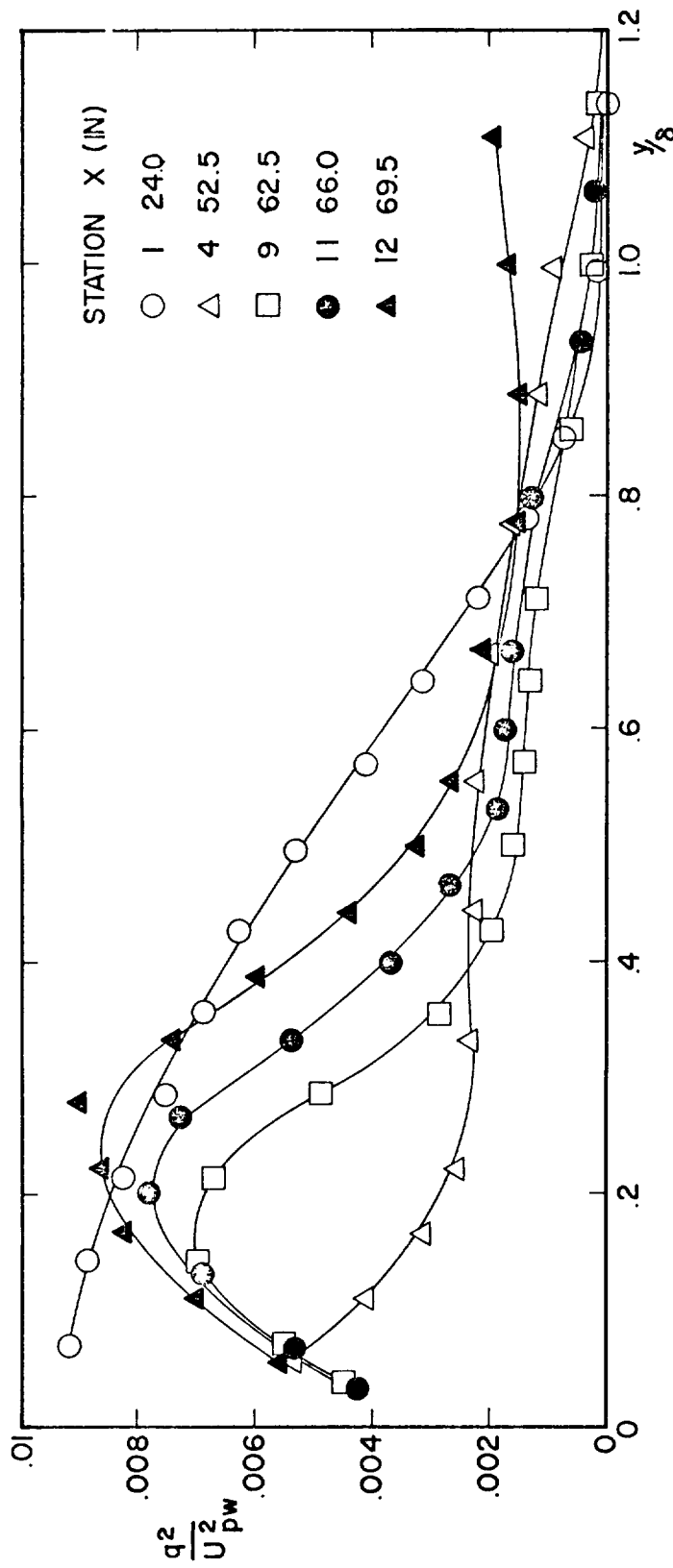


FIG. 60. TURBULENCE ENERGY DISTRIBUTION FOR SEPARATING FLOW ALONG CONVEX WALL.

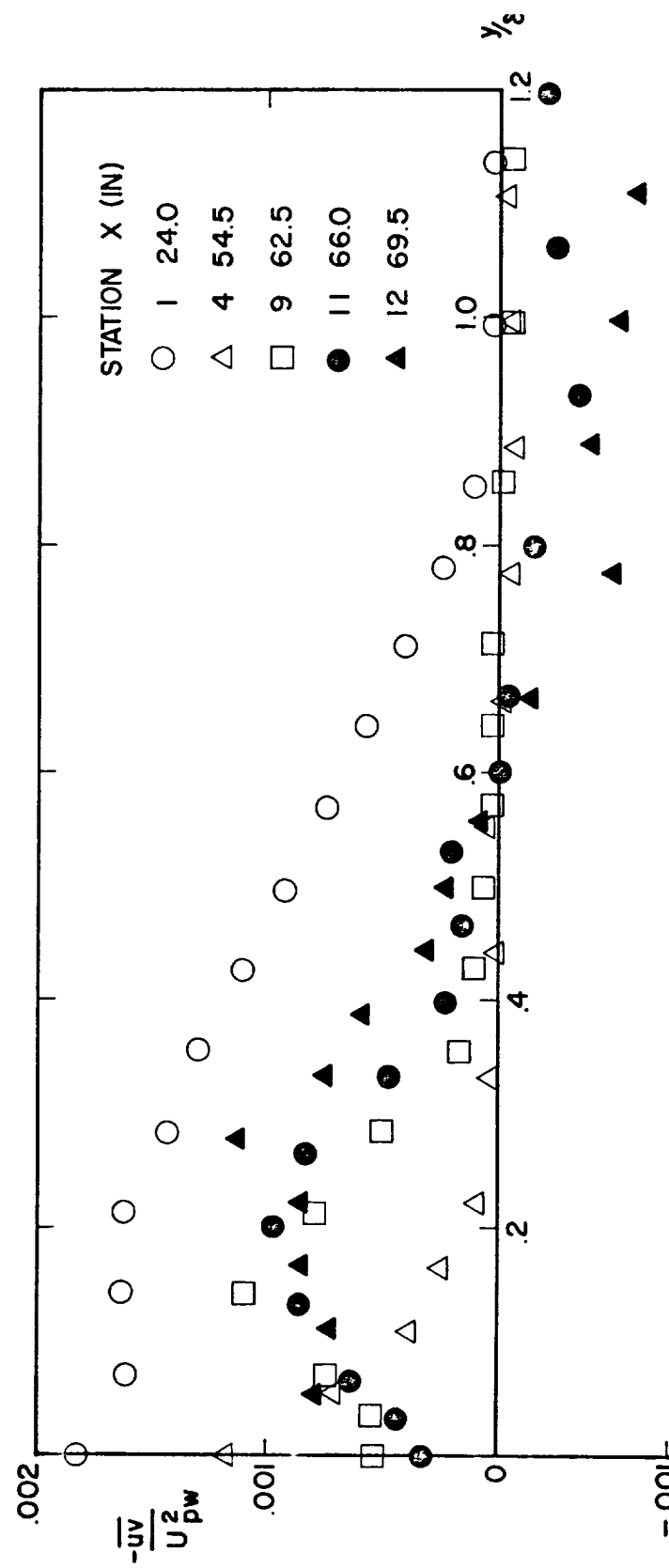


FIG. 6
SHEAR STRESS DISTRIBUTION FOR
SEPARATING FLOW ALONG CONVEX WALL

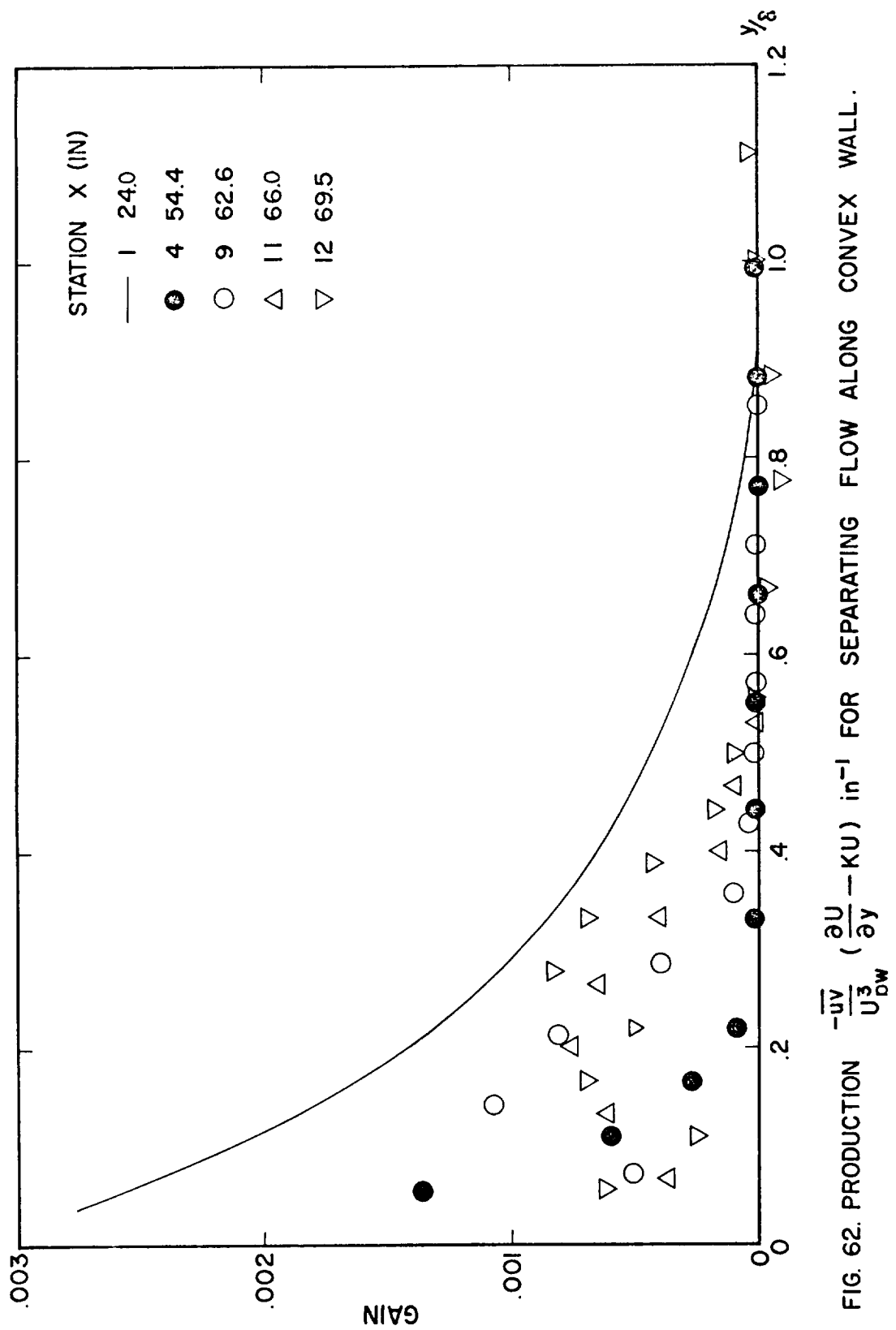


FIG. 62. PRODUCTION $-\frac{\bar{u}\bar{v}}{U_{DW}^3} \left(\frac{\partial U}{\partial y} - KU \right) \text{ in}^{-1}$ FOR SEPARATING FLOW ALONG CONVEX WALL.

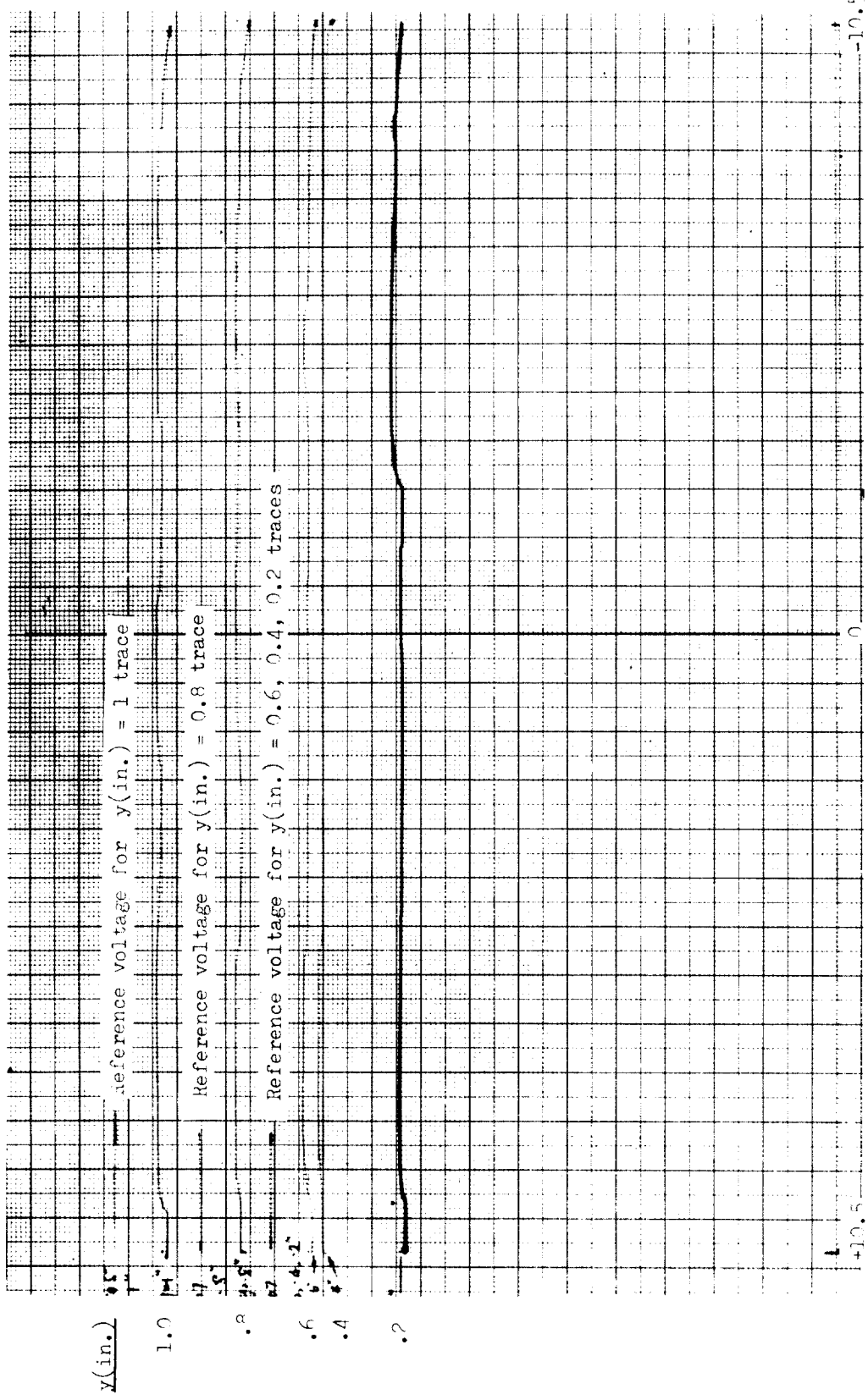


Figure 63. Hot-wire Z direction trace for fixed y at $x(\text{in.}) = 24.0$.

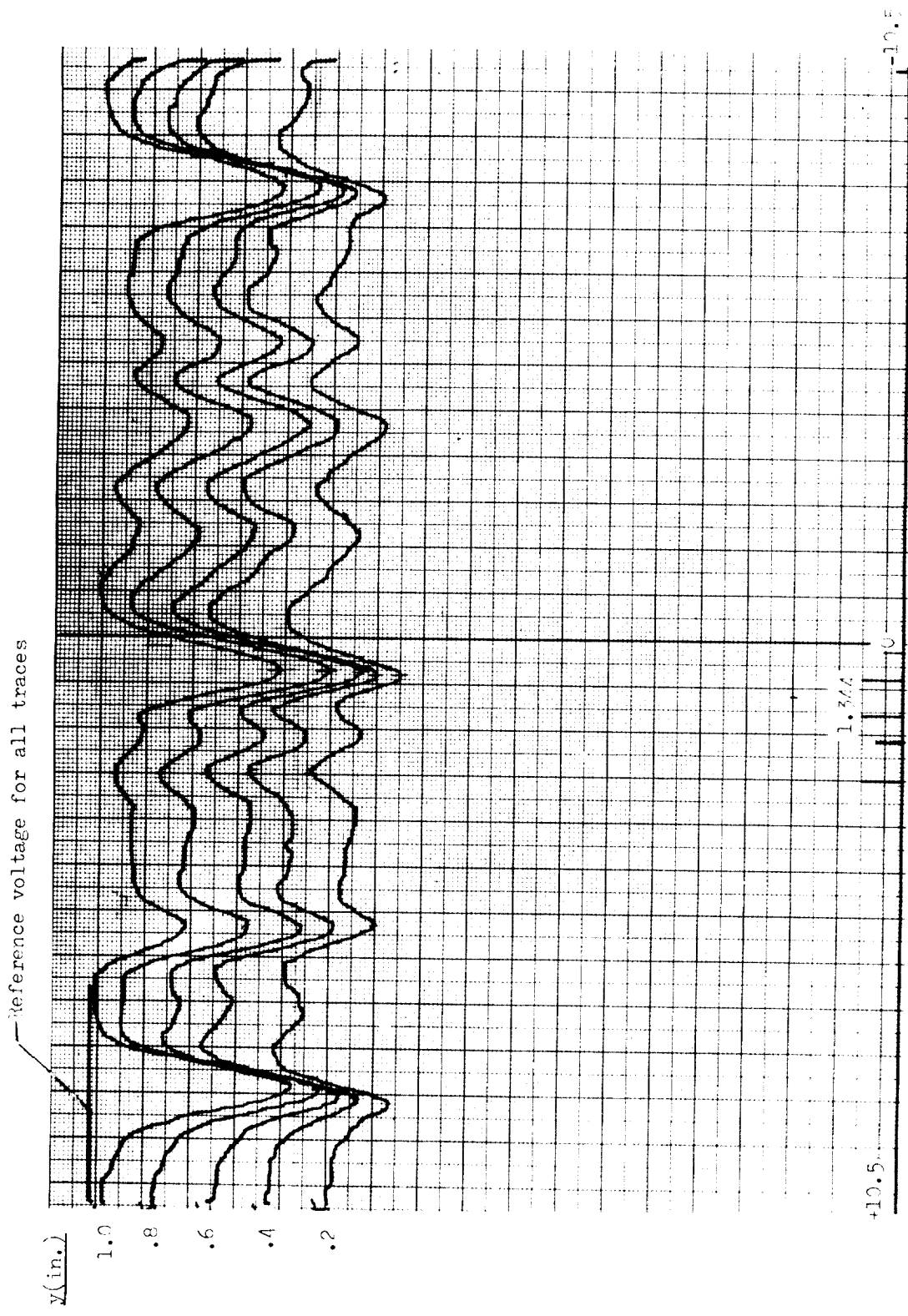
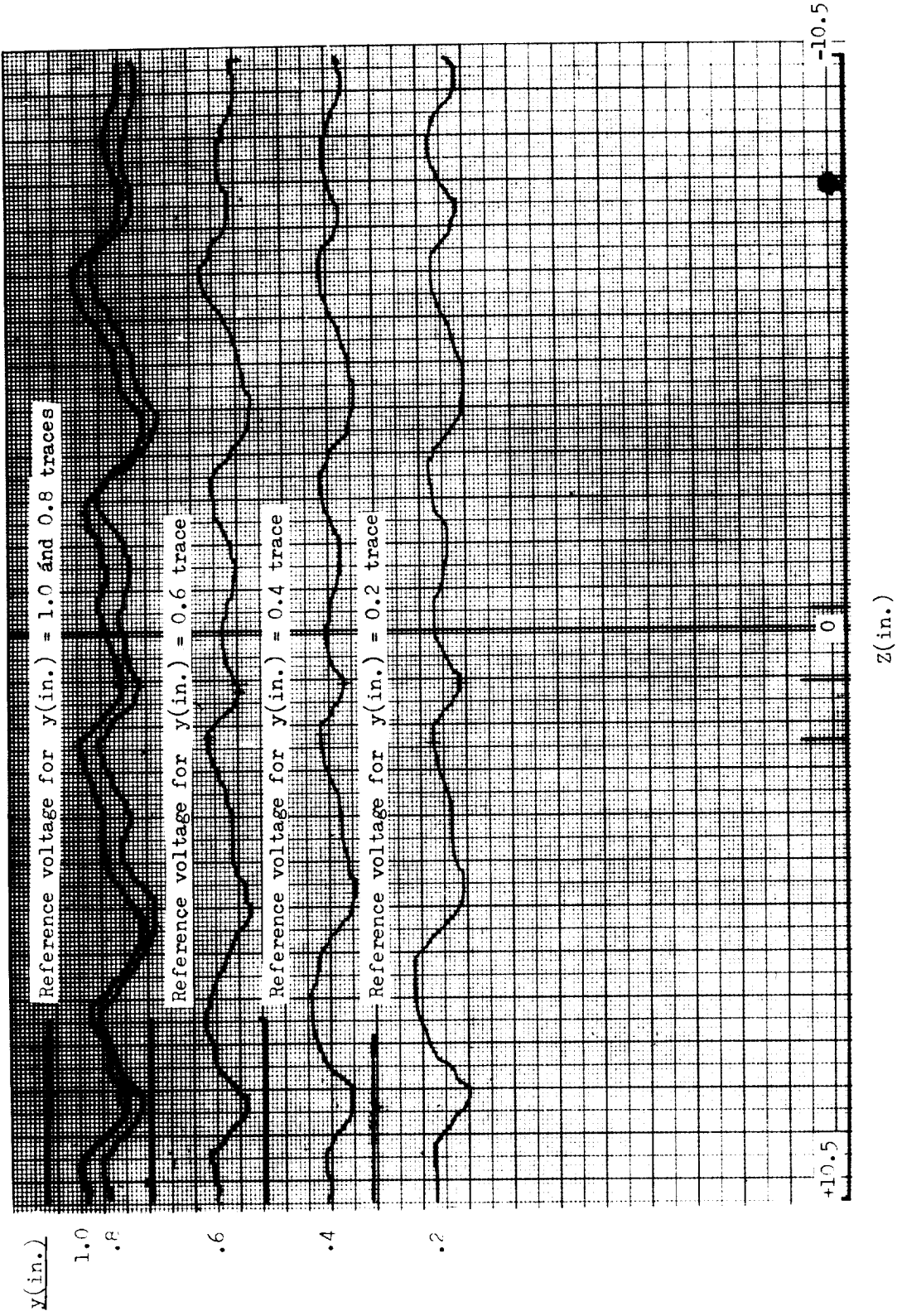


Figure 64. Hot-wire Z direction trace for fixed y at $y(5\text{in.}) = 76.5$.



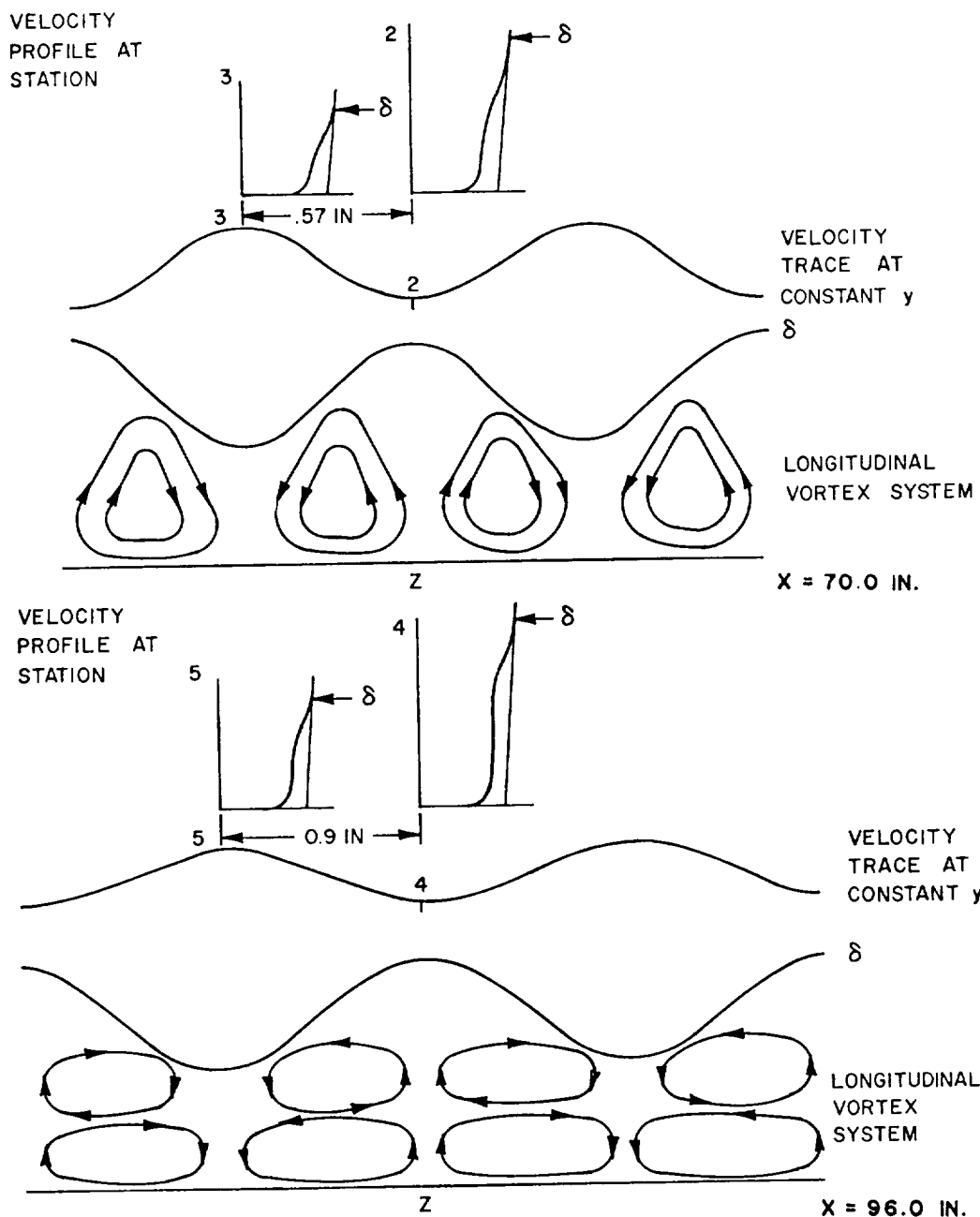


FIG. 66. ASSUMED VORTEX STRUCTURE INSIDE BOUNDARY LAYER
FOR CONSTANT PRESSURE FLOW ALONG CONCAVE WALL

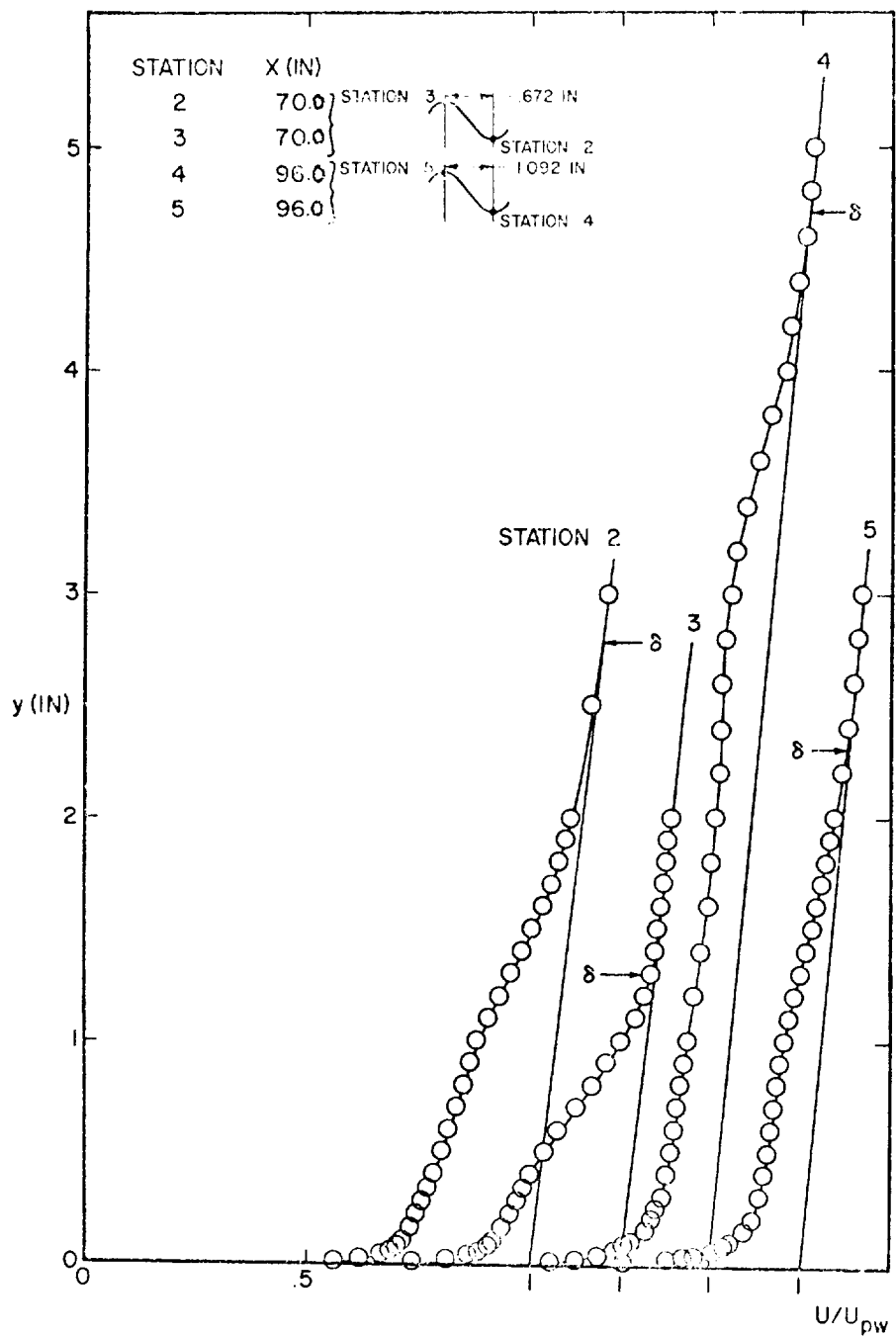


FIG. 6.7. VELOCITY PROFILES AT X (IN)=70 AND 96 FOR CONSTANT PRESSURE FLOW ALONG CONCAVE WALL. MEASUREMENTS WERE MADE AT BOTH THE CREST AND TROUGH OF THE WAVE.

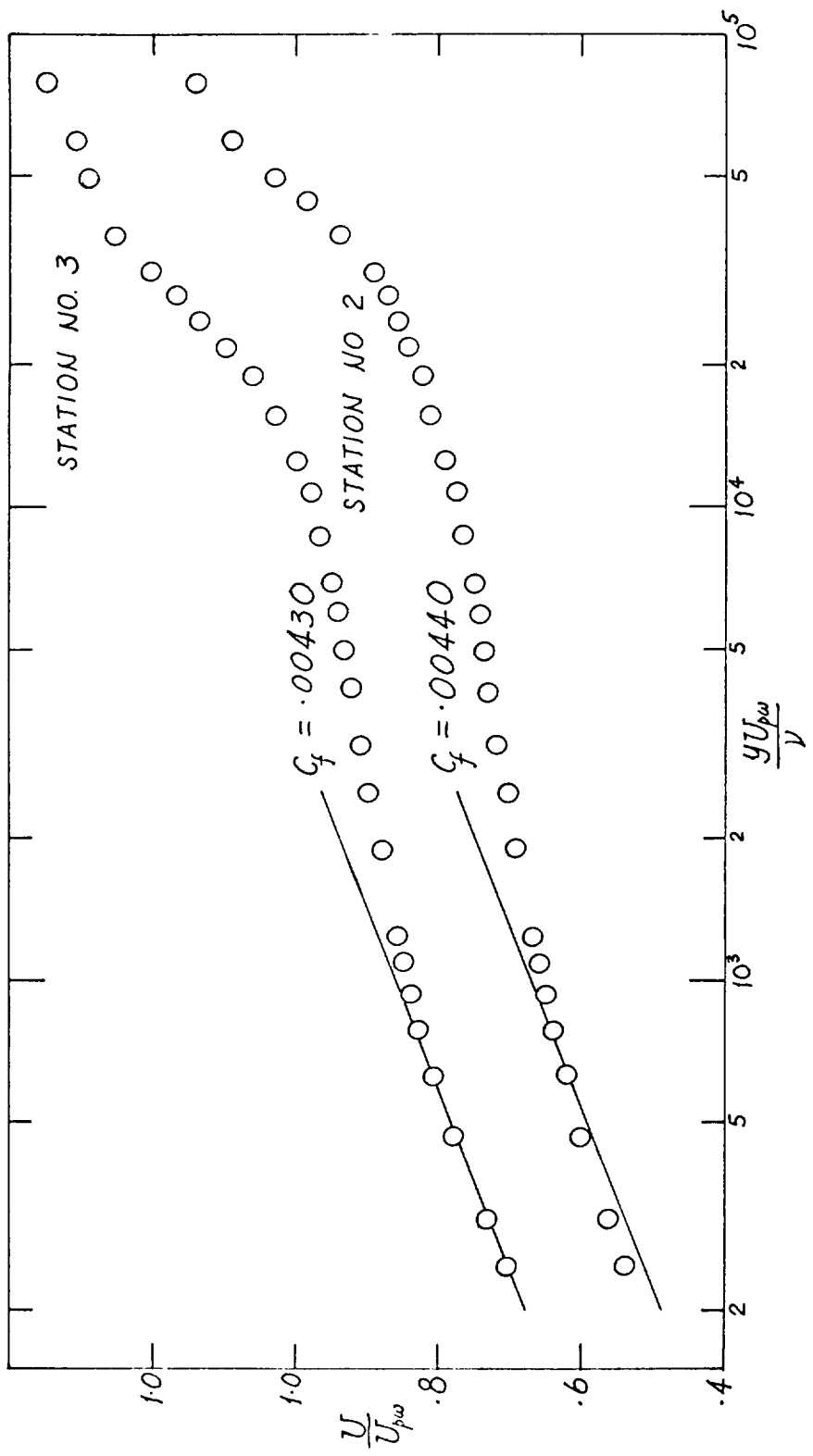


FIG. 68 CLAUSER PLOT OF VELOCITY PROFILES AT $X = 70.0$ IN.
FOR CONSTANT PRESSURE FLOW ALONG CONCAVE WALL

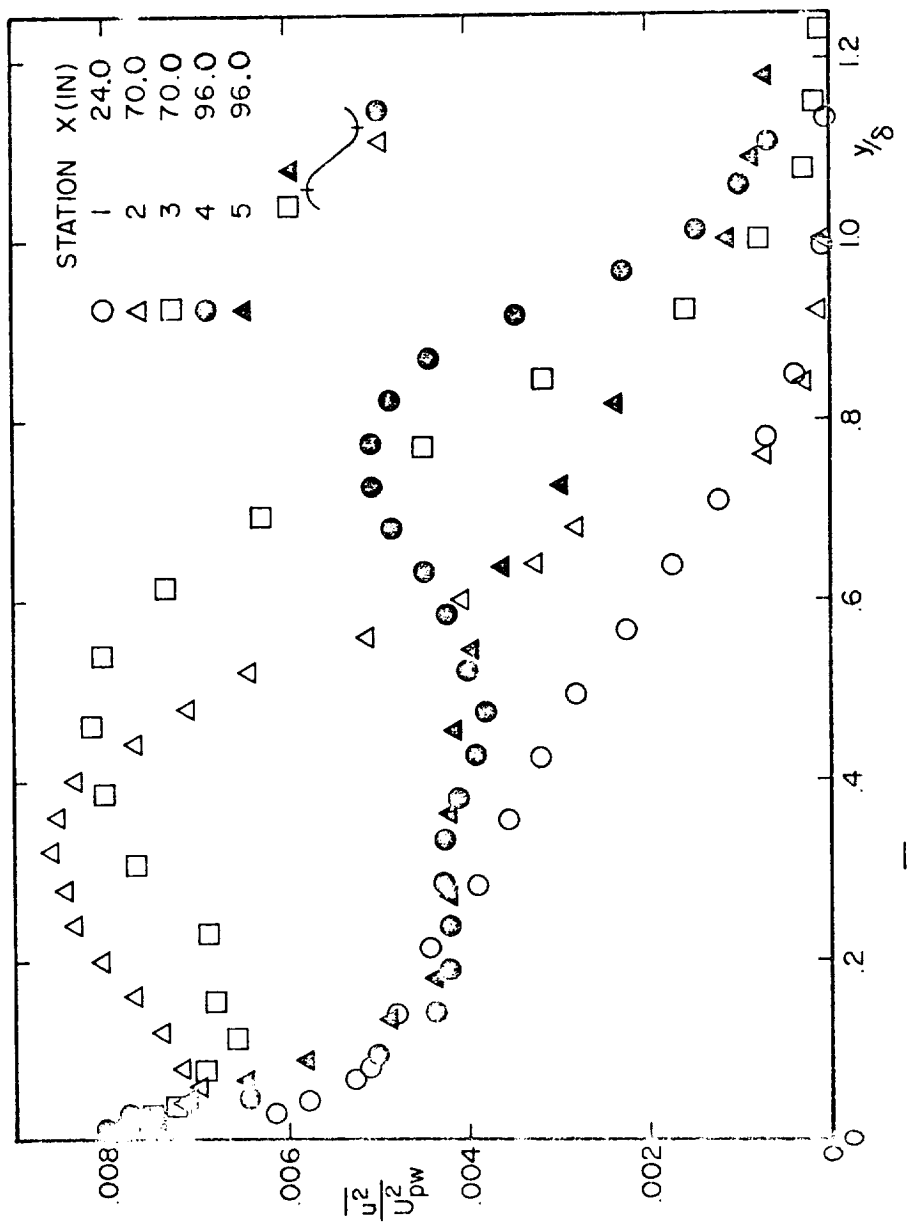


FIG. 69. DISTRIBUTION OF $\overline{u^2}/U_{pw}^2$ FOR CONSTANT PRESSURE FLOW ALONG CONCAVE WALL. MEASUREMENTS WERE TAKEN AT BOTH THE CREST AND TROUGH OF THE WAVE.

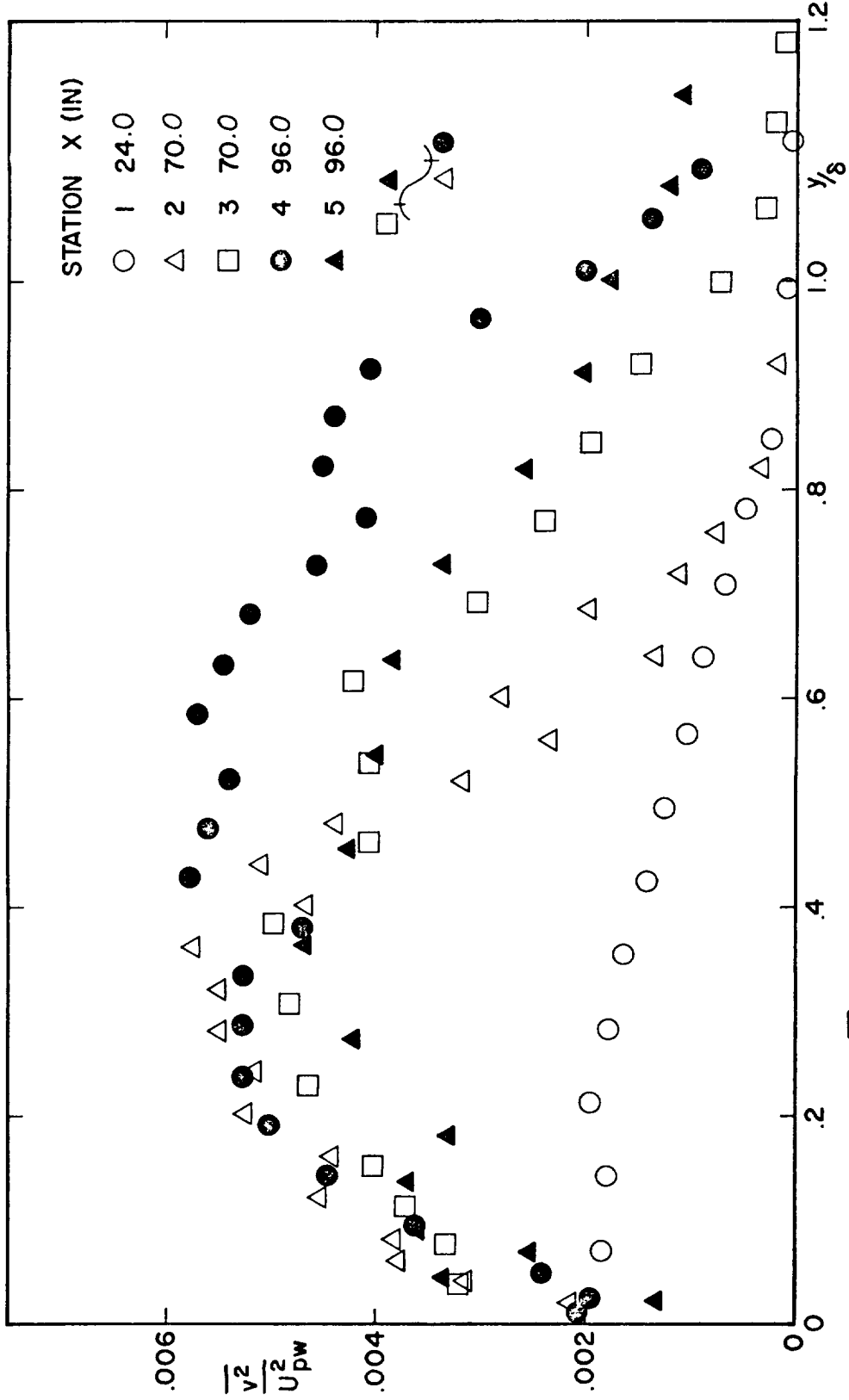


FIG. 70. DISTRIBUTION OF $\frac{v^2}{U_p^2}$ FOR CONSTANT PRESSURE FLOW ALONG CONCAVE WALL.
MEASUREMENTS WERE MADE AT BOTH THE CREST AND TROUGH OF THE WAVE.

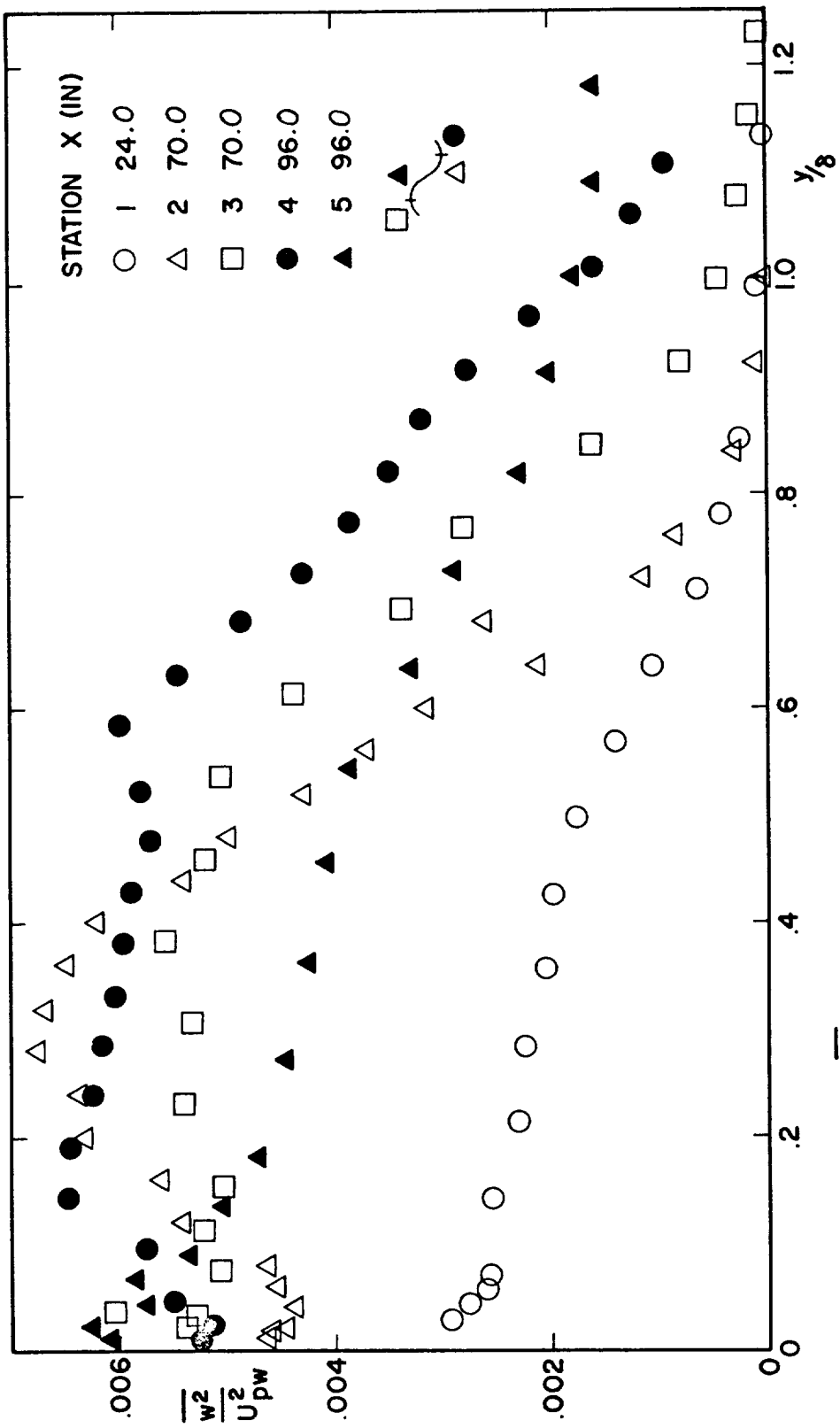


FIG. 71. DISTRIBUTION OF $\overline{w^2}/U_{pw}^2$ FOR CONSTANT PRESSURE FLOW ALONG CONCAVE WALL. MEASUREMENTS WERE MADE AT BOTH THE CREST AND TROUGH OF THE WAVE.

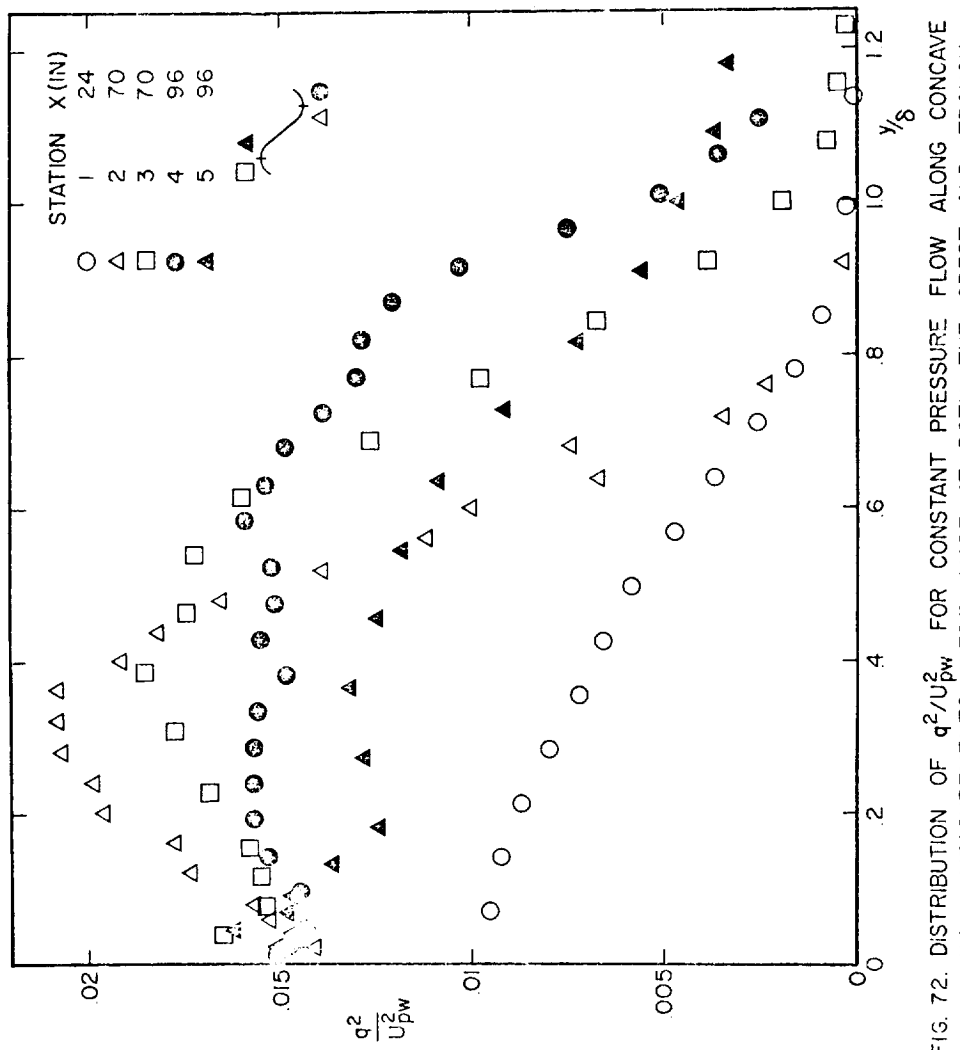
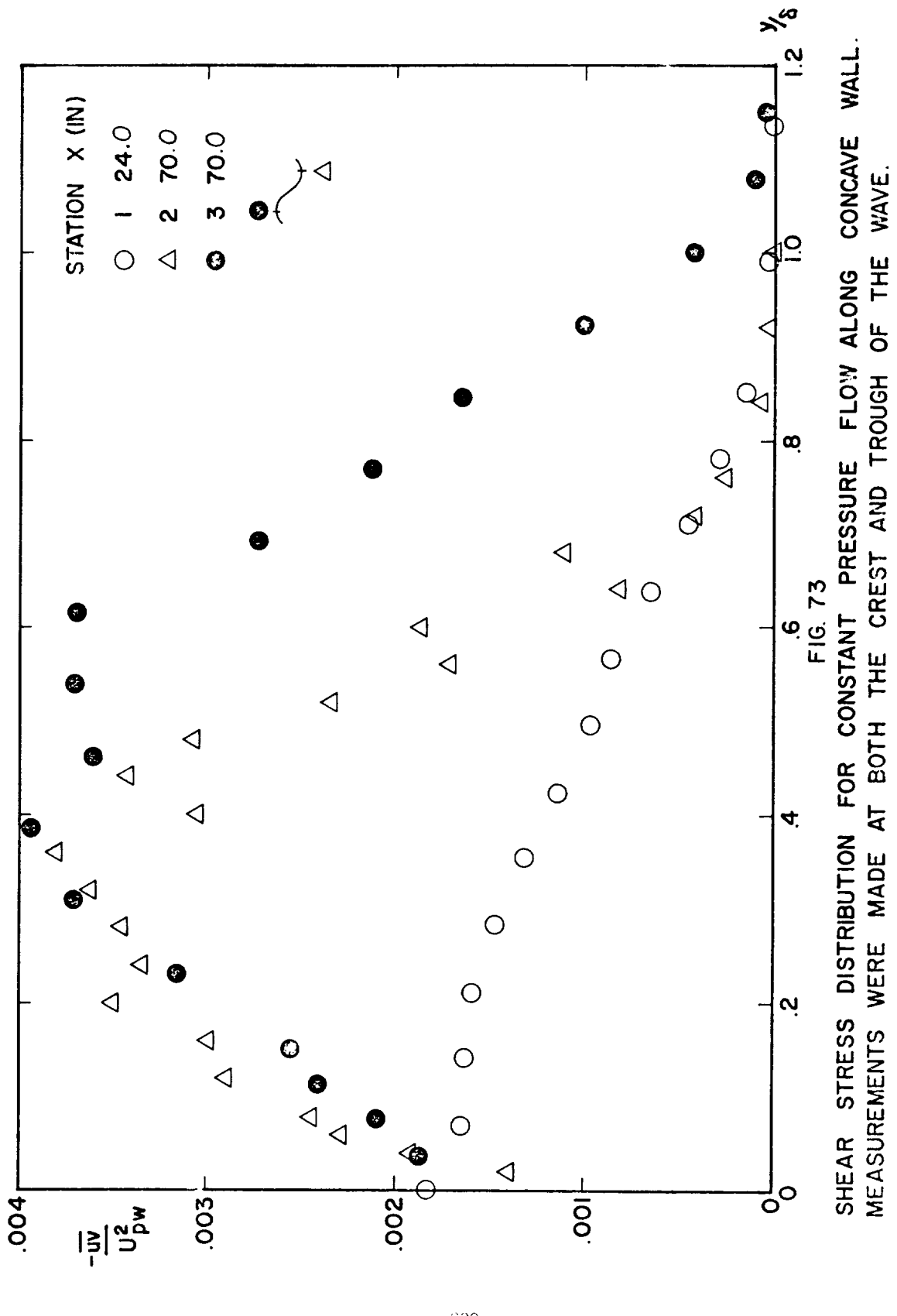


FIG. 72. DISTRIBUTION OF q^2/U_p^2 FOR CONSTANT PRESSURE FLOW ALONG CONCAVE WALL. MEASUREMENTS WERE MADE AT BOTH THE CREST AND TROUGH OF THE WAVE.



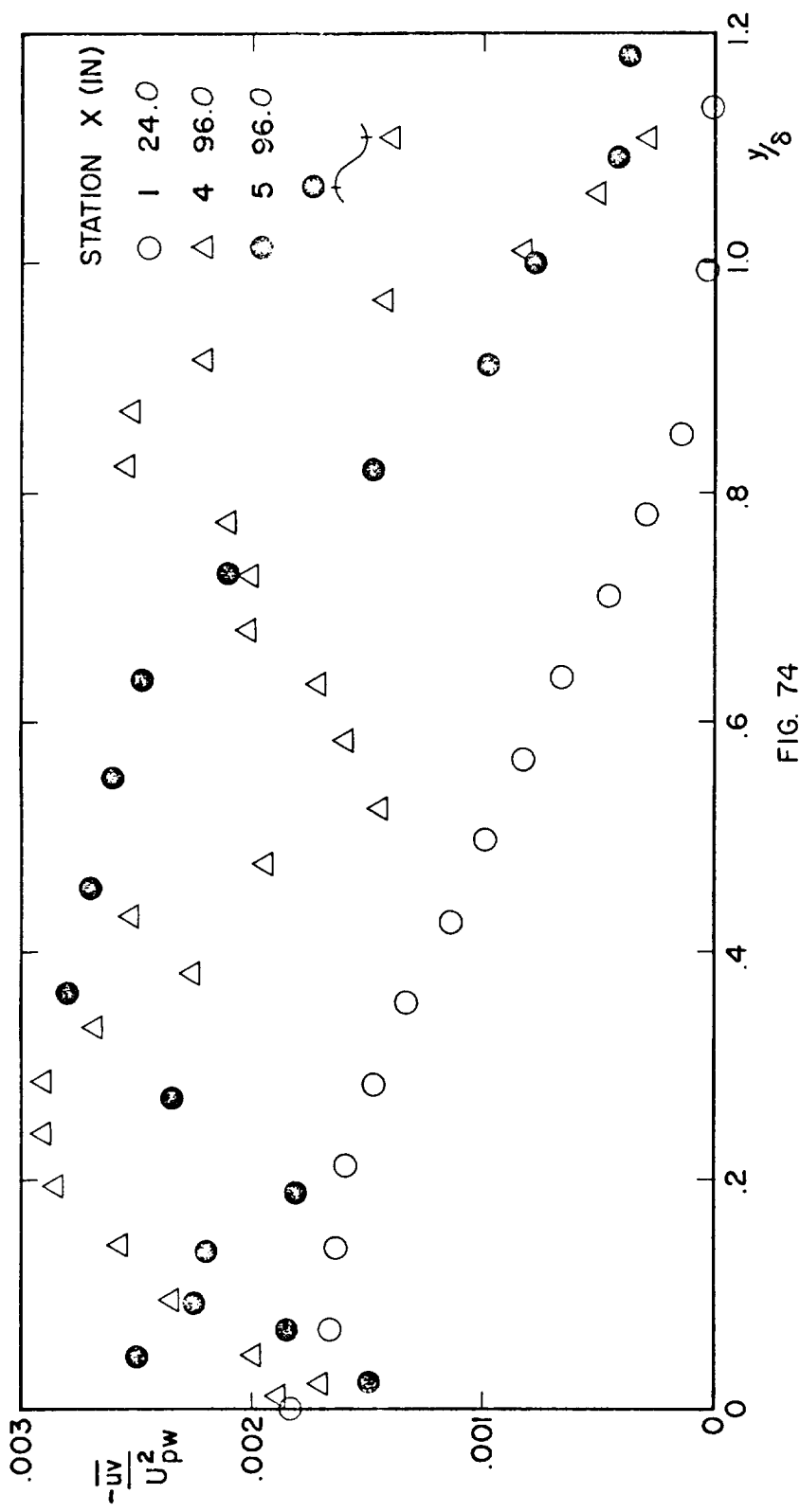


FIG. 74
SHEAR STRESS DISTRIBUTION FOR CONSTANT PRESSURE FLOW ALONG CONCAVE WALL
MEASUREMENTS WERE MADE AT BOTH THE CREST AND TROUGH OF THE WAVE.

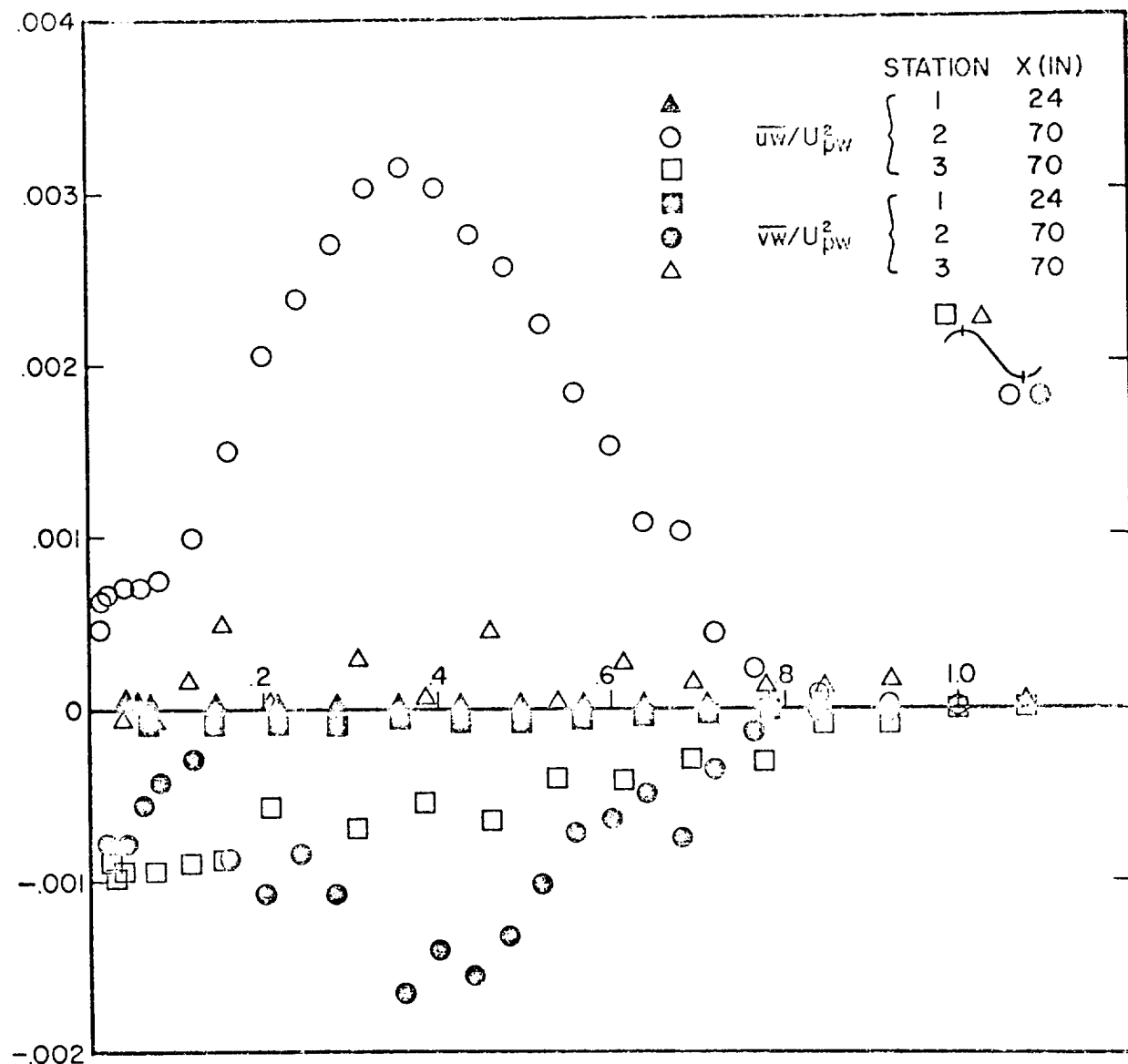
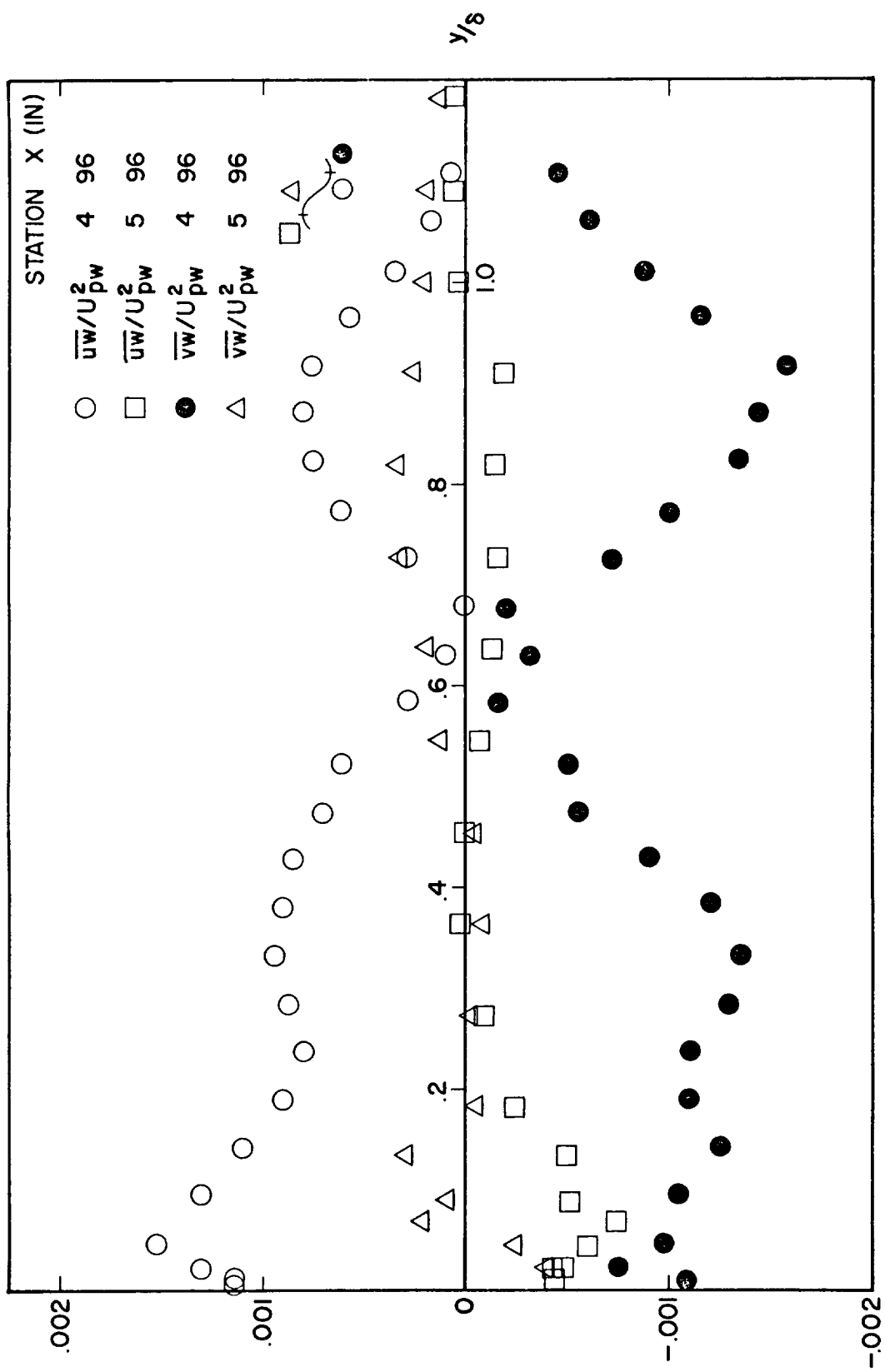


FIG. 75. DISTRIBUTION OF $\overline{u w} / U_{pw}^2$ AND $\overline{v w} / U_{pw}^2$ FOR CONSTANT PRESSURE FLOW ALONG CONCAVE WALL. MEASUREMENTS WERE MADE AT BOTH THE CREST AND TROUGH OF THE WAVE.



DISTRIBUTION OF $\bar{u}w/U_{pw}^2$ AND $\bar{v}w/U_{pw}^2$ FOR CONSTANT PRESSURE FLOW ALONG CONCAVE WALL. MEASUREMENTS WERE MADE AT BOTH THE CREST AND TROUGH OF THE WAVE. FIG. 76

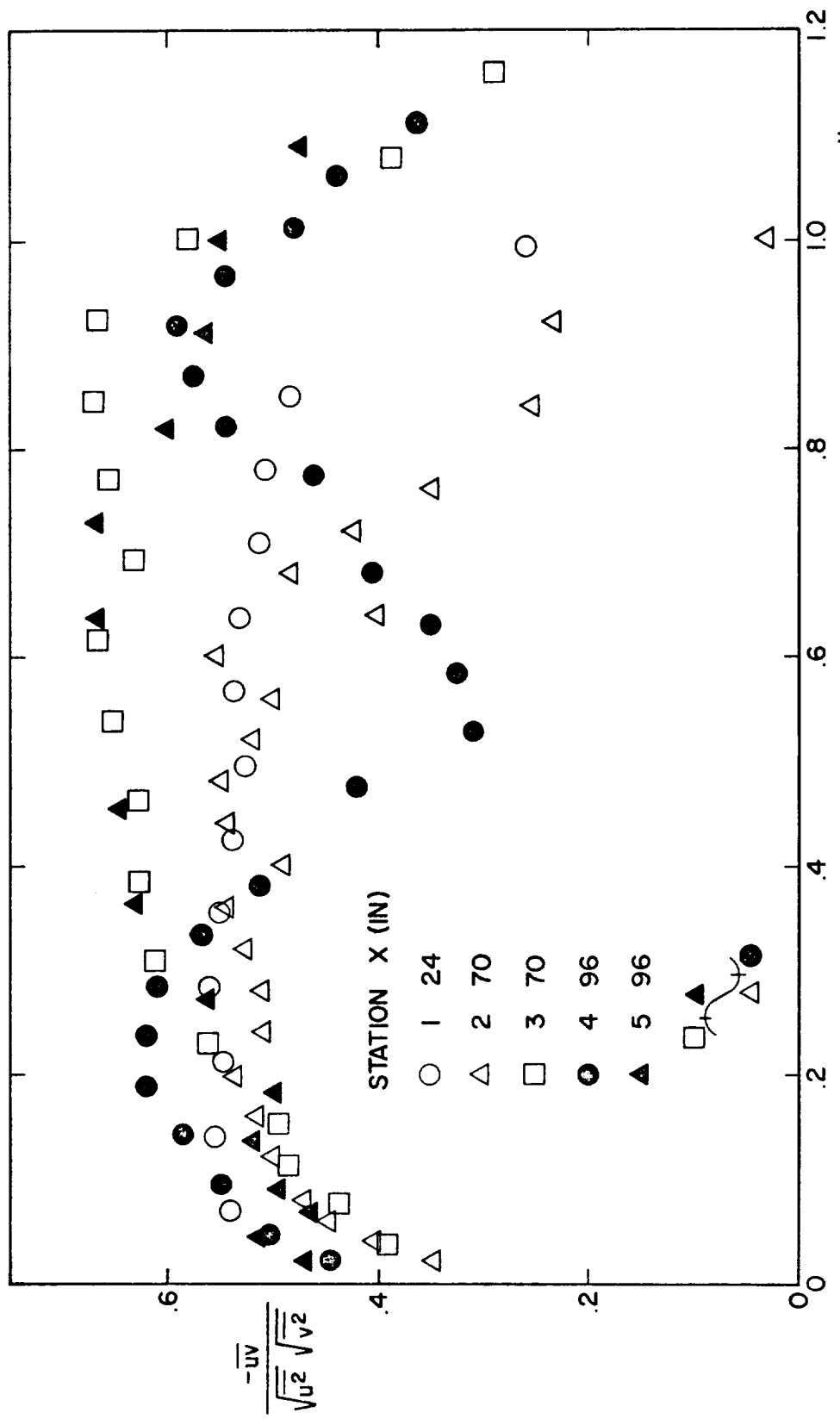
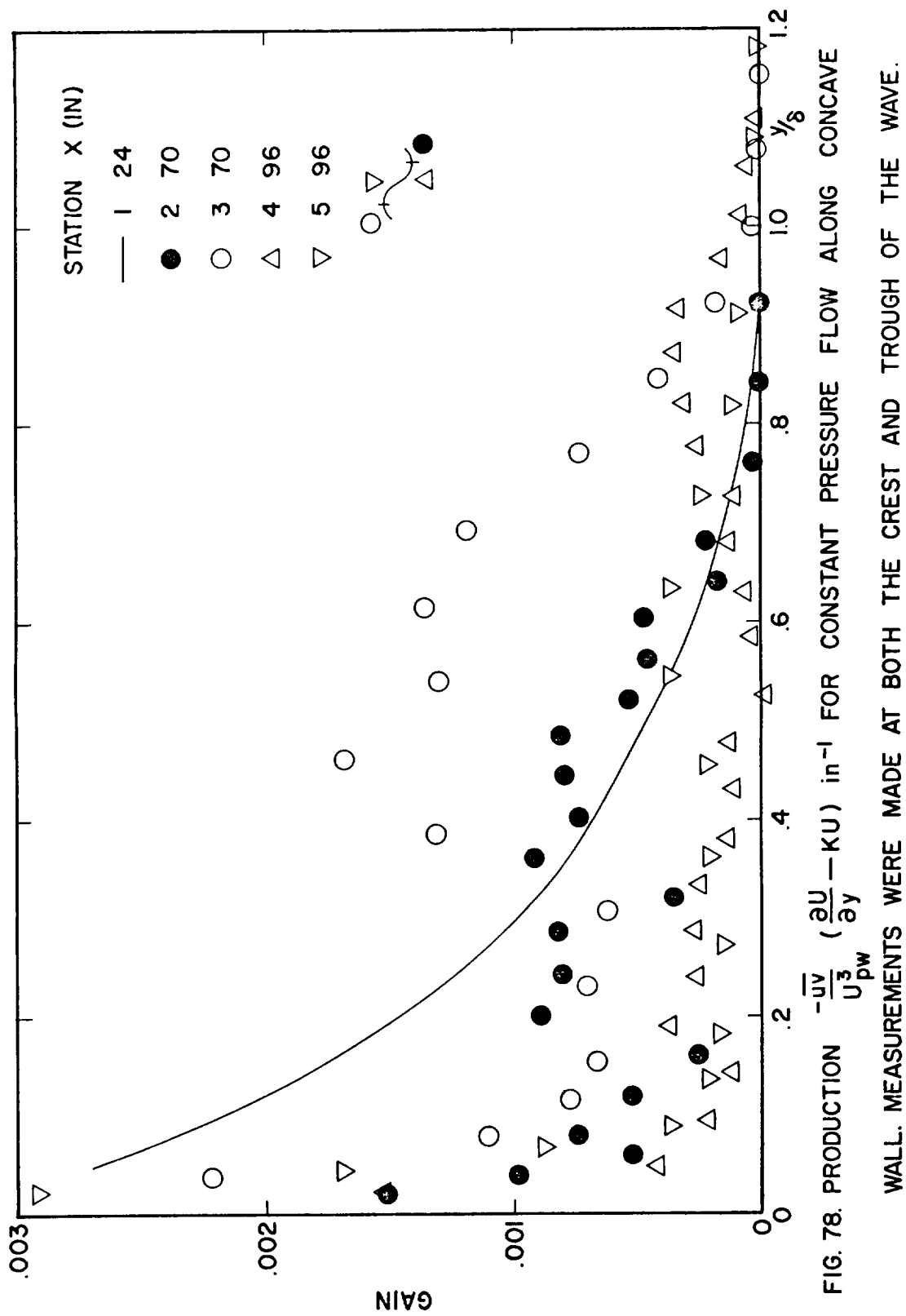


FIG. 77. DISTRIBUTION OF SHEAR CORRELATION COEFFICIENT FOR CONSTANT PRESSURE FLOW ALONG CONCAVE WALL. MEASUREMENTS WERE MADE AT BOTH THE CREST AND TROUGH OF THE WAVE.



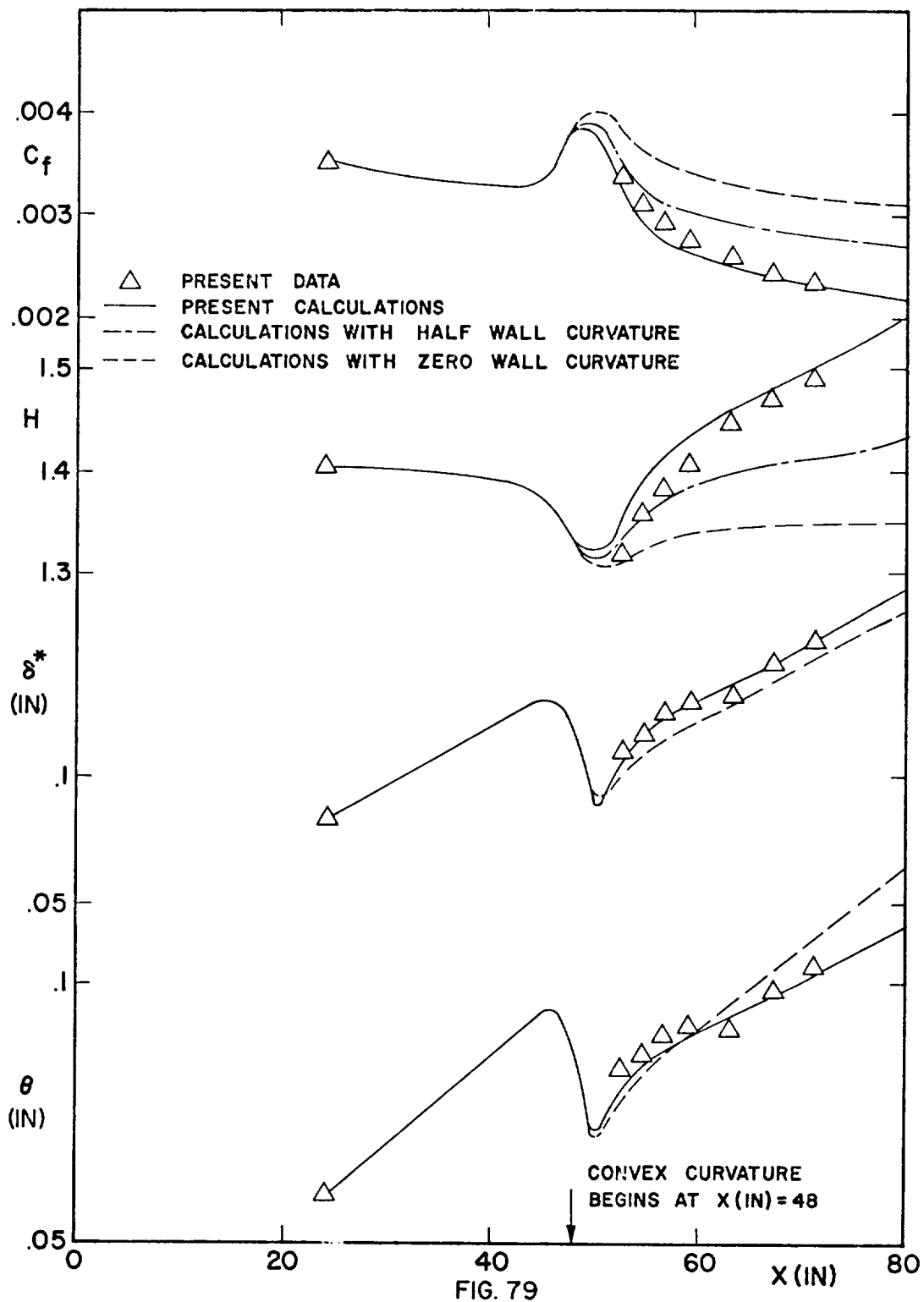


FIG. 79
COMPARISON OF SKIN FRICTION, SHAPE FACTOR, DISPLACEMENT AND MOMENTUM THICKNESS CALCULATIONS AND PRESENT DATA FOR CONSTANT PRESSURE FLOW ALONG CONVEX WALL.

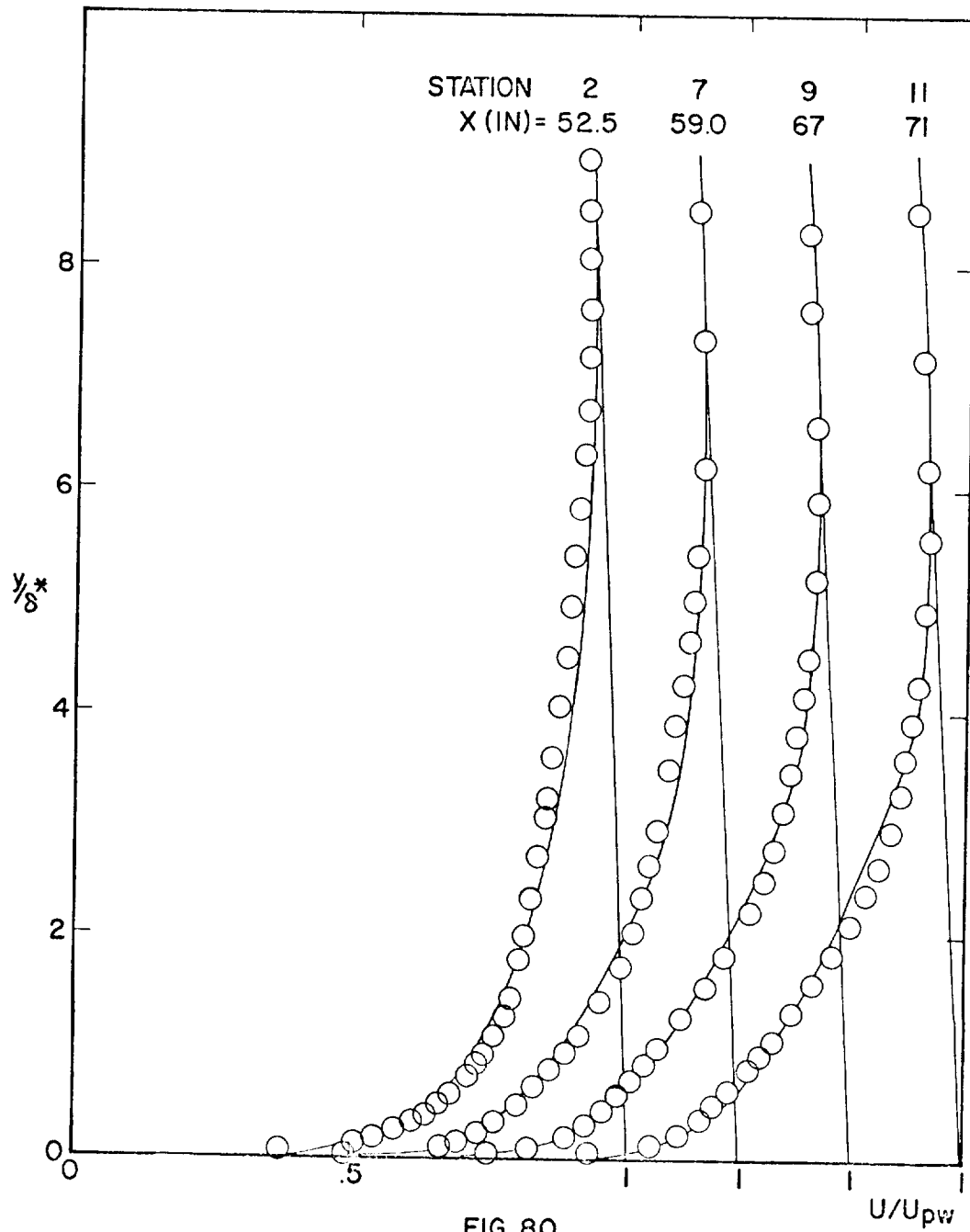


FIG. 80
 COMPARISON OF VELOCITY PROFILE CALCULATIONS AND
 PRESENT DATA FOR CONSTANT PRESSURE FLOW ALONG
 CONVEX WALL

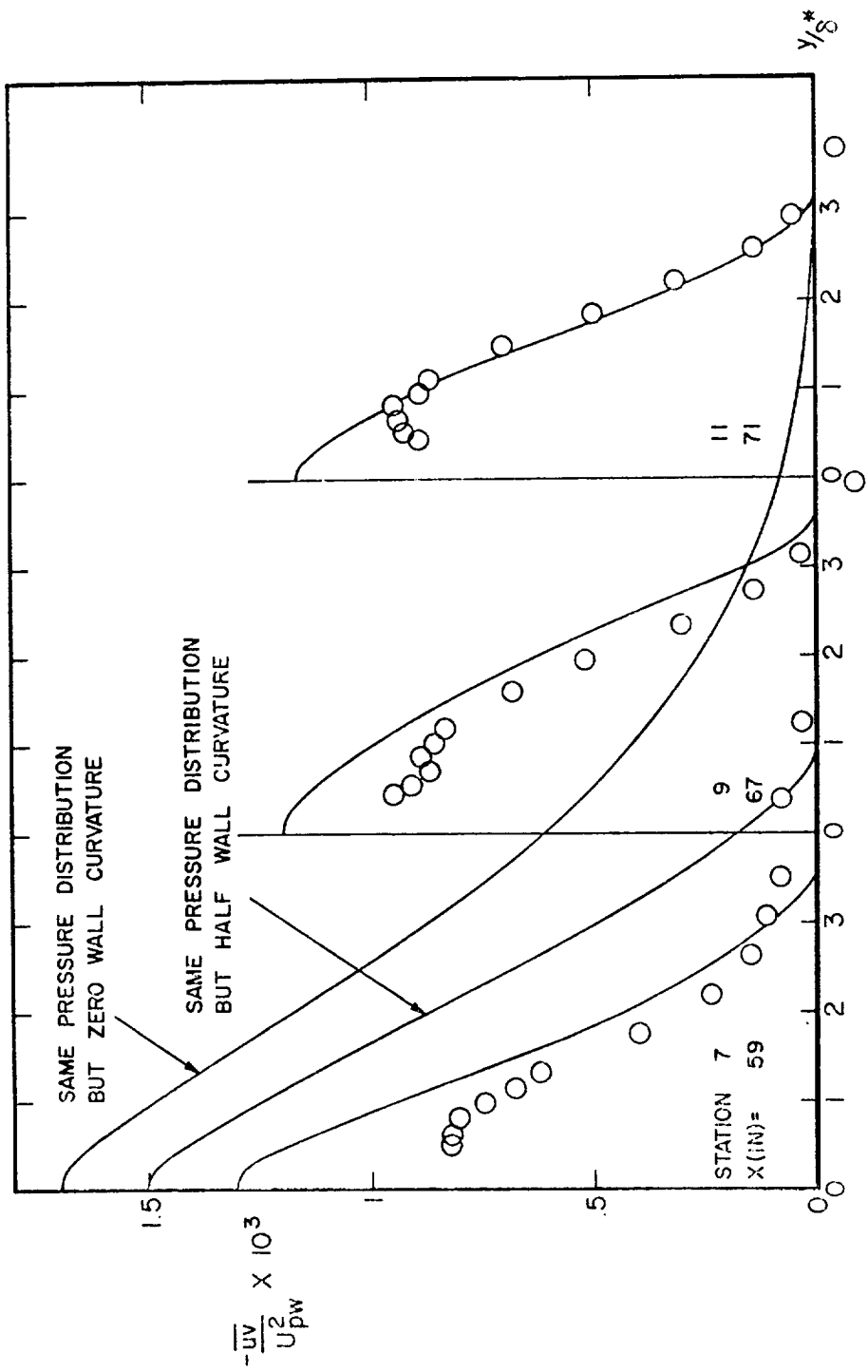
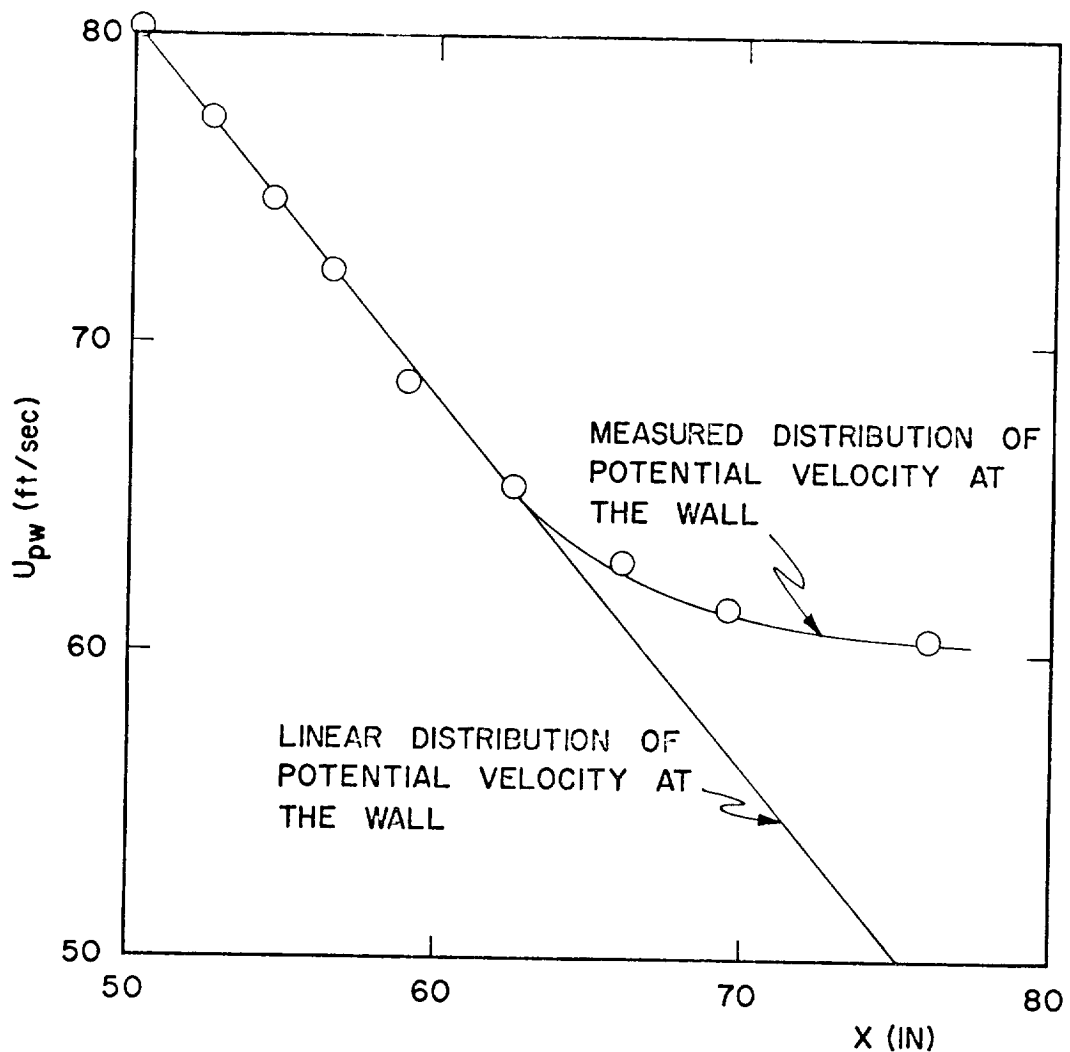


FIG 81. COMPARISON OF SHEAR STRESS CALCULATIONS AND PRESENT DATA FOR CONSTANT PRESSURE FLOW ALONG CONVEX WALL.



DISTRIBUTION OF POTENTIAL VELOCITY AT THE WALL
FOR SEPARATING FLOW ALONG CONVEX WALL.

FIG. 82

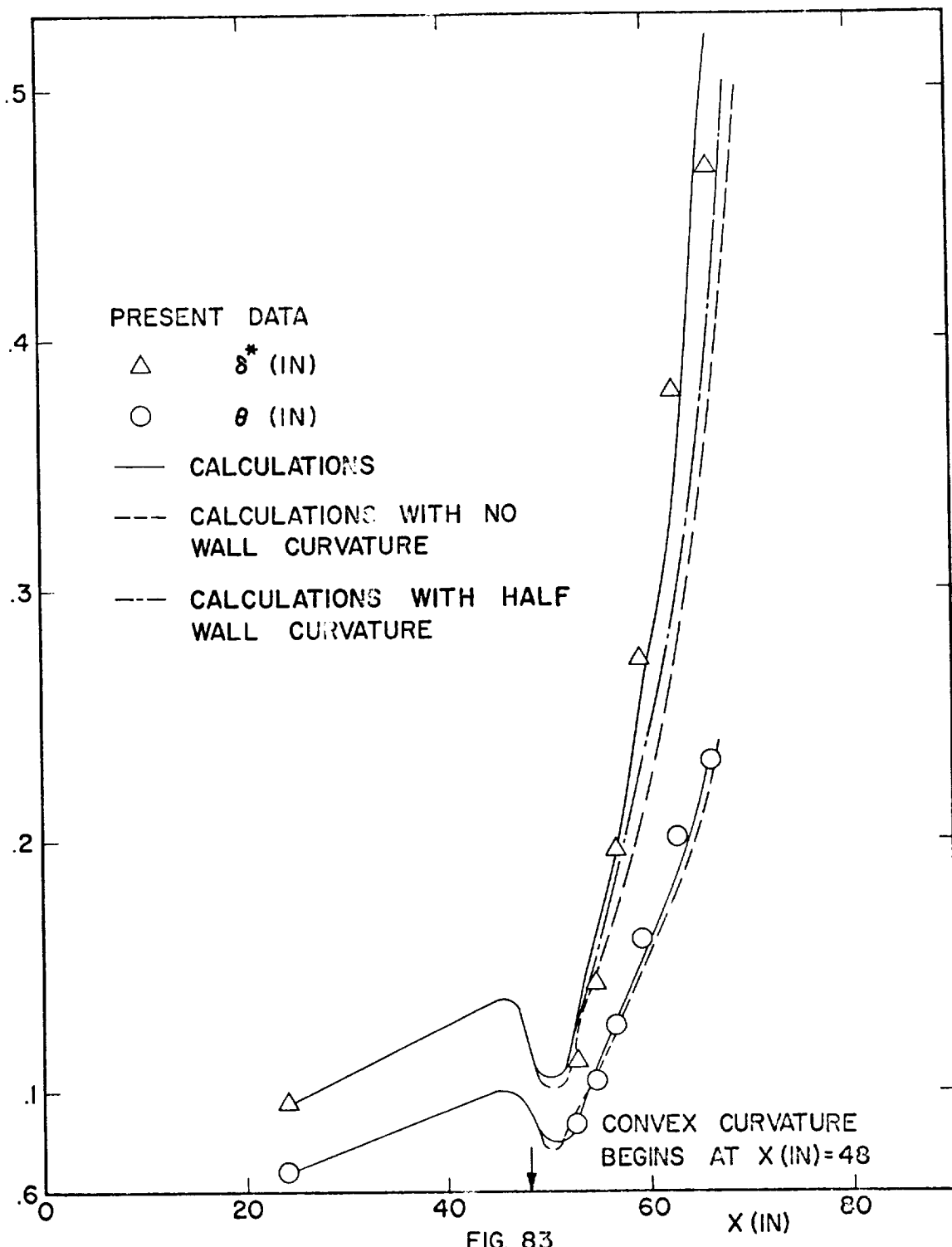


FIG. 83
COMPARISON OF DISPLACEMENT AND MOMENTUM THICKNESS
CALCULATIONS AND PRESENT DATA FOR SEPARATING
FLOW ALONG CONVEX WALL.

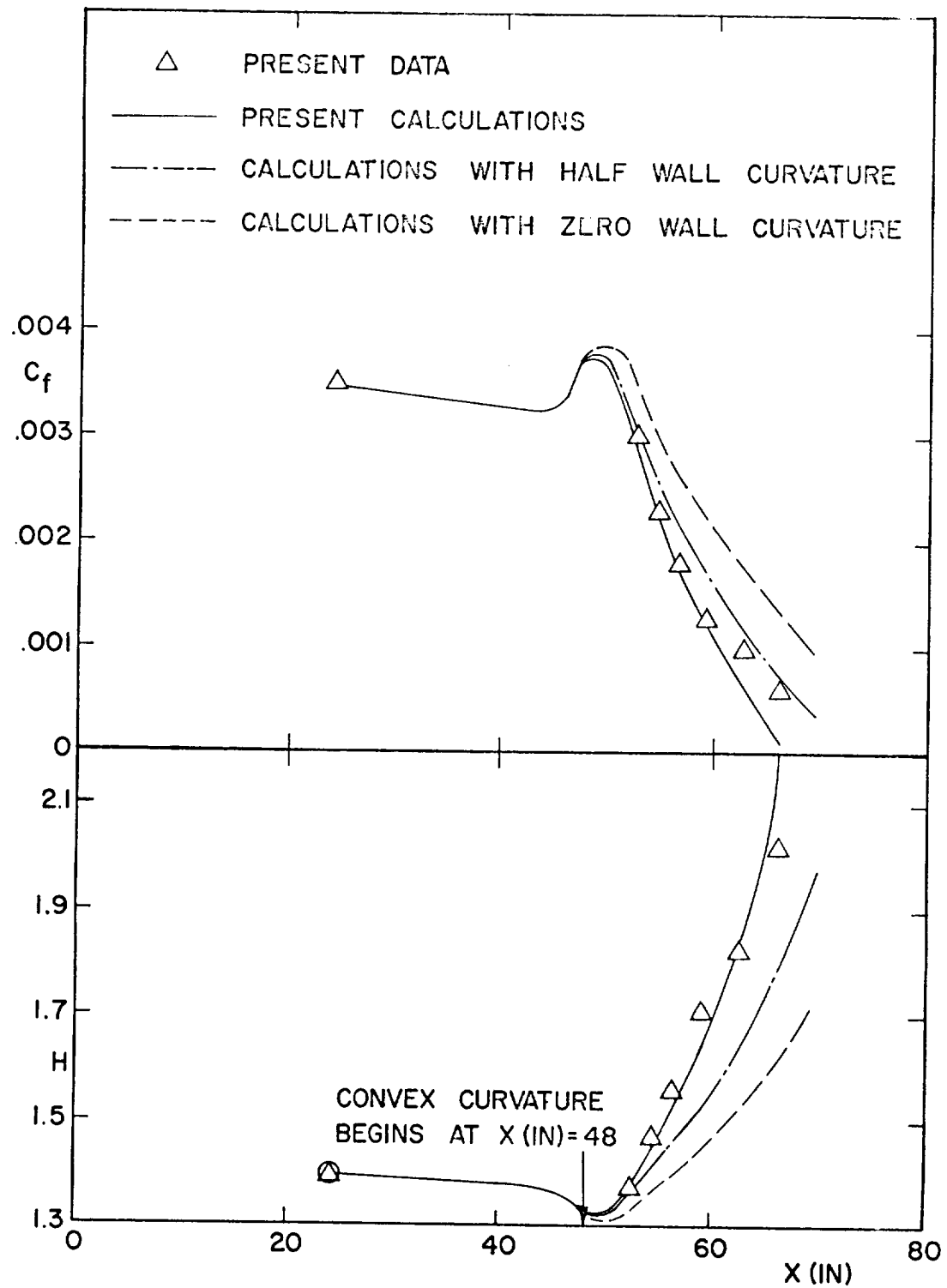


FIG. 84
COMPARISON OF SKIN FRICTION AND SHAPE FACTOR
CALCULATIONS WITH PRESENT DATA FOR SEPARATING
FLOW ALONG CONVEX WALL.

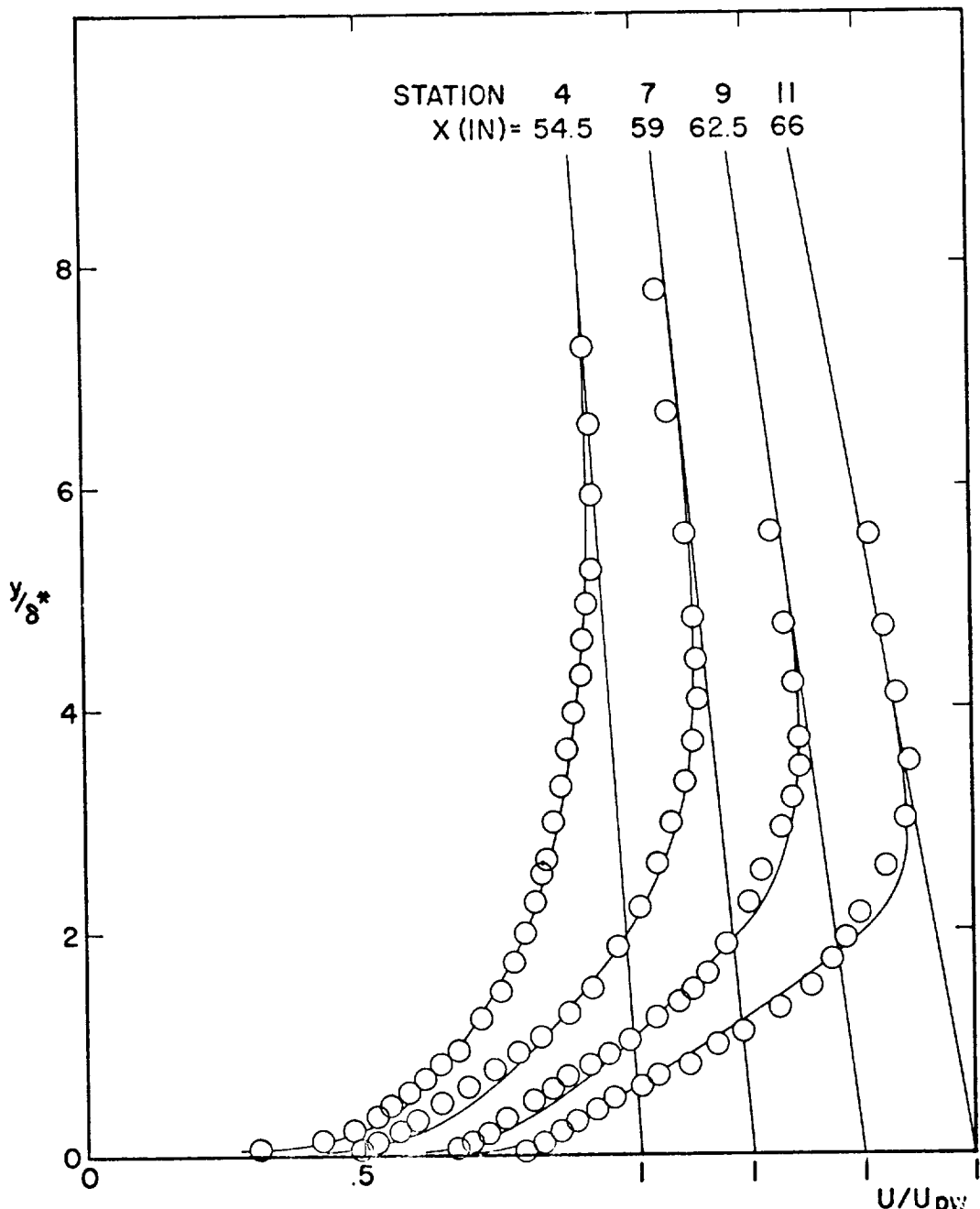


FIG. 85

COMPARISON OF VELOCITY PROFILE CALCULATIONS AND PRESENT DATA FOR SEPARATING FLOW ALONG CONVEX WALL.

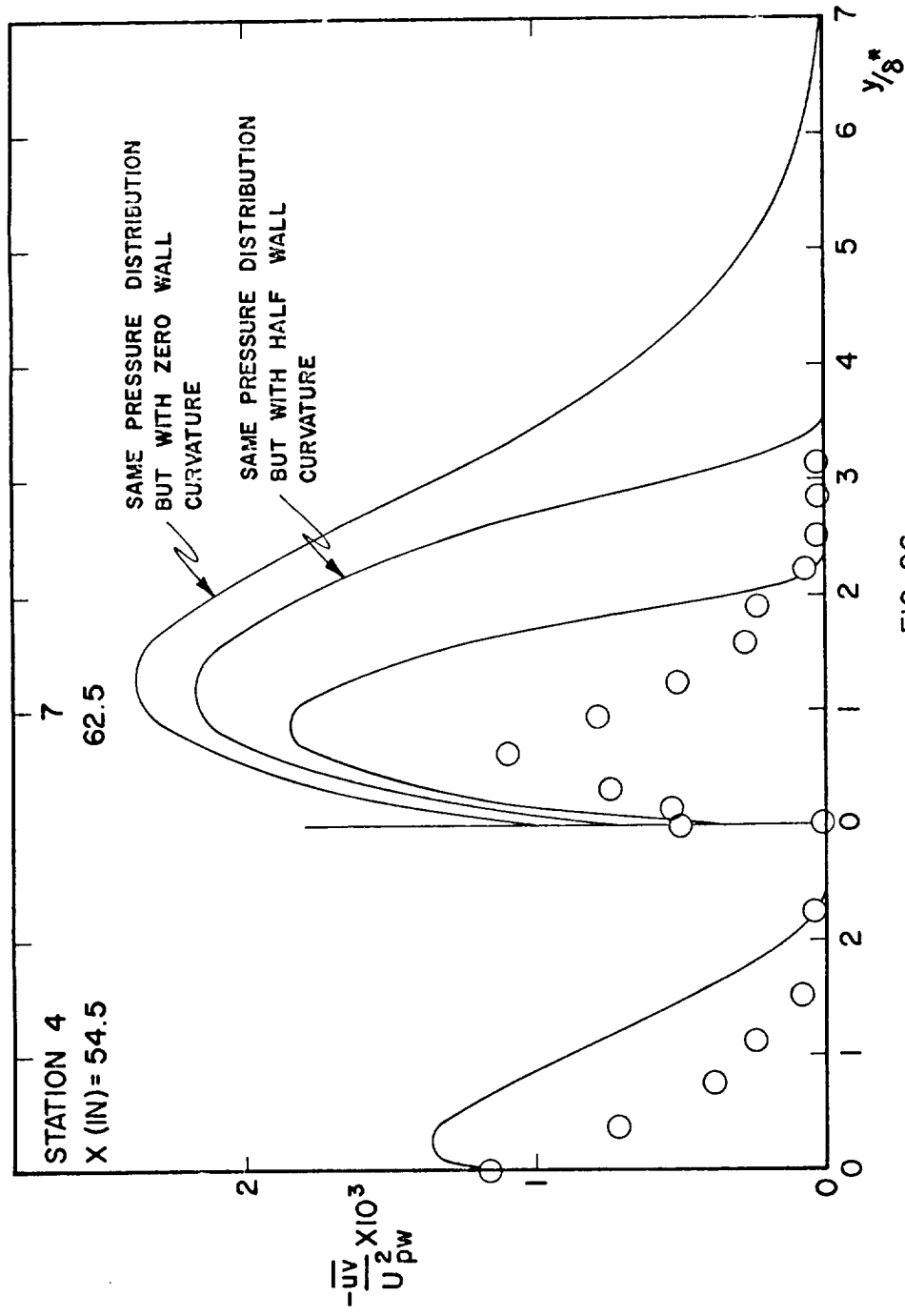


FIG. 86
COMPARISON OF SHEAR STRESS CALCULATIONS AND PRESENT DATA FOR
SEPARATING FLOW ALONG CONVEX WALL.

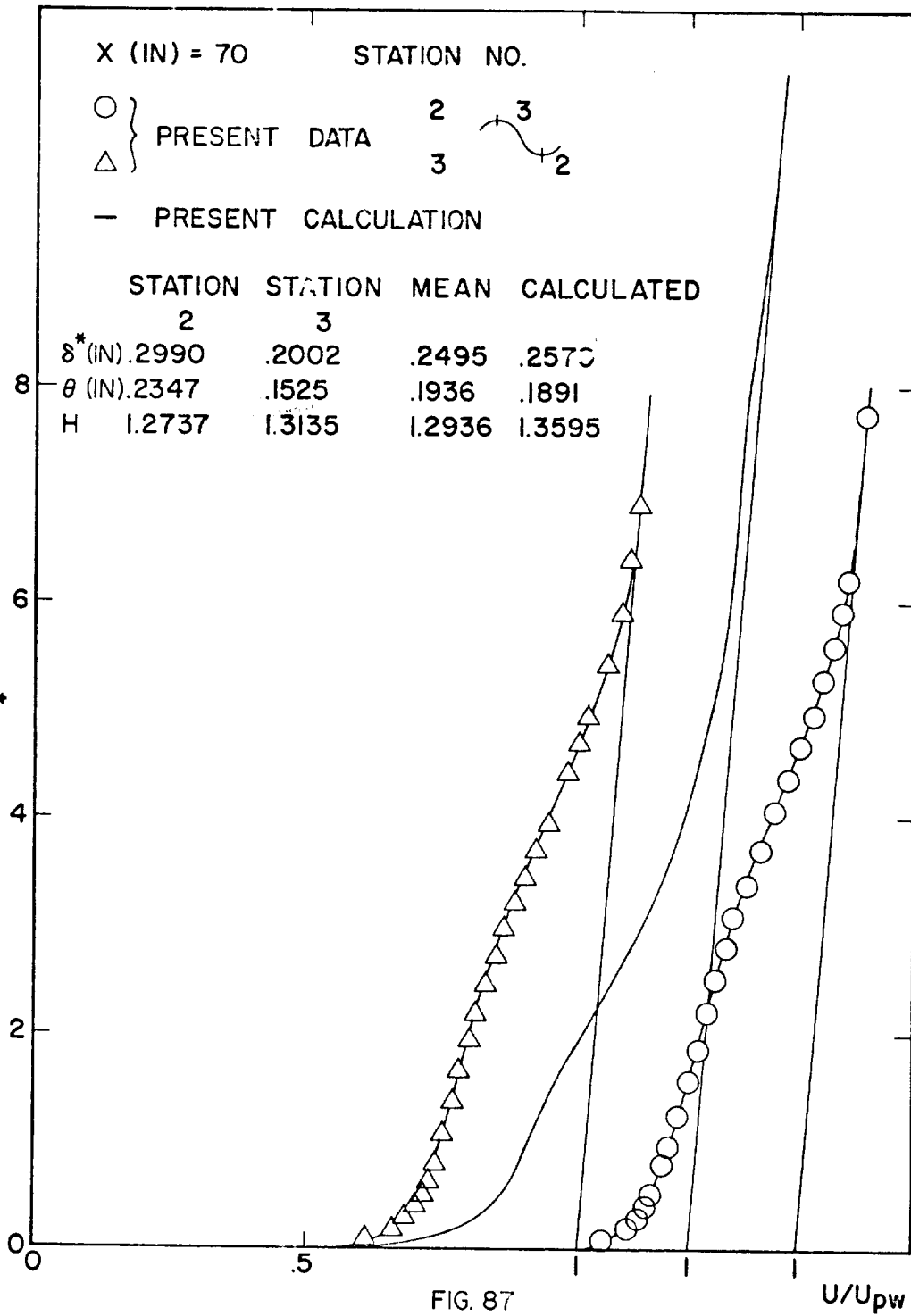
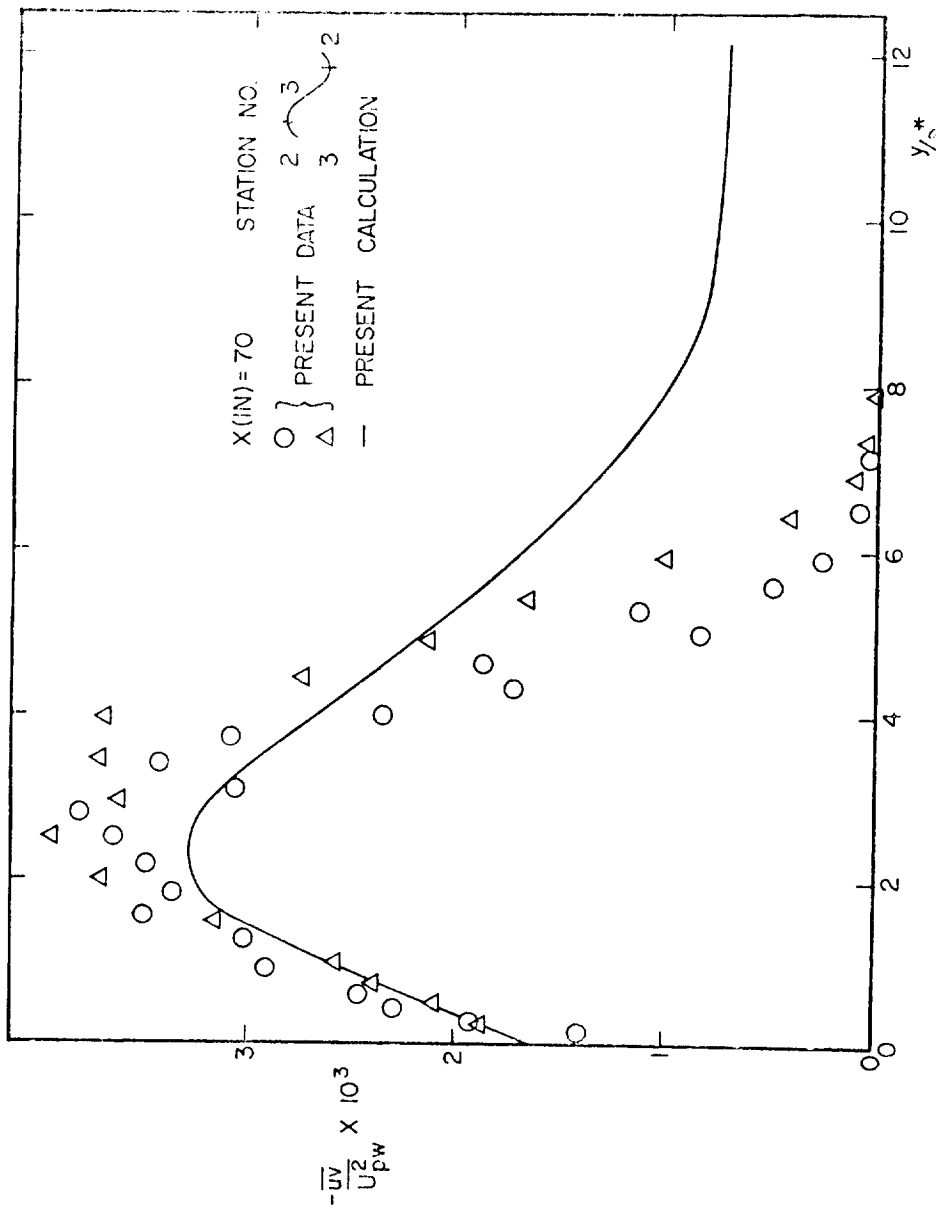


FIG. 87
 COMPARISON OF VELOCITY PROFILE CALCULATIONS
 AND PRESENT DATA FOR CONSTANT PRESSURE FLOW
 ALONG CONCAVE WALL AT $X \text{ (IN)} = 70$



COMPARISON OF SHEAR STRESS CALCULATIONS WITH PRESENT DATA
FOR CONSTANT PRESSURE FLOW ALONG CONCAVE WALL AT $X(N) = 70$,

FIG. 86

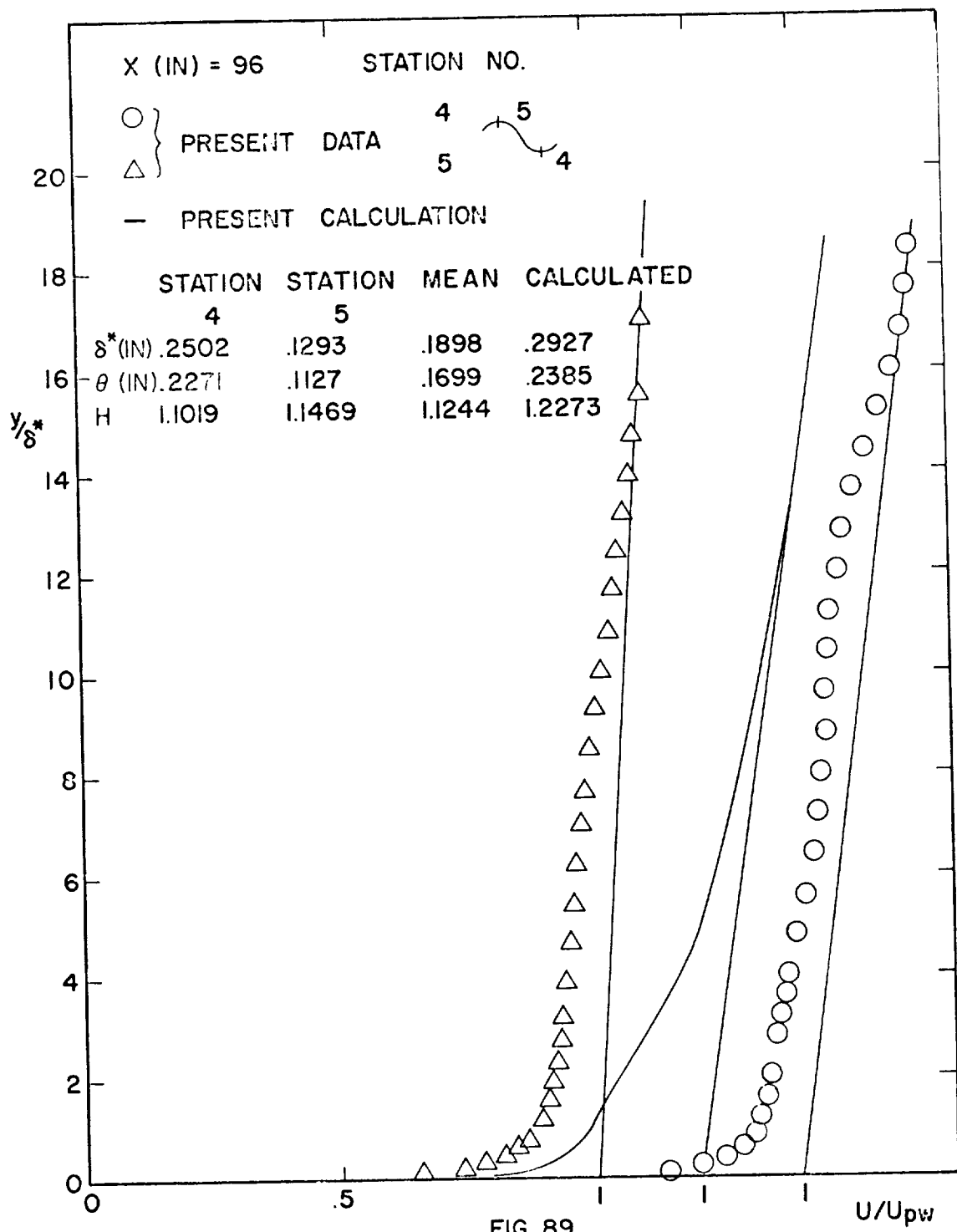


FIG. 89

COMPARISON OF VELOCITY PROFILE CALCULATIONS
AND PRESENT DATA FOR CONSTANT PRESSURE FLOW
ALONG CONCAVE WALL AT X (IN)=96

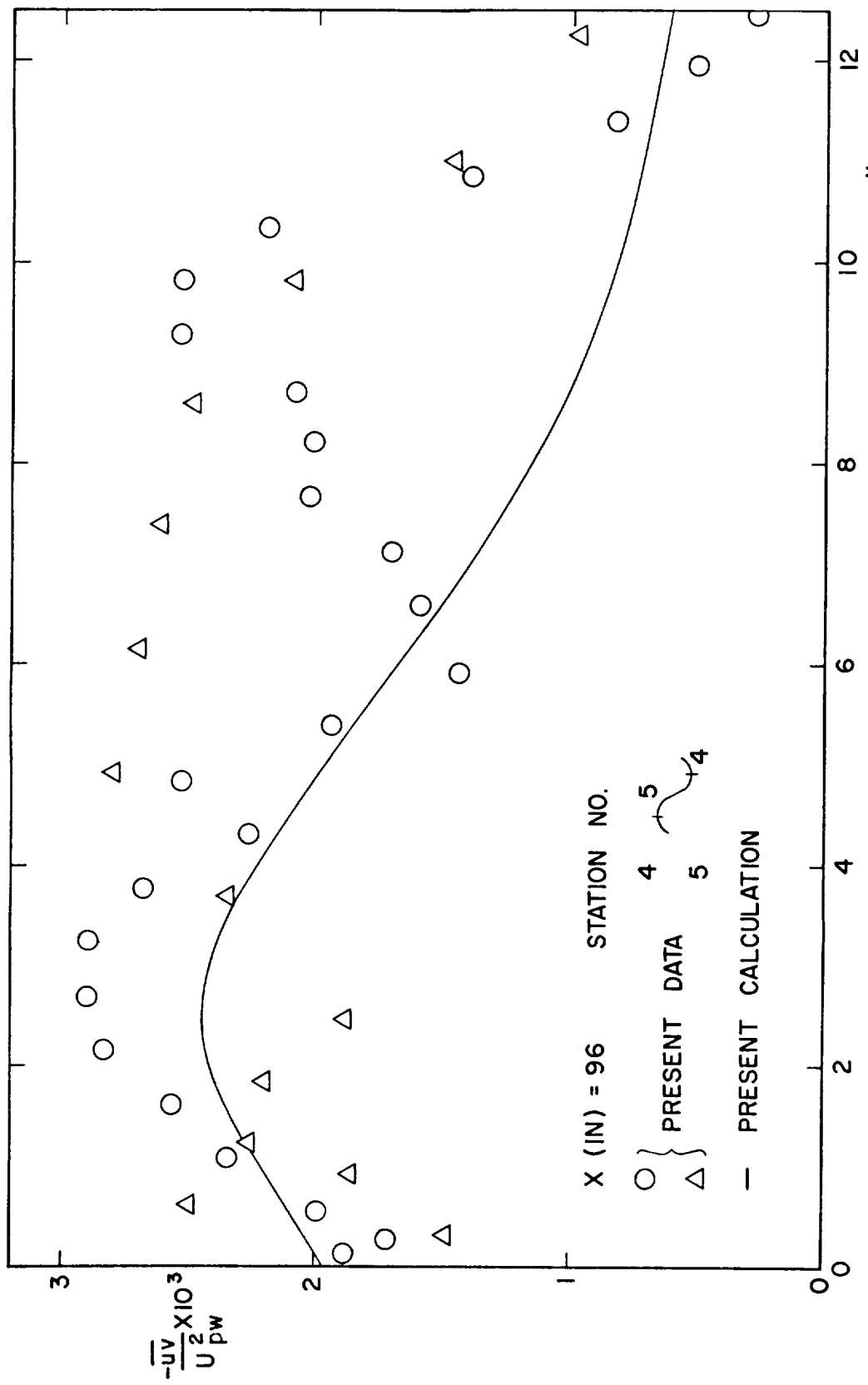


FIG. 90
COMPARISON OF SHEAR STRESS CALCULATIONS WITH PRESENT DATA FOR CONSTANT PRESSURE FLOW ALONG CONCAVE WALL AT x (IN) = 96.

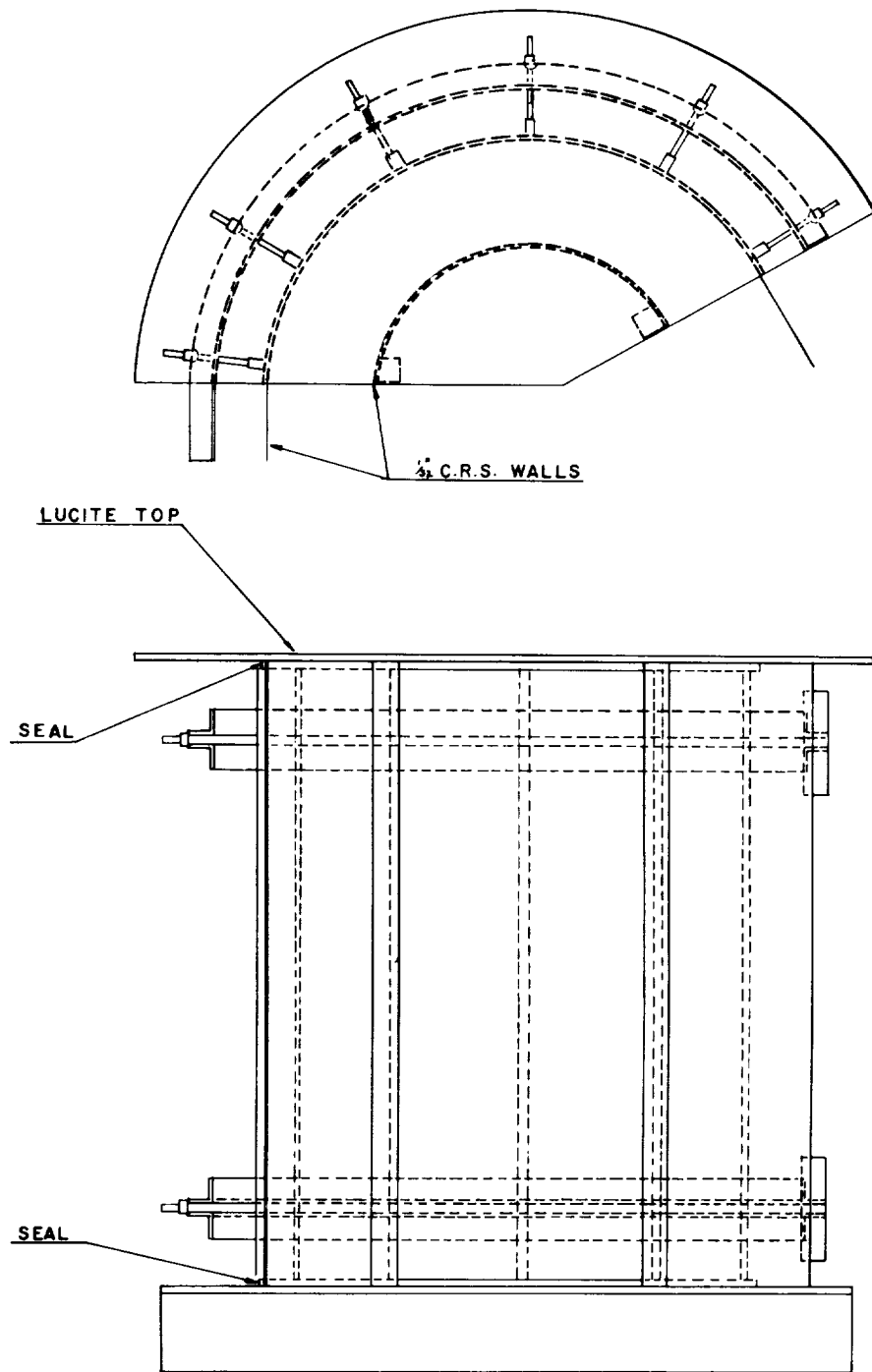


Figure 91. Adjustable outer wall test section.

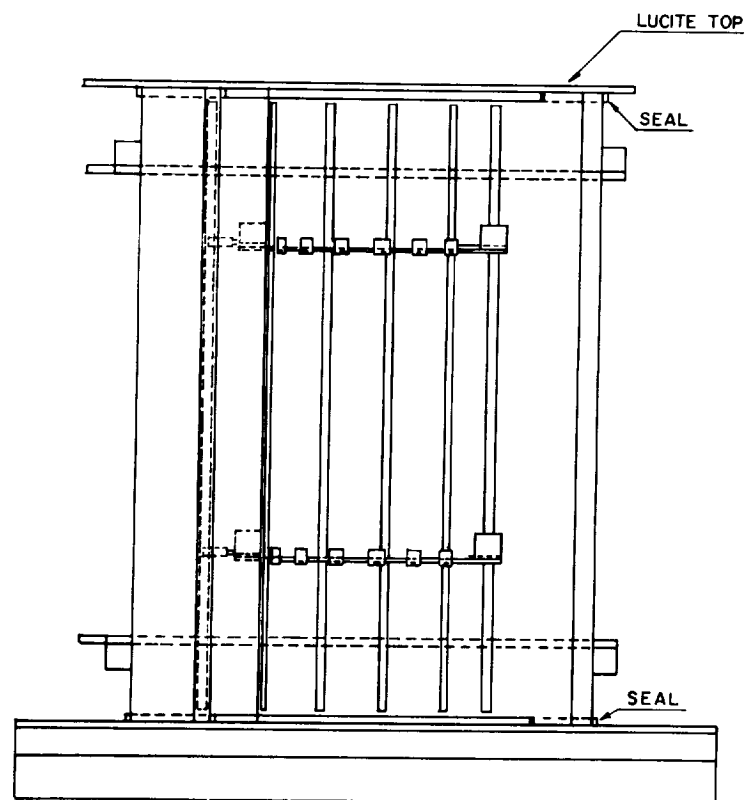
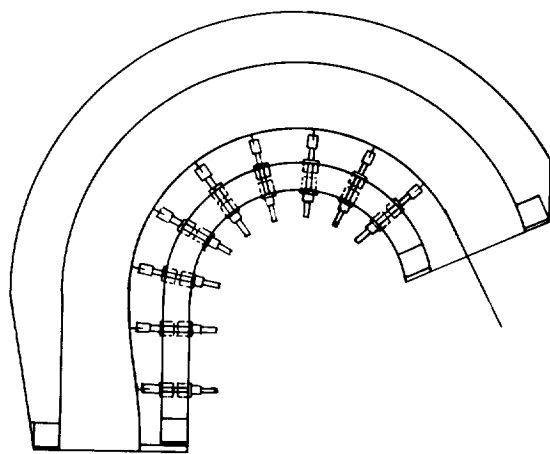
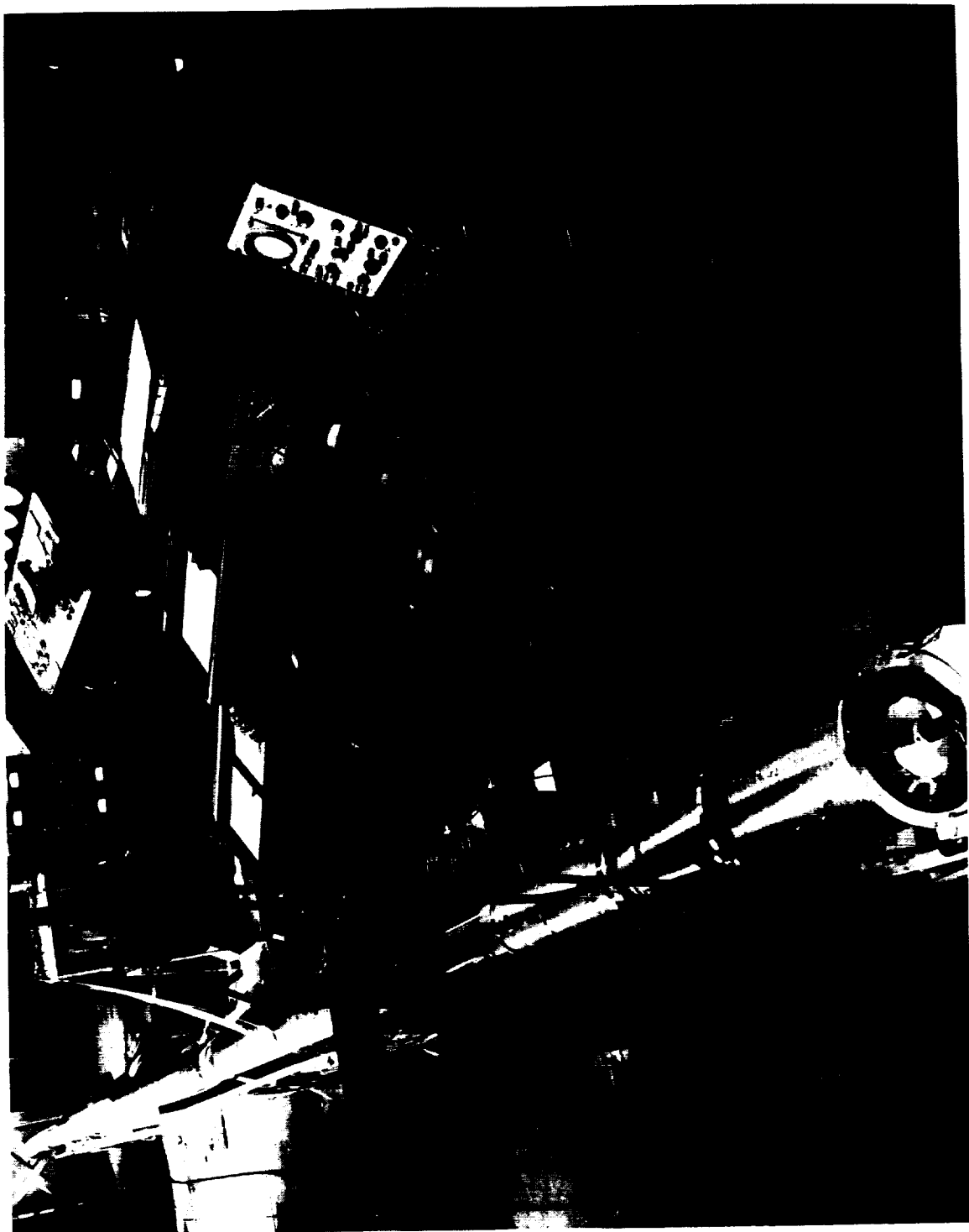


Figure 92. Adjustable inner wall test section.

FIGURE 93
Photograph of the Equipment
for Pipe Flow Experiment



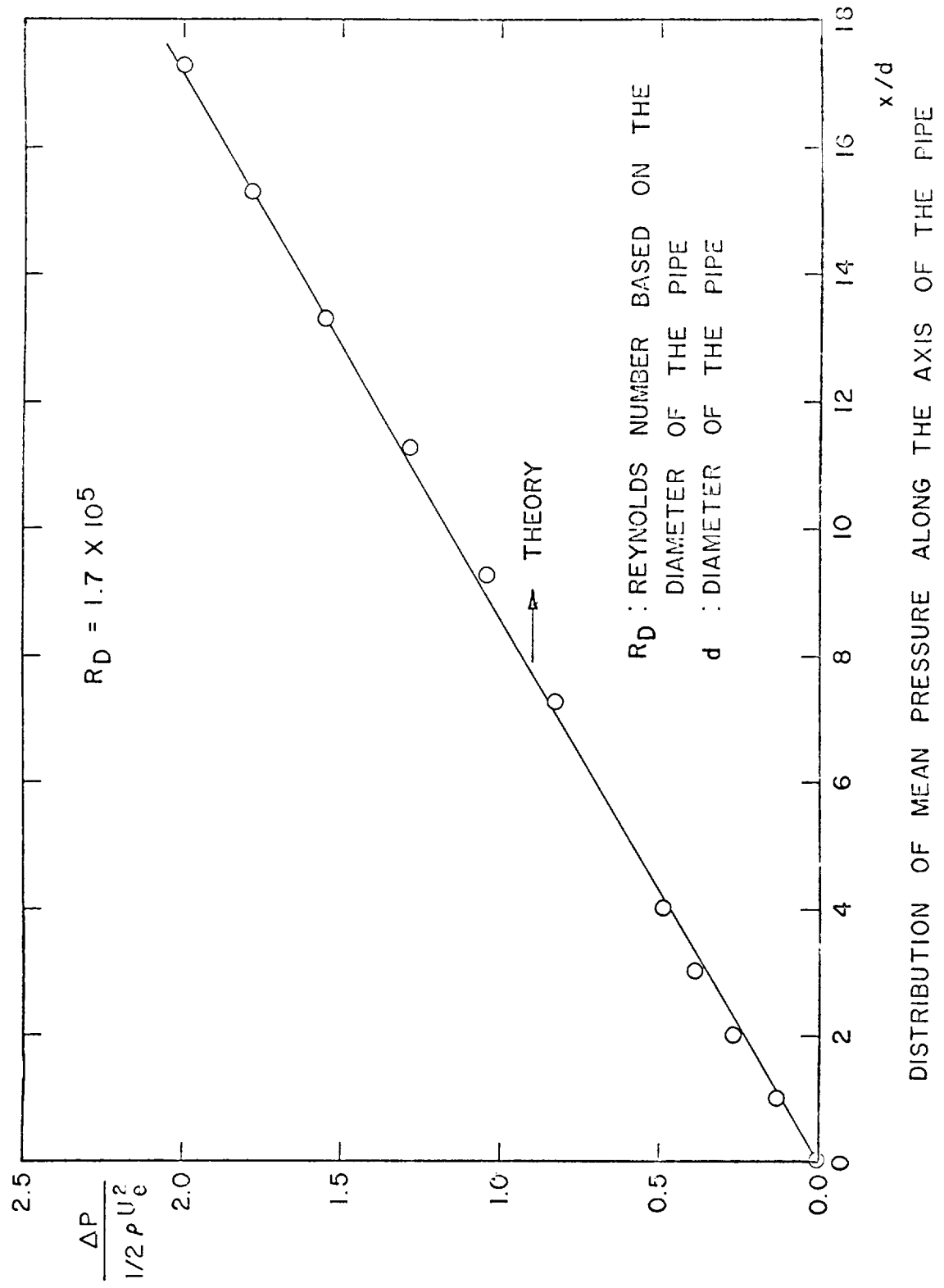


Figure 94

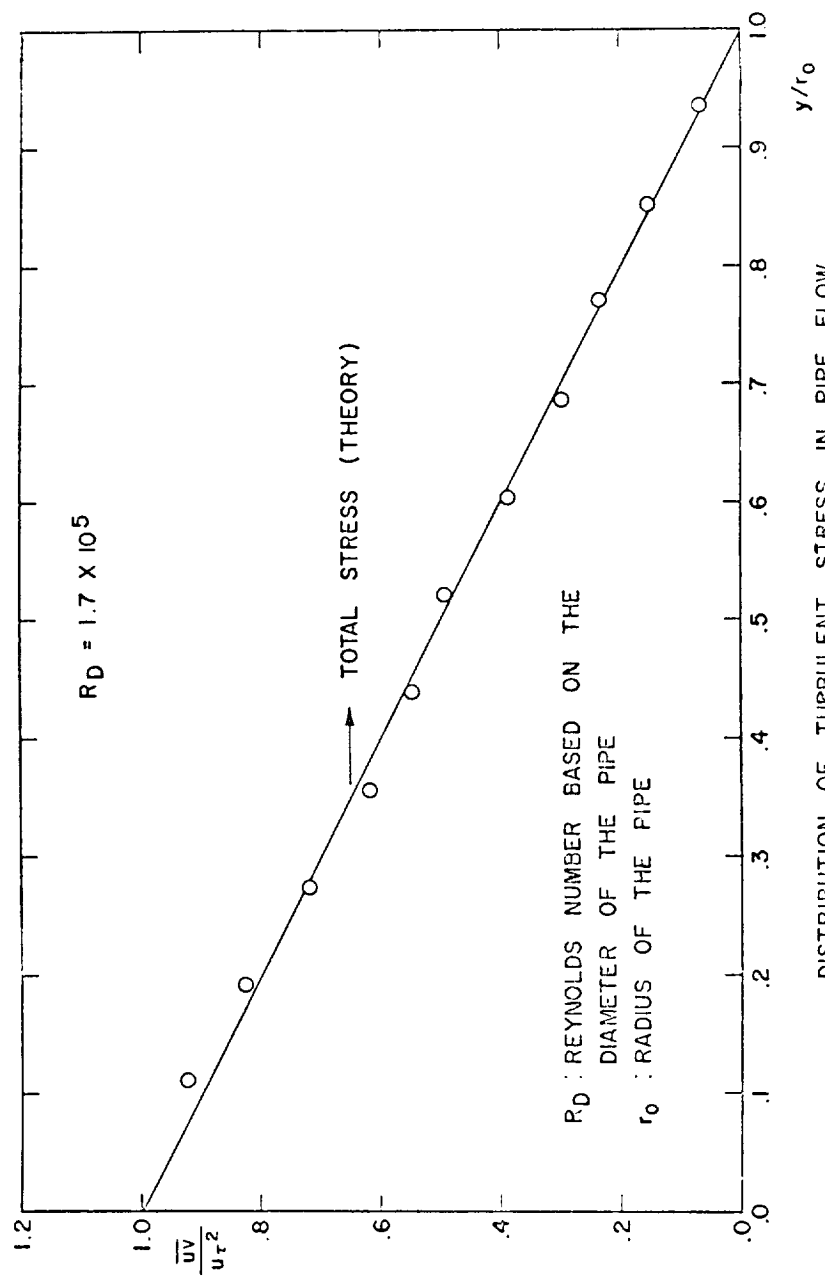


FIGURE 95

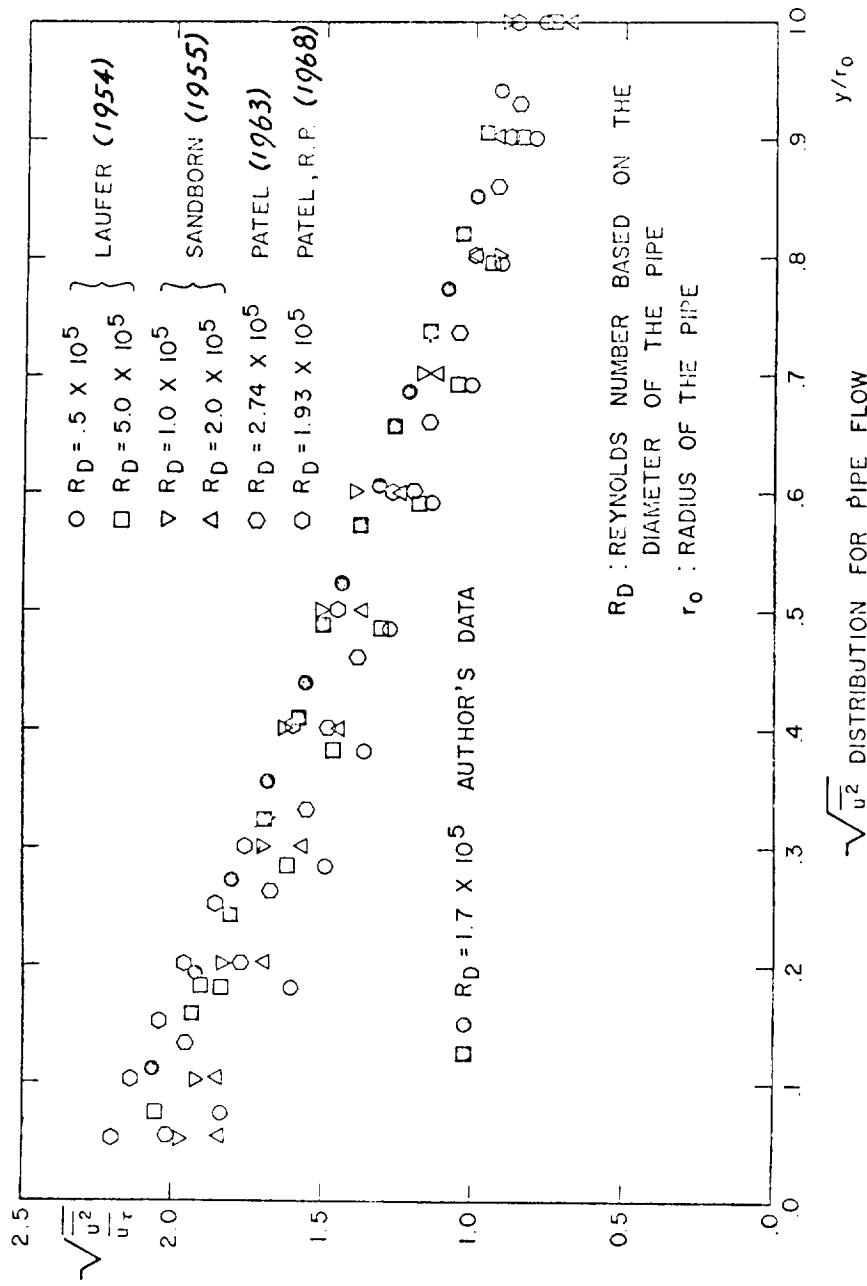


Figure 96

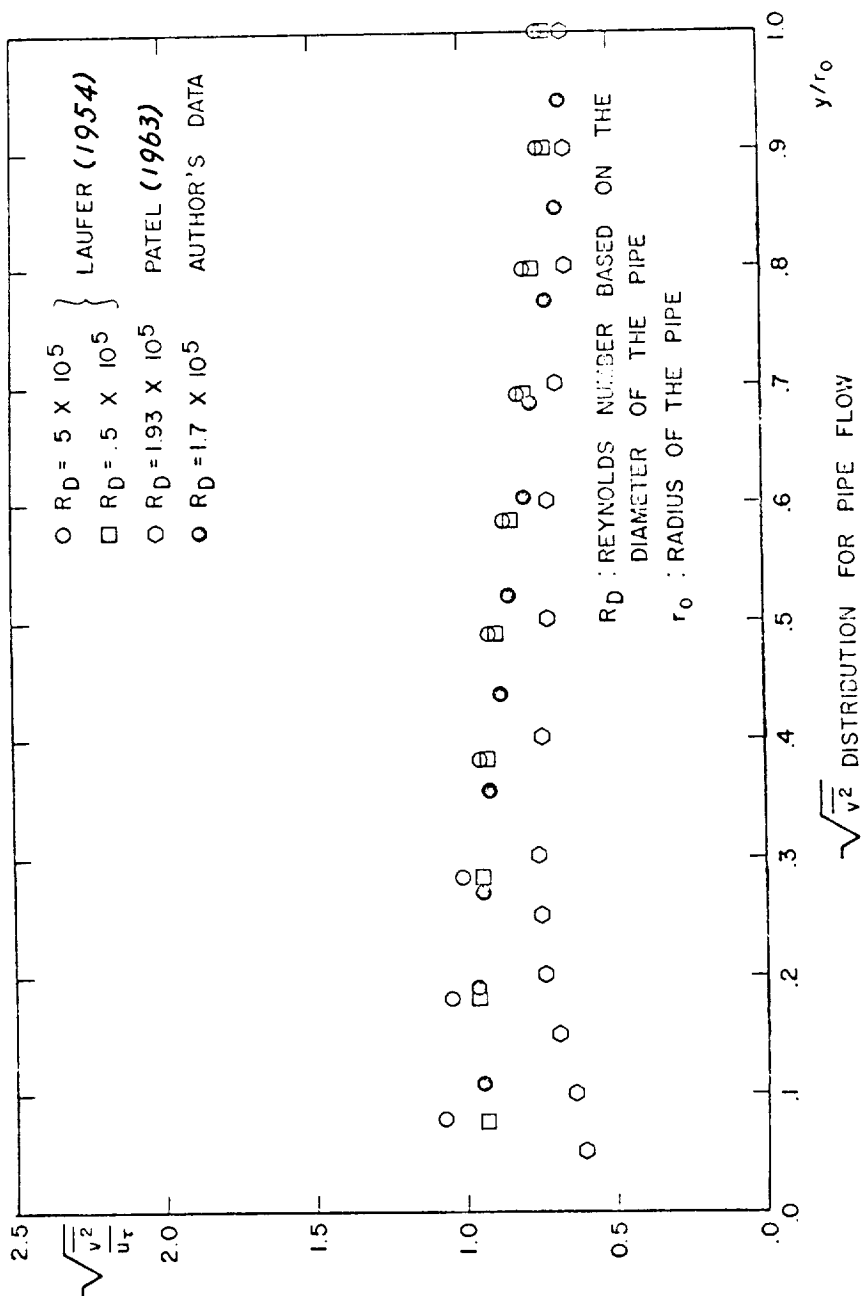


FIGURE 97

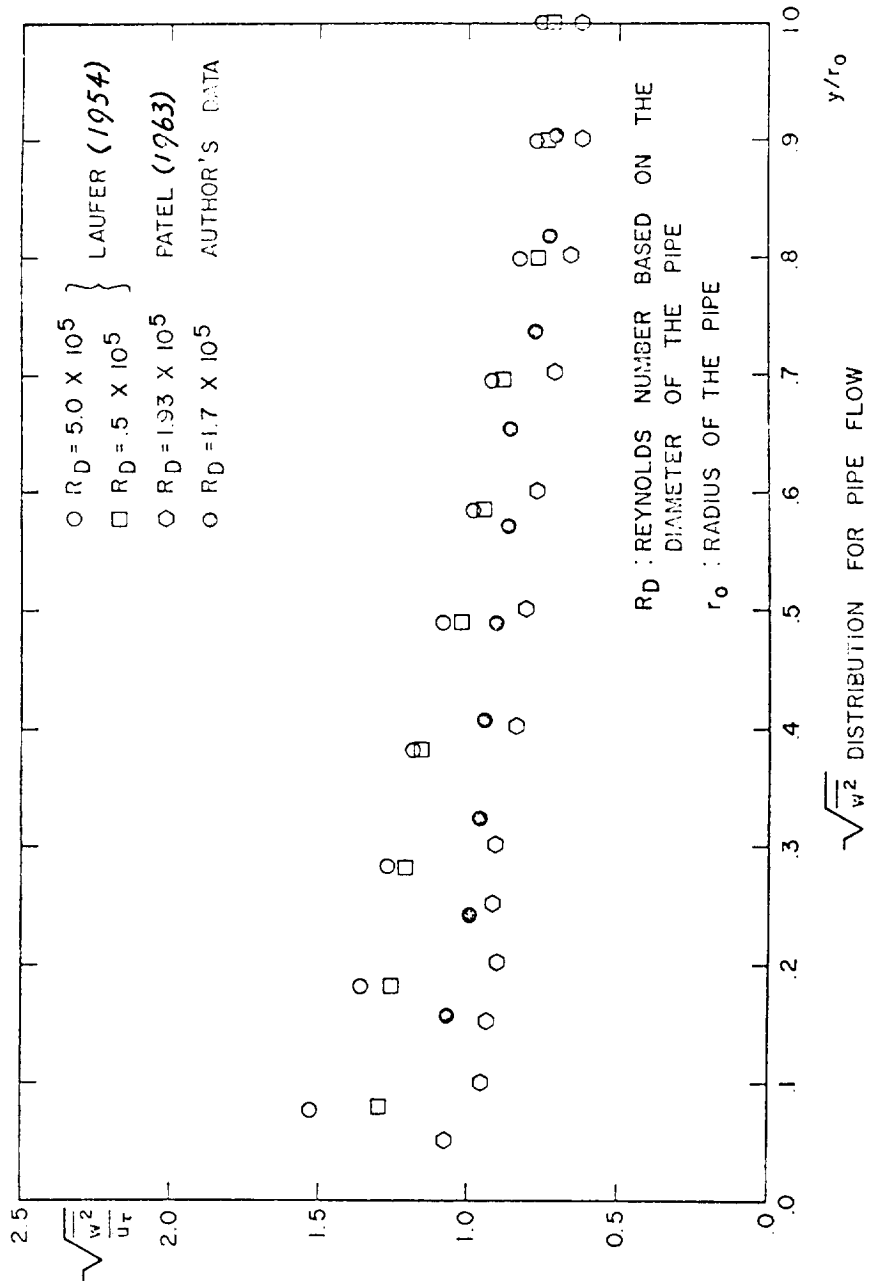


FIGURE 98

STATION 1 DELS (IN)	TABLE 1 CONSTANT PRESSURE FLOW ALONG CONVEX WALL		
	X (IN)	Y (IN)	P (IN)
0.083	24.00	0.054	0.0
0.004			70.27
0.006			U (FT/SEC)
0.008			23.83
0.010			26.29
0.012			30.13
0.014			33.61
0.019			35.19
0.024			36.83
0.029			39.33
0.034			40.92
0.039			42.34
0.044			43.15
0.054			43.92
0.064			44.72
0.074			45.81
0.084			47.16
0.094			48.12
0.104			49.24
0.124			50.13
0.144			50.69
0.164			52.41
0.184			54.15
0.204			55.96
0.224			57.06
0.244			58.70
0.264			59.82
0.284			61.11
0.304			62.30
0.324			63.20
0.344			64.20
0.364			65.08
0.384			65.90
0.404			66.76
0.454			67.08
0.504			67.61
0.554			68.77
0.604			69.50
0.654			69.87
0.704			70.12
0.754			70.27
0.804			70.27
0.854			70.27
0.904			70.27
0.954			70.27
1.004			70.27
1.104			70.27
1.204			70.27
1.304			70.27
1.404			70.27
1.504			70.27
1.604			70.27
1.704			70.27

TABLE 2 CONSTANT PRESSURE FLOW ALONG CONVEY WALL		
STATION 2	γ (IN) = 52.50	l (IN) = 10.590
DELS (IN) = 0.112	THETA (IN) = 0.085	UPW (FT/SEC) = 79.74
Y (IN)		U (FT/SEC)
0.004		26.88
0.006		29.61
0.008		32.96
0.010		35.87
0.012		38.52
0.014		40.34
0.019		43.38
0.024		45.39
0.029		46.77
0.034		48.19
0.039		49.24
0.044		50.26
0.054		52.17
0.064		53.85
0.074		55.22
0.084		56.49
0.094		57.73
0.104		58.63
0.124		60.13
0.144		61.52
0.164		62.23
0.184		62.85
0.204		63.45
0.224		64.05
0.244		64.50
0.264		64.80
0.284		65.26
0.304		65.74
0.324		66.05
0.344		66.47
0.364		66.84
0.384		67.17
0.404		67.49
0.454		68.34
0.504		69.11
0.554		69.86
0.604		70.46
0.654		71.15
0.704		71.70
0.754		72.05
0.804		72.13
0.854		72.13
0.904		71.93
0.954		71.67
1.004		71.40
1.104		70.76
1.204		70.14
1.304		69.95
1.404		68.96
1.504		68.31
1.604		67.67
1.704		67.03

STATION 4 DEG (IN)	TABLE 3 CONSTANT PRESSURE FLOW ALONG CONVEX WALL		
	X (IN) = 54.50	T (IN) = 16.330	W (IN/SEC) = 73.37
0.118	THETA (IN) = 0.037	W (IN/SEC)	U (IN/SEC)
Y (IN)			
0.004		26.34	
0.006		30.62	
0.008		33.39	
0.010		36.36	
0.012		38.04	
0.014		39.83	
0.016		41.03	
0.024		43.04	
0.029		44.51	
0.034		45.64	
0.039		46.76	
0.044		47.73	
0.054		49.49	
0.064		51.14	
0.074		52.14	
0.084		53.52	
0.094		54.75	
0.104		55.91	
0.124		57.86	
0.144		59.48	
0.164		60.69	
0.184		61.54	
0.204		62.47	
0.224		63.08	
0.244		63.68	
0.264		64.29	
0.284		64.85	
0.304		65.35	
0.324		65.81	
0.344		66.15	
0.364		66.65	
0.384		66.99	
0.404		67.61	
0.454		68.56	
0.504		69.36	
0.554		70.24	
0.604		71.00	
0.654		71.55	
0.704		72.18	
0.754		72.41	
0.804		72.58	
0.854		72.56	
0.904		72.37	
0.954		72.15	
1.004		71.83	
1.104		71.73	
1.204		70.61	
1.304		69.97	
1.404		69.33	
1.504		68.69	
1.604		68.07	
1.704		67.44	

TABLE 4 CONSTANT PRESSURE FLOW ALONG CONVEX WALL			
STATION 6	X (IN) = 56.5	z (IN) = 11.36	
DELS (IN) =	0.125	THETA (IN) = 0.091	UPW (FT/SEC) = 78.79
	Y (IN)		U (FT/SEC)
	0.004		22.98
	0.006		25.46
	0.008		28.66
	0.010		31.94
	0.012		34.64
	0.014		36.50
	0.019		39.41
	0.024		41.53
	0.029		42.97
	0.034		44.05
	0.039		45.19
	0.044		45.92
	0.054		47.56
	0.064		48.92
	0.074		50.22
	0.084		51.56
	0.094		52.74
	0.104		53.81
	0.124		55.90
	0.144		57.77
	0.164		59.02
	0.184		60.45
	0.204		61.41
	0.224		62.30
	0.244		63.11
	0.264		63.74
	0.284		64.39
	0.304		64.84
	0.324		65.39
	0.344		65.92
	0.364		66.33
	0.384		66.86
	0.404		67.21
	0.454		68.19
	0.504		69.11
	0.554		69.80
	0.604		70.47
	0.654		71.37
	0.704		71.91
	0.754		72.24
	0.804		72.46
	0.854		72.55
	0.904		72.44
	0.954		72.19
	1.004		71.93
	1.104		71.34
	1.204		70.74
	1.304		70.13
	1.404		69.50
	1.504		68.89
	1.604		68.27
	1.704		67.67

TABLE 5 CONSTANT PRESSURE FLOW ALONG CONVEX WALL			
STATION 7 DELS(IN) =	X(IN) = 59.00 THETA(IN) = 0.093	E(IN) = 11.520 UFW(FT/SEC) = 78.34	U(FT/SEC)
	Y(IN)		
	0.004		21.84
	0.006		23.05
	0.008		27.93
	0.010		32.00
	0.012		35.15
	0.014		36.83
	0.019		39.00
	0.024		40.39
	0.029		41.82
	0.034		42.74
	0.039		43.31
	0.044		44.21
	0.054		45.68
	0.064		47.27
	0.074		48.43
	0.084		49.65
	0.094		50.84
	0.104		51.77
	0.124		53.99
	0.144		55.62
	0.164		57.61
	0.184		58.70
	0.204		60.16
	0.224		61.45
	0.244		62.21
	0.264		62.97
	0.284		63.74
	0.304		64.22
	0.324		64.83
	0.344		65.31
	0.364		65.88
	0.384		66.25
	0.404		66.77
	0.454		67.67
	0.504		68.63
	0.554		69.48
	0.604		70.28
	0.654		71.00
	0.704		71.63
	0.754		72.10
	0.804		72.37
	0.854		72.41
	0.904		72.23
	0.954		71.99
	1.004		71.72
	1.104		71.15
	1.204		70.53
	1.304		69.93
	1.404		69.35
	1.504		68.76
	1.604		68.16
	1.704		67.57

TABLE 6 CONSTANT PRESSURE FLOW ALONG CONVEX WALL			
STATION 8	X (IN) = 63.00	E (IN) = 11.840	
DELS (IN) = 0.133	TRFTA (IN) = 0.094	UPW (FT/SEC) = 78.66	
Y (IN)		U (FT/SEC)	
0.004		18.31	
0.006		20.05	
0.008		23.50	
0.010		27.51	
0.012		30.48	
0.014		32.82	
0.019		36.27	
0.024		38.28	
0.029		39.82	
0.034		40.91	
0.039		42.29	
0.044		42.93	
0.054		44.47	
0.064		45.66	
0.074		46.85	
0.084		48.02	
0.094		49.32	
0.104		50.16	
0.124		51.86	
0.144		54.33	
0.164		56.13	
0.184		57.64	
0.204		59.15	
0.224		60.40	
0.244		62.17	
0.264		63.09	
0.284		64.23	
0.304		65.03	
0.324		65.53	
0.344		66.09	
0.364		66.57	
0.384		67.20	
0.404		67.64	
0.454		68.50	
0.504		69.60	
0.554		70.19	
0.604		71.08	
0.654		71.83	
0.704		72.41	
0.754		72.77	
0.804		72.86	
0.854		72.78	
0.904		72.61	
0.954		72.36	
1.004		72.08	
1.104		71.52	
1.204		70.97	
1.304		70.41	
1.404		69.83	
1.504		69.28	
1.604		68.69	
1.704		68.11	

STATION DELS (IN)	TABLE 7 CONSTANT PRESSURE FLOW ALONG CONVEX WALL		
	X (IN)	Y (IN)	R (IN)
0.146	67.00	0.100	12.820
	THETA (IN)		78.79
			U (FT/SEC)
0.004			25.35
0.006			25.80
0.008			27.80
0.010			30.17
0.012			32.13
0.014			33.54
0.019			35.86
0.024			37.39
0.029			38.79
0.034			39.71
0.039			40.46
0.044			41.49
0.054			42.53
0.064			43.80
0.074			44.53
0.084			45.58
0.094			46.66
0.104			47.80
0.124			49.44
0.144			51.27
0.164			52.97
0.184			54.53
0.204			56.42
0.224			57.86
0.244			59.36
0.264			60.73
0.284			61.93
0.304			63.23
0.324			64.12
0.344			65.02
0.364			66.00
0.384			66.45
0.404			67.10
0.454			68.47
0.504			69.63
0.554			70.48
0.604			71.29
0.654			71.85
0.704			72.36
0.754			72.83
0.804			73.03
0.854			73.10
0.904			72.98
0.954			72.77
1.004			72.52
1.104			72.02
1.204			71.53
1.304			71.04
1.404			70.55
1.504			70.05
1.604			69.53
1.704			68.99

TABLE 8 CONSTANT PRESSURE FLOW ALONG CONVEX WALL			
STATION 11	X (IN) = 71.00	R (IN) = 12.820	
DELS (IN) = 0.155	THETA (IN) = 0.105	UPW (FT/SEC) = 78.98	
Y (IN)		U (FT/SEC)	
0.004		22.81	
0.006		24.40	
0.008		26.50	
0.010		30.32	
0.012		32.23	
0.014		33.30	
0.019		35.33	
0.024		37.01	
0.029		38.07	
0.034		39.23	
0.039		40.04	
0.044		40.60	
0.054		42.04	
0.064		42.98	
0.074		43.93	
0.084		44.91	
0.094		45.84	
0.104		46.89	
0.124		48.56	
0.144		50.13	
0.164		51.84	
0.184		53.01	
0.204		54.73	
0.224		56.17	
0.244		57.45	
0.264		59.18	
0.284		60.11	
0.304		61.39	
0.324		62.66	
0.344		63.61	
0.364		64.66	
0.384		65.60	
0.404		66.33	
0.454		68.00	
0.504		69.31	
0.554		70.23	
0.604		71.02	
0.654		71.86	
0.704		72.47	
0.754		72.82	
0.804		73.13	
0.854		73.20	
0.904		73.12	
0.954		72.95	
1.004		72.74	
1.104		72.22	
1.204		71.72	
1.304		71.22	
1.404		70.73	
1.504		70.21	
1.604		69.69	
1.704		69.15	

TABLE 9
CONSTANT PRESSURE FLOW ALONG CONVEX WALL

STATION 1	X (IN) = 24.00			R (IN) = 0.0		
Y (IN)	U**2	V**2	W**2	UV	UW	VW
0.70	0.176	0.053	0.026	-0.001	0.004	0.0
0.60	0.256	0.145	0.080	-0.024	-0.006	0.0
0.50	0.893	0.913	0.526	-0.379	-0.005	0.0
0.40	4.978	2.388	2.755	-1.902	0.108	0.0
0.35	8.278	3.113	5.065	-3.026	0.155	0.0
0.30	11.396	4.586	6.813	-4.183	0.247	0.0
0.25	14.743	6.243	8.588	-5.492	0.328	0.0
0.20	17.117	8.408	10.028	-6.626	0.107	0.0
0.15	19.664	9.890	11.007	-8.035	0.235	0.0
0.13	20.520	9.613	11.447	-7.923	0.195	0.0
0.11	21.443	10.156	11.979	-7.842	0.447	0.0
0.09	21.917	9.651	11.620	-8.057	0.452	0.0
0.07	23.085	8.512	12.649	-7.781	0.218	0.0
0.06	23.466	10.602	12.320	-8.210	0.384	0.0
0.06	23.466		12.320		0.384	
0.05	23.926		12.488		0.305	
0.04	24.293		12.752		0.511	
0.03	25.527		13.105		0.023	
0.02	27.932		13.151		0.051	

TABLE 10
CONSTANT PRESSURE FLOW ALONG CONVEX WALL

STATION 7	X (TN) = 59.00	R (TN) = 11.520				
Y (TN)	U**2	V**2	W**2	UV	UW	VW
1.50	0.138	0.018	0.055	-0.002	0.003	0.0
1.30	0.151	0.020	0.063	-0.004	-0.007	0.0
1.10	0.184	0.127	0.098	-0.006	-0.013	0.0
0.90	0.326	0.655	0.294	-0.012	-0.014	0.0
0.70	1.867	2.079	1.213	-0.210	-0.005	0.0
0.60	3.575	2.281	2.175	-0.395	0.072	0.0
0.50	4.309	1.912	3.211	-0.490	0.189	0.0
0.40	4.988	1.913	3.855	-0.538	0.224	0.0
0.35	5.495	2.015	4.106	-0.721	0.315	0.0
0.30	6.051	2.486	4.625	-0.935	0.329	0.0
0.25	7.309	4.916	4.998	-1.444	0.470	0.0
0.20	9.795	4.293	6.244	-2.458	0.670	0.0
0.15	11.967	7.664	7.389	-3.781	0.593	0.0
0.13	12.967	7.435	8.250	-4.166	0.673	0.0
0.11	14.001	8.662	8.336	-4.519	0.437	0.0
0.09	14.532	9.469	8.534	-4.884	0.520	0.0
0.07	14.977	9.015	8.759	-4.999	0.322	0.0
0.06	15.200	8.120	8.784	-5.053	0.345	0.0
0.06	15.200		8.784		0.345	
0.05	15.513		8.642		0.295	
0.04	15.479		8.614		0.371	
0.03	16.089		9.021		0.325	
0.02	16.533		8.653		0.252	

TABLE 11

CONSTANT PRESSURE FLOW ALONG CONVEX WALL

STATION	9	X (IN) =	67.00	P (IN) = 12.820		
Y (IN)	U**2	V**2	W**2	UV	UW	VW
1.50	0.428	0.016	0.364	0.059	-0.136	0.0
1.30	0.388	0.043	0.307	0.064	0.001	0.0
1.10	0.400	0.200	0.333	0.051	-0.016	0.0
0.90	0.536	0.888	0.415	-0.002	0.027	0.0
0.70	1.994	1.708	1.254	0.027	0.095	0.0
0.60	2.973	1.816	1.608	0.200	0.209	0.0
0.50	3.512	1.952	2.124	0.340	0.245	0.0
0.40	4.013	3.196	2.631	-0.230	0.285	0.0
0.35	4.737	5.047	3.153	-0.867	0.274	0.0
0.30	6.081	6.516	4.037	-1.846	0.131	0.0
0.25	8.646	9.081	6.024	-3.242	-0.122	0.0
0.20	10.827	8.723	7.505	-4.197	-0.125	0.0
0.15	13.563	10.292	9.388	-4.526	-0.244	0.0
0.13	14.514	9.408	9.955	-4.641	-0.180	0.0
0.11	15.564	10.424	10.240	-4.857	-0.212	0.0
0.09	16.109	9.404	10.203	-4.697	-0.122	0.0
0.07	16.506	8.441	10.179	-4.950	0.105	0.0
0.06	16.520	7.357	10.442	-5.843	0.094	0.0
0.06	16.520		10.442		0.094	
0.05	16.868		10.417		0.007	
0.04	17.063		10.445		0.009	
0.03	17.696		10.379		0.011	
0.02	18.699		10.167		0.063	

TABLE 12

CONSTANT PRESSURE FLOW ALONG CONVEX WALL

STATION 11	X (IN) = 71.00			F (IN) = 12.820		
Y (IN)	U**2	V**2	W**2	UV	UW	vw
1.50	0.876	1.911	1.121	0.426	-0.015	0.0
1.30	0.733	1.620	0.857	0.404	0.046	0.0
1.10	0.710	1.361	0.681	0.401	0.072	0.0
0.90	0.820	1.117	0.761	0.182	-0.023	0.0
0.70	2.098	1.539	1.424	0.115	0.052	0.0
0.60	2.632	1.775	1.746	0.242	0.133	0.0
0.50	2.900	1.920	2.100	0.209	0.134	0.0
0.40	3.207	2.604	2.363	-0.313	0.055	0.0
0.35	3.676	2.757	2.758	-0.854	-0.182	0.0
0.30	4.681	5.028	3.097	-1.941	-0.323	0.0
0.25	6.497	6.950	4.157	-3.097	-0.451	0.0
0.20	9.927	8.916	5.606	-4.328	-0.446	0.0
0.15	12.951	9.478	8.078	-5.383	-0.488	0.0
0.13	13.903	10.100	8.505	-5.478	-0.699	0.0
0.11	15.193	9.762	9.329	-5.870	-0.382	0.0
0.09	15.515	9.956	9.565	-5.817	-0.500	0.0
0.07	15.915	10.581	9.098	-5.741	-0.298	0.0
0.06	16.086	8.444	9.433	-5.518	-0.332	0.0
0.06	16.086		9.433		-0.332	
0.05	16.174		9.607		-0.200	
0.04	16.337		9.696		-0.006	
0.03	16.743		9.263		-0.215	
0.02	17.635		9.603		0.169	

TABLE 13 SEPARATING FLOW ALONG CONVEX WALL			
STATION 1 DELS (IN) =	X (IN) = 24.00 THETA (IN) = 0.068	R (IN) = 0.0	U (FT/SEC) = 70.95
	Y (IN)		U (FT/SEC)
	0.004		21.91
	0.006		25.64
	0.008		29.57
	0.010		32.47
	0.012		34.71
	0.014		36.13
	0.019		38.99
	0.024		40.39
	0.029		41.82
	0.034		42.93
	0.039		43.75
	0.044		44.73
	0.054		45.82
	0.064		47.12
	0.074		48.15
	0.084		48.96
	0.094		49.69
	0.104		50.50
	0.124		51.82
	0.144		53.28
	0.164		54.43
	0.184		56.11
	0.204		57.31
	0.224		58.96
	0.244		59.79
	0.264		60.95
	0.284		62.18
	0.304		63.26
	0.324		64.31
	0.344		64.98
	0.364		65.68
	0.384		66.36
	0.404		66.97
	0.454		68.14
	0.504		69.01
	0.554		69.63
	0.604		70.05
	0.654		70.49
	0.704		70.76
	0.754		70.88
	0.804		70.95
	0.854		70.95
	0.904		70.95
	0.954		70.95
	1.004		70.95
	1.104		70.95
	1.204		70.95
	1.304		70.95
	1.404		70.95
	1.504		70.95
	1.604		70.95
	1.704		70.95
	1.804		70.95
	1.904		70.95
	2.004		70.95

TABLE 14
SEPARATING FLOW ALONG CONVEX WALL

STATION 2	X (IN) =	52.50	R (IN) =	10.500
DELS (IN) =	0.118	THETA (IN) =	0.087	UPW (FT/SEC) = 77.33
	Y (IN)			U (FT/SFC)
	0.004			25.17
	0.006			27.52
	0.008			30.71
	0.010			33.30
	0.012			35.33
	0.014			36.91
	0.019			40.72
	0.024			42.21
	0.029			42.92
	0.034			44.42
	0.039			45.13
	0.044			45.86
	0.054			47.33
	0.064			49.24
	0.074			50.42
	0.084			51.62
	0.094			53.26
	0.104			54.31
	0.124			56.30
	0.144			57.86
	0.164			59.07
	0.184			60.11
	0.204			60.94
	0.224			61.72
	0.244			62.18
	0.264			62.79
	0.284			63.25
	0.304			63.81
	0.324			64.22
	0.344			64.74
	0.364			65.25
	0.384			65.71
	0.404			66.18
	0.454			67.20
	0.504			68.00
	0.554			68.99
	0.604			69.73
	0.654			70.32
	0.704			70.76
	0.754			70.99
	0.804			71.14
	0.854			71.07
	0.904			70.91
	0.954			70.63
	1.004			70.34
	1.104			69.68
	1.204			69.02
	1.304			68.37
	1.404			67.73
	1.504			67.09
	1.604			66.46
	1.704			65.84
	1.804			65.22
	1.904			64.61
	2.004			64.00

TABLE 15 SEPARATING FLOW ALONG CONVEX WALL			
STATION 4	X (IN) = 54.50	R (IN) = 10.890	
DELS (IN) =	0.153	THETA (IN) = 0.105	UPW (FT/SEC) = 74.61
	Y (IN)		U (FT/SEC)
	0.004		20.95
	0.006		22.33
	0.008		23.37
	0.010		24.77
	0.012		26.98
	0.014		28.55
	0.019		31.82
	0.024		33.49
	0.029		34.93
	0.034		35.98
	0.039		37.09
	0.044		37.98
	0.054		39.13
	0.064		40.74
	0.074		41.91
	0.084		43.18
	0.094		44.29
	0.104		45.50
	0.124		47.57
	0.144		49.80
	0.164		51.44
	0.184		53.07
	0.204		54.59
	0.224		55.73
	0.244		56.68
	0.264		57.48
	0.284		58.17
	0.304		58.85
	0.324		59.49
	0.344		60.01
	0.364		60.51
	0.384		61.06
	0.404		61.55
	0.454		62.74
	0.504		63.75
	0.554		64.70
	0.604		65.59
	0.654		66.46
	0.704		67.12
	0.754		67.71
	0.804		68.14
	0.854		68.33
	0.904		68.39
	0.954		68.27
	1.004		68.04
	1.104		67.42
	1.204		66.80
	1.304		66.19
	1.404		65.58
	1.504		64.99
	1.604		64.39
	1.704		63.80
	1.804		63.22
	1.904		62.64
	2.004		62.07

TABLE 16
SEPARATING FLOW ALONG CONVEX WALL

STATION 6	X (IN) = 56.50	P (IN) = 11.200
DELS (IN) =	0.197	THETA (IN) = 0.127
	Y (IN)	UPW (FT/SEC) = 72.32
	0.004	U (FT/SEC)
	0.006	18.60
	0.008	20.85
	0.010	21.90
	0.012	23.06
	0.014	24.26
	0.019	25.36
	0.024	26.73
	0.029	28.38
	0.034	29.36
	0.039	29.69
	0.044	30.47
	0.054	31.07
	0.064	32.24
	0.074	33.41
	0.084	34.82
	0.094	35.66
	0.104	36.59
	0.124	37.62
	0.144	39.94
	0.164	41.43
	0.184	43.19
	0.204	45.09
	0.224	46.68
	0.244	48.53
	0.264	49.69
	0.284	51.07
	0.304	52.09
	0.324	53.08
	0.344	54.14
	0.364	54.73
	0.384	55.57
	0.404	56.09
	0.454	56.70
	0.504	58.08
	0.554	59.26
	0.604	60.34
	0.654	61.28
	0.704	62.28
	0.754	63.17
	0.804	63.98
	0.854	64.73
	0.904	65.36
	0.954	65.67
	1.004	65.85
	1.104	65.91
	1.204	65.53
	1.304	64.94
	1.404	64.37
	1.504	63.79
	1.604	63.23
	1.704	62.67
	1.804	62.11
	1.904	61.56
	2.004	61.01
		60.47

STATION 7 DELS(IN) =	TABLE 17 SEPARATING FLOW ALONG CONVEX WALL		
	X(IN) = 59.00	P(IN) = 11.520	U(FT/SEC) = 68.76
Y(IN)			
0.004			16.01
0.006			17.30
0.008			17.54
0.010			18.78
0.012			19.51
0.014			20.40
0.019			21.13
0.024			21.90
0.029			22.42
0.034			22.93
0.039			23.69
0.044			23.91
0.054			24.86
0.064			25.53
0.074			26.18
0.084			26.96
0.094			27.13
0.104			27.97
0.124			29.62
0.144			31.06
0.164			32.78
0.184			33.92
0.204			36.05
0.224			37.15
0.244			38.99
0.264			40.22
0.284			41.60
0.304			43.02
0.324			44.14
0.344			45.40
0.364			46.39
0.384			47.48
0.404			48.05
0.454			50.13
0.504			51.47
0.554			53.09
0.604			54.31
0.654			55.28
0.704			56.49
0.754			57.35
0.804			58.29
0.854			59.33
0.904			60.14
0.954			60.87
1.004			61.52
1.104			61.89
1.204			61.90
1.304			61.40
1.404			60.87
1.504			60.34
1.604			59.82
1.704			59.30
1.804			58.79
1.904			58.28
2.004			57.78

TABLE 18
SEPARATING FLOW ALONG CONVEX WALL

STATION 9 DELS(IN) =	X (IN) = 62.50 THITA (IN) = 0.212	R (IN) = 11.840 UPW (FT/SEC) = 65.58
Y (IN)		U (FT/SEC)
0.004		15.33
0.006		15.28
0.008		15.71
0.010		16.13
0.012		16.61
0.014		16.86
0.019		17.96
0.024		18.81
0.029		18.97
0.034		19.46
0.039		19.36
0.044		19.71
0.054		20.15
0.064		20.28
0.074		20.82
0.084		20.95
0.094		21.42
0.104		21.71
0.124		22.56
0.144		23.38
0.164		24.32
0.184		25.53
0.204		26.16
0.224		27.51
0.244		28.54
0.264		29.24
0.284		30.69
0.304		32.01
0.324		33.24
0.344		34.31
0.364		35.60
0.384		36.74
0.404		37.52
0.454		40.23
0.504		42.72
0.554		44.52
0.604		46.16
0.654		47.30
0.704		48.54
0.754		49.58
0.804		50.53
0.854		51.31
0.904		52.20
0.954		52.99
1.004		53.85
1.104		55.59
1.204		57.07
1.304		58.00
1.404		57.99
1.504		57.76
1.604		57.27
1.704		56.79
1.804		56.32
1.904		55.84
2.004		55.37

TABLE 19 SEPARATING FLOW ALONG CONVEX WALL			
STATION 11 DELS(IN) =	X (IN) = 66.00 THETA(IN) = 0.233	R (IN) = 12.820 UPW(FT/SEC) = 62.95	U (FT/SEC)
	Y(IN)		
	0.004		11.39
	0.006		11.34
	0.008		11.28
	0.010		11.23
	0.012		11.17
	0.014		11.12
	0.019		10.98
	0.024		11.93
	0.029		12.01
	0.034		12.59
	0.039		13.34
	0.044		13.86
	0.054		14.00
	0.064		14.65
	0.074		14.44
	0.084		14.66
	0.094		15.04
	0.104		15.25
	0.124		15.88
	0.144		16.37
	0.164		17.48
	0.184		18.40
	0.204		19.52
	0.224		20.22
	0.244		21.20
	0.264		22.30
	0.284		23.24
	0.304		24.35
	0.324		25.26
	0.344		26.38
	0.364		27.78
	0.384		28.97
	0.404		29.83
	0.454		32.44
	0.504		35.39
	0.554		37.82
	0.604		39.89
	0.654		41.89
	0.704		43.52
	0.754		45.00
	0.804		45.88
	0.854		47.08
	0.904		47.93
	0.954		48.88
	1.004		49.50
	1.104		51.13
	1.204		52.53
	1.304		54.01
	1.404		55.08
	1.504		55.69
	1.604		55.54
	1.704		55.31
	1.804		54.68
	1.904		54.26
	2.004		53.84

TABLE 29
SEPARATING FLOW ALONG CONVEX WALL

STATION 12 DELS(IN) =	X (IN) = 69.50	R (IN) = 12.820
	THETA (IN) = 0.270	UPW (FT/SEC) = 61.39
Y (IN)		U (FT/SEC)
0.004		13.04
0.006		12.99
0.008		12.95
0.010		12.90
0.012		12.83
0.014		12.91
0.019		12.70
0.024		12.58
0.029		12.66
0.034		13.03
0.039		13.10
0.044		13.18
0.054		13.05
0.064		13.93
0.074		13.72
0.084		13.51
0.094		13.75
0.104		14.07
0.124		14.53
0.144		14.48
0.164		14.51
0.184		14.96
0.204		15.31
0.224		15.58
0.244		16.24
0.264		16.86
0.284		17.19
0.304		17.71
0.324		18.63
0.344		19.05
0.364		19.91
0.384		20.85
0.404		21.34
0.454		23.38
0.504		25.64
0.554		27.95
0.604		30.32
0.654		33.17
0.704		35.58
0.754		37.69
0.804		39.40
0.854		41.07
0.904		42.59
0.954		43.90
1.004		45.08
1.104		46.77
1.204		48.25
1.304		49.58
1.404		50.85
1.504		51.93
1.604		52.85
1.704		53.29
1.804		53.22
1.904		52.92
2.004		52.51

TABLE 21

SEPARATING FLOW ALONG CONVEX WALL

STATION 1		X (IN) = 24.00		R (IN) = 0.0		
Y (IN)	U**2	V**2	W**2	UV	UW	VW
3.00	0.146	0.057	0.006	-0.010	-0.001	0.019
1.00	0.158	0.057	0.006	-0.010	-0.001	0.019
0.90	0.173	0.080	0.020	-0.031	0.0	0.023
0.80	0.214	0.097	0.060	-0.051	0.003	0.024
0.70	0.408	0.286	0.189	-0.102	0.006	-0.004
0.60	1.591	1.094	1.067	-0.536	0.020	-0.115
0.55	3.294	1.643	1.829	-1.236	0.034	-0.277
0.50	5.559	2.883	2.696	-2.052	0.113	-0.190
0.45	7.748	3.361	4.619	-2.878	0.104	-0.254
0.40	9.800	4.411	6.456	-3.750	0.045	-0.222
0.35	13.524	5.400	7.712	-4.649	0.085	-0.371
0.30	15.546	6.608	9.443	-5.559	-0.063	-0.409
0.25	17.276	7.102	10.091	-6.516	-0.091	-0.476
0.20	18.470	8.608	10.667	-7.223	-0.070	-0.496
0.15	21.140	9.102	11.097	-8.116	-0.046	-0.326
0.10	23.306	9.192	12.176	-8.245	-0.074	-0.236
0.05	24.760	8.902	12.206	-8.135	-0.139	-0.191
0.05	24.760		12.206		-0.139	
0.04	25.414		12.859		0.029	
0.03	28.137		13.503		-0.030	
0.02	28.788		14.528		-0.081	

TABLE 22
SEPARATING FLOW ALONG CONVEX WALL

STATION 4	X (IN) = 54.50			R (IN) = 10.890		
Y (IN)	U**2	V**2	W**2	UV	UW	VW
1.40	0.159	-0.384	0.060	0.249	0.007	0.019
1.20	0.250	-0.212	0.193	0.193	0.029	0.045
1.00	0.901	0.243	0.701	0.265	0.169	0.442
0.90	2.026	1.159	1.609	0.318	0.671	0.391
0.80	3.011	1.574	1.859	0.413	0.505	1.194
0.70	4.019	2.180	2.656	0.355	0.772	1.000
0.60	4.954	2.793	3.254	0.161	0.583	1.393
0.50	5.460	3.295	3.651	-0.234	0.532	1.132
0.40	5.899	2.741	3.943	-0.035	0.480	1.082
0.30	6.132	2.841	4.067	-0.187	0.446	1.035
0.20	6.945	2.558	4.754	-0.544	0.239	0.907
0.15	8.450	3.232	5.750	-1.307	-0.127	1.420
0.10	12.718	2.622	7.542	-2.113	-0.335	0.948
0.05	14.740	5.136	9.608	-3.933	-0.778	1.205
0.05	14.740		9.608		-0.778	
0.02	12.602		5.734		-0.265	

TABLE 23
SEPARATING FLOW ALONG CONVEX WALL

STATION	9	X (IN) =	62.50	R (IN) =	11.840		
Y (IN)		U**2	V**2	W**2	UV	UW	VW
2.00		0.350	-0.347	0.188	0.414	0.006	0.188
1.80		0.358	-0.172	0.243	0.427	0.007	0.172
1.60		0.381	-0.283	0.156	0.352	0.009	0.163
1.40		0.532	0.065	0.250	0.401	0.019	0.283
1.20		1.221	0.394	0.813	0.146	-0.139	0.549
1.00		2.402	1.101	1.643	-0.086	-0.275	0.456
0.90		2.830	0.797	1.955	-0.082	-0.444	0.290
0.80		3.250	0.713	2.152	-0.073	-0.548	0.196
0.70		3.653	0.992	2.372	-0.273	-0.608	0.086
0.60		4.351	1.213	2.863	-0.442	-0.616	0.005
0.50		6.795	1.262	4.220	-0.709	-0.625	0.189
0.40		11.144	2.660	7.169	-2.142	-0.483	0.706
0.30		14.963	3.885	9.820	-3.366	-0.408	1.100
0.20		15.452	4.560	9.944	-4.672	-0.257	1.781
0.10		12.169	4.325	7.226	-3.187	-0.186	0.549
0.05		9.967	3.011	6.137	-2.295	-0.060	0.452
0.05		9.967		6.137		-0.060	
0.02		9.166		5.105		-0.102	

TABLE 24
SEPARATING FLOW ALONG CONVEX WALL

STATION 11		X (IN) = 66.00	F (IN) = 12.820			
Y (IN)	U**2	V**2	W**2	UV	UW	VW
2.00	1.207	-0.302	0.565	0.625	-0.025	0.501
1.80	1.137	-0.272	0.454	0.878	-0.029	0.383
1.60	1.044	-0.541	0.331	1.012	0.003	0.227
1.40	1.468	-0.557	0.634	1.399	0.002	0.270
1.20	2.569	0.909	1.388	0.651	-0.286	0.482
1.00	3.317	1.097	1.934	0.191	-0.618	0.341
0.90	3.526	1.203	2.165	0.045	-0.708	0.471
0.80	3.942	0.979	2.570	-0.079	-0.745	0.417
0.70	5.196	1.787	3.480	-0.648	-0.623	0.631
0.60	7.905	1.828	5.018	-0.902	-0.345	0.967
0.50	11.354	2.793	7.103	-1.874	-0.063	1.196
0.40	14.703	4.580	9.557	-3.325	0.022	1.702
0.30	15.509	5.090	10.366	-3.874	-0.057	1.664
0.20	14.560	4.263	8.410	-3.356	0.026	1.040
0.10	10.682	3.460	6.967	-2.503	0.150	0.999
0.05	8.857	2.561	5.543	-1.727	0.187	0.262
0.05	8.857		5.543		0.187	
0.02	7.778		4.280		0.165	

TABLE 25
SEPARATING FLOW ALONG CONVEX WALL

STATION 12		X (IN) = 69.50	P (IN) = 12.820			
Y (IN)	U**2	V**2	W**2	UV	UW	VW
2.00	4.113	1.236	1.892	2.325	-0.147	1.839
1.80	3.603	1.489	1.244	1.993	0.023	1.428
1.60	3.103	1.450	1.169	1.530	-0.082	0.980
1.40	3.499	0.664	1.522	1.881	-0.345	0.774
1.20	3.907	1.925	2.132	0.557	-0.691	0.732
1.00	4.495	2.405	2.991	-0.299	-0.685	0.613
0.90	5.858	2.389	4.045	-0.859	-0.584	0.744
0.80	8.502	2.153	5.826	-1.176	-0.411	0.560
0.70	11.985	3.142	7.322	-2.208	-0.153	0.885
0.60	15.402	2.710	9.762	-2.816	-0.493	2.177
0.50	17.019	5.309	11.581	-4.279	-0.507	2.080
0.40	17.899	3.601	11.068	-3.190	-0.921	2.218
0.30	16.634	2.981	11.354	-3.215	-1.254	2.786
0.20	14.534	3.286	8.707	-2.726	-0.925	2.603
0.10	10.651	4.211	6.083	-2.973	-0.623	1.311
0.10	10.651		6.083		-0.623	
0.05	9.295		5.005		-0.514	
0.02	5.511		2.411		-0.287	

TABLE 25 CONSTANT PRESSURE FLOW ALONG CONCAVE WALL			
STATION 1 DELS(IN) =	X(IN) = 24.00 THFTA(IN) = 0.062	P(IN) = 0.0 UPW(FT/SEC) = 70.63	U(FT/SEC)
	Y(IN)		
	0.006		25.50
	0.008		29.09
	0.010		32.77
	0.015		36.96
	0.020		39.15
	0.025		40.64
	0.030		41.84
	0.035		42.83
	0.040		43.93
	0.050		45.33
	0.060		46.52
	0.070		47.82
	0.080		48.91
	0.090		50.01
	0.100		50.80
	0.120		52.20
	0.140		53.89
	0.160		55.39
	0.180		57.18
	0.200		58.18
	0.220		59.77
	0.240		61.06
	0.260		62.06
	0.280		63.46
	0.300		64.05
	0.320		65.05
	0.340		65.75
	0.360		66.64
	0.380		67.14
	0.400		67.64
	0.450		68.54
	0.500		69.23
	0.550		69.73
	0.600		70.13
	0.650		70.23
	0.700		70.33
	0.750		70.53
	0.800		70.63
	0.850		70.63

TABLE 2 CONSTANT PRESSURE FLOW ALONG CONCAVE WALL			
STATION 2 DELS (IN) =	X (IN) = 70.00 THETA (IN) = 0.235	U (IN) = -17.830 UPW (FT/SEC) = 61.20	U (FT/SEC)
	Y (IN)		
	0.008		33.19
	0.010		34.53
	0.015		36.68
	0.020		38.11
	0.025		39.03
	0.030		39.85
	0.035		40.47
	0.040		40.98
	0.060		42.41
	0.080		43.20
	0.100		43.95
	0.130		44.68
	0.160		44.98
	0.190		45.49
	0.220		46.00
	0.250		46.51
	0.280		46.82
	0.310		47.23
	0.340		47.54
	0.370		47.95
	0.400		48.36
	0.450		48.77
	0.500		49.48
	0.550		50.10
	0.600		50.40
	0.650		51.02
	0.700		51.43
	0.750		52.04
	0.800		52.45
	0.850		52.86
	0.900		53.48
	0.950		54.09
	1.000		54.50
	1.100		55.04
	1.200		57.37
	1.300		58.91
	1.400		60.34
	1.500		61.83
	1.600		63.31
	1.700		64.54
	1.800		65.47
	1.900		66.69
	2.000		67.31
	2.500		70.09
	3.000		72.33

TABLE 28 CONSTANT PRESSURE FLOW ALONG CONCAVE WALL			
STATION 3	X (IN) = 70.00	v (IN) = -17.830	
DELS (IN) =	0.200	THETA (IN) = 0.153	UPW (FT/SEC) = 61.20
	Y (IN)		U (FT/SEC)
	0.008		31.18
	0.010		32.70
	0.015		35.52
	0.020		37.44
	0.025		38.45
	0.030		39.26
	0.035		39.76
	0.040		40.37
	0.060		41.78
	0.080		42.89
	0.100		43.60
	0.130		44.41
	0.160		44.91
	0.190		45.52
	0.220		46.02
	0.250		46.42
	0.280		47.03
	0.310		47.43
	0.340		47.84
	0.370		48.24
	0.400		48.85
	0.450		49.55
	0.500		50.66
	0.550		51.64
	0.600		52.68
	0.650		53.99
	0.700		55.10
	0.750		56.21
	0.800		57.43
	0.850		58.43
	0.900		59.24
	0.950		60.45
	1.000		61.46
	1.100		63.28
	1.200		64.59
	1.300		65.50
	1.400		66.00
	1.500		66.31
	1.600		66.71
	1.700		67.01
	1.800		67.32
	1.900		67.72
	2.000		68.32
	2.500		70.55
	3.000		72.97

STATION	TABLE 29		
	4	CONSTANT PRESSURE FLOW ALONG CONCAVE WALL	
DELS(IN) =	0.250	X(IN) = 96.00	R(IN) = -21.870
		THETA(IN) = 0.227	UPW(FT/SEC) = 61.60
	Y(IN)		U(FT/SEC)
	0.006		37.69
	0.008		39.48
	0.010		40.74
	0.015		43.17
	0.020		44.43
	0.025		45.38
	0.030		46.22
	0.035		47.06
	0.040		47.59
	0.060		49.69
	0.080		51.17
	0.100		52.22
	0.150		54.33
	0.200		55.27
	0.250		55.90
	0.300		56.54
	0.350		56.85
	0.400		57.38
	0.500		57.91
	0.600		58.42
	0.700		58.75
	0.800		59.17
	0.900		59.80
	1.000		60.11
	1.200		61.17
	1.400		62.22
	1.600		63.17
	1.800		63.80
	2.000		64.33
	2.200		64.85
	2.400		64.85
	2.600		65.17
	2.800		65.59
	3.000		66.43
	3.200		67.17
	3.400		68.04
	3.600		70.12
	3.800		71.70
	4.000		73.38
	4.200		74.65
	4.400		75.70
	4.600		76.75
	4.800		77.38
	5.000		78.01

TABLE 30 CONSTANT PRESSURE FLOW ALONG CONCAVE WALL			
STATION 5	X (IN) = 96.00	R (IN) = -21.876	
DELS (IN) = 0.129	THETA (IN) = 0.113	UPW (FT/SEC) = 61.60	
Y (IN)		U (FT/SEC)	
0.006		31.26	
0.008		35.17	
0.010		37.94	
0.015		41.85	
0.020		43.91	
0.025		45.24	
0.030		46.38	
0.035		47.09	
0.040		47.81	
0.060		50.28	
0.080		51.93	
0.100		52.96	
0.150		54.70	
0.200		55.83	
0.250		56.35	
0.300		56.86	
0.350		57.17	
0.400		57.48	
0.500		57.99	
0.600		58.40	
0.700		58.82	
0.800		59.23	
0.900		59.74	
1.000		60.36	
1.100		60.98	
1.200		61.80	
1.300		62.62	
1.400		63.34	
1.500		64.16	
1.600		64.78	
1.700		65.50	
1.800		66.22	
1.900		66.73	
2.000		67.25	
2.200		68.28	
2.400		69.10	
2.600		69.92	
2.800		70.54	
3.000		71.16	

TABLE 31
CONSTANT PRESSURE FLOW ALONG CONCAVE WALL

STATION 1	X (IN) = 24.00			R (IN) = 0.0		
Y (IN)	U**2	V**2	W**2	UV	UW	vw
3.00	0.129	0.057	0.007	-0.008	0.000	-0.001
1.00	0.134	0.057	0.007	-0.008	0.001	-0.001
0.90	0.143	0.063	0.008	-0.024	0.001	-0.002
0.80	0.160	0.119	0.034	-0.039	0.002	-0.004
0.70	0.286	0.455	0.306	-0.093	0.014	-0.022
0.60	1.840	1.188	1.274	-0.716	0.024	-0.040
0.55	3.406	2.445	2.058	-1.461	0.049	-0.083
0.50	6.139	3.348	3.281	-2.343	0.105	-0.175
0.45	8.670	4.462	5.340	-3.306	0.123	-0.205
0.40	11.278	5.318	7.102	-4.159	0.128	-0.383
0.35	14.142	6.259	8.898	-4.929	0.116	-0.432
0.30	16.071	7.110	9.920	-5.743	0.021	-0.395
0.25	17.841	8.274	10.290	-6.694	0.166	-0.276
0.20	19.697	8.919	11.368	-7.410	0.170	-0.469
0.15	22.263	9.773	11.623	-8.073	0.101	-0.432
0.10	24.178	9.132	12.920	-8.246	0.068	-0.502
0.05	25.615	9.339	12.900	-8.341	0.049	-0.582
0.05	25.615		12.900		0.049	
0.04	26.440		13.135		0.103	
0.03	29.048		13.892		0.115	
0.02	30.763		14.816		0.003	

TABLE 32
CONSTANT PRESSURE FLOW ALONG CONCAVE WALL

STATION 2	X (IN) = 70.00			R (IN) = -17.830		
Y (IN)	U**2	V**2	W**2	UV	UW	VW
2.50	0.265	0.274	0.171	-0.007	0.012	-0.115
2.30	0.428	0.633	0.428	-0.123	0.064	-0.133
2.10	1.023	1.256	1.189	-0.287	0.279	-0.152
1.90	2.729	2.855	3.109	-0.979	0.881	-0.523
1.80	4.507	4.117	4.300	-1.818	1.607	-1.340
1.70	10.465	7.393	9.803	-4.241	3.805	-2.863
1.60	12.165	4.966	7.945	-3.117	4.036	-1.882
1.50	15.225	10.543	11.865	-6.996	5.688	-2.427
1.40	19.158	8.721	13.893	-6.440	6.845	-2.743
1.30	23.977	11.927	16.053	-8.810	8.312	-3.835
1.20	26.683	16.379	18.762	-11.497	9.615	-4.943
1.10	28.707	19.113	20.287	-12.791	10.330	-5.818
1.00	31.184	17.434	23.252	-11.414	11.335	-5.220
0.90	31.951	21.482	24.280	-14.246	11.762	-6.212
0.80	32.199	20.588	25.043	-13.577	11.361	-6.040
0.70	31.592	20.573	25.258	-12.980	10.069	-4.070
0.60	31.202	19.287	23.820	-12.538	8.897	-3.188
0.50	30.065	19.652	23.688	-13.062	7.678	-4.034
0.40	28.760	16.533	21.046	-11.204	5.587	-3.269
0.30	27.672	16.946	20.323	-10.866	3.714	-1.148
0.20	26.840	14.287	17.352	-9.170	2.803	-1.605
0.15	26.070	14.054	17.045	-8.561	2.587	-2.100
0.10	26.757	11.789	16.431	-7.190	2.600	-2.952
0.05	28.105	8.112	16.755	-5.260	2.497	-2.923
0.05	28.105		16.755		2.497	
0.04	28.609		17.198		2.389	
0.03	28.967		17.434		1.728	

TABLE 33
CONSTANT PRESSURE FLOW ALONG CONCAVE WALL

STATION 3	X (IN) = 70.00			R (IN) = -17.830		
Y (IN)	U**2	V**2	W**2	UV	UW	vw
1.60	0.305	0.354	0.238	-0.041	0.001	0.050
1.50	0.466	0.649	0.452	-0.159	0.006	0.031
1.40	0.929	0.977	0.934	-0.369	-0.008	0.015
1.30	2.799	2.646	1.704	-1.579	-0.092	0.140
1.20	5.862	5.391	2.930	-3.740	-0.376	0.585
1.10	11.722	7.308	6.091	-6.212	-0.406	0.408
1.00	16.769	8.896	10.578	-7.986	-1.216	0.459
0.90	23.398	11.293	12.566	-10.232	-1.182	0.423
0.80	27.340	15.746	16.376	-13.797	-1.621	0.969
0.70	29.905	15.233	18.886	-13.877	-1.548	0.138
0.60	30.405	15.230	19.516	-13.477	-2.494	1.651
0.50	29.866	18.552	20.790	-14.716	-2.106	0.205
0.40	28.639	17.947	19.940	-13.869	-2.637	1.069
0.30	25.624	17.314	20.202	-11.828	-2.177	0.085
0.20	25.337	15.047	18.767	-9.610	-3.352	1.679
0.15	24.552	13.944	19.534	-8.951	-3.425	0.597
0.10	25.957	12.342	19.071	-7.839	-3.604	-0.286
0.05	27.037	12.032	22.593	-7.017	-3.620	-0.256
0.05	27.037		22.593		-3.620	
0.04	28.165		19.969		-3.757	
0.03	28.711		20.146		-3.400	

TABLE 34
CONSTANT PRESSURE FLOW ALONG CONCAVE WALL

STATION 4	X (IN) = 96.00			T (IN) = -21.870		
Y (IN)	U**2	V**2	W**2	UV	UW	VW
4.65	2.530	3.402	3.550	-1.065	0.300	-1.713
4.45	3.700	5.255	4.650	-1.939	0.660	-2.343
4.25	5.550	7.656	6.050	-3.149	1.270	-3.335
4.05	8.600	11.419	8.250	-5.390	2.190	-4.398
3.85	13.130	15.324	10.530	-8.387	2.870	-6.013
3.65	16.650	16.656	12.100	-9.587	3.070	-5.480
3.45	18.380	17.139	13.250	-9.655	2.850	-5.126
3.25	19.070	15.454	14.630	-7.936	2.300	-3.864
3.05	19.100	17.336	16.250	-7.644	1.070	-2.742
2.85	18.300	19.719	18.370	-7.690	0.200	-0.773
2.65	16.870	20.656	20.700	-6.504	0.400	-1.247
2.45	16.000	21.573	22.650	-6.049	1.090	-0.633
2.20	15.214	20.458	21.952	-5.461	2.329	-1.939
2.00	14.493	21.283	21.620	-7.362	2.675	-2.097
1.80	14.847	21.885	22.328	-9.611	3.219	-3.442
1.60	15.611	17.918	22.609	-8.569	3.367	-4.615
1.40	16.076	19.986	22.880	-10.158	3.557	-5.135
1.20	16.162	19.973	23.301	-10.993	3.317	-4.902
1.00	15.853	19.916	23.669	-11.027	3.086	-4.233
0.80	15.948	18.906	24.485	-10.777	3.404	-4.202
0.60	16.546	16.874	24.583	-9.765	4.169	-4.774
0.40	19.124	13.810	21.845	-8.895	4.932	-3.972
0.20	24.427	9.155	20.899	-7.552	5.806	-3.712
0.10	29.209	7.386	19.581	-6.496	4.973	-2.863
0.05	30.481	7.798	19.059	-7.130	4.280	-4.109
0.05	30.481		19.059		4.280	
0.04	29.747		19.903		4.240	
0.03	29.977		19.251		4.322	

TABLE 35
CONSTANT PRESSURE FLOW ALONG CONCAVE WALL

STATION	5	X (IN) = 96.00	F (IN) = -21.870			
Y (IN)	U**2	V**2	W**2	UV	UW	VW
3.00	2.113	3.525	4.795	-1.195	0.418	-0.287
2.80	2.405	3.524	5.117	-1.144	0.350	0.190
2.60	2.563	4.091	5.985	-1.437	0.195	0.512
2.40	3.176	4.594	6.094	-1.629	0.215	0.638
2.20	4.275	6.593	6.846	-2.927	0.135	0.779
2.00	5.696	7.581	7.741	-3.709	-0.074	0.941
1.80	8.852	9.756	8.856	-5.572	-0.562	1.269
1.60	11.180	12.720	10.948	-7.960	-0.623	1.241
1.40	13.699	14.683	12.510	-9.442	-0.467	0.742
1.20	15.007	15.249	14.629	-9.904	-0.275	0.462
1.00	15.777	16.130	15.549	-10.268	0.033	-0.159
0.80	15.939	17.774	16.125	-10.619	0.093	-0.318
0.60	15.871	15.940	16.896	-8.924	-0.354	-0.091
0.40	16.536	12.503	17.886	-7.145	-0.938	-0.243
0.30	18.417	14.046	19.109	-8.366	-1.955	1.141
0.20	21.998	13.590	20.270	-8.578	-1.989	0.362
0.15	24.501	9.445	22.179	-7.045	-2.881	0.826
0.10	26.907	12.731	21.805	-9.511	-2.313	-0.965
0.05	28.437	5.068	23.729	-5.634	-1.845	-1.584
0.05	28.437		23.729		-1.845	
0.04	28.769		23.128		-1.654	
0.03	28.963		23.100		-1.679	

NATIONAL AERONAUTICS AND SPACE ADMINISTRATION
WASHINGTON, D.C. 20546

OFFICIAL BUSINESS
PENALTY FOR PRIVATE USE \$300

FIRST CLASS MAIL

POSTAGE AND FEES PAID
NATIONAL AERONAUTICS AND
SPACE ADMINISTRATION



POSTMASTER: If Undeliverable (Section 158
Postal Manual) Do Not Return

"The aeronautical and space activities of the United States shall be conducted so as to contribute . . . to the expansion of human knowledge of phenomena in the atmosphere and space. The Administration shall provide for the widest practicable and appropriate dissemination of information concerning its activities and the results thereof."

— NATIONAL AERONAUTICS AND SPACE ACT OF 1958

NASA SCIENTIFIC AND TECHNICAL PUBLICATIONS

TECHNICAL REPORTS: Scientific and technical information considered important, complete, and a lasting contribution to existing knowledge.

TECHNICAL NOTES: Information less broad in scope but nevertheless of importance as a contribution to existing knowledge.

TECHNICAL MEMORANDUMS: Information receiving limited distribution because of preliminary data, security classification, or other reasons.

CONTRACTOR REPORTS: Scientific and technical information generated under a NASA contract or grant and considered an important contribution to existing knowledge.

TECHNICAL TRANSLATIONS: Information published in a foreign language considered to merit NASA distribution in English.

SPECIAL PUBLICATIONS: Information derived from or of value to NASA activities. Publications include conference proceedings, monographs, data compilations, handbooks, sourcebooks, and special bibliographies.

TECHNOLOGY UTILIZATION PUBLICATIONS: Information on technology used by NASA that may be of particular interest in commercial and other non-aerospace applications. Publications include Tech Briefs, Technology Utilization Reports and Technology Surveys.

Details on the availability of these publications may be obtained from:

SCIENTIFIC AND TECHNICAL INFORMATION OFFICE

NATIONAL AERONAUTICS AND SPACE ADMINISTRATION

Washington, D.C. 20546